SEARCH FOR HEAVY NEUTRAL GAUGE BOSON *Z'* USING CMS DETECTOR AT THE LHC

A THESIS

Submitted to the

PANJAB UNIVERSITY, CHANDIGARH

For the Award of

DOCTOR OF PHILOSOPHY

2022

in

FACULTY OF SCIENCE

BY
AMANDEEP KAUR

GUIDE

Prof. J. B. Singh **Dr. Sunil Bansal**

DEPARTMENT OF PHYSICS
PANJAB UNIVERSITY
CHANDIGARH, INDIA

Dedicated To My

Family

&

Friends

Acknowledgement

"Great teachers emanate out of knowledge, passion and compassion"

- Dr. A.P.J Abdul Kalam

I have witnessed all these qualities in my wonderful teachers. I would like to express my sincere gratitude to my Ph.D. supervisors, Prof. J.B. Singh and Dr. Sunil Bansal, for their constant support, continued guidance and encouragement. Their dedication and direction have helped me to become a better and more thorough physicist.

I would also like to thank Prof. Suman Beri, Prof. Manjit Kaur, Prof. Vipin Bhatnagar, Dr. Nitish Dhingra and Dr. Sushil Singh Chauhan for their continuous support and efforts to provide us adequate facilities in the PU EHEP lab. Many thanks to India-CMS Collaboration and PU EHEP group for conducting regular meetings to discuss our work and give valuable suggestions.

I am thankful to Prof. Rajiv Kumar Puri, Chairman, Department of Physics, Panjab University, for providing adequate facilities to work in the department. Many thanks to former Chairperson Prof. Devinder Mehta for his continuous support and innumerable physics discussions, which have helped me improve my knowledge of the subject.

This research would not have been possible without the financial support of the Department of Science and Technology (DST). I am highly grateful to our CMS technical staff, Mr. Shiv, Mr. Amarjeet, Mr. Subhash and Mr. Navjot for their assistance in the GEM Laboratory. I would also like to thank Mr. Ajit and Mr. Gyan for helping me in the administrative work. I would like to thank the administrative, library, and purchase section staff at PU who contributed directly or indirectly throughout this research work.

I owe my sincere gratitude to the European Council for Nuclear Physics (CERN) for providing me the computing resources and hosting me at different points in time. I have thoroughly enjoyed going through all the intricacies of acquisition,

retrieval, analysis, and presentation of experimental data.

I would like to express my heartfelt gratitude to Prof. Sunanda Banerjee for his continuous guidance and support throughout my Ph.D Journey. I would also like to thank Prof. Teruki Kamon, Dr. Alfredo Gurrola, Dr. Andres Florez and the entire BSM3G group for all the discussions, that helped me to refine my understanding of physics beyond the standard model. Many thanks to Savanna R. Starko and Susan Olmsted for making my work life easier and a whole lot of fun. Thanks to Susan's cat for his purrfect sleepy poses, whenever I needed to see him.

Many thanks to my lab-mates for making this journey easy. I would like to express my gratitude to each one of my friends, whom I have met in different timezones, at different places and have always stood by my side through thick and thin. Each one of you taught me something. Special thanks to Rajat, Jyoti and Meena for putting up with my stupid jokes.

Words cannot express my gratitude to my family, who have supported me throughout this journey. This thesis owes most to them. I am indebted to my mother, Mrs. Surinder Kaur, for her love and unconditional support. I could never have reached this far without the efforts and support of my father, S. Balwinder Singh. Thanks for believing in me, Mummy and Papa. I am extremely grateful to my sisters for their immense support in this journey. I would not miss mentioning my nieces and nephews, who have always welcomed me with their tight little hugs and cute laughs.

Finally, I would like to convey my gratitude to everyone who contributed to the successful completion of this thesis, as well as my regret for not being able to thank everyone personally who helped me complete it.

Date: **(Amandeep Kaur)**

Abstract

The Standard Model of particle physics is a well-established framework which describes the nature of the matter in the universe and the way this matter interacts with each other. Though it is a well-tested framework and acts as a fundamental theory till now, it fails to describe various physics phenomena such as the existence of dark matter and dark energy in the universe, matter-antimatter asymmetry in the universe, prediction of neutrino masses and prediction of force carrier for the fourth fundamental force i.e. the gravitational force. To address these questions, many theories beyond the standard model have evolved with time such as the Grand Unified Theories, Supersymmetry, and String theory. These theories predict new gauge fields and interactions. A common manifestation of these new gauge fields and interactions is particles with TeV scale masses. One such particle is the heavy neutral spin-1 gauge boson, Z', which arises from extensions of the electroweak symmetry of the standard model. Z' is assumed to be a mediator between visible and dark sector solving the mysteries of dark matter and dark energy. Besides this, Z' with non-universal coupling to fermions qualifies as the most suitable candidate to answer the lepton flavour universality violating processes in the B-meson decays observed by LHCb, BaBar and Belle experiments. Additionally, recent results of the muon g-2 experiment at Fermilab strongly motivate the search for Z' to explain the anomalous magnetic moment of the muon. As Z' is predicted to be of the order of TeV mass, it is well within the energy reach (14 TeV) of the LHC experiment at CERN. The ATLAS and the CMS detector at the LHC have a wide range of Z' search programs. The recent results from these Z' searches have eluded the discovery thus far. These searches have assumed the production of Z' via Drell-Yan process at the LHC with sizable coupling to light quarks. One hypothesis is that the Z' coupling to quarks is smaller than that required for sensitivity in the Drell-Yan Z' searches.

To complement these searches, a new search for Z' boson produced via vector boson fusion (VBF) processes is presented in this Thesis. The VBF processes consider smaller Z' coupling to light quarks and allow the coupling to standard

model vector bosons (W or Z). Of particular interest are models with enhanced Z' couplings to third-generation fermions, which may explain the B-meson anomalies observed at LHCb, BaBar, and Belle experiments. Extensions to the standard model, proposed as an explanation for the high mass of the top quark, also predict Z' bosons that typically couple to third-generation fermions, motivating the $Z' \to \tau\tau$ decay states. Additionally, since Z' coupling to the standard model vector bosons is allowed, therefore, the $Z' \to WW$ decay width can be large, and thus motivates using this decay channel to re-interpret results for the $Z' \to WW$ scenario.

In this Thesis, we report the first results of the search for Z' through VBF processes at the LHC, using proton-proton (pp) collision data at the center-of-mass energy of 13 TeV collected by the CMS detector. The search comprises two decay channels of VBF $Z' \to \tau\tau$ and VBF $Z' \to WW$ production: $Z' \to (WW \to)\tau\tau \to \tau_e\tau_h$ and $Z' \to (WW \to)\tau\tau \to \tau_\mu\tau_h$ where τ_e and τ_μ are the leptonic decays of tau lepton and τ_h refers to hadronically decaying tau lepton. The potential backgrounds are estimated using data-driven techniques and excess of events above the standard model background predictions are investigated for. In the absence of significant excesses over standard model predictions, 95% CL upper limits on the cross-section times branching ratio are calculated and the estimated value is presented as a limit. For a broad and generic discussion, the upper limits are calculated for various coupling scenarios with different values of branching ratios of VBF $Z' \to \tau\tau$ and VBF $Z' \to WW$ decays. With the present analysis, Z' for masses lower than 1.77 TeV is excluded for $B(Z' \to \tau\tau) = 20\%$ with enhanced coupling to third-generation fermions. Similarly, the Z' for masses lower than 1.20 TeV is excluded for $B(Z' \to WW) = 80\%$ with enhanced coupling to third-generation fermions. These are the first and the most stringent limits set so far.

The present Thesis is also based on the upgradation of the CMS muon detector system with the gaseous electron multiplier (GEM) detectors. These detectors are added in the forward region of the muon detector system to improve the triggering of the forward muons and to increase the reconstruction performance of muons. A total of 144 GEM detector chambers are installed during the long shutdown 2

(LS2) period, out of which 8 of the chambers are assembled and tested at Panjab University, Chandigarh. A brief summary of the assembly procedure and the testing of the fabricated chambers is presented in the Thesis. This Thesis also presents the sensitivity studies for the GEM detector for different background particles such as hadrons, electrons, positrons and neutrons. These studies are performed using FLUKA and GEANT4 simulation packages. The results are then compared with the *pp* collision data collected by the GEM chambers installed in the CMS detector during 2017 and 2018 LHC runs. The results obtained from the simulation agree well with the data collected by the slice test of GEM detectors in CMS.

The present Thesis also covers radiation damage studies of the barrel hadron calorimeter (HB) and the endcap hadron calorimeter (HE) using isolated muons from the *pp* collision data. These radiation damage studies measure the depletion in the light yield of the plastic scintillators of the HB and the HE as a function of the LHC delivered luminosity. In the present analysis, it is observed that the towers in the central barrel region show a very small degradation, i.e., of the order of 2%. However, the level of degradation increases in the endcap. It is found that the towers in the forward region of the endcap show 15% degradation in their light output as compared to their observed light output in the beginning of 2018 data-taking.

Contents

List of Figures

List of Tables

Chapter 1

Introduction

Particle physics is a field of physics that deals with the nature and properties of particles at the sub-atomic level. It explains the fundamental laws which govern the matter in the universe. Many theories and experimental evidence supporting the predictions have resulted in a benchmark model for particle physics, known as "The Standard Model (SM) of particle physics" [1]. SM started coming into the picture during the 1960s with a collective worldwide effort to combine theory and experiment. The discovery of various particles led to the proposal that nucleons have an internal structure. The whole spectrum of new particles was discovered in different particle physics experiments during 1960 and '70s as shown in Figure 1.1. Murray Gell-Mann gave the concept of "Eightfold Way" to arrange the baryons and mesons into geometrical patterns depending upon their charge and strangeness [2]. This concept reduced all of the particles known at the time down to just a few elementary ones. By applying the famous mathematical theorem developed by Emmy Noether in 1918 [3] which links symmetries with nature's conservation laws at the subatomic level, the fundamental particles were arranged in lists and groups, much like the periodic table of elements. This helped particle physicists to look for patterns and links. By the mid-1970s, the theory was well-established and became popular as the Standard Model. The SM successfully explains the fundamental particles and forces acting between them. The discovery of Higgs Boson of mass 125 GeV at the Large

Hadron Collider (LHC) in the year 2012 is under the predictions of the SM [4] [5] and provided the final piece of the Standard Model puzzle. The postulates of the SM are well tested by different experiments at the Large Electron-Positron (LEP) collider, Tevatron, B-factories, etc.

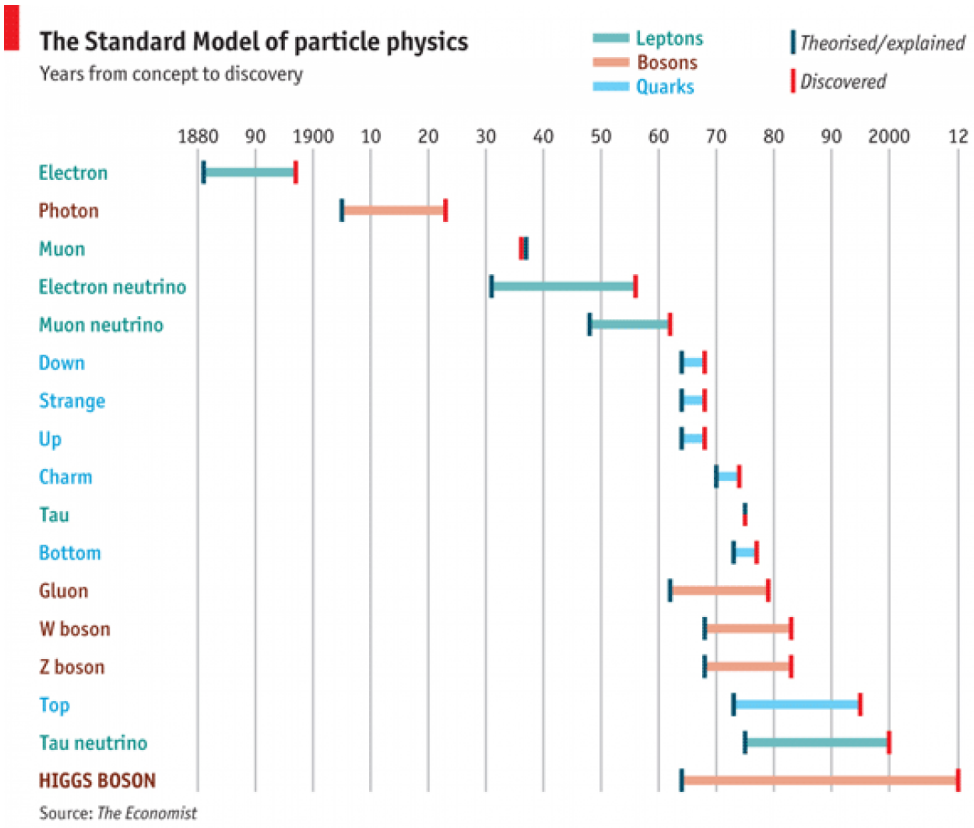

Figure 1.1: Spectra of SM particles and their year of discovery [6].

1.1 Standard Model

The Standard Model is a quantum field theory (QFT) describing the fundamental particles and the forces acting between them. These fundamental particles are the building blocks of the matter and present day visible universe. This theory started coming into picture when in 1928, Paul Dirac for the first time proposed the incorporation of relativity with the quantum mechanics of the electrons which resulted in Dirac and Klein-Gordan equations [7]. The SM, which is actually a Lagrange

density (Lagrangian), remains invariant under various symmetry transformations. For example, the symmetry (or invariance) of a Lagrangian under spacetime translations implies that the resulting dynamics will conserve energy-momentum. Gauge symmetry, on the other hand, ensures that particle interactions will conserve the currents associated with the corresponding gauge field (implying e.g. conservation of electric charge for the photon gauge field). The SM describes the strong interaction, represented by the theory of Quantum chromodynamics (QCD), and the weak and the electromagnetic interaction, combined in the Electroweak Theory (EWT). Gravity, as described by Einstein's General Theory of Relativity, is the only known fundamental force, which is not described by the SM framework. The SM is a non-Abelian gauge theory built on the following symmetry group:

$$\underbrace{SU(3)_C}_{\text{Strong Interaction}} \otimes \underbrace{SU(2)_L \otimes U(1)_Y}_{\text{Electroweak Interaction}} \tag{1.1}$$

where Y stands for hypercharge (Y = B + S, where, B represents Baryon Number and S the Strangeness), L for weak isospin and C for color charge. The particles and interactions described by each symmetry group are discussed in the next Subsections.

1.1.1 Particles of the Standard Model

According to the SM, the fundamental particles which are the building blocks of the matter are spin 1/2 particles which obey Fermi-Dirac statistics and are known as fermions [8] [9]. These fermions are further divided into two categories, leptons and quarks. Leptons and quarks have three generations with increasing mass in each generation. All the visible universe is made up of first generation fermions. The second and third generation fermions are unstable. They have a very short lifetime, and decay quickly to first generation. The first generation of leptons includes electron (e) and electron neutrino (ν_e) which are stable forever. Similarly, the second generation includes muon μ and corresponding muon neutrino (ν_μ), while the third

generation includes the tau (τ) lepton and tau neutrino (ν_τ). Electron, muon and tau are charged leptons with electric charge of $-1e$ whereas their respective neutrinos are charge neutral. Apart from their electric charge, leptons also carry additional quantum numbers: the lepton flavour number ($L_{e/\mu/\tau}$) and the weak isospin (I_3). All the leptons have their anti-particles, known as anti-leptons, with reversed signs of all quantum numbers[1].

In the quark family, the first generation of quarks consists of "up" (u) quark which carry electric charge of $+2e/3$ and "down" (d) quark which carry electric charge of $-1e/3$. These quarks combine to form protons and neutrons within the atom. The second generation of quarks has "strange" (s) and "charm" (c) quarks with electric charge of $+2e/3$ and $-1e/3$, respectively, and are slightly massive than the first generation quarks. Similarly, the third generation of quarks contains "top" (t) and "bottom" (b) quarks with electric charge of $+2e/3$ and $-1e/3$, respectively, with top quark (with mass 171.77 GeV) being the heaviest in the entire quark family. Like leptons, quarks also carry different flavour numbers: the baryon number (B), strangeness (S), charmness (C'), bottomness (B') and topness (T). There are six antiquarks present in the SM with reversed signs of all quantum numbers. In addition to this, the quarks carry a quantum number, the color charge, that is always preserved in the SM interactions. Each quark flavor may exist in three different colors: red (R), blue (B) or green (G); the antiquarks, instead, have the anti-colors (anti-red, anti-blue and anti-green). Quarks cannot exist alone but only together with other quarks, exclusively forming states with no color charge. These color-neutral bound states are called hadrons and they are divided in baryons and mesons. For example, the mesons are composed of one quark and one antiquark and the baryons are made out of three quarks. There are also more exotic situations of quarks bound states, like tetra-quarks or penta-quarks, composed of 4 or 5 quarks, respectively.

Besides fermions, SM contains 12 spin-1 gauge bosons which are force carriers or mediators of interactions between the fermions. The latest addition in the SM

[1] In the SM, neutrinos are massless Dirac particles, which have anti-particles. The possibility for neutrinos to be their own anti-particles (Majorana particles), is still under investigation.

is the "Higgs Boson", which is a scalar boson (spin-0) and is responsible for the mass of SM particles. These bosons carry integral spin and obey Bose-Einstein Statistics [10]. Figure 1.2 shows the fermions and gauge bosons categorized in their respective generations. The properties of fermions [11] are listed in Table 1.1.

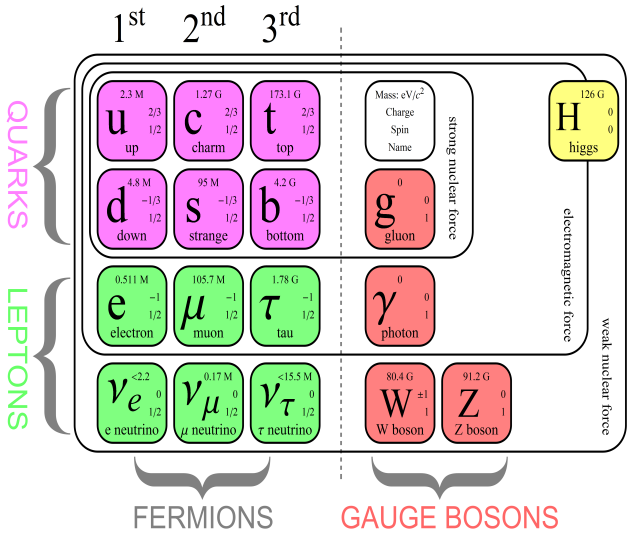

Figure 1.2: Particles of the Standard Model [12].

Generation	Leptons			Quarks		
	Flavor	Charge	Mass(MeV)	Flavor	Charge	Mass(MeV)
1	e	-e	0.51	u	+2e/3	2.2
	ν_e	0	$<2.2\times10^{-6}$	d	-e/3	4.7
2	μ	-e	105.66	c	+2e/3	1.27×10^{3}
	ν_μ	0	<0.17	s	-e/3	96
3	τ	-e	1.78×10^{3}	t	+2e/3	171.77×10^{3}
	ν_τ	0	15.5	b	-e/3	4.18×10^{3}

Table 1.1: Properties of fundamental particles in the Standard Model [13].

1.1.2 Forces acting between Fundamental Particles

There are four fundamental forces through which all the matter in the universe interact with each other: Strong, Electromagnetic, Weak and Gravitational. These forces are mediated by spin-1 gauge bosons and depending on the mass of their mediator,

these forces are characterized based on their strength and range of interaction. A brief description of these fundamental forces is given below:

1. **Strong Interaction:** This force acts between the quarks and is the strongest interaction which binds the nucleus of an atom together. It is mediated by massless gluons and has a very short range of the order of 1 femtometer (10^{-15}m) which is about the size of a nucleon. The strong interactions are described by Quantum Chromodynamics (QCD) with a symmetry group $SU(3)_C$. The particles interacting via strong interaction (quarks) require an additional charge, called color charge. The strength of the strong interactions is given by a strong coupling constant, α_s which is expressed as:

$$\alpha_s = \frac{g_s^2}{4\pi} \tag{1.2}$$

where g_s is the QCD gauge coupling. The α_s behaves differently at low and high energies depending on the four-momentum (Q^2) transferred and is referred to as *running coupling constant* which is given by:

$$\alpha_{\mathrm{s}}(\mathrm{Q}^2) = \frac{12\pi}{(33 - 2\mathrm{N_f})\ln(\frac{\mathrm{Q}^2}{\Lambda^2_{\mathrm{QCD}}})} \tag{1.3}$$

where $\Lambda^2_{QCD} \sim 200\,\mathrm{GeV}$, represents the QCD scale. Figure 1.3 shows the trend of running coupling constant (α_s) as a function of Q, together with several measurements.

For very small distances and high values of Q^2, the quark-quark coupling decreases, vanishing asymptotically. At very large values of Q^2, the quarks are considered as "free". This property is known as "*Asymptotic freedom*" [15]. On the other hand, at very small values of Q^2, the quark-quark coupling becomes very large which accounts for the stability of the nucleus. This property is known as "*Quark Confinement*" [16]. A large amount of energy is required to separate these confined quarks. As a result, the color force breaks into new quark-antiquark pairs conserving the energy and other quantum numbers.

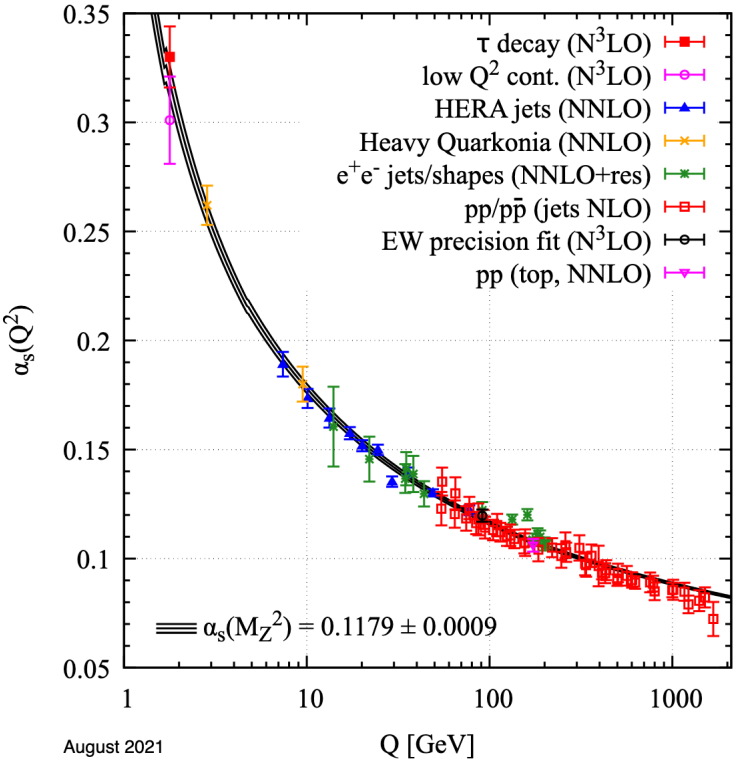

Figure 1.3: Diagram representing the trend of running coupling constant (α_s) as a function of Q [14].

2. **Electromagnetic Interaction:** This interaction is governed by Quantum Electrodynamics (QED) with $U(1)_Y$ symmetry group. This force exists between particles carrying an electric charge via exchange of photons (γ) which are electrically neutral and massless force carrier for these interactions. This is a long range force and is inversely proportional to square of the distance. The strength of these interactions is given by fine structure constant (α) which has a value $\sim 1/137$.

3. **Weak Interaction:** This force is a short range force and acts on the subatomic level. The force carriers for this interaction are heavy vector bosons: $W^{\pm}$ and Z, and are described by $SU(2)_L$ symmetry group. The weak interaction acts between both quarks and leptons, and is stronger than the gravitational force at the subatomic scale.

   Unlike QED, the theory of weak interactions was nonrenormalizable which

makes the higher order effects difficult to calculate. To solve this discrepancy, the unification of Electromagnetic Interaction and Weak Interaction into a single theory, known as *Electroweak theory*, was proposed by Glashow, Salam and Weinberg [17] [18]. This unification led to a new type of interaction, known as "Electroweak (EW) interaction" which comes into picture beyond the EW scale ($\sim$100 GeV).

The electroweak interaction is explained by non-Abelian gauge symmetry group : $SU(2)_L \otimes U(1)_Y$, where L represents left handedness and Y is the hypercharge defined as $Y = 2(Q - T^3)$ with Q as particle's charge and T as weak isospin. The third component of weak isospin, T^3 defines the arrangement of left handed (negatively chiral) fermions which can transform each other through the absorption or emission of a charged boson $W^{\pm}$. The $SU(2)_L$ introduces three fields with T^3 : $\pm 1/2$ and 0, corresponding to three gauge bosons: W^+, W^-, W^0. Similarly, the symmetry group associated to the weak hypercharge $U(1)_Y$ gives rise to one gauge field, B_μ. Thus, the unified symmetry group, $SU(2)_L \otimes U(1)_Y$, proposes four force carrying bosons : photon, positively charged and negatively charged W's and neutral Z to be described as compositions of the same underlying states.

However, the unification does not predict mass terms for weak bosons ($W^{\pm}, Z$) which actually have a mass. To resolve this discrepancy, a spontaneous symmetry breaking mechanism was proposed by Brout, Englert, Higgs (BEH) and others simultaneously in the 1960s [19] [20]. With this proposed mechanism, mass terms are generated by breaking the local gauge invariance in the symmetry group $SU(2)_L \otimes U(1)_Y$ and introducing a new scalar field, *the Higgs field, ϕ*. This leaves the Lagrangian invariant under a given symmetry, while the state with lowest energy (ground or vacuum state) is not. Once the vacuum state is attained, the $SU(2)_L \otimes U(1)_Y$ symmetry group is spontaneously broken, giving rise to three massive Nambu-Goldstone bosons which give mass to gauge bosons $W^{\pm}$ and Z and an additional neutral massive scalar particle H^0, the Higgs boson. The vacuum state (or ground) is invariant under $U(1)_q$

symmetry subgroup transformations, leaving the photon γ massless.

The spontaneous symmetry breaking mechanism was incorporated in EW theory in the late 1960s by Weinberg and Salam [21] [22]. Later t'Hooft published the proof describing that non-Abelian gauge field theory with spontaneous breakdown of gauge symmetries is renormalizable [23]. The discovery of $W^{\pm}$ and Z bosons at CERN in 1983 by the UA1 and UA2 experiments further strengthened the theory [24]. After decades of probing for new physics, a new particle consistent with the SM Higgs boson with mass 125 GeV was finally discovered at the LHC in 2012 [4] [5].

4. **Gravitational Interaction:** This force is a long range force (infinite range) and is attractive in nature. This is the weakest force among all the fundamental forces and has relative strength of 10^{-38} with respect to the strong force at the atomic scale. This force is predicted to be mediated by a gauge boson called "graviton" which has not been observed experimentally yet.

   Table 1.2 lists the fundamental forces and their properties with their relative strengths at the atomic scale.

Interaction	Mediators	Charge	Spin	Mass (GeV)	Range (m)	Relative strength at atomic scale
Strong	8 gluons (g)	0	1	0	10^{-15}	1
EM	Photon (γ)	0	1	0	∞	10^{-2}
Weak	$W^{\pm}$	±1	1	80.40±0.03	10^{-18}	10^{-9}
	Z	0	1	91.18±0.01		
Gravitational	graviton	0	2	0	∞	10^{-38}

Table 1.2: List of fundamental interactions known in nature [13].

The SM of particle physics has been extremely successful in predicting and explaining the present day universe. Nonetheless, it presents several limitations which are briefly discussed in the next Section.

1.1.3 Shortcomings of the Standard Model

The SM of particle physics has been an extremely successful theory in explaining various particle physics phenomena. Nonetheless, it remains unsuccessful in explaining several fundamental phenomena in nature, indicating that SM is not a complete theory. Below are the main limitations of the SM:

- **Hierarchy Problem:** The spontaneous symmetry breaking mechanism introduces masses to the SM particles by the vacuum expectation value of the Higgs field. However, the bare Higgs boson mass ($m_{H,bare}$) receives large quantum loop corrections (Δm_H^2) from every particle that interacts with the Higgs field :

$$m_H = m_{H,bare} + \Delta m_H^2 \tag{1.4}$$

  These corrections are possibly a contribution from fermions or heavy scalars coupling to the higgs field and its contribution is given by:

$$\Delta m_{H,f}^2 = -\frac{|\lambda_f|^2}{8\pi^2}\Lambda_{UV}^2 + ... \tag{1.5}$$

  where λ_f measures the coupling between fermions and Higgs field and Λ_{UV}^2 defines the energy scale at which new physics would enter. Now considering the contribution from top quark with $\lambda_f \sim 1$ and assuming SM valid up to the Planck scale i.e. $\Lambda_{UV}^2 = m_P^2$, the quantum corrections becomes huge, $\Delta m_H^2 \sim \mathcal{O}(10^{30})$. To get the observable Higgs mass of 125 GeV, the bare mass has to be fine tuned to 34 digits. Therefore to stabilize the Higgs boson mass, a new mechanism is needed, which typically requires new heavy particles to cancel the contributions from the loop corrections.

- **Gravity:** SM fails to explain the fourth fundamental force in nature i.e. the gravitational force. The force carriers for other fundamental interactions are well predicted by the SM but it fails to explain the hypothetical carrier of the gravitational force, the spin-2 graviton.

- **Dark Matter:** Latest results from Cosmological observations [25] [26] have shown that the composition of the universe requires much more matter than the of visible matter. SM only explains the 5% of the visible universe. The remaining 25% is composed of *dark matter* that either interacts very weakly or not at all with the SM fields. These "Weakly Interacting Massive Particles" (WIMP) are predicted to have mass around $\sim$ few GeV to $\sim$ 500 GeV [27] and interact with themselves and with other matter only through weak force and gravity. Such particles are not described by the SM. The remaining percentage of the universe ($\sim$70%) is predicted to be composed of *dark energy* which is responsible for the accelerated expansion of the universe [28] [25]. SM does not describe the nature of any such mechanism.

- **Matter-Antimatter Asymmetry:** At the big bang, the universe should have equal parts of matter and antimatter. However, the present day universe is composed of only matter. The absence of antimatter in the present day universe indicates that either the matter and antimatter are separated away in space or some unknown mechanism has resulted in excess of matter. While the SM does have some CP violation which allows for some matter-antimatter asymmetry [29] [30], but the effect is insufficient to explain the observed asymmetry in the universe. Hence, this is still an open question.

- **Neutrino Masses:** SM predicted neutrinos to be massless Dirac particles. But the observation of neutrino oscillations ($\nu_e \rightarrow \nu_\mu$ or $\nu_\mu \rightarrow \nu_e$) by various experiments [31] [32] requires the neutrinos to have mass, though very small.

In order to address these phenomena, several possible extensions to the SM have been proposed over the last few decades. Some of these theories are briefly discussed in the next Section.

1.2 Physics beyond the Standard Model

The success of gauge theory to describe particle physics, and in particular the Higgs mechanism for spontaneously breaking symmetry in the Electroweak sector encouraged several theoretical physicists to propose theories containing additional gauge groups to resolve the limitations of the SM. It was predicted that the SM actually can be a part of a more fundamental underlying theory, such as grand unification or superstring theory, perhaps combined with supersymmetry broken at the TeV scale. Some of the important theories are briefly discussed as follows.

1.2.1 Grand Unified Theories

Grand Unified Theories (GUTs) proposes the unification of electroweak and strong interactions into a single force much like the SM, as it does for electromagnetic and weak interactions. This concept was first proposed by Howard Georgi and Sheldon Glashow [33]. GUTs require the unified group to be a simple group, e.g., SU(5), SO(10), or E6 and it must satisfy two conditions: SM group must be a subgroup of this unified group and it must have complex representations that reproduce the chiral structure of the SM [34].

The SU(5) model: The smallest gauge group to postulate is SU(5) [35] [36], which allows a very neat representation of all the SM particles. This unified group SU(5) is then assumed to be spontaneously broken into the standard model subgroup below a very high energy scale called the grand unification scale ($\sim 10^{16}$ GeV). SU(5) is a group of unitary 5×5-dimensional matrices with unit determinant and consists of 24 traceless, Hermitian matrices ($n^2 - 1$). In this model, all the left-handed fermions of a single generation fell into two representations of the group, $\bar{5}$ and 10 in the following way with the possible addition of an SU(5)-singlet right-handed

neutrino field ν_R^c.

$$\bar{5} = \begin{pmatrix} d_1^c \\ d_2^c \\ d_3^c \\ e \\ -\nu \end{pmatrix}, 10 = \begin{pmatrix} 0 & u_3^c & -u_2^c & u_1 & d_1 \\ -u_3^c & 0 & u_1^c & u_2 & d_2 \\ u_2^c & -u_1^c & 0 & u_3 & d_3 \\ -u_1 & -u_2 & -u_3 & 0 & e^c \\ -d_1 & -d_2 & -d_3 & -e^c & 0 \end{pmatrix} \tag{1.6}$$

where d_i and u_i are left-handed up and down quark, d_i^c and u_i^c are their right-handed counterparts, ν is the neutrino and e, e^c are the left and right-handed electron. The full SM particle content is contained in the three generations of the following representation:

$$SM = \bar{5} \oplus 10 \oplus 1 \tag{1.7}$$

The spontaneous symmetry breaking of SU(5) occurs when GUTs scalar field, analogous to the Higgs field, acquires a vacuum expectation value (VEV).

$$SU(5) \rightarrow SU(3) \times SU(2) \times U(1) \tag{1.8}$$

This way, the 24 symmetry generators of SU(5) are broken into the 8 + 3 + 1 generators of the SM. This leaves 12 new massive gauge bosons that will generically couple quarks and leptons in the same interaction. These new massive bosons will mediate proton decay, among the many new interactions.

***E_6* model:** Another popular unification gauge group is the E_6 group which is large enough to contain the SM as a subgroup [37] [38]. It is of rank 6, and breaks under spontaneous symmetry breaking to $SO(10)\times U(1)$ or $SU(3)_C \times SU(3)_L \times SU(3)_R$. Each fermion family is assigned to an irreducible 27-dimensional representation of the group, which contains the SM fermions plus exotic fields as:

$$27 \sim \bar{5} \oplus 10 \oplus 1 \oplus \bar{5} \oplus 5 \oplus 1 \tag{1.9}$$

The first three representations are precisely the set needed for the SM and the 1 is an additional SM singlet which can break the $U(1)_\psi$ symmetry when it obtains a vacuum expectation value. The $\bar{5} \oplus 5$ contains new predicted exotic fermions which can be given masses when $U(1)_\psi$ symmetry breaks. The higher-scale breaking of E_6 is given as:

$$E_6 \rightarrow SU(5) \times U(1) \times U(1) \tag{1.10}$$

The particles associated with the $U(1)$s are new, heavy gauge bosons which can gain mass through the addition of more Higgs fields and potentially couple to the matter fields of the SM.

Sequential Standard Model: Another well motivated and the most basic extension of the SM is the Sequential Standard Model (SSM) [39]. It predicts the new gauge boson as the heavy version of the SM Z boson which has same coupling to the fermions as the SM Z boson but with suppressed coupling to W and Z bosons. This model proposes the additional $U(1)'$ symmetry to the existing SM structure $(SU(3)_C \times SU(2)_L \otimes U(1)_Y)$. Like SM Z boson, this Z'_{SSM} is predicted to decay into known SM fermion-antifermion pair.

1.2.2 Supersymmetry

Supersymmetry (SUSY) refers to possible relations between the spectrum and interactions of fermions and bosons. A supersymmetry transformation turns a bosonic state into a fermionic state, and vice versa [40]. The operator Q that generates such transformations must be an anti-commuting spinor, with

$$Q|Boson\rangle = |Fermion\rangle, \;\; Q|Fermion\rangle = |Boson\rangle \tag{1.11}$$

In supersymmetry, each particle from one class has an associated particle in the other, known as its superpartner, the spin of which differs by a half-integer. For example, if the tau lepton exists in a supersymmetric theory, then there would be

a particle called a "stau" (superpartner tau), a bosonic partner of the tau. One of the most attractive features of SUSY is that it can stabilize the electroweak scale against quantum corrections and hence solves the hierarchy problem [41] and provides a mechanism for dynamic electroweak symmetry breaking [42]. In addition, with R-parity being conserved [43], the lightest supersymmetric particle (LSP) is stable and cannot decay. Therefore, SUSY automatically predicts the existence of a Dark Matter candidate and can easily produce scenarios with the correct relic abundance [44] [45].

1.2.3 String Theory

String theory is a candidate for a unified theory of the four fundamental interactions: electromagnetic, weak, strong, and gravitational. The basic idea of this theory is that matter does not consist of point-like particles but rather strings extended in one-dimension [46–48]. These one-dimensional strings oscillate and look like localized, particle-like excitations at low energy. Thus, depending on the state of oscillation, a single oscillating string can give rise to different kinds of particles. An interesting feature of this theory is that it automatically contains a massless spin-2 particle, which can be identified as the graviton. Thus, string theory is a natural candidate for a complete theory of quantum gravity. The natural energy scale for quantum theory of gravity is at the Planck scale $\sim 10^{16}$ GeV, which is well beyond any current testable energy regime. String theory incorporates many different possible extensions to the SM, including gauge unification, supersymmetry, and extra dimensions.

Each of these extensions predicts new gauge fields and interactions beyond the SM. The common manifestation of these interactions is particles at the TeV scale. One such particle is a heavy neutral spin-1 gauge boson, Z', which arises from the extensions of the electroweak symmetry of the SM. The new $U(1)$ gauge symmetry arising in E_6 model predicts a new gauge boson $Z'(\theta) = Z'_{\psi}cos\theta + Z'_{\chi}sin\theta$ where θ is the mixing angle determining the coupling of Z' to fermions. Similarly, the SSM is the most commonly used model, which assumes the Z' gauge boson has same

couplings to fermions as the SM Z boson and assumes no coupling to the $W^{\pm}$ and Z bosons. Similar to the discovery of the Higgs boson, hypothetical Z' boson arising from new gauge symmetries is another example of new massive resonances that can be searched for at the LHC.

1.3 Search for Z' at the LHC

In most of the proposed new physics models, the symmetry breaking scale is at high energy ($\mathcal{O}(\sim TeV)$) accounting for non-observation of the Z' boson at LEP and Tevatron. The Z' predicted by these models is in reach of the Large Hadron Collider experiment at CERN. The current searches for Z' are carried out by mainly two detectors: Compact Muon Solenoid (CMS) detector [49] and A Toroidal LHC ApparatuS (ATLAS) [50] which are general purpose detectors situated at the LHC ring. The search for Z' conducted thus far considered the direct production of Z' through quark-antiquark annihilation, known as the Drell-Yan process [51] [52]. Representative Feynman diagram for the production of Z' and their decay to lepton pair of either electrons or muons or taus is shown in Figure 1.4. Recent search by the

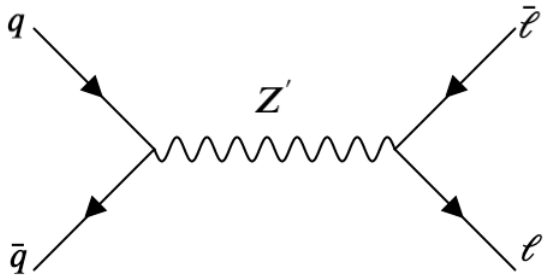

Figure 1.4: Representative Feynman diagrams for the Drell-Yan production of neutral heavy gauge boson Z'.

CMS Collaboration, targeting Z' proposed by the E6 model (Z'_{ψ}) and the Sequential Standard Model (Z'_{SSM}), considered $Z' \rightarrow ee/\mu^{+}\mu^{-}$ decay. In this search, no excess above SM expectations has been observed and excluded Z'_{SSM} (Z'_{ψ}) below 5.15 (4.56) TeV [53] as shown in Figure 1.5 (left). These are the most stringent limits

set so far by CMS for Z' decaying to first (e^+e^-) and second $(\mu^+\mu^-)$ generation leptons. ATLAS Collaboration at CERN performed a similar search for the Z', assuming production via Drell-Yan mechanism, targeting E6 motivated Z'_ψ and SSM motivated Z'_{SSM}. No deviation from SM expectations has been observed thus far and excluded Z'_ψ (Z'_{SSM}) for masses below 4.5 (5.1) TeV [54] as shown in Figure 1.5 (right). The Z' search via Drell-Yan mechanism necessitate a sizable coupling for

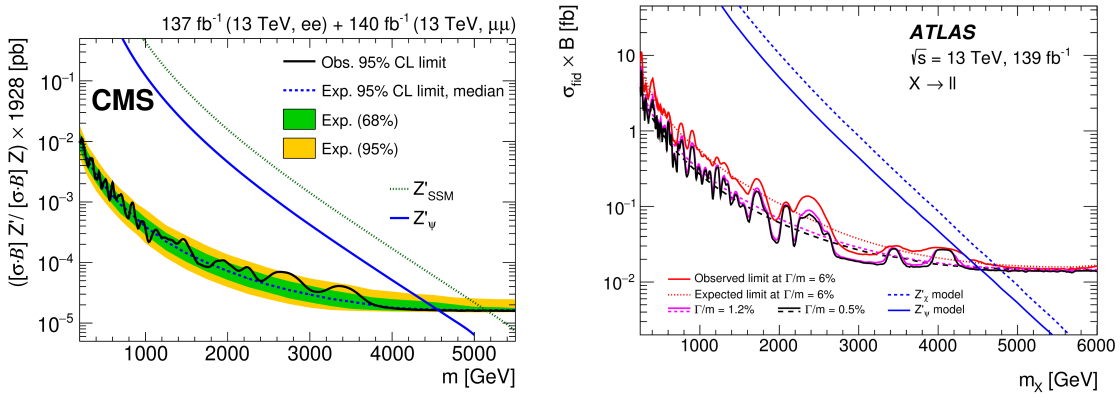

Figure 1.5: 95% CL exclusion limit on the product of the production cross-section and the branching fraction for Z' relative to the product of the production cross-section and the branching fraction for a Z boson as a function of Z' mass obtained by CMS [53] (left). Upper limits at 95% CL on the cross-section times branching fraction as a function of Z' mass obtained by ATLAS [54] (right).

the Z' to light quarks (κ_q) for large production cross-sections. One hypothesis as to why the Z' boson has eluded discovery in the searches conducted thus far is that the coupling for Z' to light quarks is actually smaller than that required for sensitivity in the DY searches. These searches can be complemented by investigating the vector boson fusion production mode of Z' as discussed in the next Section.

1.4 Vector Boson Fusion production of Z'

Vector Boson Fusion (VBF) process is an electroweak mechanism in which the incoming quarks from the LHC radiate vector bosons that undergo fusion forming the particle under study (i.e. Z'). This process occurs in t-channel [13] and gives two quarks (or jets) in the forward regions of the detector having large dijet invari-

ant mass. Additionally, no QCD color is exchanged in these processes leading to suppressed hadronic activity between the two forward jets. This distinct topology provides good discrimination against any kind of QCD background processes thus providing the motivation for the analysis reported in this Thesis. Figure 1.6 shows the Feynman diagram for the VBF production of Z'. In this new approach, the Z' produced via VBF process is considered to couple to SM fermions similar to SM Z boson, much like as in Sequential Standard model but with allowed coupling to heavy vector bosons ($g_{Z'VV}$, V= Z or W).

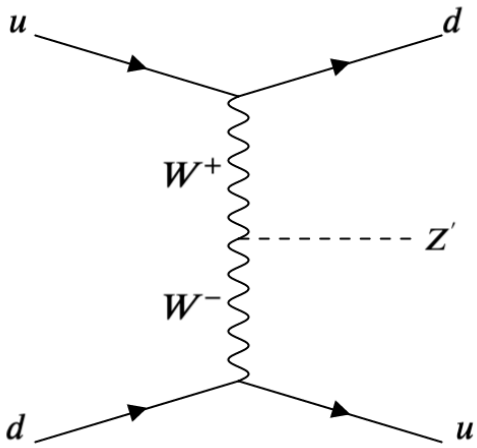

Figure 1.6: Representative Feynman diagram for the VBF production of neutral heavy gauge boson Z'.

Unlike Drell-Yan mechanism, Z' coupling to quarks in VBF processes is considered to be small ($\kappa_q < 0.3$). As a result, the sensitivity of this search is higher than the traditional DY Z' search conducted thus far [55]. As can be seen in Figure 1.7, VBF Z' signal significance gets higher than DY Z' at smaller coupling to quarks ($\kappa_q < 0.3$). Furthermore, VBF processes become increasingly more important for probing large mass scales due to collinear logarithmic enhancements in the production cross-sections [56–58].

To allow a broad and model-independent search, the Z' coupling to heavy vector boson, $g_{Z'VV}$ is kept as a free parameter. The range is constrained naturally by the limits of no $Z'VV$ coupling and a very broad Z' decay width. The maximal

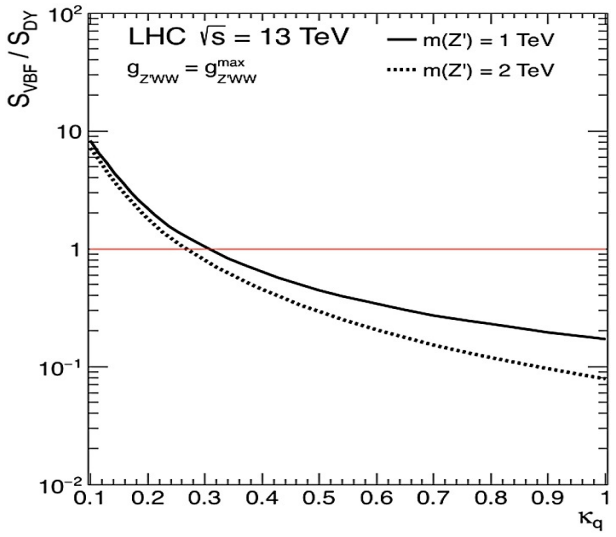

Figure 1.7: The ratio of VBF Z' to traditional Z' signal significance, as a function of κ_q and for fixed κ_V =1 [55].

allowed coupling of Z' to vector bosons is given by:

$$g^{max}_{Z'VV} = (5.3 \times \frac{M_W}{M_{Z'}})^2 \tag{1.12}$$

where M_W is the mass of W boson. Hence, Z' coupling to vector bosons can be written as :

$$g_{Z'VV} = \kappa_V \times g^{max}_{Z'VV} \tag{1.13}$$

where $\kappa_V \leq 1$, to avoid unitarity violation. In addition to this, there is a strong motivation to consider enhanced coupling to third generation fermions (proposed by topcolor-assisted technicolor model) [59] to answer B-meson decay anomalies observed by LHCb, BaBar and Belle experiments [60–63]. The idea of the model is that the fermions gauge groups are split into two SU(2). One for the light fermions of the first and second generation and one for the heavy third generation. The two groups would mix and result in the SM gauge bosons plus heavy gauge bosons. While the light bosons would have a universal coupling to all fermions, the new heavy gauge bosons would have a non-universal coupling. To parameterize this possibility, two couplings can be introduced, g_ℓ and g_h, for the light and heavy fermions, respectively.

In the context of enhanced coupling to third generation fermions, Z' decaying to $\tau^+\tau^-$ is considered. Besides this, due to pure electroweak production of Z' in the VBF processes, the SM jet backgrounds are suppressed significantly leading to increased signal sensitivity for this channel. In addition to this, with allowed coupling of Z' to the SM vector bosons, the $Z' \to WW$ decay width can be large, and thus VBF Z' decaying to WW is considered for re-interpretations. In light of these facts, the first LHC search for the Z' produced by the VBF mechanism at center-of-mass energy of 13 TeV is performed and presented in this Thesis.

1.5 Organization of the Thesis

This Thesis is based on the participation in the CMS experiment with detector performance studies and the search for physics beyond the standard model. The layout of the Thesis is as follows:

Chapter 1 covers a brief overview of the Standard Model (SM) and its findings and shortcomings. The need for the physics beyond Standard Model and motivation for the search for Z' through VBF processes is also presented in this Chapter.

Chapter 2 gives a brief overview of the Large Hadron Collider (LHC) and the various detectors at the LHC. The main emphasis is given on the Compact Muon Solenoid (CMS) detector on which present study is based on. A brief overview of the various sub-detectors of the CMS detector has also been presented.

Chapter 3 gives a brief description of the event generation methodology with different Monte Carlo event generators, simulation of the detector geometry and reconstruction of the particles in the detector. Also, a brief overview of the reconstruction of various physics objects used in the analysis such as electron, tau lepton, muon, jets and the missing transverse energy has been presented.

Chapter 4 covers the radiation damage studies of the Hadron Calorimeter (HCAL) of the CMS detector using isolated muons from pp collision data.

Chapter 5 covers the details of the analysis workflow for the search for Z' through

VBF processes using the data collected by the CMS experiment at the center-of-mass energy of 13 TeV. In this Chapter, the signal and potential background processes have been discussed in details. The estimation of each contributing background process in the high mass region i.e. signal region is presented along with the final results.

Chapter 6 summarizes the experimental results and observations of the physics analysis performed in this Thesis.

Bibliography

[1] M. Herrero, "The Standard model", *NATO Sci. Ser. C* **534** (1999) 1–59, doi:10.1007/978-94-011-4689-0_1, arXiv:hep-ph/9812242.

[2] M. Gell-Mann, "A Schematic Model of Baryons and Mesons", *Phys. Lett.* **8** (1964) 214–215, doi:10.1016/S0031-9163(64)92001-3.

[3] E. Noether, "Invariant Variation Problems", *Gott. Nachr.* **1918** (1918) 235–257, doi:10.1080/00411457108231446, arXiv:physics/0503066.

[4] CMS Collaboration, "Observation of a new boson at a mass of 125 GeV with the CMS experiment at the LHC", *Physics Letters B* **716** (Sep, 2012) 30–61, doi:10.1016/j.physletb.2012.08.021.

[5] ATLAS Collaboration, "Observation of a new particle in the search for the Standard Model Higgs boson with the ATLAS detector at the LHC", *Physics Letters B* **716** (Sep, 2012) 1–29, doi:10.1016/j.physletb.2012.08.020.

[6] Quantum Theory Timeline. https://particleadventure.org/other/history/quantumt.html.

[7] P. A. M. Dirac, "The quantum theory of the electron", *Proc. Roy. Soc. Lond. A* **117** (1928) 610–624, doi:10.1098/rspa.1928.0023.

[8] E. Fermi, "On the Quantization of the Monoatomic Ideal Gas", *arXiv* (12, 1999) arXiv:cond-mat/9912229.

[9] P. A. M. Dirac, "On the Theory of quantum mechanics", *Proc. Roy. Soc. Lond. A* **112** (1926) 661–677, doi:10.1098/rspa.1926.0133.

[10] D. Greenberger, K. Hentschel, and F. Weinert, "Compendium of Quantum Physics". 2009. doi:10.1007/978-3-540-70626-7.

[11] M. Goldhaber, "A closer look at the elementary fermions", *Proceedings of the National Academy of Sciences* **99** (Jan, 2002) 33–36, doi:10.1073/pnas.221582298.

[12] The Standard Model. https://www.physik.uzh.ch/groups/serra/StandardModel.html.

[13] D. H. Perkins, "Introduction to High Energy Physics". Cambridge University Press, 4 edition, 2000. doi:10.1017/CBO9780511809040.

[14] Particle Data Group Collaboration, "Review of Particle Physics", *PTEP* **2020** (2020), no. 8, 083C01, doi:10.1093/ptep/ptaa104. and 2021 update.

[15] H. D. Politzer, "Asymptotic Freedom: An Approach to Strong Interactions", *Phys. Rept.* **14** (1974) 129–180, doi:10.1016/0370-1573(74)90014-3.

[16] J. L. Marrero and A. R. Swift, "Color confinement and the quantum-chromodynamic vacuum. II. Gluon propagation and the Coulomb interaction", *Phys. Rev. D; (United States)* **31:4** (2, 1985) doi:10.1103/PhysRevD.31.917.

[17] S. L. Glashow, "Partial-symmetries of weak interactions", *Nuclear Physics* **22** (1961) 579–588, doi:https://doi.org/10.1016/0029-5582(61)90469-2.

[18] A. Salam and J. C. Ward, "Electromagnetic and weak interactions", *Phys. Lett.* **13** (1964) 168–171, doi:10.1016/0031-9163(64)90711-5.

[19] F. Englert and R. Brout, "Broken Symmetry and the Mass of Gauge Vector Mesons", *Phys. Rev. Lett.* **13** (1964) 321–323, doi:10.1103/PhysRevLett.13.321.

[20] P. W. Higgs, "Broken Symmetries and the Masses of Gauge Bosons", *Phys. Rev. Lett.* **13** (1964) 508–509, doi:10.1103/PhysRevLett.13.508.

[21] S. Weinberg, "A Model of Leptons", *Phys. Rev. Lett.* **19** (1967) 1264–1266, doi:10.1103/PhysRevLett.19.1264.

[22] A. Salam, "Weak and Electromagnetic Interactions", *Conf. Proc. C* **680519** (1968) 367–377, doi:10.1142/9789812795915_0034.

[23] G. 't Hooft, "Renormalizable Lagrangians for Massive Yang-Mills Fields", *Nucl. Phys. B* **35** (1971) 167–188, doi:10.1016/0550-3213(71)90139-8.

[24] UA1 Collaboration, "Experimental Observation of Lepton Pairs of Invariant Mass Around 95-GeV/c**2 at the CERN SPS Collider", *Phys. Lett. B* **126** (1983) 398–410, doi:10.1016/0370-2693(83)90188-0.

[25] C. L. Bennett et al., "Nine-Year Wilkinson Microwave Anistropy Probe (WMAP) Observations: Final maps and results", *American Astronomical Society* **208** (sep, 2013) 20, doi:10.1088/0067-0049/208/2/20.

[26] P. A. R. Ade et al., "Planck2015 results", *Astronomy & Astrophysics* **594** (Sep, 2016) A13, doi:10.1051/0004-6361/201525830.

[27] A. Green, "Determining the weakly interacting massive particles mass using direct detection experiments", *Journal of Cosmology and Astroparticle Physics* **2007** (08, 2007) 022, doi:10.1088/1475-7516/2007/08/022.

[28] Particle Data Group Collaboration, "Review of Particle Physics (RPP)", *Phys. Rev. D* **86** (2012) 010001, doi:10.1103/PhysRevD.86.010001.

[29] M. Dine and A. Kusenko, "The Origin of the matter - antimatter asymmetry", *Rev. Mod. Phys.* **76** (2003) 1, doi:10.1103/RevModPhys.76.1, arXiv:hep-ph/0303065.

[30] KTeV Collaboration, "Observation of direct CP violation in $K_{S,L} \to \pi\pi$ decays", *Phys. Rev. Lett.* **83** (1999) 22–27, doi:10.1103/PhysRevLett.83.22, arXiv:hep-ex/9905060.

[31] R. Davis, Jr., D. S. Harmer, and K. C. Hoffman, "Search for neutrinos from the sun", *Phys. Rev. Lett.* **20** (1968) 1205–1209, doi:10.1103/PhysRevLett.20.1205.

[32] Y. Ashie et al., "Evidence for an oscillatory signature in atmospheric neutrino oscillations", *Physical Review Letters* **93** (Sep, 2004) doi:10.1103/physrevlett.93.101801.

[33] H. Georgi and S. L. Glashow, "Unity of All Elementary Particle Forces", *Phys. Rev. Lett.* **32** (1974) 438–441, doi:10.1103/PhysRevLett.32.438.

[34] J. C. Baez and J. Huerta, "The Algebra of Grand Unified Theories", *Bull. Am. Math. Soc.* **47** (2010) 483–552, doi:10.1090/S0273-0979-10-01294-2, arXiv:0904.1556.

[35] Ross G. Graham, "Grand unified theories". Benjamin/Cummings Pub. Co., 1984.

[36] Rabindra N. Mohapatra, "Unification and Supersymmetry". Springer, New York, NY, 1986. doi:https://doi.org/10.1007/978-1-4757-1928-4.

[37] F. Gursey, P. Ramond, and P. Sikivie, "A Universal Gauge Theory Model Based on E6", *Phys. Lett. B* **60** (1976) 177–180, doi:10.1016/0370-2693(76)90417-2.

[38] D. London and J. L. Rosner, "Extra Gauge Bosons in E(6)", *Phys. Rev. D* **34** (1986) 1530, doi:10.1103/PhysRevD.34.1530.

[39] G. Altarelli, B. Mele, and M. Ruiz-Altaba, "Searching for New Heavy Vector Bosons in $p\bar{p}$ Colliders", *Z. Phys. C* **45** (1989) 109, doi:10.1007/BF01556677. [Erratum: Z.Phys.C 47, 676 (1990)].

[40] S. P. Martin, "A Supersymmetry primer", *Adv. Ser. Direct. High Energy Phys.* **18** (1998) 1–98, doi:10.1142/9789812839657_0001, arXiv:hep-ph/9709356.

[41] S. Dimopoulos, S. Raby, and F. Wilczek, "Supersymmetry and the Scale of Unification", *Phys. Rev. D* **24** (1981) 1681–1683, doi:10.1103/PhysRevD.24.1681.

[42] E. Witten, "Dynamical breaking of supersymmetry", *Nuclear Physics B* **188** (1981), no. 3, 513–554, doi:https://doi.org/10.1016/0550-3213(81)90006-7.

[43] G. R. Farrar and P. Fayet, "Phenomenology of the Production, Decay, and Detection of New Hadronic States Associated with Supersymmetry", *Phys. Lett. B* **76** (1978) 575–579, doi:10.1016/0370-2693(78)90858-4.

[44] G. Jungman, M. Kamionkowski, and K. Griest, "Supersymmetric dark matter", *Phys. Rept.* **267** (1996) 195–373, doi:10.1016/0370-1573(95)00058-5, arXiv:hep-ph/9506380.

[45] J. R. Ellis et al., "Supersymmetric Relics from the Big Bang", *Nucl. Phys. B* **238** (1984) 453–476, doi:10.1016/0550-3213(84)90461-9.

[46] M. B. Green, J. H. Schwarz, and E. Witten, "SUPERSTRING THEORY. VOL. 1: INTRODUCTION". Cambridge Monographs on Mathematical Physics. Cambridge University Press, 7, 1988. doi:https://doi.org/10.1002/asna.2113090428, ISBN 978-0-521-35752-4.

[47] J. Polchinski, "String theory. Vol. 1: An introduction to the bosonic string". Cambridge Monographs on Mathematical Physics. Cambridge University Press, 12, 1998. doi:10.1017/CBO9780511816079, ISBN 978-0-511-25227-3, 978-0-521-67227-6, 978-0-521-63303-1.

[48] O. Aharony et al., "Large N field theories, string theory and gravity", *Phys. Rept.* **323** (2000) 183–386, doi:10.1016/S0370-1573(99)00083-6, arXiv:hep-th/9905111.

[49] CMS Collaboration, "The CMS Experiment at the CERN LHC", *JINST* **3** (2008) S08004, doi:10.1088/1748-0221/3/08/S08004.

[50] ATLAS Collaboration, "The ATLAS Experiment at the CERN Large Hadron Collider", *JINST* **3** (2008) S08003, doi:10.1088/1748-0221/3/08/S08003.

[51] S. D. Drell and T.-M. Yan, "Massive lepton-pair production in hadron-hadron collisions at high energies", *Phys. Rev. Lett.* **25** (Aug, 1970) 316–320, doi:10.1103/PhysRevLett.25.316.

[52] S. D. Drell and T.-M. Yan, "Massive lepton-pair production in hadron-hadron collisions at high energies", *Phys. Rev. Lett.* **25** (Sep, 1970) 902–902, doi:10.1103/PhysRevLett.25.902.2.

[53] CMS Collaboration, "Search for resonant and nonresonant new phenomena in high-mass dilepton final states at $\sqrt{s} = 13$ TeV", *JHEP* **07** (2021) 208, doi:10.1007/JHEP07(2021)208, arXiv:2103.02708.

[54] ATLAS Collaboration, "Search for high-mass dilepton resonances using 139 fb^{-1} of pp collision data collected at $\sqrt{s}$ =13 TeV with the ATLAS detector", *Phys. Lett. B* **796** (2019) 68–87, doi:10.1016/j.physletb.2019.07.016, arXiv:1903.06248.

[55] A. Flórez et al., "Searching for New Heavy Neutral Gauge Bosons using Vector Boson Fusion Processes at the LHC", *Phys. Lett. B* **767** (2017) 126–132, doi:10.1016/j.physletb.2017.01.062, arXiv:1609.09765.

[56] D. Choudhury et al., "Slepton production from gauge boson fusion", *Phys. Rev. D* **68** (2003) 075007, doi:10.1103/PhysRevD.68.075007, arXiv:hep-ph/0304192.

[57] B. Dutta et al., "Vector Boson Fusion Processes as a Probe of Supersymmetric Electroweak Sectors at the LHC", *Phys. Rev. D* **87** (2013), no. 3, 035029, doi:10.1103/PhysRevD.87.035029, arXiv:1210.0964.

[58] A. G. Delannoy et al., "Probing Dark Matter at the LHC using Vector Boson Fusion Processes", *Phys. Rev. Lett.* **111** (2013) 061801, doi:10.1103/PhysRevLett.111.061801, arXiv:1304.7779.

[59] C. T. Hill, "Topcolor assisted technicolor", *Phys. Lett. B* **345** (1995) 483–489, doi:10.1016/0370-2693(94)01660-5, arXiv:hep-ph/9411426.

[60] G. D'Amico et al., "Flavour anomalies after the $R(K*)$ measurement", *Journal of High Energy Physics* **2017** (Sep, 2017) doi:10.1007/jhep09(2017)010.

[61] B. Capdevila et al., "Patterns of New Physics in $b \to s\ell^+\ell^-$ transitions in the light of recent data", *Journal of High Energy Physics* **2018** (Jan, 2018) doi:10.1007/jhep01(2018)093.

[62] Belle Collaboration, A. Abdesselam et al., "Angular analysis of $B^0 \to K^*(892)^0\ell^+\ell^-$", in *LHC Ski 2016: A First Discussion of 13 TeV Results*. 4, 2016. arXiv:1604.04042.

[63] J. P. Lees et al., "Search forB→K(*)$\nu\overline{\nu}$ and invisible quarkonium decays", *Physical Review D* **87** (Jun, 2013) doi:10.1103/physrevd.87.112005.

Chapter 2

Experimental Setup

New physics beyond the standard model is expected to have mass at the TeV scale. To search for particles at the TeV scale, the particles must be produced with the TeV energy. The Large Hadron Collider (LHC) at CERN is the largest proton-proton collider in the world which is designed to collide proton beams at the center-of-mass energy ($\sqrt{s}$) of 14 TeV. The search presented in this Thesis is performed by analyzing data collected by the Compact Muon Solenoid (CMS) detector situated at the interaction point 5 at the LHC ring as shown in Figure 2.1. A brief description of the LHC accelerator complex and its experiments, followed by a detailed description of the CMS experiment and its main components is given in the later Sections of this Chapter.

2.1 The LHC accelerator

The LHC [2] is a proton-proton (and heavy ions) collider based at CERN in Geneva, Switzerland. The accelerator ring, which lies between 45 m and 170 m below the surface and is 26.7 km in circumference, was constructed between 1984 and 1989 for the CERN LEP machine. Inside the accelerator ring, two beams of high-energy particles (6.5 TeV for each beam) travel in opposite directions and collide at four points of the ring. During the first running period (Run 1) from 2010 to 2012,

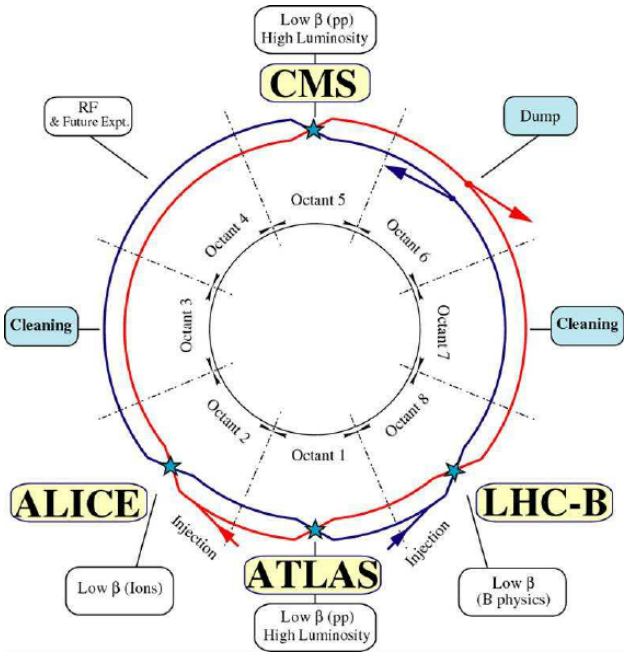

Figure 2.1: A schematic view of LHC ring and its four interaction points [1].

the LHC was operated at a center-of-mass energy of 7 TeV and 8 TeV for the *pp* collisions. The data collected from the first run (Run 1) led to the discovery of the Higgs Boson in 2012 [3], for which the LHC was designed for. After the long shutdown for the technical upgrades, the LHC was operated at a center-of-mass energy of 13 TeV during the second running period (Run 2) from 2015 to 2016. The LHC uses proton beams accelerated in bunches and each bunch consists of approximately 1.15×10^{11} protons [4]. These protons are extracted from the hydrogen gas by stripping electrons from the hydrogen atom. By design, each beam has 2808 bunches, which are separated by 25 ns. The proton beams are guided along the ring by strong magnetic fields maintained by superconducting electromagnets operated at very low temperatures (around $1.9^{\circ}K$) by a cryostats system filled with liquid helium. The magnets used are of various shapes and sizes; 1232 magnetic dipoles of 15 m in length are used to guide the proton beams around the ring; 392 magnetic quadrupoles of $5-7$ m each are used to focus the beams; just before the collision, an another type of magnet is used to reduce the size of the proton bunches, in order to maximize the collision probability and therefore the luminosity.

Before injecting these protons in the LHC ring, they are accelerated in a series

of machines that increase the energy of the beams in subsequent steps as shown in Figure 2.2. At first, they are accelerated to 50 MeV in the linear accelerator (LINAC 2) and are formed in bunches. The proton bunches are then injected in a sequence of circular accelerators. Starting with the Proton Synchrotron Booster (PSB) and the Proton Synchrotron (PS), the protons are accelerated to an energy of 26 GeV. The energy of the protons is further increased in the Super Proton Synchrotron (SPS) to 450 GeV, before being transferred to the LHC ring in both clockwise and anti-clockwise direction. In the LHC ring, the radio-frequency cavities increase the proton energy by 0.5 MeV per turn. The protons can be accelerated up to the design energy of 7 TeV (4 TeV in 2012). The particles are kept in a circular orbit via superconducting dipole magnets.

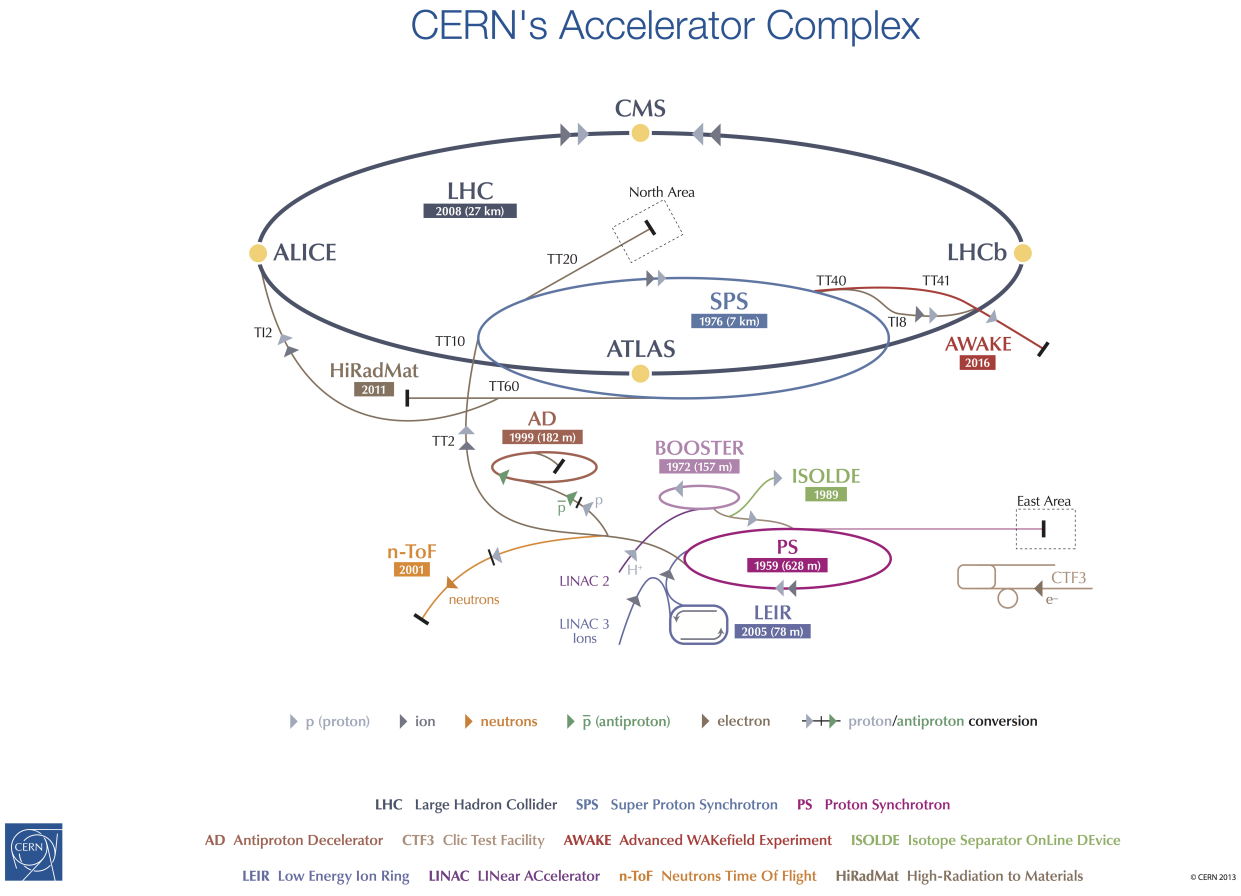

Figure 2.2: Overview of the accelerator complex and the various experiments at CERN [5].

In the LHC, the proton (and heavy ion) beams are focused and brought to collision at four interaction points where four detectors are situated. The ATLAS (A Toroidal LHC ApparatuS) and the CMS (Compact Muon Solenoid) detectors, located at opposite points at the LHC (Point 1 and 5 respectively), explore a wide range of physics phenomena and are referred to as general purpose detectors. The ALICE (A Large Ion Collider Experiment) and the LHCb (LHC-Beauty) detectors on the contrary are dedicated to more specific studies. The ALICE, located at point 2, investigates the quark-gluon plasma created by heavy ion collisions and the LHCb, located at point 8, focuses on B meson physics and the CP-symmetry violation.

Some of the interesting processes to search for new physics beyond the standard model, in particular those presented in this Thesis, happen not only at high energies, but also with low cross-section values. To produce enough statistics of such rare processes, it is necessary to have a large number of proton–proton collisions, and the magnitude to measure the number of collisions is defined by the *luminosity*, which is described briefly in the next Section.

2.1.1 Luminosity

The performance of the experiments in the search for new physics and for the precision measurements of the standard model physics depends on the two parameters of the LHC proton beams: the energy and the luminosity. The energy of the colliding protons is determined by how strong the magnets must be to keep the beams traveling in a circle. The dipole magnets with a magnetic field of $\sim$8.33 T are the primary magnets which keep the protons with momenta of the order of TeV inside the LHC ring by bending the trajectories of circulating protons. The superconductive coils of the magnets are placed on two sides of the beam pipe obtaining a magnetic field orthogonal to the LHC ring plane as shown in the Figure 2.3. The magnetic field is directed in the opposite direction in each beam pipe, allowing the proton bunches to circulate in opposite directions.

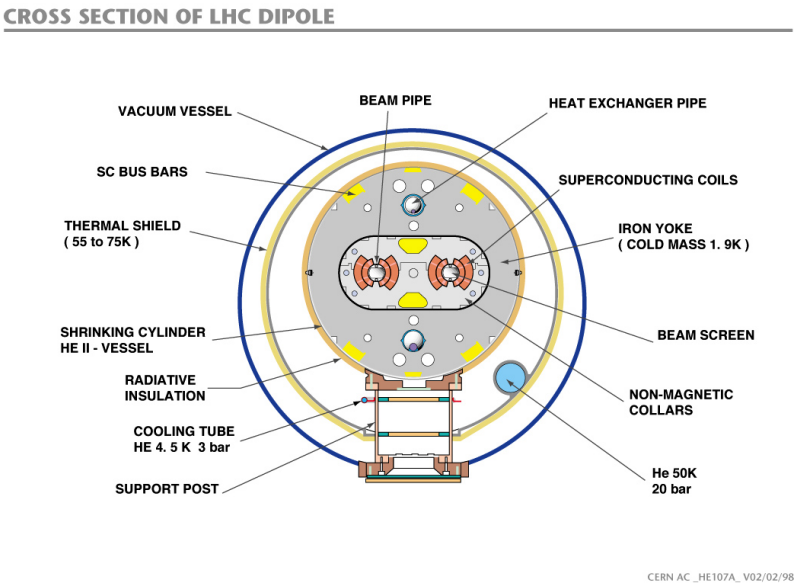

Figure 2.3: Cross section of a LHC dipole magnet [6].

The luminosity is determined by several factors such as how many protons are kept together in a bunch, how many bunches are present in the ring, and how small the size of a bunch can be maintained in the ring. The luminosity, L of a collider experiment is a measurement of the number of collisions that can occur in a detector per square centimeter and per second and is defined as:

$$L = \frac{N_b^2 n_b f_{rev} \gamma}{4\pi\epsilon\beta^*} F,$$
$$\text{where } F = \left[1 + \left(\frac{\theta_c \sigma_z}{2\sigma^*}\right)^2\right]^{-1/2} \tag{2.1}$$

here, N_b is the number of protons in a bunch, n_b is the number of bunches in the ring, f_{rev} is the frequency of revolution of the beam, γ is the relativistic Lorentz factor of the particles being collided, ϵ is the normalized transverse beam emittance, β^* is the value of the betatron function at the interaction point (IP). F describes the reduction factor due to the non-zero crossing angle of the beams which depends on the crossing angle (θ_c), the length of the proton bunch (σ_z) and the transverse beam size (σ^*). To maximize the number of interactions per bunch crossing, the transverse size of the beams and consequentially the β^* parameter, is reduced when approaching the

interaction point. At the same time, the crossing angle and the transverse offset of the beam crossing are minimized in order to have proton bunches meet almost head-on.

The expected rate of events produced in a given process with a cross-section, σ is given by

$$\frac{dN}{dt} = \sigma L \tag{2.2}$$

and therefore, high luminosity values are needed in order to study physics processes with low production cross-sections. The total number of events over a time period is proportional to the integrated luminosity:

$$L_{int} = \int L dt \tag{2.3}$$

During the Run 2 of the LHC, a total integrated luminosity of $\sim 163\,\mathrm{fb}^{-1}$ was delivered by the LHC, of which CMS recorded $\sim 150\,\mathrm{fb}^{-1}$ [7] as can be seen in Figure 2.4. The empty spaces depicts the timeline of the end-of-year technical stops (EYETS). This Thesis work is based on the analysis of the data collected by the CMS experiment between 2016 and 2018, leading to total integrated luminosity of $\sim 137\,\mathrm{fb}^{-1}$.

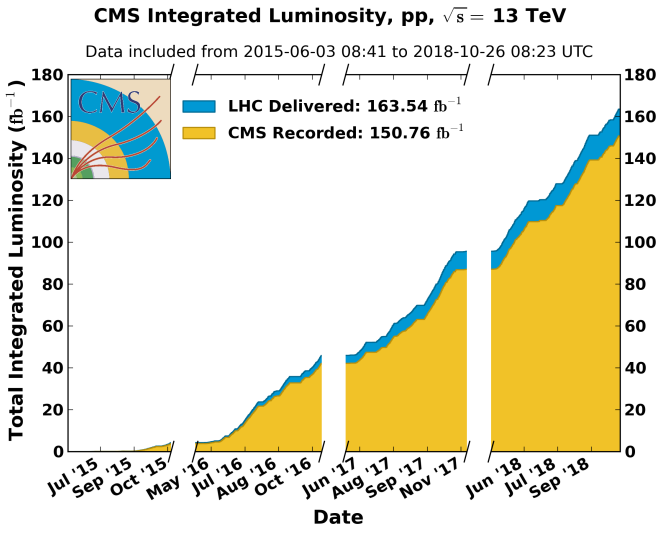

Figure 2.4: Graph of the total integrated luminosity delivered by the LHC and recorded by the CMS detector during Run 2 data-taking period [8].

2.1.2 Pileup

Colliding proton beams travel in bunches, with $\sim 10^{11}$ protons in each bunch. As a result, more than one interaction takes place in each bunch crossing. The number of additional collisions, with respect to the collision with the largest momentum transferred (hard interaction), are called *pileup* (PU) and are strongly affected by the beam squeezing via reduction of the β^* parameter. The major improvements in the beam squeezing were performed during EYETS between 2015 and 2016, and in the later part of 2017. This resulted in an increase in the number of PU interactions during Run 2, which can be seen in Figure 2.5. This clearly reveals the increased instantaneous luminosity, achieved each year of the data-taking during Run 2 of the LHC, and consequently increasing the probability of production of rare processes to search for new physics beyond the standard model.

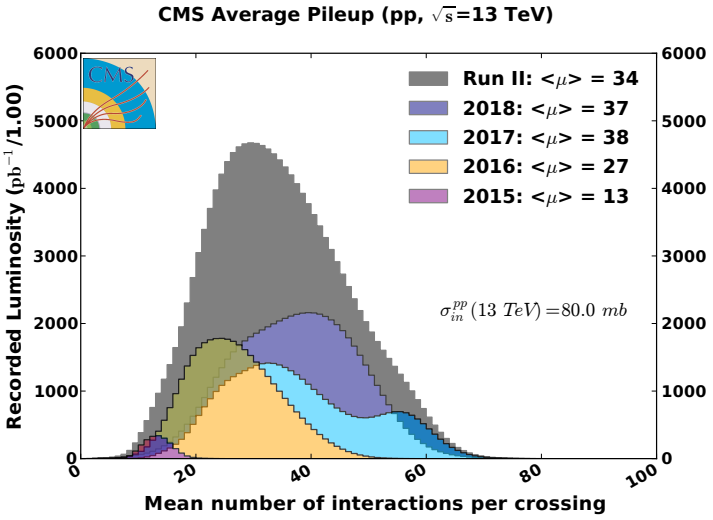

Figure 2.5: Distribution of the pileup for proton-proton collisions recorded by the CMS experiment during Run 2 [8].

At the time of writing this Thesis, the LHC is going under the second long-shutdown (LS2) (2019–2021), in preparation for the Run 3 operations. Run 3 is expected to start in mid-july of 2022, and to last until 2025. Then, after the third long-shutdown (LS3) of 2–3 years, the LHC will operate at its ultimate high luminosity configuration, the HL-LHC. During this phase, several upgrades are planned for the accelerator complex, which should allow to increase the peak instantaneous

luminosity to at least five times the nominal value. Several upgrades are foreseen also for the detectors [9] to account for the increase in the number of PU interactions and in the collision rate. The plan for the HL-LHC is to collect data between 3000 and 4000 fb^{-1} by 2040, increasing the total recorded luminosity by at least 10 times.

2.2 The CMS Experiment

The Compact Muon Solenoid (CMS) is one of the two large general purpose detectors, placed about 100 m underground at point 5 of the LHC accelerator complex. The detector has a cylindrical symmetry around the LHC beam axis and is designed to study a wide range of physics processes. The detector got its name based on three notable features it possesses:

- It has *compact* geometry, weighing 14,000 tonnes while being 28.7 m long and with an overall diameter of 15 m;
- It is designed to achieve optimal *muon* identification and momentum resolution;
- It has *solenoid* magnet providing magnetic field of 3.8 T with large bending power for the precise measurement of the charge and the momenta of charged particles. This is one of the largest superconducting solenoids ever built.

One of its main goals has been the search for the Higgs boson. Since its discovery, the CMS physics program is focused on the precise measurements of its characteristics as well as its couplings with other standard model particles. The experiment has also measured the properties of several other processes predicted in the standard model and continues its efforts in the search for signals of new physics at the TeV scale.

The compactness of the detector emerges from the need to host its various subdetectors (as shown in Figure 2.6), aimed at particle identification and reconstruction, in an artificial cavern built at a depth of 100 m. The main aspect of its design is easier

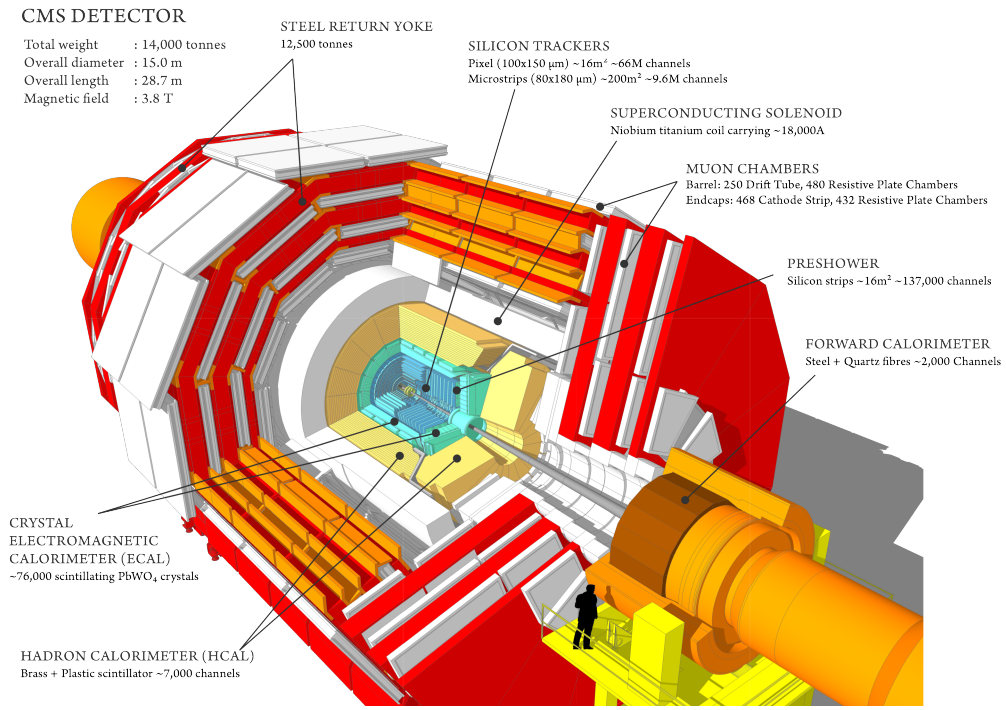

Figure 2.6: Sectional view of the CMS detector [10].

access to subdetectors for easier and faster maintenance. The CMS detector was built in fifteen separate sections or "slices" on the surface and then lowered down in the cavern. All these sections can be moved to access its various modules without uncabling the attached subdetectors. This is important for upgrading the detector during technical stops and long-shutdown. The detector is cylindrical symmetric with respect to the nominal beam intersection point and can be divided in two main groups:

- *barrel:* the central region of the detector which is closest to the primary interaction point;
- *two endcaps:* the endcap discs which are placed farther from the interaction point to detect particles emitted at a low angle with respect to the beam line.

The energy and momenta of particles produced in the proton-proton collisions are obtained by the information of all subdetectors, which are described in detail below. A more detailed description can be found at [11]. In order to describe the coverage

and placing of the subdetectors, it is necessary to define a frame of reference which is discussed below:

CMS Coordinate system Due to the cylindrical symmetry of the CMS detector, the most suitable choice is to use cartesian (x, y, z) or cylindrical coordinates (r, θ, ϕ) [12]. The origin of both the coordinate systems is located at the nominal collision point. The x-axis points radially toward the center of the LHC accelerator ring, the y-axis vertically upward and the z-axis parallel to the beam line in the anticlockwise direction as illustrated in Figure 2.7. The azimuthal angle ϕ is measured with respect to the $+x$-axis in the $x - y$ plane. The polar angle θ is defined with respect to the z-axis over the $y - z$ plane such that θ is zero at the positive and π at the negative z-axis. For convenience, *pseudorapidity* (η) is used instead of polar angle (θ) and is defined as:

$$\eta = -\ln \tan \frac{\theta}{2} \tag{2.4}$$

The angular distance,ΔR, between the two physics objects originating at the interaction point with coordinates (η_1, ϕ_1) and (η_2, ϕ_2) is given by:

$$\Delta R \equiv \sqrt{\Delta\eta^2 + \Delta\Phi^2}, \tag{2.5}$$

where $\Delta\eta \equiv \eta_1 - \eta_2$ and $\Delta\phi \equiv \phi_1 - \phi_2$. Quantities lying in the $x - y$ plane, or the transverse plane, are denoted in the text with a T subscript: X_T. For instance, the momentum of an object perpendicular to the LHC beam axis is termed as transverse momentum p_T. Similarly, the energy imbalance in the transverse plane is defined by the missing transverse energy, E_T^{miss}.

2.2.1 CMS Magnet System

The central feature of the CMS detector is the superconducting solenoid magnet of length 12.5 m and 6 m internal radius [13]. It is the key component for the measurement of the particle charge and momentum by bending the trajectory of

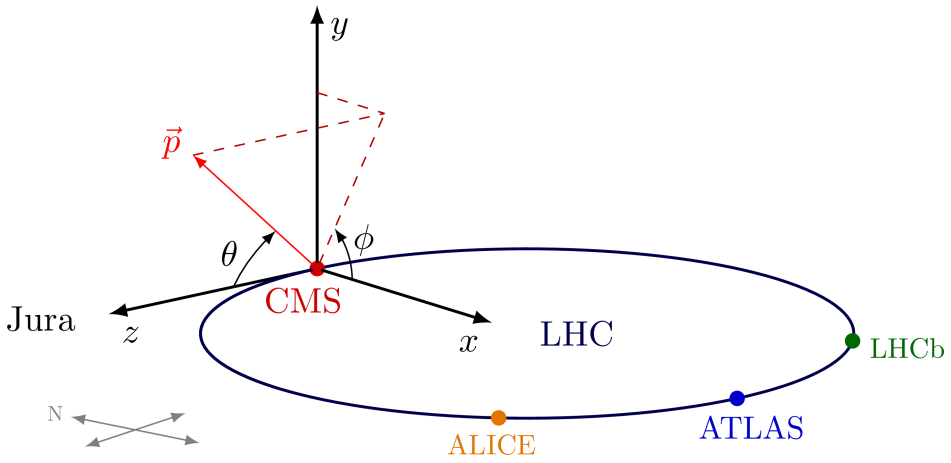

Figure 2.7: Coordinate system followed by the CMS detector.

charged particles. The magnet occupies the 2.9 m $< r <$ 3.8 m, $|\eta| < 1.5$ region, making it the largest magnet of its type ever constructed.

The magnet is made up of four layers of aluminum-coated NbTi superconducting coil, through which $\sim$ 18kA current is made to flow. The entire solenoid is placed within a vacuum tank cooled down to 4.7 K using a liquid helium cooling system. The magnet generates a magnetic field of 3.8 T in the central region of the detector. The magnetic field lines are confined to the volume of the detector through a steel return *yoke* of 14 m in diameter and 21.6 m in length. The yoke weighs over 10,000 tonnes. The magnetic field in the return yoke has an intensity of 1.8 T and is directed in the opposite direction with respect to the magnetic field in the central region. The layers of the return yoke are interleaved with the muon chambers, allowing a more precise reconstruction of the muon trajectory. With the exception of the muon chambers, all other detectors are placed inside the solenoid coil. This allows the tracking and the energy measurement of the particles to be performed without interaction with the bulk of magnet material.

2.2.2 Silicon tracker detector

The Silicon tracker system is the innermost subsystem of the CMS detector placed around the interaction point at a distance of $\approx$ 4.3 cm, where the rate of particles is

around 10^7 s^{-1}. Due to high radiation levels produced in the collisions, the detector is built with radiation hard silicon and also it provides the needed spatial and momentum resolution. The purpose of the silicon tracker is to provide efficient measurement of trajectories of the charged particles which are bent in the magnetic field. This allows to reconstruct the primary points of interactions of protons, referred to as *vertices*. This system is also an essential component to reconstruct *secondary vertices*, decay vertices for particles with average decay length of the order of centimeter, like hadrons that contain b or c quarks. Furthermore, the tracker plays a crucial role in the high-level trigger system of the CMS detector which is needed for the reduction of the event rate (from 40 MHz to about 100 Hz) to reach values compatible with detector readout, offline storage and analysis capability. The detector design features high granularity and fast timing response such that the trajectories can be identified reliably and can be attributed to the correct bunch crossing. The detector material is kept as minimum as possible, in order to limit the multiple scattering processes which can cause the charged particles to lose energy in the detector layers and alters their trajectory, causing inefficiency in the track reconstruction. The overall layout of the CMS tracking system is shown in Figure 2.8.

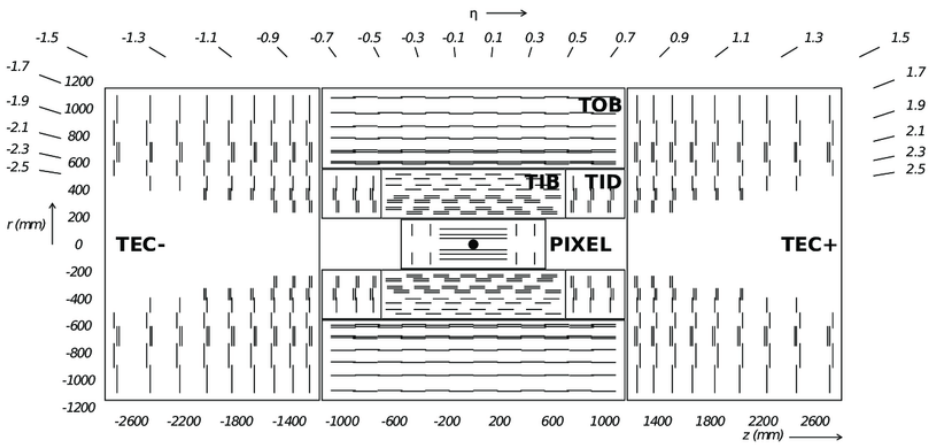

Figure 2.8: Layout of the CMS tracking system section in the $r - z$ plane. Each black line represents a detector module and closely spaced double lines represents back-to-back silicon strip modules. Note. This layout illustrates the pixel detector before its upgrade [14].

The tracking system occupies a cylindrical volume, 5.8 m in length and 2.5 m in diameter, around the interaction point, covering a pseudorapidity range $|\eta| < 2.5$. It consists of two distinct subdetectors : a silicon pixel detector surrounding the beam pipe ($r < 160$ mm) coping with larger particle densities, and a silicon strip detector surrounding the pixel detector. During the EYETS between 2016 and 2017, the pixel detector was upgraded [15] from its design during Run 1 and 2016 data-taking (*Phase-0*) to *Phase-1*, which will be kept unchanged till the end of Run 3. Since this Thesis work uses data collected across Run 2, the description of the silicon tracker is presented for the Phase-1 tracker, with a brief mention to its Phase-0 design.

Silicon Pixel detector The silicon pixel detector is the innermost detector, distributed concentrically in cylindrical layers surrounding the interaction point. It has an essential role in identifying the primary vertices of the interactions and, if present, the secondary vertices as well. It also provides the seed, i.e. the starting point, for the algorithm which fits a track onto the measured tracker hits. In 2017, the detector was upgraded by moving the innermost layer closer to the interaction point in the barrel section (BPIX), from 4.4 cm to 2.9 cm, and adding a new fourth outer layer at 16 cm. Each cylindrical structure is divided in two semi-cylinders each equipped with a support structure and a cooling system. The two endcap regions of the pixel detector, referred to as forward pixel detector (FPIX), comprise of total 3 disks structures during Phase-1 replacing two forward disks during Phase-0 design. The Phase-1 design and its differences with respect to the Phase-0 are illustrated in Figure 2.9.

The layout of the CMS Phase-1 pixel detector is optimized to have four–hit coverage and an improved track reconstruction. It is built from 1856 segmented silicon sensor modules, where 1184 modules are used in the Barrel Pixel detector (BPIX) and 672 modules are used for the Forward Pixel (FPIX). Each module is made up of 66,560 pixel sensors connected to 16 readout chips (ROCs). In total there are 124 million readout channels. These pixel sensors have a size of 100

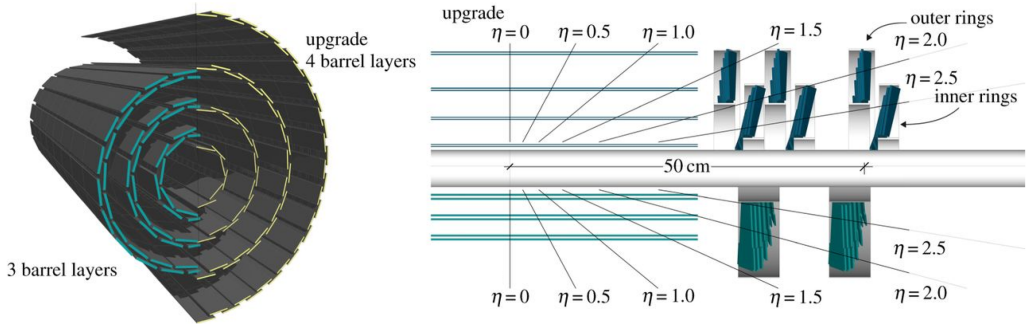

Figure 2.9: The CMS pixel detector. Left: Pixel barrel layers geometry previously (left) and after the upgrade (yellow area). Right: Pixel longitudinal view comparing Phase-1 in the upper part with Phase-0 in the lower part.

$\times$ 150μm^2 and are made with a substrate of type n on which $n+$ electrodes are mounted. Phase-1 tracker is designed to operate at very high luminosity (up to $2 \times 10^{34}\,\mathrm{cm}^{-2}\mathrm{s}^{-1}$). The track hit position resolution[1] provided by the pixel detector is 10 μm and 20 μm in the $r-\phi$ plane and $r-z$ plane, respectively.

Strip detector The silicon strip detector is placed around the pixel detector in the radial region from 20 to 110 cm with an overall length of 5.6 m and diameter of 2.4 m. Like the pixel detector, the strip detector has cylindrical elements in the barrel and disks in the endcap and is divided in four sections as shown in Figure 2.8:

- Tracker Inner Barrel (TIB) with 4 coaxial cylinders in the inner part of the barrel section covers the radial range 20-55 cm over a distance $|z| < 65$ cm;
- Tracker Outer Barrel (TOB) consists of 6 coaxial cylinders in the outer part of the barrel surrounding TIB up to a radius r = 110 cm;
- Tracker EndCaps (TEC) with 9 external layers are placed between 120 cm $< |z| <$ 280 cm on each side of the endcap. In the radial direction, the TEC coverage extends from r = 20 cm to r = 100 cm to cover the range up to $|\eta|$ = 2.5;

[1] In $r-\phi$ plane, due to strong magnetic field of 3.8 T, the resolution benefits from Lorentz angle of 27°in the barrel, spreading the ionization charge over several pixels. In the endcap, the pixel detector is rotated by 20°to benefit from the same effect.

- Tracker Inner Disk (TID) consists of 3 layers in the inner part of the endcaps and fill the gap between TIB, TOB and TEC.

Both TEC and TID modules are arranged in rings with their strips pointing towards the beam line. The Strip detector has 15148 silicon modules with 9.3 million strips in total. Each module has a silicon sensor with a substrate of type n on which $p+$ are implanted. Both the pitch between the strips and the thickness of the modules vary according to their position in the detector. Modules in the inner layers are 320 μm thick and contain sensors with a strip pitched every 80 μm, while in the outer layers thickness and strip pitch increase to 500 μm and 205 μm respectively. At a distance of $r < 60$ cm, the tracker hit point resolution varies from 23-35 μm in the $r - \phi$ plane and is 230 μm in the z direction in the TIB. Due to maximum cell size and large thickness (500 μm) of silicon strips at $r > 60$ cm, the tracker hit point resolution varies from 35-53 μm in the $r - \phi$ plane and is 530 μm in the z direction of the TOB.
The transverse momentum resolution is ≈1.5% for tracks of low momentum charged particles ($< 10\,\text{GeV}$) and ≈2.8% for high momentum muons ($= 100\,\text{GeV}$) in the central region of the CMS experiment [16].

2.2.3 Electromagnetic calorimeter

The Electromagnetic Calorimeter (ECAL) is a homogeneous calorimeter with cylindrical geometry and is placed right after the silicon tracker. It is the main component for measuring the energy and position of photons and electrons, as well as for the identification of electrons and neutral pions and measurement of the energy in electromagnetic showers. The ECAL consists of total 76 k scintillating lead tungstate ($PbWO_4$) crystals located in a cylindrical barrel section and in two endcap disks. The crystals have the shape of a truncated pyramid and are grouped into 5×5 matrices called *towers*. The geometrical layout of the ECAL can be found in Figure 2.10. The $PbWO_4$ crystals act as scintillator and absorber simultaneously and are characterized for having high density ($8.28\,\text{g/cm}^3$). These crystals are chosen

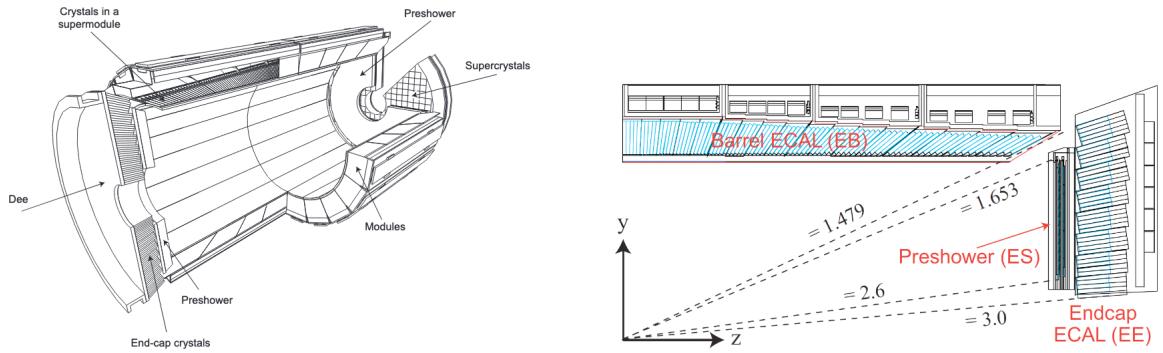

Figure 2.10: Geometric view of the ECAL [17].

due to their short radiation length X_0 of 0.89 cm and small Moliere radius of 2.2 cm, resulting in a compact calorimeter with a fine granularity. The fast time response of the crystals allows $\sim$ 80% of the scintillating light to be collected within the 25 ns gap between two consecutive bunch crossings. The crystals are also characterized by a good radiation resistance enabling the calorimeter to operate with limited deterioration on the scale of several year. The shortcoming of this crystal is the low light production $\sim$ 10 photoelectrons/ MeV, which makes a light amplification system necessary. This is achieved by using *Avalanche PhotoDiodes* (APD) in the electromagnetic barrel (EB) and *Vacuum PhotoTriodes*(VPT) in the electromagnetic endcaps (EE). Both types of photomultipliers are able to tolerate the hard radiation and strong magnetic field inside CMS. The ECAL is sub-divided in three regions as can be seen in Figure 2.10:

- ECAL barrel (EB), covers the pseudorapidity region up to $|\eta| < 1.479$ and has a cylindrical symmetry;
- ECAL endcap (EE), covers the pseudorapidity region with $1.479 < |\eta| < 2.6$;
- a preshower (ES), lies in the $|\eta| < 0.9$ and $1.65 < |\eta| < 2.61$ region.

The cylindrical EB calorimeter is located in a region of $r = (1.29 \text{ to } 1.75)\,\text{m}$ with a length of 6.09 m, thus covering $|\eta| < 1.479$ and has a volume of $8.14\,\text{m}^3$. It consists of 61200 tapered (23 cm long) crystals with a $(2.2 \times 2.2)\,\text{cm}^2$ front face and a

$(2.6 \times 2.6)\,\mathrm{cm}^2$ back face (25.8 radiation lengths). The crystals are inclined by 3° with respect to a line through the nominal interaction point. The EB crystals are arranged into modules, whereby four modules ($85 \times 20 = 1700$ crystals) are packed into one supermodule.

The EE disks are located at a longitudinal distance $|z| = 3.14$ - $3.9\,\mathrm{m}$ from the interaction point. Each endcap disk is made of two so-called "Dee"s, each consisting of 3662 $PbWO_4$ crystals. A 22 cm long tapered $PbWO_4$ crystal has a $(2.86 \times 2.86)\,\mathrm{cm}^2$ front face and a $(3 \times 3)\,\mathrm{cm}^2$ back face pointing to a focus 1.3 m beyond the nominal interaction point. The 7324 crystals of an EE disk correspond to a thickness of 24.7 radiation lengths. An area of 5×5 crystals is defined as one supercrystal as seen in Figure 2.10. The transition region ($1.4442 < |\eta| < 1.566$) between the EB and the EE results in smaller reconstruction efficiencies and is not considered in analyses requiring good electron and/or photon reconstruction.

A preshower system is placed in front of the EE disks to improve the position resolution for electrons and photons and discriminate between highly energetic photons and two closely spaced lower energy photons coming from $\pi^0 \to \gamma\gamma$ decays. The 20 cm thick preshower detector has an inner radius of 45.7 cm, an outer radius of 123 cm and covers a region of $1.65 < |\eta| < 2.6$. This sampling calorimeter consists of two lead absorber layers with a thickness of 2 X_0 and 1 X_0, respectively, interleaved with two planes of silicon strip sensors.

The energy resolution for ECAL can be written as a function of the energy E:

$$\frac{\sigma_E}{E} = \frac{a}{\sqrt{E}} + \frac{b}{E} + c, \tag{2.6}$$

where: a is a stochastic term related to the statistical fluctuations of the photon collection; b is related to the electronic noise and PU effects; c dominates at high energy and takes into account systematic effects like shower leakage and imperfections of the calorimeter. The ECAL barrel energy resolution was measured for electrons obtaining the following values: $a = 2.8\%$, $b = 12\%$ and $c = 0.3\%$ [18] [19].

2.2.4 Hadronic calorimeter

The Hadronic Calorimeter (HCAL) is a sampling calorimeter with brass absorber plates interleaved with plastic scintillator tiles acting as the active medium. It completely surrounds the ECAL and covers pseudorapidity range -5.2 $< \eta <$ 5.2. It is responsible for measuring the energy deposited by charged and neutral hadrons which is crucial for the reconstruction of hadronic jets and the missing transverse energy. Incident hadrons interact with the absorber via nuclear force and generate hadronic showers in the absorber and scintillator. The total amount of light produced by a shower in the scintillator is collected by wavelength-shifting fibers (WLS) and transported to photodetectors for readout. The interaction length (λ_I) of a material is the average distance traveled by a hadron before an inelastic nuclear interaction. Depending on η, the HCAL thickness varies within 10 - 15 λ_I, and thus provides good containment of the hadronic shower [11] [12]. Figure 2.11 shows the layout of the HCAL detector, showing the different subsystems: barrel (HB), endcap (HE), outer (HO), and forward (HF).

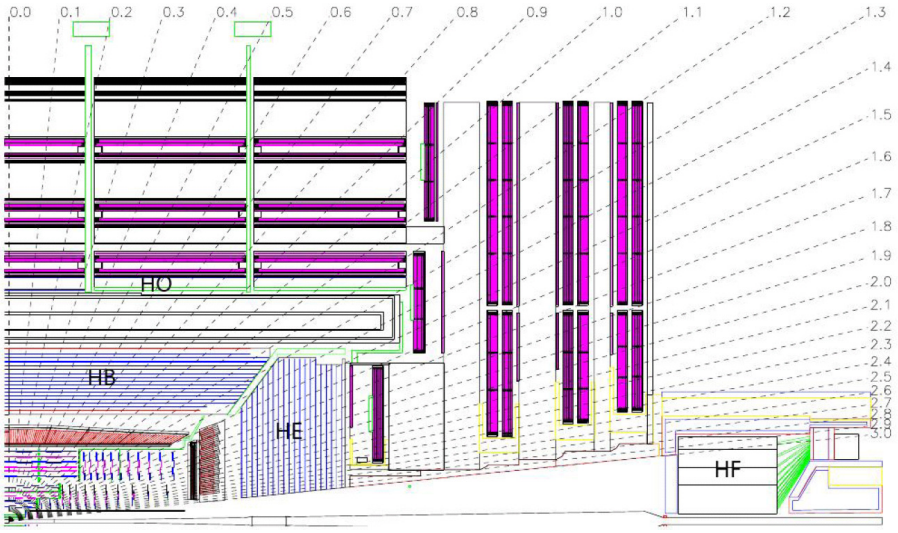

Figure 2.11: Longitudinal layout of the CMS hadronic calorimeter (HCAL) [20].

Hadronic Barrel Calorimeter (HB) HB is located between radii of 1775 and 2876.5 mm and covers $|\eta| < 1.39$. The HB is divided into two half–barrels in the direction along the beam (z). It consists of 70 k scintillator tiles distributed in 2304 towers with a granularity of $\Delta\eta \times \Delta\phi = 0.087 \times 0.087$. Each tower in the HB is composed of 15 layers of 5 cm thick brass absorbers and 3.7 mm thick plastic scintillators. The additional inner-most and outermost absorber plates are made of stainless steel to strengthen the mechanical structure. The innermost towers start with a 9 cm thick plastic scintillator layer directly behind the ECAL, which collects 1.5 times the energy in comparison to the other layers. The energy is read out with multi-channel Hybrid Photo-Detectors (HPDs) that can operate in a high magnetic field and give an amplified response for a large range of particle energies. The energy from each of the 17 active layer is optically added, thus forming 32 barrel HCAL towers in η with tower index ($i\eta$) from 1 to 16 as shown in Figure 2.12. The exceptions are towers 15 and 16 located at the edge of the HB half-barrel (orange layers in Figure 2.12) where multiple optical readouts are present and are read out with separate HPDs. During LS2 after Run 2 data taking, HPDs in the HB are replaced by Silicon Photomultipliers (SiPMs) leading to increased photon detection efficiency and increased depth segmentation. More details about this upgrade can found at this Reference [21] [22].

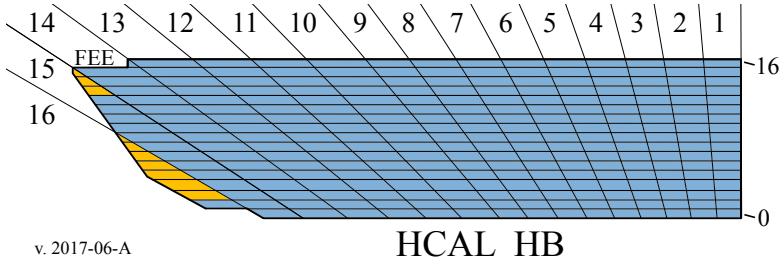

Figure 2.12: The schematic view of the tower mapping in $r - z$ plane of HCAL Barrel region.

Hadronic Endcap Calorimeter (HE) HE covers the region with $1.3 < |\eta| < 3$ partially overlapping HB. The innermost surface of HE is located 4006.5 mm from the interaction point and is radially divided into 14 rings containing 20 k scintillator tiles distributed in 2304 towers per endcap disk. The structure and the design is similar to the HB calorimeter with larger brass absorbers of 8 cm. For $|\eta| < 1.6$, the towers has 5° segmentation in ϕ similar to the HB with a granularity of $\Delta\eta \times \Delta\phi = 0.087 \times 0.087$. However, in the high-$\eta$ region ($|\eta| > 1.6$), the ϕ segmentation of the tiles is reduced to 10° to accommodate the bending radius of the WLS fiber readout, whilst the η segmentation varies from 0.09 to 0.35 at the highest η. Starting from Run 1 till 2017 data-taking, HPDs are used as a photodetectors in the HE similar to the HB. As of 2018, the HPDs are replaced by Silicon Photomultipliers (SiPMs) increasing gain factor from 2×10^2 to 10^6 [21]. SiPMs are quite compact (a surface area of 1 mm ^{2} to 9 mm ^{2}) and require an applied voltage less than 100 V. The high performance of the SiPM devices have allowed significant increase in depth segmentation in the HE. Figure 2.13 shows the layout of depth segmentation of the HE indicated by the color/shading of the tile structure for 2016-2017 geometry in the left and 2018 geometry in the right. This segmentation has allowed better tracking of hadronic shower development which is important for the particle identification and jet reconstruction techniques. The increased depth segmentation has also allowed better management of the radiation damage which is sizable in the high-η region of the HE calorimeter. More details on the radiation damage studies for the HB and the HE towers are discussed in the next Chapter of this Thesis.

Hadronic Outer Calorimeter (HO) In order to increase the number of interaction lengths in the barrel region and due to space limitations inside the magnet, an additional outer hadronic (HO) calorimeter is placed on the outer surface of the solenoid. It samples the energy from penetrating hadron showers leaking through the rear of the calorimeters and so serve as a "tail-catcher" after the solenoid magnet [23]. It follows the segmentation geometry of the HB calorimeter, consisting of a 10 mm thick layer of scintillators, except in a region $|z| < 2.868$ m, where the

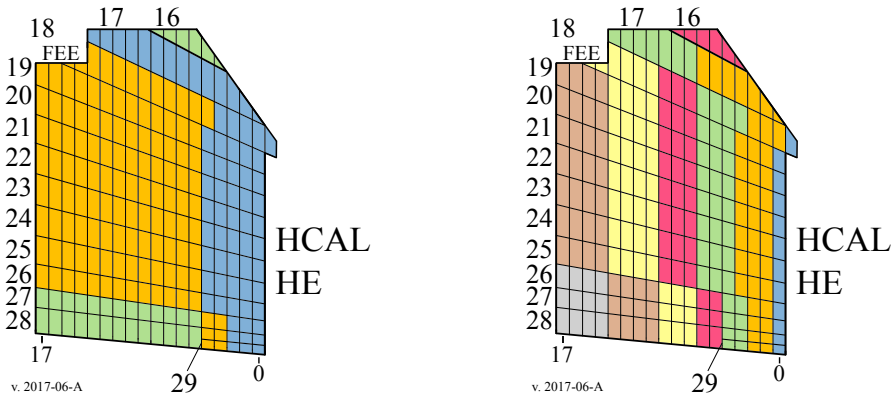

Figure 2.13: The schematic view of the towers mapping in $r-z$ plane of the HE during 2016 and 2017 (left) and after the SiPM upgrade in 2018 (right).

HO consists of two 10 mm thick layers of scintillators on either side of a 19.5 cm thick iron absorber. The HO calorimeter covers $|\eta| < 1.3$, increasing the minimal interaction lengths in the barrel region to $11.8\lambda_I$ using the iron return yoke as an additional absorber material as shown in Figure 2.14. The scintillating light is collected by wavelength shifter fibers (WLF) and transported to SiPMs placed on the side of the return yoke [24].

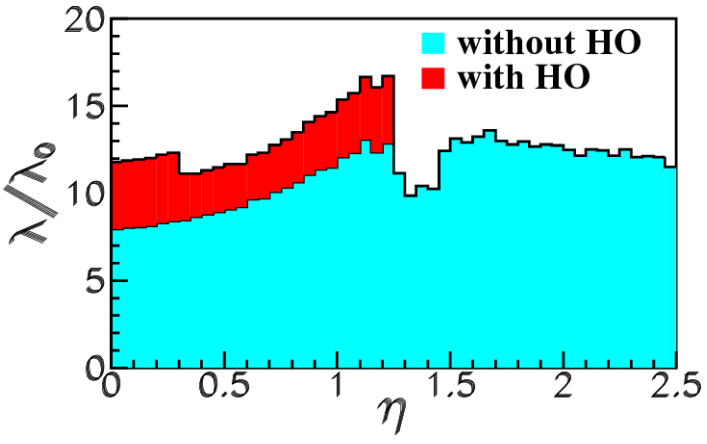

Figure 2.14: Number of interaction lengths till the last sampling layer of the hadron calorimeter as a function of η. The two shaded regions correspond to the setup with or without the outer hadron calorimeter (HO) [23].

Hadronic Forward Calorimeter (HF) To close the detector hermetically and ensure a good reconstruction of E_T^{miss}, an additional hadronic forward (HF) calorimeter surrounds the beam pipe covering the radial range from 12.5 cm to 130 cm at a distance $|z| = 11.2\,\mathrm{m}$ from the interaction point, thus enlarging the pseudorapidity coverage to $2.9 < |\eta| < 5.0$. HF is placed in the forward region order to contain hadronic showers from energetic forward jets in the intense radiation levels in the forward region [25] [26]. Plastic scintillators are not suited for such high radiation environment, hence they are made of 5 mm thick steel absorber plates interleaved with 0.6 mm thick layers of radiation hard quartz fibers, resulting in a thickness of $10\lambda_I$. The incoming particles release energy in the form of Cerenkov light emitted in the quartz fibers, which is then channeled by the fibers to photomultipliers.
The energy resolution for the hadronic calorimeters in the barrel region and in the endcaps can be parameterized as a function of the energy E:

$$\frac{\sigma_E}{E} = \frac{0.9}{\sqrt{E(\,\mathrm{GeV})}} + 0.045, \tag{2.7}$$

while for HF the energy resolution is:

$$\frac{\sigma_E}{E} = \frac{1.72}{\sqrt{E(\,\mathrm{GeV})}} + 0.09. \tag{2.8}$$

The fluctuations in sampling and energy loss through leakage make the performance of HCAL worse than the ECAL.

2.2.5 Muon system

Outside the solenoid magnet and embedded in the iron return yoke, the muon system is designed for muon identification, precise momentum measurement and trigger capabilities, given the key role muons play in both, SM measurements, and in new physics searches. Muons have an average lifetime of 2.2 µs [27], their decay length is therefore much larger than the size of the CMS detector. They interact weakly with the calorimeters and escape the magnet without being stopped since they are mini-

mum ionizing particles. Their detection, and momentum measurement are operated by the tracking system in conjunction with the muon system. Figure 2.15 shows improvement in the muon momentum resolution at high momentum combining the measurements of inner tracker and muon detectors. CMS muon system has three

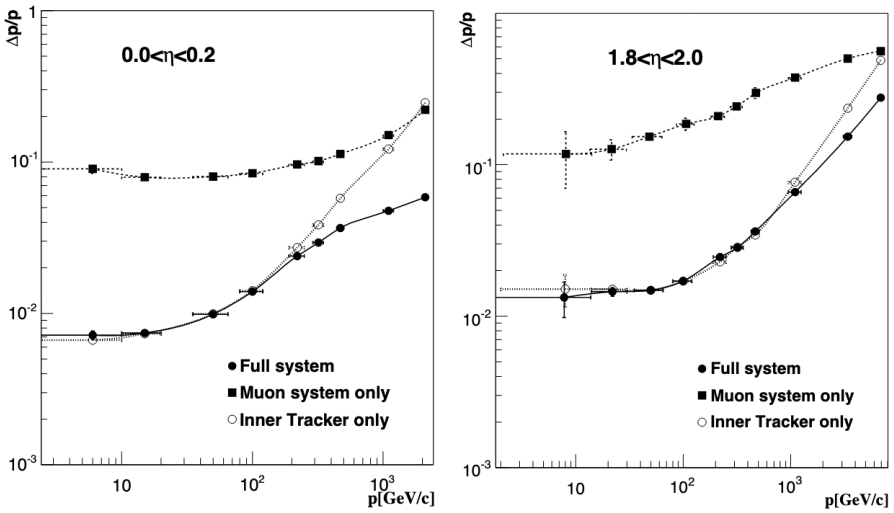

Figure 2.15: Comparison of muon momentum resolution as a function of momentum (p) with muon system only, the inner tracker only, or both [12].

different kinds of gaseous chambers inserted in the segmented iron return yoke as shown in Figure 2.16. The different particle flux and residual magnetic field found in the various regions covered by the muon detectors required the use of different technologies to build each subsystem. In the barrel region with relatively low muon and neutron induced background rates, layers of drift tubes (DT), green-coded in the Figure, are used up to $|\eta| = 1.2$. In the forward region both these rates are higher and therefore cathode strip chambers (CSC), pictured in blue in Figure 2.16, are used in this region up to a pseudorapidity of 2.4. Additionally to the DTs and CSCs resistive plate chambers (RPCs) are installed (colored in red in Figure 2.16). The 1400 muon chambers (250 DTs, 540 CSCs and 610 RPCs) have a total surface of 25000 m^2 with about 1 million electronic channels. Tracks in the muon detector are built by combining the hits from the three muon sub-detectors, DT, CSC, and RPC, using the Kalman–filter technique [28]. Afterwards, this track is combined with a track in the Tracker detector to reconstruct the full muon track. More details on

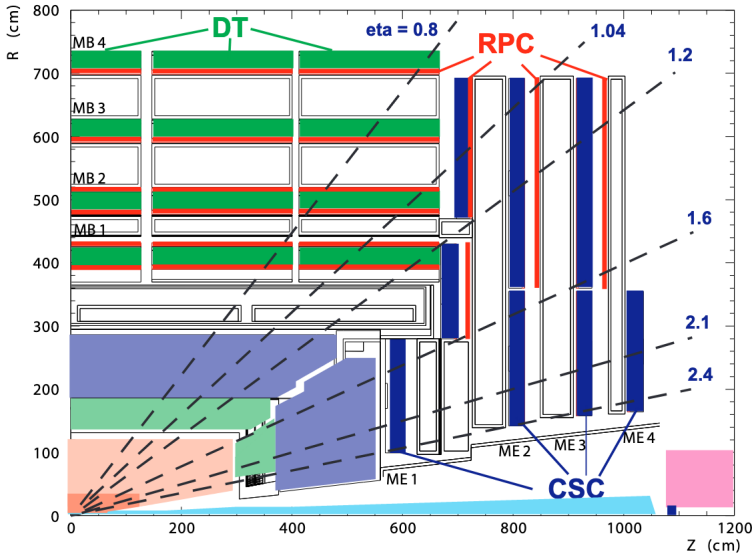

Figure 2.16: Layout of one quarter of the CMS muon system in the $r-z$ plane with the four DT stations in the barrel (MB1-MB4, green), the four CSC stations in the endcap (ME1-ME4, blue), and the RPC stations (red) [12].

muon track reconstruction can be found in the next Chapter. From the curvature of the track, the muon transverse momentum and charge are determined. The details of three muon subsystems are given below.

Drift Tubes (DT) The muon barrel detector consists of 250 aluminium drift tube chambers in the region $|\eta| < 1.2$, located in four layers inside the return yoke, labeled as muon stations MB1-4 as shown in Figure 2.17. These layers are arranged in concentric cylinders at a distance of 4.0, 4.9, 5.9 and 7.0 m from the beam axis. Each layer is divided into 5 wheels and subdivided into 12 sectors each covering an azimuthal angle of 30°. A DT cell consists of a high voltage carrying wire in the middle of a 4 cm diameter gas tube filled with a $Ar(85\%)/CO_2(15\%)$ mixture. A DT chamber consists of 12 layers of such cells arranged in three groups of four, and has a size of about 2 m × 2.5 m. The middle group, rotated by 90°, provides a measurement of the z coordinate parallel to the beam line and the two outside groups measure the perpendicular coordinate in $r-\phi$ direction. The outermost muon stations MB1 and MB4 have only eight layers of DT cells per chamber and measure only the $r-\phi$ direction. The two layers MB1 and MB2 carry RPCs on

both sides, while layers MB3 and MB4 are combined with one RPC each as seen in Figure 2.16. In the DT chambers the spatial resolution is around 100 µm with precision of approximately 1 mrad in direction.

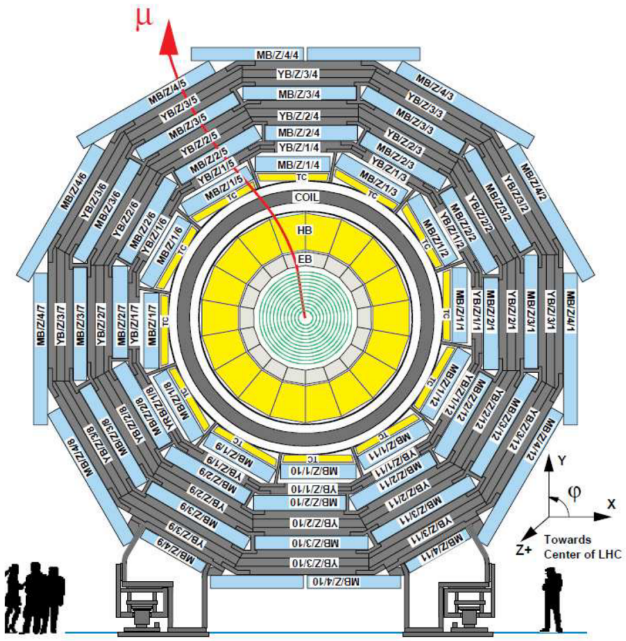

Figure 2.17: Layout of CMS barrel muon DT chambers in one of the 5 wheels [29].

Cathode Strip Chambers (CSC) CSC have shorter drift path and faster time response. For this reason they are located at the endcaps regions ($0.8 < |\eta| < 2.4$) of CMS where the muon rates and particle multiplicities are higher. In order to provide precise space and time information, the CSCs have closely spaced wires. This make the CSC a fast detector suitable for triggering. The two muon endcap detectors contain 270 CSC chambers each, distributed in four disks per endcap perpendicular to the beam line (labeled as the ME1 to ME4 stations) as shown in Figure 2.18 (left). A station is divided into 36 sectors each covering an azimuthal angle of 10 °. A CSC chamber is a trapezoidal proportional chamber consisting of six anode wire planes interleaved with seven radially arranged copper strip cathode panels as shown in Figure 2.18 (right). CSC chambers are filled with a mixture of $Ar(30\%)/CO_2(50\%)$ with $CF_4(20\%)$ as a quencher, that provides a drift path shorter than DT. The size of each CSC chamber is about 2-3 m × 1-1.5 m. A charged particle passing

through the chamber produces a charge on the anode wire and an image charge on a group of cathode strips. In each CSC chamber up to six space coordinates (r, ϕ, z) are computed for each track. The spatial resolution is about 100 µm. The timing resolution per layer is approximately 5 ns [30].

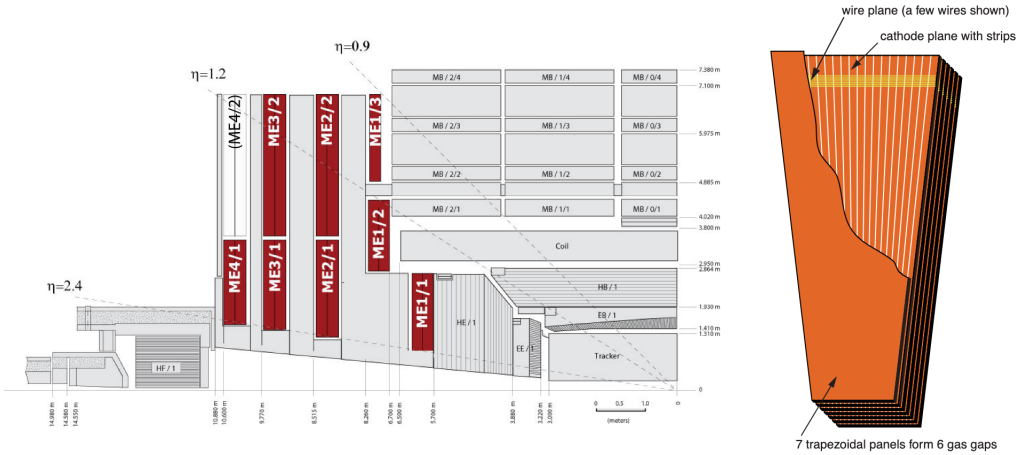

Figure 2.18: Layout of CSCs (red in color) in one quarter of the CMS(left) [31] and Schematic view of a CSC chamber (right) [12].

Resistive Plate Chambers (RPC) RPCs are placed both in the barrel and endcaps for robustness and redundancy. They are fast gaseous detectors that provide a muon trigger system with a time resolution better than 3 ns, complementary to those given by the DT and CSC chambers [32]. However, the RPCs give coarse spatial resolution of about 1 cm since they work in avalanche mode) [33]. There are 480 RPC chambers in the barrel region placed parallel to the wires of the DT chambers and 36 RPC chambers parallel to the CSC strips in the endcap. The RPC are made of four Bakelite planes coated with graphite as electrodes and two gas gaps between them of 2 mm. The central part of every chamber is equipped with insulated aluminum strips in order to collect the signals generated by crossing particles. The gas gaps are filled with mixture of $C_2H_2F_4(95\%)/iC_4H_{10}(5\%)$.
The transverse momentum resolution for muons in CMS with $p_T < 100$ GeV ranges from 1.3-2.0% in the barrel region to less than 6% in the endcap region [34] as shown in Figure 2.19.

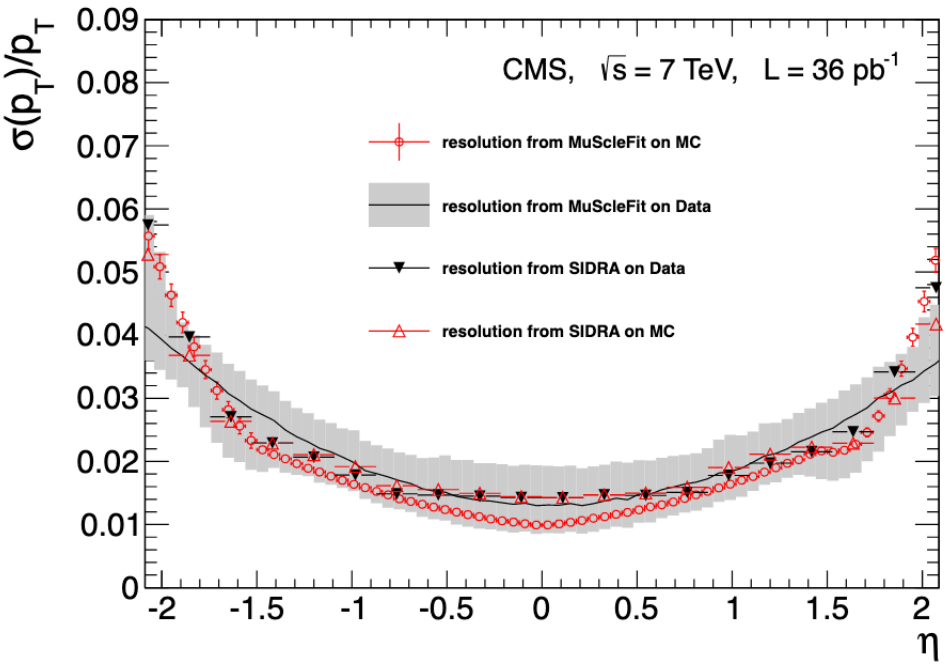

Figure 2.19: Relative transverse momentum resolution in data and simulation using muons produced in the decays of Z bosons [34].

Gas Electron Multipliers (GEM) During LS2 after Run 2 data-taking, GEM detectors are installed in the forward muon endcap covering pseudorapidity range $1.6 < |\eta| < 2.2$ at a distance of 5.6 m from the interaction point. There are total 144 chambers in both endcaps of muon system and are placed in front of CSC chambers as shown in Figure 2.20 and are referred as *GE1/1 detector*. This detector will enhance the existing muon triggering and tracking capabilities in combination with CSC information in the forward region [35]. GEM detectors are micropattern gas detectors invented by Fabio Sauli in 1997 [36]. GEM detectors installed in CMS muon endcap system are trapezoidal in shape with an active area of 990 $\times$ (220 - 445) mm ^{2} and consist of three foils having 3/1/2/1 mm electrode gap filled with $Ar(70\%)/CO_2(30\%)$ gas mixture. GEM detectors provide an excellent timing resolution of ∼8 ns with a spacial resolution of ∼250 µm [37]. Besides other production sites across the world, Panjab University fabricated eight of the GEM chambers. After performing needed quality control tests, the chambers were shipped to CERN and later installed at CMS detector. More details on the fabrication and

the testing of these chambers by Panjab University are discussed in the next Section. GEM detectors are placed in the forward region of the CMS detector, where they are subjected to intense particle flux. For an optimum design and efficient operation of the detectors, a precise knowledge of the detector performance in the presence of such a high background is essential. As a result, a detailed study of the GEM detector response to incident background particles is performed and is discussed in the following Section.

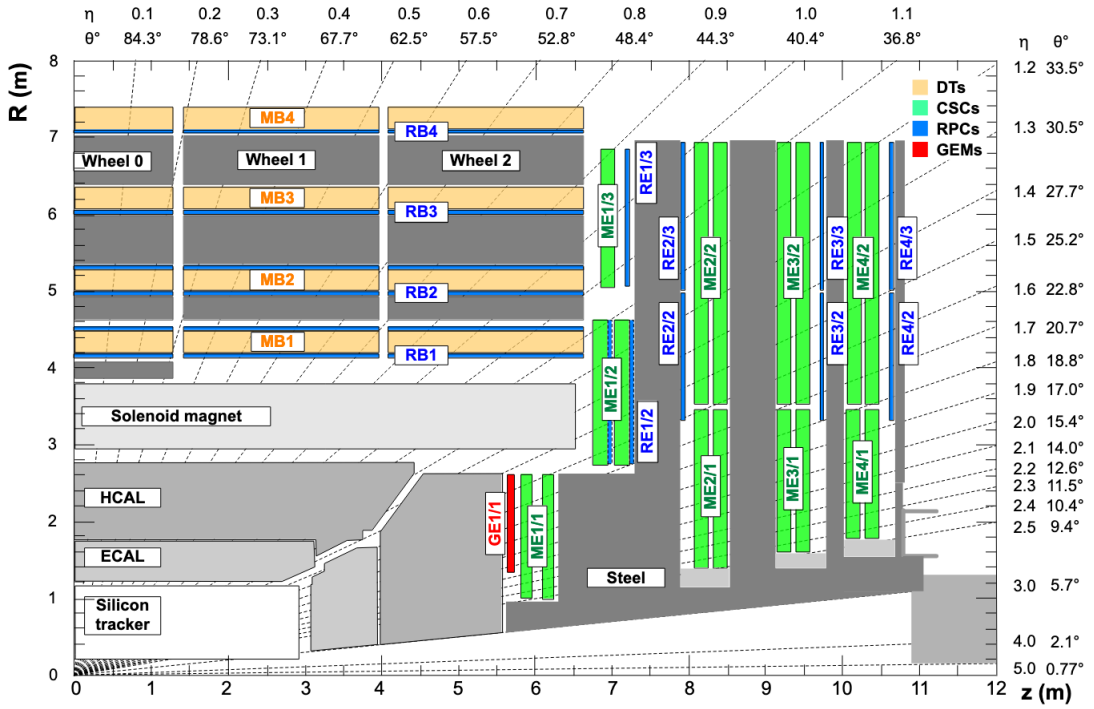

Figure 2.20: A quadrant of CMS detector in $r - z$ plane, highlighting (in red) the location of the GE1/1 detector [35].

- **GEM detector fabrication and testing :** Each of the eight GEM chambers are assembled mainly in two steps at the Panjab University site. The first step, named as the *Pre-assembly*, involves the preparation of the readout board, soldering of resistances (potential divider) on the drift board, cleaning of internal frames and external frame of the detector. The second step involves the *main assembly* of the detector, which includes the testing of foils, assembly of the GEM stack and closing of the chamber. Both the steps are

performed in the class-100 clean room, to avoid any dust particles entering the detector which can lead to irregular operation of the detector or can even damage the detector. The entire assembly takes 3-4 days to complete. For the main assembly, the GEM foils are cleaned thoroughly, first using a sticky roller to remove any visible dust and then the foils are placed overnight in a N_2 gas chamber to remove moisture or any impurities. The foils are then tested, by applying 550 V for several minutes using a Multi-Mega ohmmeter (also known as Megger). If the observed resistance of the foils reaches 20 GΩ, the foils are marked *OK* for the next steps of the assembly. Similarly, all the three foils are tested and are prepared for the main assembly. The tested foils are then stacked together using the dedicated spacers of 3 mm, 1 mm, 2 mm and then 1 mm and are fixed loosely using dedicated screws. The foils are then stretched carefully by attaching a tape to the dead area on the side of the foils, to fix for any deformities as shown in Figure 2.21 (left). The stack is then tightly packed by tightening the screws. The stacked foils are again tested by applying 550 V using the Megger as shown in Figure 2.21 (right). The observed resistance should again reach 20 GΩ.

Figure 2.21: Placing the metallic screws in the spacers (Left). Testing the GEM foils using the Megger (Right).

The assembled stack is then placed on the drift board carefully and is packed

tightly using the FR4 frame, to avoid gas leaks in the closed chamber. After cleaning and testing the foils again, the GEM chamber is closed by placing the readout board on top of the GEM stack and tightly packing it using the screws as shown in Figure 2.22 (left). The assembled GEM chamber is again tested at 550 V to check for any impurities as shown in Figure 2.22 (right).

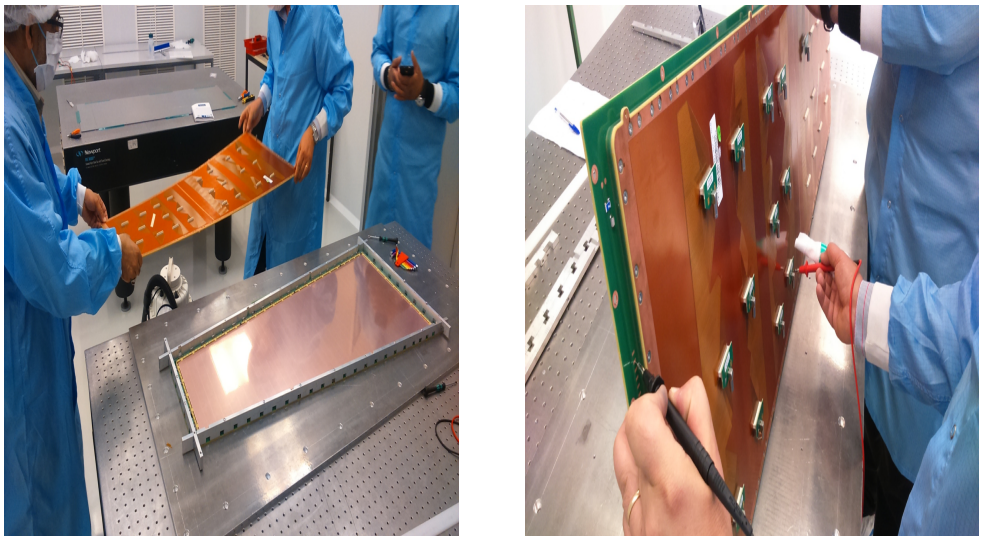

Figure 2.22: Mounting the readout board on the stack (Left). Testing the assembled chamber using Megger (Right).

After testing, the assembled chamber is fully ready for the next quality control (QC) tests, to ensure fully efficient assembled GEM chamber. The assembled detectors are then named as "GE1/1_X_S_INDIA_00YY" (where YY stand for 02, 07, 08, 09, 10, 15, 16, 17). The main QC tests performed at the Panjab University site are discussed below:

QC2 Leakage Current test : The QC2 leakage current test is aimed to determine the production quality of a GEM-foil. The test includes the measurement of maximum leakage current flowing on the surface of the GEM foils. The foils and the gas gaps are tested with 550 V using the Megger and then the impedance as well as the number of sparks are measured after 30 s and then every minute over a period of 10 minutes. The detector is accepted if the impedance of all the GEM-foils is above 10 GΩ after a few minutes, and no

sparks are observed after a period of 10 minutes. Similarly, the impedance of all the gas gaps must be measured, and it should reach 100 GΩ or more after only a few minutes, with no sparks. Similarly, an impedance of 100 GΩ should also be measured over all the 24 Panasonic connectors. All the eight chambers qualified the QC2 test successfully and are then taken to the QC3 test.

QC3 Gas Leak test : The QC3 gas leak test is performed to identify any possible leakage of gas from the detector. Since the drift board and readout board are closed using several hundred screws, hence it is possible that gas can get leak from these screw points either due to some screws remain loose during assembly or some are tightened with too much force that they get break inside the frames. The QC3 gas leak test is performed on the assembled detector when the detector is connected in between the inlet and outlet of the gas system. The flow-rate is again set to 5 L/hr using the input valve of flow meter, and the over-pressure in a detector is set to about 25 mbar. The DAQ system records the over-pressure inside the detector and other environmental parameters (room temperature, relative humidity and atmospheric pressure) as a function of time. The GE1/1 detector is validated, if the pressure drop in the detector + gas system does not exceed 7 mbar per hour. The QC3 gas leak test result of all the GE1/1 detectors assembled at the Panjab University site is shown in Figure 2.23. All the detectors assembled at the Panjab University production site successfully passed the QC3 gas leak test.

QC4 HV test The aim of the QC4 High Voltage (HV) test is to determine the current vs. voltage (I–V) characteristics of the assembled GE1/1 detector to identify the possible malfunctions and defects in the HV circuit and to calculate the intrinsic noise rate. The GE1/1 detector under test is first flushed with pure CO_2 gas for at least 5 hours before the test and is connected to negative high voltage (V_{set}) provided by programmable HV power supply which allow a user to control the current limit (I_{set}), steps to ramp up and ramp down

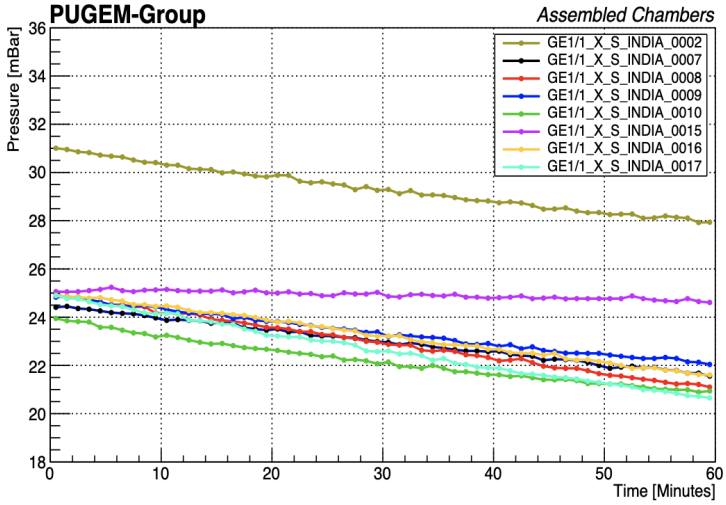

Figure 2.23: Results from the QC3 Gas Leak Test on the GE1/1 detectors assembled at Panjab University. All the detectors successfully passed the QC3 gas leak test.

the voltage, maximum voltage and the trip time. The ORTEC pre-amplifier is connected to the bottom electrode of the third GEM-foil through a decoupling RC circuit, which is already present on the detector's drift board. The output of the pre-amplifier is then sent to an amplifier+shaper unit and then to the discriminator. For the rate measurement, the resulting digital pulses are sent to the dual timer and then to the scaler unit. To cut the high-frequency noise, HV low-pass filter is connected between the SHV connector of the detector and the power supply. Also, copper ribbons should be used for the proper grounding of the detector, the pre-amplifier, and the HV filter. To perform the QC4 HV test on the assembled detector, the total resistance of the HV circuit (including the divider and all HV filter) is measured using a digital multimeter. The discriminator threshold and the scaler clock are set to -140 mV and 60s, respectively. After the operating current and voltage gets stable, the actual voltage V_{mon} and the current I_{mon} is recorded, and the number of counts is measured using the scaler unit for 60s. All these parameters are recorded in online DAQ system. These steps are repeated until the voltage reaches 4900 V on the detector with a step of 100 V. The I-V curve is plotted, which is expected to be a straight line, and the reciprocal of its slope gives the

total equivalent resistance of the HV distribution system. This value is then compared to the value of resistance measured using a digital multimeter. The test is said to be validated if the difference between the two resistance values is less than 2%. Further, the intrinsic noise rate, which is defined as the rate of signals not arising due to ionization of the gas, is calculated. The detector is said to pass the test if the average intrinsic noise rate of the GE1/1 detectors is found to be less than 15 Hz at 4.9 kV. Figures 2.24 (left) and 2.24 (right) show the V_{mon} as a function of I_{mon} and intrinsic noise rate as a function of I_{mon} for different GE1/1 detectors assembled at Panjab University site. All the detectors assembled at the Panjab University site passed all the QC tests [38] and were shipped to CERN for further testing followed by installed in the CMS detector.

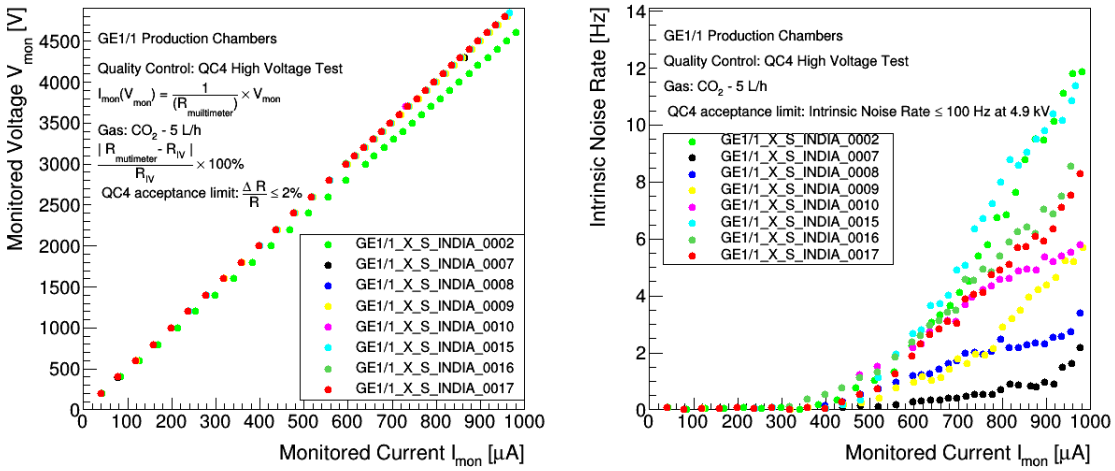

Figure 2.24: Mounting the readout board on the stack (Left). Testing the assembled chamber using Megger (Right).

- **GEM background particle simulation :** The GEM detectors are installed in the forward region of the CMS detector, where particles from the multiple interactions during the *pp* collision reach the GEM detector. These incident particles from the *pp* interactions interact with matter, resulting in low energy neutrons, photons, electron/positrons and charged hadrons. These particles are commonly referred to as *background particles*. These background particles

can damage the detector elements and can cause spurious signals that degrade the detector performance. To study the radiation environment and its impact on the detector performance, the estimation of the hit rate for various background particles is performed. The hit rate is defined as the number of particles detected per unit of time in a single chamber and is given as follows:

$$\text{Hit rate} = \text{Sensitivity} \times \text{Flux} \tag{2.9}$$

where, Sensitivity is defined as the probability for a charged particle to deposit energy in the sensitive volume of the detector (i.e., Ar/CO_2 gas mixture), and to produce primary ionized electrons [39] [40]. Hence, the sensitivity can be expressed as the ratio of the number of hits recorded above a certain energy threshold to the total number of incident particles entering the active surface of the GEM detector from any direction. The readout electronics for the GEM detector have a threshold of 3 fC. The sensitivity is measured from the GEANT4 simulation package [41], by defining the accurate geometry of the GEM detector. Flux is defined as the incident number of particles per unit area per unit time weighted for their track length in the GEM detector volume. Particle flux is estimated using the FLUKA simulation package [40] with Run 2 CMS detector condition and at LHC instantaneous luminosity of 1.5×10^{34} $\text{cm}^{-2}\text{s}^{-1}$. The FLUKA simulation provides the information needed for all possible particle types arriving from different directions at a given position and time. The flux of the incident background particles such as neutrons, photons, $e^{\pm}$ and charged hadrons is shown in Figure 2.25. As can be seen from the figure, the major contribution in the GEM region comes from low energy neutrons, photons whereas very small contribution comes from the $e^{\pm}$ and the charged hadrons. Minor contribution comes from the muons from gauge boson decays, and are neglected in the presented study.

Sensitivity is the measure of the detector response and depends on the particle type, its kinematic properties, and the composition of the material in which

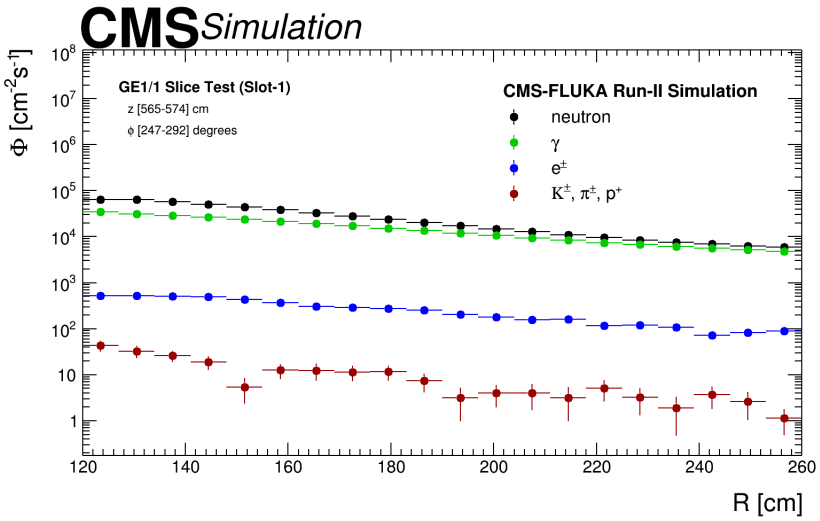

Figure 2.25: Flux of particles, normalized to the instantaneous luminosity, incident at the GE1/1 volume.

the particle interacts. The sensitivity is estimated using the same detector configuration as used in the GE1/1 slice test performed during Run 2 [43]. The GEM detectors are installed in a pair, and are referred to as *supercham-ber*, with Layer 1 and Layer 2. The average sensitivity is obtained from the convolution of the sensitivity at a given energy and incident angle with the normalized abundance of particles at that energy and incident angle as shown in Figure 2.26.

The accuracy of the sensitivity relies on the correct description of the physics processes and on realistic detector modeling. The physics processes considered in this simulation are well known and have been validated in the GEANT4 framework [44] [45]. To quantify the impact of the detector modeling on the sensitivity, detector configuration, such as drift gap width, gas mixture proportion and the distance of impact parameter, is varied. The drift gap variation of ± 0.3 mm is considered w.r.t. the nominal value of 3 mm. Similarly, to measure the effect of the gas mixture proportion, two Ar/CO_2 compositions w.r.t. the nominal (70:30) composition, 60:40 and 80:20 are considered. The impact parameter distance of 3 mm, perpendicular to the GEM surface, is considered in this study. The effect of this on the sensitivity is measured by

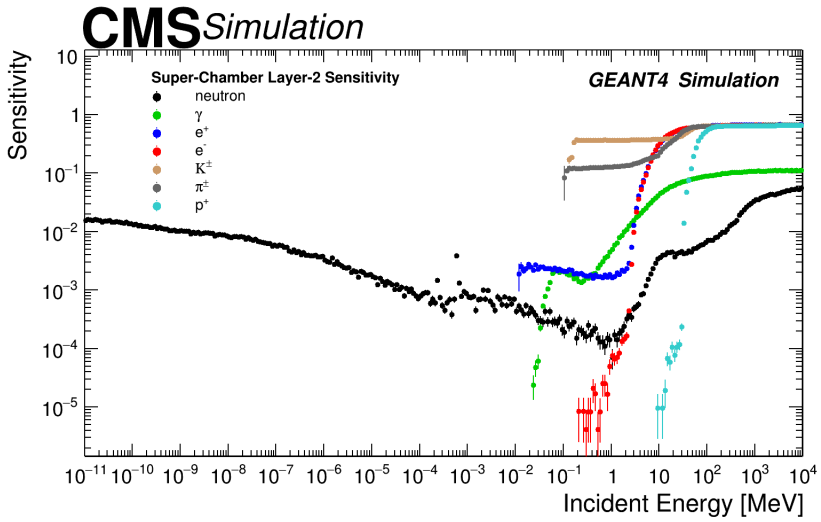

Figure 2.26: Sensitivity of the GEM detector as a function of incident energy for different particles. The sensitivity is convoluted over all possible incident angles.

varying the distance by ±2 mm. A total variation of 0.5-0.8%, 0.0-1.0%, 0.2-0.4%, and 3.9-8.8% on the average sensitivity for neutrons, photons, $e^{\pm}$, and charged hadrons, respectively, is estimated. The systematic uncertainty associated with the particle flux is estimated by comparing the Run 2 scenario in FLUKA with an alternative scenario. In this alternative scenario, the material composition of the shielding in front of the Hadron Forward (HF) calorimeter is changed, replacing borated polyethylene by non-borated polyethylene; this change impacts the number of particles reaching the muon stations. The uncertainty is evaluated by comparing the particle flux between the two scenarios and a variation of 10 to 20% is found, depending on the perpendicular distance from the beam line (R), with a mean value of 15%.

At last, the hit rate from simulation is obtained from the convolution of the average sensitivity and the particle flux, and is shown in Figure 2.27. As expected, the hit rate is higher at lower R (higher η) because the flux from the collision is higher in this region. The largest contribution in the hit rate comes from the neutrons while photons contribute about $\sim$ 15%. Charged hadrons and $e^{\pm}$ contribute about 1% only. The estimated hit rate is compared with the data collected by the GEM detector during the slice test performed

during Run 2 operation. As can be seen from this figure, the measured hit rate for the GEM detector agrees with the estimated hit rate from the simulation within the uncertainty [46] except for η-sectors 1 and 2 for which data were taken with higher readout thresholds i.e., 8.8 fC and 4.0 fC respectively. The developed framework can be used for evaluation of hit rates on other detectors at HL-LHC, providing a better understanding of trigger rates and longevity of detectors.

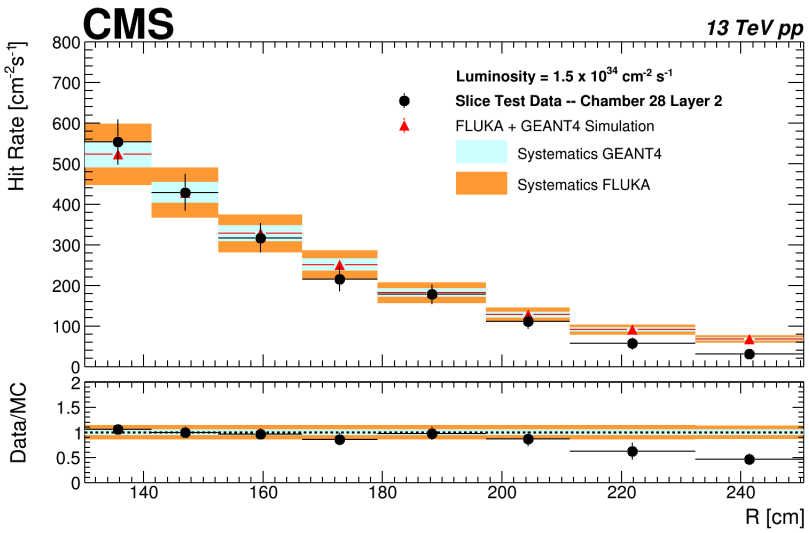

Figure 2.27: Comparison of the background particles hit rate observed in data with the estimated hit rate using the particle flux from FLUKA simulation and sensitivity from GEANT4 simulation. The bottom panel shows the ratio of hit rates from data to those predicted from the simulation.

2.2.6 CMS Trigger system

At the design luminosity and center-of-mass energy of 14 TeV, around 10^9 interactions per second are produced at the LHC. Only a small fraction of these collisions contain events of interest to the CMS physics program, and only a small fraction of those can be stored for later offline analysis. It poses challenge to the CMS trigger system to select only interesting events for offline storage from the bulk of the inelastic collision events. Of the proton-proton collisions happening per bunch crossing in every 25 ns, most can be classified as *almost elastic or diffractive* events, which

correspond to interactions where the colliding protons either recoil from each other without being destroyed in the process, or the proton structure is broken leading to the emission of highly forward jets. These events present low transverse transferred momentum and therefore are of minor interest when looking at processes involving exchange of on-shell gauge boson, or Higgs physics. Only a fraction of these *minimum bias* events are written on disk, and are mainly used for detector calibration or luminosity measurements. In order to select and store interesting events, a reduction is applied via a triggering system [47]. The CMS trigger system has two levels: the hardware based first level (L1) trigger [48] and the software based second level trigger (high level trigger - HLT) [49]. The two systems achieve the combined reduction rate of the order of 10^6. More description of the two systems is given below.

Level–1 Trigger (L1) The L1 trigger system is composed of custom hardware processors that rely on information from the calorimeters and from the muon system. The decision process starts in the local detector subsystems. Muon identification is performed separately for the different muon chambers (DT, CSC, RPC) using e.g. hit patterns to supply independent information. This information is combined in the *Global Muon Trigger* (GMT) system. The four best muon candidates in the endcap and barrel regions are further sent from the GMT to the *Global Trigger* (GT) system. Energy deposits in the ECAL and HCAL towers are processed in the *Regional Calorimeter Trigger* (RCT) system. Regional energy sums, i.e. electron/photon and jet candidates are identified in the RCT and further sent to the *Global Calorimeter Trigger* (GCT) system. From the GCT system, the four best isolated and non-isolated electron and photon candidates as well as the four best jets per barrel, endcap and tau category and the total (and consequently also missing) E_T sums are sent to the GT system. The GT system contains 128 trigger algorithms with different requirements on the candidates from the GCT and GMT systems such as E_T, p_T and combinations of objects. After 3.2 µm, the L1 trigger system reaches a result and the detector data, which was stored in buffers, is either discarded or

transferred to the front end read out devices. The L1 trigger system has zero dead time (128 events are processed in parallel and there is a pipeline delay of ≈3 µm and reduces the event rate from 40 MHz to around 100 kHz. Much of the logic in the trigger system is contained in custom Application Specific Integrated Circuits (ASICs), semi-custom and gate-array ASICs, Field Programmable Gate Arrays (FPGAs), Programmable Logic Devices (PLDs), and discrete logic such as Random Access Memories that are used for memory Look-Up Tables (LUTs). Figure 2.28 shows the architecture of the CMS Level-1 Trigger system.

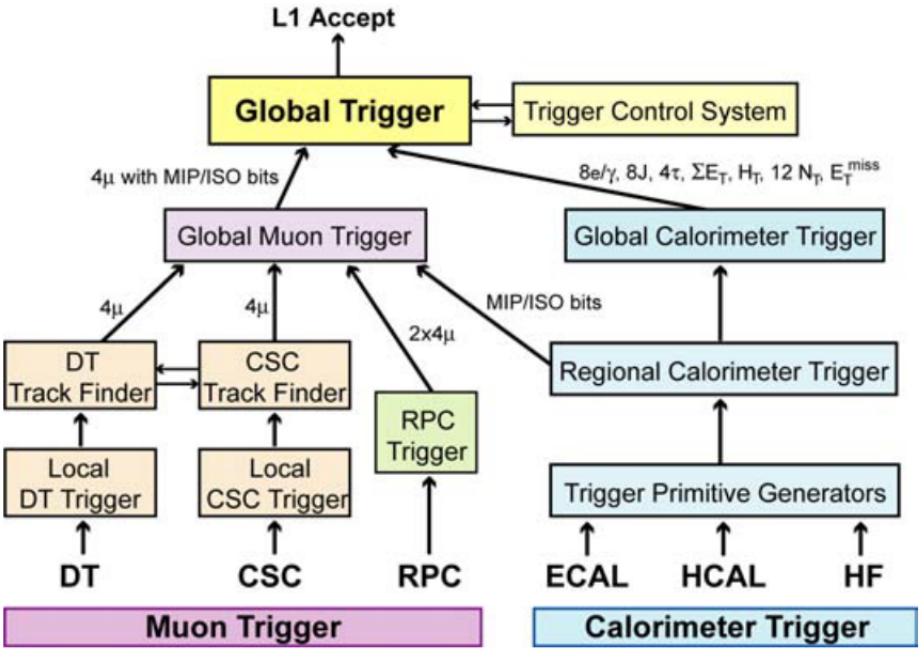

Figure 2.28: Architecture of CMS Level-1 Trigger [11].

High Level Trigger (HLT) The HLT system uses a slim version of the CMS offline reconstruction software distributed on a cluster of commercial rack-mounted computers comprising over 13 k CPU cores. The HLT system exploits the information of the whole detector. The fast reconstruction algorithms start with the L1 trigger candidates and add information from other sub-detectors such as the tracker system to reconstruct the HLT trigger objects (electrons, photons, muons, jets). A sequence of requirements on the trigger objects correspond to a specific trigger path

(or data stream), addressing specific physics object selections. If the event reconstructed by the HLT system meets the requirements of any such trigger path, it is recorded. The HLT system reduces the event rate to a few hundred Hz. Events passing the HLT system are stored on disk for offline data analysis, with an average event size of about 1.5 MB for pp interactions.

In this Chapter, a brief discussion of the LHC collider, the CMS detector and its various subdetectors, is presented. The LHC is designed for the measurement of the standard model physics as well as the physics beyond the standard model. The CMS detector is one of the two general purpose detectors at the LHC, and can reconstruct various particles originating from the pp collisions at the LHC and can measure their energy and momentum. Therefore, the data collected from the CMS detector can be useful for the search for the heavy neutral gauge boson, Z', which is the objective of this Thesis.

The mechanism through which different particles deposit their energy in various CMS subdetectors is discussed in the next Chapter.

Bibliography

[1] A. P. Singh, P. C. Bhat, N. V. Mokhov, and S. Beri, "Beam-induced radiation in the compact muon solenoid tracker at the Large Hadron Collider", *Pramana* **74** (2010) 719–729, doi:10.1007/s12043-010-0093-9.

[2] L. Evans and P. Bryant, "LHC Machine", *JINST* **3** (2008) S08001, doi:10.1088/1748-0221/3/08/S08001.

[3] P. Jenni and T. S. Virdee, "The Discovery of the Higgs Boson at the LHC", pp. 263–309. Springer, Cham, 2020. doi:10.1007/978-3-030-38207-0_6.

[4] M. Benedikt et al., "LHC Design Report". CERN Yellow Reports: Monographs. CERN, Geneva, 2004. doi:10.5170/CERN-2004-003-V-3.

[5] C. Lefèvre, "The CERN accelerator complex. Complexe des accélérateurs du CERN", Dec, 2008. CERN.

[6] J.-L. Caron, "Cross section of LHC dipole.. Dipole LHC: coupe transversale.", May, 1998. AC Collection. Legacy of AC. Pictures from 1992 to 2002.

[7] R. Bruce et al., "Review of LHC Run 2 Machine Configurations", in *9th LHC Operations Evian Workshop*, pp. 187–197. 11 p. 2019.

[8] CMS Collaboration. https://twiki.cern.ch/twiki/bin/view/CMSPublic/LumiPublicResults.

[9] CMS Collaboration, "Technical Proposal for the Phase-II Upgrade of the CMS Detector", *CMS Technical Design Report* (6, 2015).

[10] CMS Collaboration, "A New Boson with a Mass of 125 GeV Observed with the CMS Experiment at the Large Hadron Collider", *Science* **338** (2012) 1569–1575, doi:10.1126/science.1230816.

[11] CMS Collaboration, "The CMS Experiment at the CERN LHC", *JINST* **3** (2008) S08004, doi:10.1088/1748-0221/3/08/S08004.

[12] CMS Collaboration, "CMS Physics: Technical Design Report Volume 1: Detector Performance and Software", *CERN Document Server* (2006).

[13] V. I. Klyukhin et al., "The cms magnetic field map performance", *IEEE Transactions on Applied Superconductivity* **20** (Jun, 2010) 152–155, doi:10.1109/tasc.2010.2041200.

[14] CMS Collaboration, "Description and performance of track and primary-vertex reconstruction with the CMS tracker", *JINST* **9** (2014), no. 10, P10009, doi:10.1088/1748-0221/9/10/P10009, arXiv:1405.6569.

[15] CMS Collaboration, "CMS Technical Design Report for the Pixel Detector Upgrade", *CMS Technical Design Report* (9, 2012) doi:10.2172/1151650.

[16] CMS Collaboration, "Description and performance of track and primary-vertex reconstruction with the CMS tracker", *JINST* **9** (Oct, 2014) P10009–P10009, doi:10.1088/1748-0221/9/10/p10009.

[17] CMS Collaboration, "The CMS ECAL performance with examples", *JINST* **9** (2014) C02008, doi:10.1088/1748-0221/9/02/C02008.

[18] CMS Collaboration, "Energy Calibration and Resolution of the CMS Electromagnetic Calorimeter in *pp* Collisions at $\sqrt{s} = 7$ TeV", *JINST* **8** (2013) P09009, doi:10.1088/1748-0221/8/09/P09009, arXiv:1306.2016.

[19] P. Adzic et al., "Energy resolution of the barrel of the CMS electromagnetic calorimeter", *JINST* **2** (2007) P04004, doi:10.1088/1748-0221/2/04/P04004.

[20] C. M. S. at CERN, "XDAQ-CMS Online Software project page". doi:http://xdaq.web.cern.ch/xdaq/setup/images/HCAL.png.

[21] CMS Collaboration, "CMS Technical Design Report for the Phase 1 Upgrade of the Hadron Calorimeter", *CMS Technical Design Report* (9, 2012) doi:10.2172/1151651.

[22] S. I. Cooper, "Phase I Upgrade of the CMS Hadron Calorimeter", *Nuclear and Particle Physics Proceedings* **273-275** (2016) 1002–1007, doi:https://doi.org/10.1016/j.nuclphysbps.2015.09.157. 37th International Conference on High Energy Physics (ICHEP).

[23] CMS Collaboration, "The CMS outer hadron calorimeter", *CERN Document Server* (6, 2006).

[24] B. Lutz, "Upgrade of the CMS Hadron Outer Calorimeter with SiPM sensors", *Journal of Physics: Conference Series* **404** (12, 2012) 012018, doi:10.1088/1742-6596/404/1/012018.

[25] CMS HF Calorimeter Collaboration, "CMS hadronic forward calorimeter", *Nucl. Phys. B Proc. Suppl.* **61** (1998) 41–46, doi:10.1016/S0920-5632(97)00536-7.

[26] CMS Collaboration, "CMS Hadron Forward Calorimeter Phase I Upgrade Status", *PoS* **TIPP2014** (2014) 267, doi:10.22323/1.213.0267.

[27] Particle Data Group Collaboration, "Review of Particle Physics", *PTEP* **2020** (2020), no. 8, 083C01, doi:10.1093/ptep/ptaa104.

[28] R. Frühwirth, "Application of kalman filtering to track and vertex fitting", *Nuclear Instruments and Methods in Physics Research Section A: Accelerators, Spectrometers, Detectors and Associated Equipment* **262** (1987), no. 2, 444–450, doi:https://doi.org/10.1016/0168-9002(87)90887-4.

[29] CMS Collaboration, "Performance of the CMS Drift Tube Chambers with Cosmic Rays", *JINST* **5** (2010) T03015, doi:10.1088/1748-0221/5/03/T03015, arXiv:0911.4855.

[30] CMS Collaboration, "Performance of the CMS cathode strip chambers with cosmic rays", *JINST* **5** (Mar, 2010) T03018–T03018, doi:10.1088/1748-0221/5/03/t03018.

[31] CMS Collaboration, "Performance Testing of the CMS Cathode Strip Chambers", *CERN Document Server* (11, 2009).

[32] CMS Collaboration, "The CMS muon project: Technical Design Report", *CERN Document Server* (1997).

[33] CMS Collaboration, "The Performance of the CMS Muon Detector in Proton-Proton Collisions at $\sqrt{s} = 7$ TeV at the LHC", *JINST* **8** (2013) P11002, doi:10.1088/1748-0221/8/11/P11002, arXiv:1306.6905.

[34] CMS Collaboration, "Performance of CMS Muon Reconstruction in pp Collision Events at $\sqrt{s} = 7$ TeV", *JINST* **7** (2012) P10002, doi:10.1088/1748-0221/7/10/P10002, arXiv:1206.4071.

[35] CMS GEM Collaboration, "CMS Technical Design Report for the Muon Endcap GEM Upgrade", *Technical Design Report* (6, 2015).

[36] F. Sauli, "The gas electron multiplier (GEM): Operating principles and applications", *Nucl. Instrum. Meth. A* **805** (2016) 2–24, doi:10.1016/j.nima.2015.07.060.

[37] T. Maerschalk, "Study of Triple-GEM detector for the upgrade of the CMS muon spectrometer at LHC", 2016. https://cds.cern.ch/record/2291028.

[38] A. K. Virdi et al., "Fabrication and Characterization of Gaseous Detector for the identification of High Energy Particles.", *IOP Conf. Ser. Mater. Sci. Eng.* **1033** (2021), no. 1, 012055, doi:10.1088/1757-899X/1033/1/012055.

[39] CMS GEM Collaboration, "CMS Technical Design Report for the Muon Endcap GEM Upgrade", technical report, Jun, 2015.

[40] A. Ferrari, P. R. Sala, A. Fassò, and J. Ranft, "FLUKA: A multi-particle transport code (program version 2005)". CERN Yellow Reports: Monographs. CERN, Geneva, 2005. doi:10.5170/CERN-2005-010.

[41] GEANT4 Collaboration, "GEANT4–a simulation toolkit", *Nucl. Instrum. Meth. A* **506** (2003) 250–303, doi:10.1016/S0168-9002(03)01368-8.

[42] A. Ferrari et al., "FLUKA: A Multi-Particle Transport Code", doi:10.2172/877507.

[43] CMS GEM Collaboration, "Performance of a triple-GEM demonstrator in pp collisions at the CMS detector", *JINST* **16** (nov, 2021) P11014, doi:10.1088/1748-0221/16/11/p11014.

[44] A. Howard, G. Folger, J. M. Quesada, and V. Ivanchenko, "Validation of neutrons in geant4 using tarc data - production, interaction and transportation", in *2008 IEEE Nuclear Science Symposium Conference Record*, pp. 2885–2889. 2008. doi:10.1109/NSSMIC.2008.4774970.

[45] J. Apostolakis et al., "Validation and verification of geant4 standard electromagnetic physics", *Journal of Physics: Conference Series* **219** (apr, 2010) 032044, doi:10.1088/1742-6596/219/3/032044.

[46] CMS Collaboration, "Benchmarking LHC background particle simulation with the CMS triple-GEM detector", *JINST* **16** (2021), no. 12, P12026, doi:10.1088/1748-0221/16/12/P12026, arXiv:2107.03621.

[47] CMS Collaboration, "The CMS trigger system", *JINST* **12** (2017), no. 01, P01020, doi:10.1088/1748-0221/12/01/P01020, arXiv:1609.02366.

[48] CMS Collaboration, "CMS Technical Design Report for the Level-1 Trigger Upgrade", *CMS Technical Design Report* (6, 2013).

[49] CMS Collaboration, "CMS: The TriDAS project. Technical design report, Vol. 2: Data acquisition and high-level trigger", *CMS Technical Design Report* (12, 2002).

Chapter 3

Event Reconstruction and Data Samples

Event simulation is a fundamental step for a high energy physics experiment from the very early detector design stage up to the final commissioning stage. The simulation study of the detector and the physics processes is quite important before the start of the experiment as well as after the start of real data taking in the experiment. Performance and calibration of various components of the detector is monitored using simulation techniques. With the help of simulation studies, it is also possible to decide the nature of backgrounds for a particular physics process and then decide the analysis strategy accordingly. Event simulation involves generation of events using a numerical method, known as "Monte Carlo (MC)". This method estimates the integral based on random evaluations of the integrand. Unlike the other integration methods, where error estimation depends on the number of variables in phase space i.e. dimensions, the MC methods are independent of it, making it suitable for particle event generators for the particle physics. Figure 3.1 shows the sketch of the simulation for the proton-proton (pp) collision using the MC method. Once the pp collision events are simulated, these events are required to pass through the simulated detector so that various effects of the interaction of particles with detector material can be simulated. This process is known as detector simulation.

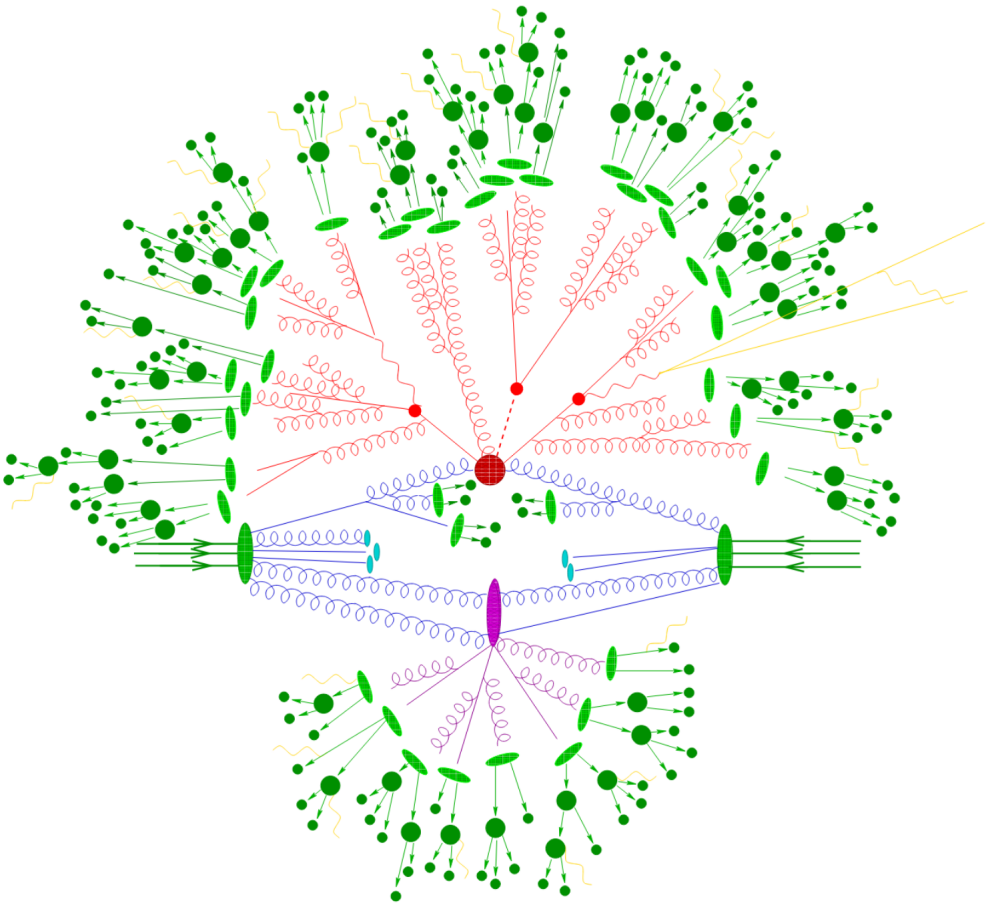

Figure 3.1: Sketch of the simulated *pp* collision event. Hard collision is represented by the red blob followed by the parton showering (red lines). Secondary hard interaction is indicated by the purple blob. Light green blobs shows the parton to hadron transitions and dark green blobs indicate the hadron decays. The soft photon emissions are represented by yellow lines [1].

At the CMS detector, event simulation takes place in two main steps. The first step is the generation of events with the help of an event generator, based on the standard model of the particle physics or a beyond standard model theory. The event generator produces all the particles that are expected to be produced in the *pp* collisions. The second step is to simulate the interactions of these particles with the CMS detector and to translate them into electrical signals for the reconstruction of an event. The reconstruction steps are same for both the simulated and the real data events.

3.1 Event Generation

The main motive of the event generator is to generate events as realistic as could be from a real experiment. Event generators are intended to generate complete events by subdividing the task into simpler steps. For the generation of a given hard process, the basic steps are as follows: generation of the Feynman diagrams involved in the physics process of interest, construction of the matrix elements which after being integrated over whole phase space to provide the total and differential cross-section of the process. Finally, the events are randomly generated according to the full differential cross-section and provide a set of four momentum vectors associated with each of the final state particles. Different processes that occur during the pp interaction are discussed below.

- Generation of the Hard Process: Hard scattering is the interaction between two incoming partons of colliding protons that involve highest momentum exchange. Many Feynman diagrams are produced and a matrix element (ME) is constructed using the amplitude of various involved processes during the pp collision. After this, the calculation of the full differential cross-section of the hard process is done and the events are randomly generated in some phase space depending upon its cross-section. Theoretically, it is easy to calculate the MEs with reasonable accuracy i.e. up to the leading order (LO) calculations. However, this accuracy is process dependent. In some cases, it may be difficult to achieve accuracy beyond the LO calculations due to increased number of Feynman diagrams and complex calculations.

- Modeling of Initial State Radiation and Final State Radiation: Any parton carrying some charge (electromagnetic, weak or color) can radiate gluons, leading to the production of supplementary particles. The radiation emitted by the incoming partons before the hard interaction is known as Initial State Radiation (ISR). It can lead to the formation of jets near the direction of the incoming partons. Similarly, the radiation emitted by the final state partons yields Final State Radiation (FSR). This radiation is responsible for building

the structure of the jets.

- The short-lived particles produced in the pp interaction are rather unstable and can decay to stable final state particles.

- Since the colliding beam protons are made up of partons, there is a possibility of additional interaction to occur during the hard interaction. Such interactions are known as Multiple Parton Interactions (MPI). Also, the remnants of the colliding protons should be taken into account for the correct balance of the momentum and the charge. Therefore, It is necessary to simulate correctly those interactions as they contribute to the whole structure of an event.

- As the partons in the final state move apart from each other, the strong running coupling constant increases leading to the quark confinement. This process leads to the production of quark-antiquark ($q\bar{q}$) pairs and colorless hadrons, resulting in showering and hadronization, and is described in the next Section.

- The final state can include the decay of the comparably long-lived particles such as τ-leptons and B-hadrons, which further decay to stable particles.

3.1.1 Parton Showering and Hadronization

The Hard scattering of the incoming partons involves the large momentum transfer which leads to the acceleration of final state partons. These final state partons involve both electrically charged and colored particles. QED emissions are carried by electrically charged particles and QCD emissions by colored particles. These colored charged particles can further emit radiations leading to the development of parton showers. The parton showers generally introduce corrections to the hard processes which can not be exactly calculated. Therefore, an approximation scheme is used considering only the dominant contributions. As more of emission occurs, the interaction scale (Q) gets smaller which increases the value of α_s. At a point, where Q gets close to the QCD scale i.e. Λ_{scale}, α_s becomes large enough to stop the parton showering. In this confinement regime, the colored partons are transformed

into colorless hadrons, a process called either hadronization or fragmentation. Some specific models describing hadronization mechanism are given below:

- **Cluster Model**: In this model, splitting of gluons occur via $g \to q\bar{q}$ processes forming colorless singlet $q\bar{q}$ combinations of lower masses. Then the formation of clusters occur through the combination of neighboring color-connected $q\bar{q}$ pairs which subsequently decay to pair of hadrons [2, 3].

- **Lund String Model**: This model uses string dynamics to represent color flux stretched between $q\bar{q}$. It considers a string or colored flux tube holding the two quarks having linearly confined potential. The string breaks when the energy of string exceeds the mass of $q\bar{q}$ pair forming another pair and so on [2, 3].

During the last few decades, different experimental measurements have been used to tune these models to precisely describe the hadron multiplicity in the final state.

3.2 Monte Carlo Event Generators

The following MC generators have been used in the generation of various physics processes considered in the analysis presented in this Thesis.

- **PYTHIA**: PYTHIA [4] is a general purpose tree-level generator frequently used in the generation of events in pp, ee and pe collisions. It computes ME for large number of processes and also has tools to simulate ISR and FSR. PYTHIA can also be interfaced with other event generators for providing them parton showering and hadronization. It can generate almost all $2 \to 1$, $2 \to 2$ processes with few $2 \to 3$ processes. Hadronization is carried out using "Lund String Model" in PYTHIA.

- **MADGRAPH**: MADGRAPH [5] is a MC generator providing only ME calculations and has to be interfaced with other MC generators for the remaining steps like parton showering and hadronization. It is a tree-level generator and

can produce the events up to 4 partons in the final state. Since in MADGRAPH, tree level calculations are involved, careful tailoring of phase space is done to remove the soft and collinear divergences. These excluded regions have therefore to be treated by parton showering (PS) calculations. The ME at tree-level can be generated for any Lagrangian based model (renormalizable and effective). MADGRAPH generates all Feynman diagrams for the process depending on user's input specifying initial and final state particles, branching fractions required in models (BSM models), masses and couplings of the particles etc. The MEs at a given phase space point are calculated and the code is generated known as Les Houches format Event (LHE) file [6], which can subsequently be used by other packages for event generation. To avoid double counting of equivalent phase space configurations during the parton showering, various jet matching algorithms such as CKKW, MLM, etc. are used [7]. The analysis in this Thesis mostly uses the MADGRAPH generated samples with parton showering from PYTHIA generator such as W+ jets, Z + jets samples with exclusive jet multiplicity.

- **POWHEG**: POWHEG (Positive Weight Hardest Emission Generator) [8] is general framework providing the modeling of the hard interaction with next-to-leading order (NLO) accuracy. It has to be interfaced with PYTHIA or HERWIG for parton showering. The processes involving the production of the Higgs Boson through vector boson fusion topology are generated using the POWHEG generator.

After the hard process generation, showering and hadronization, next step is to simulate the generated events to have a prior knowledge of their behaviour and signatures in the detector.

3.3 Detector Simulation

CMS detector simulation is done using GEANT4 (GEometry ANd Tracking) [9], a package used to model the response of the CMS detector to the passage of particles through it. This software includes a wide range of known particle interactions with matter, external electromagnetic fields, detailed description of detector including its geometry, alignment, densities and types of material, and subsystem conditions. All these conditions are required for the proper simulation of particle propagation through different parts of the detector, including particle trajectories, energy loss, energy response or hits in sensitive detector components, secondary interactions, signal digitization and readout etc. The simulated signals are stored and processed in the same way as real detector signals in subsequent event reconstruction.

3.4 Reconstruction of Physics Objects

The particles produced at the interaction point of pp collision and their decay products interact with the detector active material while traversing the CMS detector, creating electric signals along their way. The data collected by various subdetectors of the CMS detector has to be further processed for physics analysis. Figure 3.2 shows different particles transversing through one section of the CMS detector. Using hit information from different subdetectors, the actual track information of the particle can be reconstructed. For instance, as shown in Figure 3.2, trajectory of all charged particles can be measured in the silicon tracker from bending in magnetic field based on their charge and momentum. Electrons and photons deposit their energy in the electromagnetic calorimeter (ECAL). Hadrons, besides the ECAL, deposit their energy in the hadron calorimeter (HCAL). Muons, being the minimum ionizing particles, travel all the way to muon system, where their trajectory is again measured due to bending in the return yoke. Neutrinos are the only particles which transverse the CMS detector completely as they hardly interact and thus escape undetected. The detector response of the different subdetectors con-

sisting of tracks, calorimeter clusters and muon tracks is used by the Particle Flow (PF) algorithm [10] [11] to identify topologically connected reconstructed elements from different subdetectors, link them via extrapolation to each other and identify particle candidates accordingly. This algorithm is performed iteratively and the elements associated with particle candidates like muons, electrons, charged/neutral hadrons and photons (in roughly this order) are removed from further processing. Afterwards the missing transverse energy (E_T^{miss}) is calculated. The different steps are discussed in further detail in the next Section.

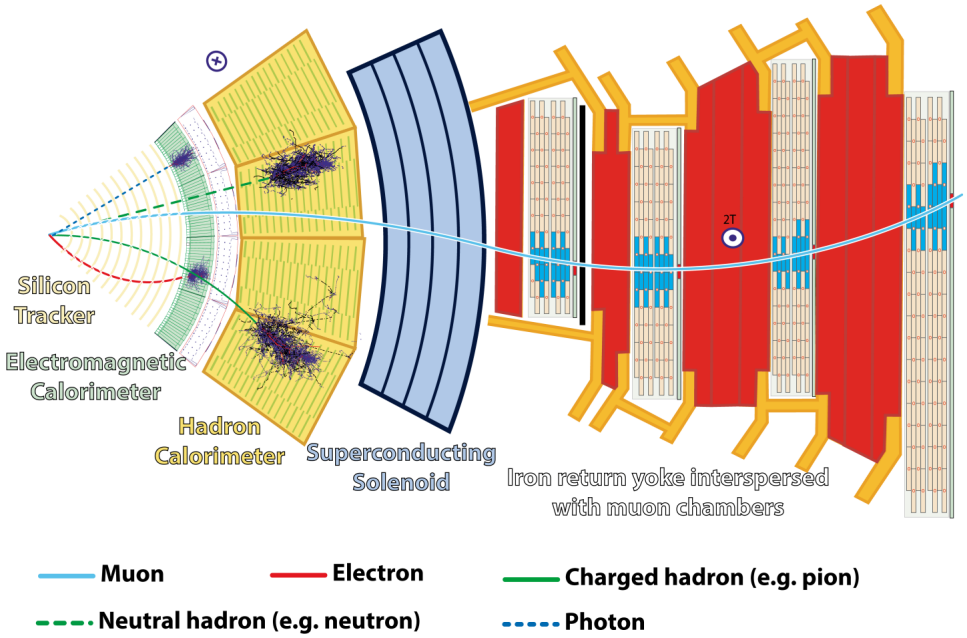

Figure 3.2: Schematic overview of different physics objects and their interaction with different subdetectors in one section of the CMS detector [12].

3.5 Track Reconstruction

Tracks of the charged particles in the CMS detector are reconstructed using the hits in the successive layers of the silicon tracker, with an exception for muon tracks, which use the hits in the muon chambers also. For efficient track recognition and propagation, the silicon modules in the tracker are arranged in layers that are hermetic for a particle originating from the center of the detector. Signal in each layer

with the highest signal to noise ratio is considered as a hit for strip and pixel detector. Then the hits in the adjacent layers are clustered and used as tracker seeds, which define the initial position and uncertainty of the clusters [13]. The track trajectory is extrapolated using a combinatorial Kalman filter (KF) algorithm [14] [15]. Firstly, the hit in the first layer is considered as a seed for the algorithm. The first track is then extrapolated as a straight line pointing outward, with a very large uncertainty as shown in the Figure 3.3. On the next layer, the KF hit (yellow diamond) associated to the track is taken as compromise between the hit determined experimentally (blue circles) and the hit predicted by extrapolating the track from the hit in the previous layer (red square). The parameters of the track candidate are updated with the addition of every new hit. The algorithm takes into account several phenomena such as missing hits, possibility of tracks crossing each other and multiple scattering. This is done by following an iterative approach were the hits of the best reconstructed tracks are removed at each step, and the remaining hits are combined into new tracks. The track finding algorithm progressively relaxes the seed requirements to find less energetic tracks and tracks not crossing part or all of the pixel tracker (e.g. coming from secondary vertices).

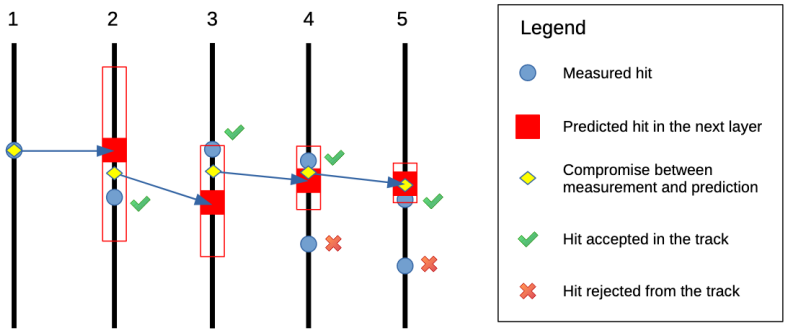

Figure 3.3: Schematic depiction of a Kalman Filter algorithm.

3.6 Primary Vertex Reconstruction

Due to high instantaneous luminosity, there are several additional pp interactions occurring besides one hard collision (with the highest momentum transferred) in the same bunch crossing. This implies that there are several vertices present, distributed over a luminous region known as the beam spot. This region, typically the center of the region where the LHC beams collide at P5, has an average size along the x and y coordinates of $8\,\mu m \times 7\,\mu m$, while it is larger along the z axis, with an average size between 3 and 3.5 cm. The beam spot primarily depends on the beam focusing and hence is approximately stable throughout an LHC fill.

Vertex reconstruction consists of two main steps, vertex finding and vertex fitting. Firstly, the high quality tracks originating from same region are selected and are grouped together. The track clustering is performed with a Deterministic Annealing (DA) technique [16]. Vertex candidates selected by the DA algorithm, which are associated to at least two tracks, are then processed by an Adaptive Vertex Fitter (AVF) [17]. This robust KF-based algorithm provides the estimate of the vertex coordinates, their correlation matrices, and assigns a weight to each track associated to the vertex. The closer the weight is to 1, the more the corresponding track is compatible with originating vertex. A reconstructed vertex with the maximum sum of p_T^2 of its associated tracks is called *Primary Vertex* (PV), and all the remaining reconstructed vertices are called pileup vertices. A good primary vertex is the one for which the absolute distance to the center of the CMS detector has to be smaller than 24 cm along the z-axis, say d_z and 2 cm in the $x-y$ plane, say d_{xy}. In addition to this, the number of degrees of freedom of the vertex fit must be at least 5 for a good primary vertex.

3.7 Muon Reconstruction

Muon reconstruction [18] utilizes the information from muon system and silicon tracker. It starts with the *local reconstruction* of hits in the muon chambers. In the

drift tube (DT) chambers, muon hits with coordinates obtained from the the drift velocity are used to built three dimensional track segments from the different DT layers. The cathode strip chambers (CSC) provide the position and time of arrival of muons, obtained from the distribution of charge induced on the cathode strips, leading to the reconstruction of three dimensional muon segments by combining the information from multiple CSC layers. The local reconstruction of the RPC hits provides only the position of the muon hits. *Standalone muon* tracks are obtained by combining the information of all muon chambers using a Kalman filter tracking algorithm, which takes into account the information of the magnetic field and the energy loss in the material budget of the muon chambers and the iron return yoke. If a standalone muon track can be matched to a tracker reconstructed track in the silicon tracker system, it is identified as a *global muon*. The matching of the silicon tracker tracks to the standalone muon tracks is performed by first of all comparing their parameters propagated onto a reference surface on the outside layer of the solenoid magnet. The best combination of a silicon tracker track and a standalone muon is chosen by iterating over all track combinations in this common surface with more stringent momentum and spatial matching criteria. The global muon candidate with the best normalized χ^2 is chosen. The trajectory is re-fitted starting from the outer muon chambers going towards the interaction point using a combinatorial Kalman Filter technique. Energy deposits in the calorimeter and the track segments close to the extrapolated trajectory are associated with the muon candidate and removed from subsequent iterations. There is possibility for some muons to not reach the muon system from the interaction point. This includes low p_T muons which can not penetrate through the material until the last muon stations. An alternative approach is used to reconstruct such muon candidates, called as *tracker muons*. In this approach, well reconstructed silicon tracks are propagated to the muon chambers using information of muon hits in the calorimeters. The propagated track are then uniquely associated with a candidate track by looking at the nearest geometrical match in the muon system.

There is a high possibility of muons which are not coming from interaction point and

are referred to as non-prompt or backgrounds. This include muons from charged hadrons such as kaons and pions, beam-halo muons and cosmic-ray muons. To suppress these kinds of backgrounds, additional identification and isolation requirements are applied. The reconstruction and identification efficiency of muons is greater than 99% in the CMS detector. The momentum resolution for muons is 1% in barrel and 3% in endcap for muons with momenta up to approximately 100 GeV. The resolution in the barrel is better than 7% for the muons with momenta up to 1 TeV.

3.8 Electron Reconstruction

Electron, near the interaction point, first interacts with the tracker material and emits bremsstrahlung photon and the photon further converts into an electron-positron pair, producing shower called Electromagnetic Shower. Thus, by the time the electron reaches the ECAL, it may no longer be a single particle, but could consist of a shower of multiple electrons and photons. After reaching the ECAL, it deposits all of its energy in the multiple ECAL crystals. This is the first information that the energy reconstruction algorithm requires. The crystals with energies above a certain threshold ($\sim$ 80 MeV in ECAL barrel and $\sim$ 300 MeV in ECAL endcap) are grouped together to form clusters [19]. The threshold energy is chosen in such a way that it is 2-3 times greater than the electronic noise in the crystals. The cluster with maximum energy deposited and with transverse energy (E_T) greater than 1 GeV is chosen as a seed cluster. As the energy deposited by an electron shower is shared within several ECAL clusters around the seed cluster, these clusters are merged to form a supercluster. This supercluster captures the energy of the original electron. There are two main algorithm for superclustering. The first is the "mustache" algorithm [20], which is used for low energy deposits. It uses information only from the ECAL and the preshower detector. After identifying the seed cluster, additional neighboring clusters are added. The distribution of the spread of clusters w.r.t the seed cluster in η and ϕ direction has a slight bend because of the solenoidal structure of the CMS magnetic field. The shape of the supercluster is similar to a mustache

in the transverse plane. An example of the mustache supercluster distribution can be seen in Figure 3.4, for simulated electrons with $1 < E_T < 10$ GeV.

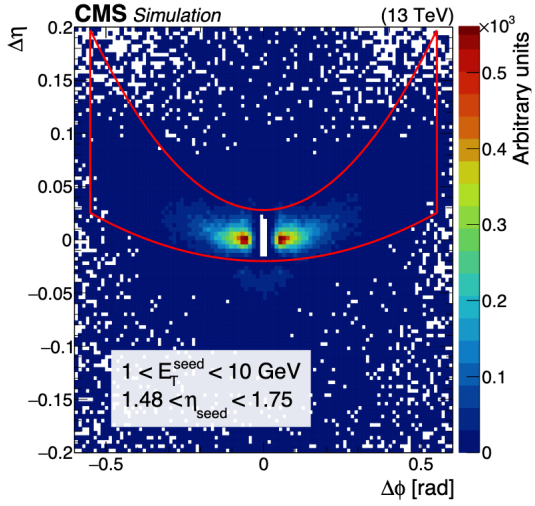

Figure 3.4: Distribution of $\Delta\eta = \eta_{seed\,cluster} - \eta_{cluster}$ and $\Delta\phi = \phi_{seed\,cluster} - \phi_{cluster}$ for simulated electrons. The z axis represents the occupancy of the number of PF clusters matched with the simulation around the seed. The red line shows the supercluster chosen by the mustache algorithm around the seed cluster shown by the white region at the center of the plot [21].

The size of the mustache region depends on E_T, as tracks with larger transverse momenta get less bent by the magnetic field. The second superclustering algorithm is known as the "refined" algorithm [20]. It utilizes tracking information to extrapolate bremsstrahlung tangents and conversion tracks to decide whether a cluster should belong to a supercluster. It uses mustache superclusters as a starting point, but is also capable of creating its own superclusters. The refined superclusters are used for the determination of all ECAL-based quantities of electron and photon objects. Starting with these ECAL superclusters, electron candidates are reconstructed by matching the superclusters to tracks in the tracker originating from the primary vertex. As electron loses its momentum by emitting bremsstrahlung photons while transversing in the dense material and changes its curvature in the presence of the magnetic field and its shower spreads along the ϕ direction. A Gaussian Sum Filter (GSF) [22] is used, which is a non-linear generalization of the Kalman Filter assuring improved pattern recognition of the electron tracks and taking Bremsstrahlung

energy losses into account. If a supercluster from the ECAL detector cannot be matched to a track in the silicon tracker detector, a photon candidate is identified.

By combining the information of the ECAL and the Tracker, the electron energy resolution reaches 0.8 % (2 %) for electrons in the barrel (endcaps), with a $p_T = 200\,\text{GeV}$.

3.9 Tau Reconstruction

Tau (τ) lepton, being the heaviest among the lepton family, has a mean lifetime $\sim \mathcal{O}(10^{-13}\,\text{s})$. It has a decay length of the order of millimeters, thus decays very close to the interaction point. τ lepton can either decay into a muon or electron and two neutrinos, or can involve hadrons, with or without intermediate mesonic resonances. Thus, the τ lepton reconstruction requires precise algorithms to separate τ decays from prompt leptons and hadrons coming from hadronization of quarks or gluons. To distinguish the two types of decays in this Section, τ lepton decaying to leptons will be referred to as *leptonic* (τ_ℓ) and τ lepton decaying to at least one hadron will be referred to as *hadronic* (τ_h).

The τ lepton decays in about two third of the cases, typically into either one or three charged pions or kaons and up to two neutral pions (π^0), and one neutrino (ν_τ). The π^0 meson decays almost exclusively into $\gamma\gamma$. In about 35% of the cases, tau leptons decay into an electron or muon and two neutrinos. The branching fractions for the main τ decay modes are given in Table 3.1. The decays $\tau^- \to h^-\pi^0\nu_\tau$, $\tau^- \to h^-\pi^0\pi^0\nu_\tau$ and $\tau^- \to h^-h^+h^-\nu_\tau$ (with corresponding channels for τ^+) proceed via intermediate $\rho(770)$ and $a_1(1260)$ meson resonances. The main challenge in identifying hadronic τ decays is distinguishing them from quark and gluon jet background. The cross-section for multijet production from perturbative quantum chromodynamical (QCD) calculations exceeds by many orders of magnitude of the rate at which τ leptons are produced at the LHC. To reduce the background arising from quark and gluon jets, we exploit the fact that hadronic τ decays result in a

lower particle multiplicity, and are more collimated and isolated relative to other particles in the event. In some analyses, the misidentification of electrons or muons as τ_h candidates may constitute a sizeable problem, and dedicated algorithms have been developed to reduce this type of background.

Decay mode	Meson resonance	$\mathcal{B}$ [%]
$\tau^- \to e^- \bar{n}u_e \nu_\tau$		17.8
$\tau^- \to \mu^- \bar{n}u_\mu \nu_\tau$		17.4
$\tau^- \to h^- \nu_\tau$		11.5
$\tau^- \to h^- \pi^0 \nu_\tau$	ρ (770)	26.0
$\tau^- \to h^- \pi^0 \pi^0 \nu_\tau$	a_1 (1260)	9.5
$\tau^- \to h^- h^+ h^- \nu_\tau$	a_1 (1260)	9.8
$\tau^- \to h^- h^+ h^- \pi^0 \nu_\tau$		4.8
others modes with hadrons		3.2
All modes containing hadrons		64.8

Table 3.1: Approximate branching fractions $\mathcal{B}$ of different τ decay modes [23].

The hadron-plus-strip algorithm The τ_h decays are reconstructed and identified using the hadrons-plus-strips (HPS) algorithm [24] [25]. The algorithm is designed to reconstruct individual decay modes of the τ lepton, taking advantage of the excellent performance of the PF algorithm in reconstructing individual charged and neutral particles. The reconstruction and identification of τ_h decays in the HPS algorithm is performed in two steps:

- **Reconstruction:** The combinations of charged and neutral particles reconstructed by the PF algorithm that are compatible with specific τ_h decays are constructed, and the four-momentum, expressed in terms of (p_T, η, ϕ, and mass) of τ_h candidates, is computed.

- **Identification:** The discriminators that separate τ_h decays from quark and gluon jets, and from electrons and muons, are computed. This provides a reduction in the misidentification rates for jet $\to \tau_h$, $e \to \tau_h$, and $\mu \to \tau_h$ misidentification.

The HPS algorithm is seeded by jets of $p_T > 14$ GeV and $|\eta| < 2.5$, reconstructed using the anti-k_T algorithm [26] with a distance parameter of 0.5. Particles in the jets are then tested as candidates for:

- *hadrons* : charged particles depositing their energy in both ECAL and HCAL
- *strips* : a cluster of electrons and photons, producing ECAL signatures compatible with a π^0 decays

Several tau hadronic decay channels include π^0 mesons, which decay into two photons almost 100% times. Photons have a chance of converting into an electron-positron pair, which then are separated along the ϕ direction due to the magnetic field. This results in an ECAL cluster narrow in η and extended in ϕ, referred to as strip. Photons and electrons in the jet cone are clustered to form a strip if they are found in a certain $\Delta\eta \times \Delta\phi$ window. During Run 2, a dynamic strip reconstruction was introduced [27] which works as follows:

- a strip is seeded by the leading photon or electron (γ/e) found in the jet, but not yet assigned to a strip;
- the position and transverse momentum of the leading e/γ are assigned to the strip as the position of its center (η^{strip} and ϕ^{strip}) and momentum (p_T^{strip});
- the next highest p_T e/γ candidate is then assigned to the strip if the distance between its position and the strip center satisfies the following relations:

$$\Delta\eta(e\gamma - strip) < max(f(p_T^{e\gamma}) + f(p_T^{strip}), 0.15) \tag{3.1}$$

$$\Delta\phi(e\gamma - strip) < max(g(p_T^{e\gamma}) + g(p_T^{strip}), 0.30) \tag{3.2}$$

with

$$f(p_T) = 0.20.p_T^{-0.66} \tag{3.3}$$

$$g(p_T) = 0.35.p_T^{-0.71} \tag{3.4}$$

- if the e/γ candidate is included in the strip then the properties of the strip are re-evaluated based on its constituents:

$$p_T^{strip} = \sum^{e/\gamma} p_T^{e\gamma} \tag{3.5}$$

$$\eta^{strip} = \frac{1}{p_T^{strip}} \sum^{e/\gamma} p_T^{e\gamma}.\eta^{e/\gamma} \tag{3.6}$$

$$\phi^{strip} = \frac{1}{p_T^{strip}} \sum^{e/\gamma} p_T^{e\gamma}.\phi^{e/\gamma} \tag{3.7}$$

- the process continues till no other e/γ candidate is found within the strip window, and the clustering of a new strip is initiated using the unassigned e/γ candidates.

The highest energy hadron and strip candidates selected (up to six each) are then combined as potential τ_h candidates and compared to the different hadronic decay modes of tau leptons. The assignment of a decay mode is based on the number of prongs and strips available and the invariant mass of the tau decay products. For each τ_h candidate, corresponding to different combinations of hadrons and strips, the invariant tau lepton mass m_{τ_h} is reconstructed. Based on the number of reconstructed hadrons and the values of m_{τ_h} of each τ_h candidate, the HPS assigns the tau decay mode [25] as follows:

- **One prong** ($h^{\pm}$): This decay mode corresponds to cases where only one charged hadron candidate was identified, not accompanied by good strip candidates, and $0 < m_{\tau_h} < 1$. The choice of this mass window allows to target not only charged pions, but also the rarer decays to kaons. For this decay mode, m_{τ_h} is then assigned to be equal to the pion mass.

- **One prong plus one strip** ($h^{\pm}\pi^0$): A charged hadron is required to be identified together with a strip, and their visible invariant mass is required to

be 0.3 -$\Delta m_{\tau_h} < m_{\tau_h}$ 1.3 $\times \sqrt{p_T/100} + \Delta m_{\tau_h}$, with the upper limit constrained between 1.3 and 4.0 GeV.

- **One prong plus two strips** ($h^{\pm}\pi^0\pi^0$): This decay mode requires one hadron to be reconstructed alongside two strips. Their visible mass should be 0.4 - $\Delta m_{\tau_h} < m_{\tau_h}$ 1.2 $\times \sqrt{p_T/100} + \Delta m_{\tau_h}$, with the upper limit constrained between 1.2 and 4.0 GeV.

- **Two prongs** ($h^{\pm}h^{\pm}$): This decay mode is assigned to τ_h candidates where two charged hadrons are identified having invariant visible mass between 0 $< m_{\tau_h} < 1.2$. For this decay mode and the next one, the requirement on the τ_h candidate electric charge is relaxed to allow values different from 1, the two charged hadron candidates can therefore have either equal or opposite charge.

- **Two prongs plus one strip** ($h^{\pm}h^{\pm}\pi^0$): Cases with two charged hadrons and a strip are assigned to this decay mode. The visible mass should fall within the range 0. $< m_{\tau_h} < 1.2 \times \sqrt{p_T/100} + \Delta m_{\tau_h}$, with the upper limit constrained between 1.2 and 4.0 GeV.

- **Three prongs** ($h^{\pm}h^{\pm}h^{\mp}$): This decay mode is associated to three charged hadrons with no additional strip, their invariant visible mass is required to be $0.8 < m_{\tau_h} < 1.4$ GeV.

- **Three prongs plus one strip**($h^{\pm}h^{\pm}h^{\mp}\pi^0$): Three charged hadrons and a strip are required to be present, furthermore the mass of the tau candidate should be in the range 0.9 -$\Delta m_{\tau_h} < m_{\tau_h} < 1.6$ +Δm_{τ_h} .

Misidentification of hadronic taus There is a high probability that several objects can be misidentified as hadronically decaying tau leptons by the HPS algorithm. A highly collimated quark or gluon jet can be mistaken for any tau decay. Muons can produce a signature similar to a one prong tau decay. Electrons can emit photons via bremsstrahlung radiation and mimic the ρ meson decay and be reconstructed as one prong plus $\pi^0 s$ decays. To reduce the misidentification rate,

and thus select a more pure sample of hadronically decaying tau leptons, a new tau identification algorithm is deployed: the DeepTau neural network-based identification (DeepTau ID) [28, 29]. The DeepTau identification is based on a multiclass convolutional neural network (CNN) used to reduce the misidentification of jets, muons and electrons as hadronically decaying tau leptons. It takes as inputs low and high level features associated to the τ_h candidate and produces 4 output scores, one for each class: genuine taus, jets, muons, electrons. Its architecture is based on the following three premises:

- Multiclass: Previously, separate dedicated algorithms were used to reject electrons, muons, or quark and gluon jets reconstructed as a τ_h candidate, either based on tree ensembles (jets and electrons) or on a number of selection criteria (muons). Including electrons, muons, and jets in the same algorithm is expected to both improve identification performance and to reduce maintenance efforts.

- Usage of lower-level information: The MVA discriminators used previously were built on higher-level input variables and showed improved performance with respect to cutoff-based criteria. However, jets hadronize and fragment in complex patterns, and particles from concurrent interactions lead to similarly complex detector patterns. We expect that a machine-learned algorithm, which uses a sufficiently large data set for the training and is able to exploit lower-level information, can lead to improved performance. Therefore, information about all reconstructed particles near the τ_h candidate is directly used as input to the algorithm.

- Domain knowledge: Sets of handcrafted higher-level input variables used previously are utilized as additional inputs to the information about the single reconstructed particles. Although it should, in principle, be possible to achieve the same performance with and without using these variables given a sufficiently large set of events for the training and a suitable network architecture, the usage of the higher-level inputs may reduce the number of training events

needed and improve the convergence of the training, as seen in other studies.

The τ_h reconstruction efficiency exceeds 80% for $p_T > 30$ GeV and is close to 90% for $p_T > 100$ GeV. The electron discriminator leads to a significantly improved rejection of electrons compared with the MVA discriminator, by consistently more than 10% for a constant misidentification probability. Gains are also observed in terms of the discrimination of τ_h candidates against muons. Compared with the cutoff-based discriminator, the muon discriminator leads to an increase of the τ_h efficiency of around 0.5% for a given prompt muon efficiency.

3.10 Jet Reconstruction

Jets are the experimental signatures of the hadronic showers from quarks and gluons. Because of the color confinement, partons produced in the hard process of a particle collision induce the production of large numbers of colorless secondary hadrons. This results in collimated particle showers, so-called jets, in the direction of the original parton preserving most of its initial properties. In Figure 3.5, a schematic overview of a pp collision, resulting in a particle jet is shown. Hadron candidates are reconstructed using the information from large energy deposits in the ECAL and HCAL detectors combined with tracker information. Jets are reconstructed

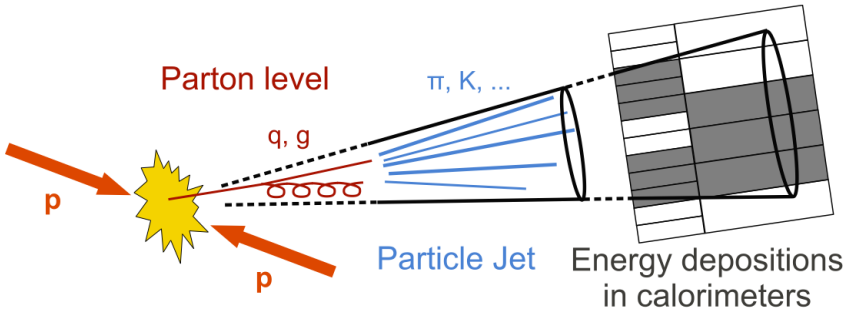

Figure 3.5: Representation of a jet formation from a proton–proton collision that leads to energy deposits in the calorimeter detectors [30].

by combining the energy deposits in the tracker and calorimeters using the anti-k_T algorithm [26] with radius, $\Delta R = 0.4$. The algorithm is infrared safe, because

it is not affected by soft radiation occurring in a parton shower, as well as safe against collinear emissions. The measured jet energy is not equal to the true parton energy due to the non-linear response of the calorimeter. Therefore, jet energy corrections are applied to the measured jet energy depositions in a factorized multi-level method developed by the CMS Collaboration. Each correction in sequence is related to different detector and physics effects and performed in a fixed order, where the output of each step is the input for the next [31].

L1 Pile-up correction : The detector responses to pileup and contributes an offset to the measured jet energy. This is subtracted from the corrections determined from QCD dijet simulations with and without pileup, parameterized as a function of the energy density ρ, the jet area A, the η and p_T of the jet [32–34].

L2 and L3 Simulation correction : The true particle energy as a function of η and p_T is derived from QCD dijet simulations by comparing the p_T -distributions. The reconstructed jet energy is corrected accordingly to achieve a uniform response distribution in η and p_T.

L2 and L3 Residual data-driven correction : Relative residual corrections as a function of η are derived from dijet data samples by comparing the p_T of a jet relative to a jet with similar p_T in the barrel region to account for a varying response along the detector. The jet energy scale receives a p_T-dependence corrections relative to the jet energy scale of the reference jet in the barrel region. Therefore, the jet energy absolute scale is additionally corrected by determining the absolute residual corrections for barrel jets as a function of p_T using well measured jets from Z/γ + jets events and comparing them to multijet events in data.

b jet tagging Jets originating from decays of heavy-flavour hadrons, b-hadrons, are an important component of the physics program of LHC, they are called b-quark jets or b-jets. The characteristics of b-hadrons are exploited to identify b-jets. The long lifetime of hadrons containing a b-quark allow them to travel around 100 - 200 µm before decaying as shown in Figure 3.6, and such distances can be measured inside the tracker due to its excellent spatial resolution. The information

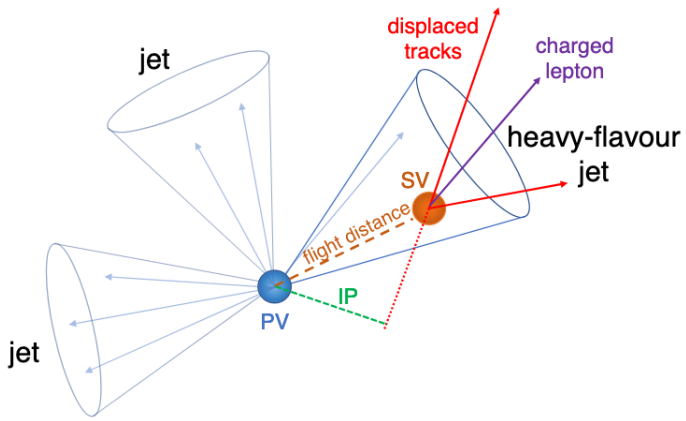

Figure 3.6: Illustration of a heavy-flavour jet with a secondary vertex (SV) from the decay of a b or c hadron resulting in charged-particle tracks (including possibly a soft lepton) that are displaced with respect to the primary interaction vertex (PV), and hence with a large impact parameter (IP) value [35].

about secondary vertex and track information is used in the Combined Secondary Vertex (CSV) algorithm [35]. In addition, another version of the CSV algorithm was developed that uses deep machine learning [36]. These algorithms are applied to jets clustered from other reconstructed objects using anti-k_T algorithm. Then, the CSV algorithm involves the use of secondary vertices, together with track-based lifetime information. A b- tagging is only applied in order to veto events containing top quarks that have greater than 99% likelihood of decaying further to a bottom quark and leptons or jets.

3.11 Missing transverse energy measurement

After the reconstruction and identification of all physics objects in the event using the PF algorithm, the remaining momentum imbalance p_T^{miss} for all reconstructed PF particles in the transverse plane to the beam direction gives rise to the missing transverse energy E_T^{miss}.

$$p_T^{miss} = \sum_{i}^{PF\,particles} p_T^i \tag{3.8}$$

The sources of p_T^{miss} are particles that are not detected by any subdetector, like the mentioned neutrinos, or unknown particles, as potentially, dark matter particles. But the p_T^{miss} determination is also affected by inefficiencies of the detector, or areas where a particle can escape without being detected due to the detector geometry. Some events could have a large p_T^{miss} due to, for example, calorimeter noise or jets in a non-operational region. These anomalous events with clear sources of instrumental p_T^{miss} are removed using specific filters, prior to any analysis [37].

All the reconstructed objects are contained in RECO [38] data tier. It provides access to the reconstructed physics objects for calibration and alignment study purposes. One can re-run various algorithms on reconstructed objects with new calibrations and alignments. An additional data tier with specific object filters is utilized specifically for detector calibration studies, known as AlCaReco (Alignment, Calibration and Reconstruction). For physics analysis, Analysis Object Data (AOD) are derived from the RECO, providing data for various physics analyses in a convenient and compact format. AOD data are usable directly by physics analyses and are available at various sites. To ease the situation for the ultimate goal of physics analysis, a special software layer called PAT (Physics Analysis Toolkit) [39] has been developed which occupies less space. It combines flexibility with user friendliness and provides easy interface to the complicated set of algorithms approved by physics object and analysis groups. However, in 2015, MINIAOD [40] data tier has been introduced in which particular physics analysis object information is saved. During Run 2, a more compressed data tier is introduced, NANOAOD [41]. In this Thesis, the analysis is performed using NANOAOD data tier.

These reconstructed objects are essential to identify the initial states and perform the related physics measurements, which will be demonstrated in the measurements performed as part of this Thesis, discussed in subsequent Chapters.

Bibliography

[1] T. Gleisberg et al., "Event generation with SHERPA 1.1", *JHEP* **02** (2009) 007, doi:10.1088/1126-6708/2009/02/007, arXiv:0811.4622.

[2] B. Webber, "Hadronization", 1994.

[3] B. R. Webber, "Fragmentation and Hadronization", 1999.

[4] T. Sjöstrand, S. Mrenna, and P. Skands, "A brief introduction to PYTHIA 8.1", *Computer Physics Communications* **178** (Jun, 2008) 852–867, doi:10.1016/j.cpc.2008.01.036.

[5] J. Alwall et al., "The automated computation of tree-level and next-to-leading order differential cross sections, and their matching to parton shower simulations", *Journal of High Energy Physics* **2014** (Jul, 2014) doi:10.1007/jhep07(2014)079.

[6] J. Alwall et al., "A Standard format for Les Houches event files", *Comput. Phys. Commun.* **176** (2007) 300–304, doi:10.1016/j.cpc.2006.11.010, arXiv:hep-ph/0609017.

[7] S. Hoeche et al., "Matching parton showers and matrix elements", in *HERA and the LHC: A Workshop on the Implications of HERA for LHC Physics: CERN - DESY Workshop 2004/2005 (Midterm Meeting, CERN, 11-13 October 2004; Final Meeting, DESY, 17-21 January 2005)*, pp. 288–289. 2005. arXiv:hep-ph/0602031. doi:10.5170/CERN-2005-014.288.

[8] S. Alioli, P. Nason, C. Oleari, and E. Re, "A general framework for implementing NLO calculations in shower Monte Carlo programs: the POWHEG BOX", *JHEP* **06** (2010) 043, doi:10.1007/JHEP06(2010)043, arXiv:1002.2581.

[9] GEANT4 Collaboration, "GEANT4–a simulation toolkit", *Nucl. Instrum. Meth. A* **506** (2003) 250–303, doi:10.1016/S0168-9002(03)01368-8.

[10] CMS Collaboration, "Particle-Flow Event Reconstruction in CMS and Performance for Jets, Taus, and MET", *CERN Document Server* (4, 2009).

[11] CMS Collaboration, "Commissioning of the Particle-Flow reconstruction in Minimum-Bias and Jet Events from pp Collisions at 7 TeV", technical report, CERN, Geneva, 2010.

[12] D. Barney, "CMS Detector Slice", Jan, 2016. CMS Collection.

[13] CMS Collaboration, "Description and performance of track and primary-vertex reconstruction with the CMS tracker", *JINST* **9** (2014), no. 10, P10009, doi:10.1088/1748-0221/9/10/P10009, arXiv:1405.6569.

[14] R. E. Kalman, "A New Approach to Linear Filtering and Prediction Problems", *Journal of Basic Engineering* **82** (03, 1960) 35–45, doi:10.1115/1.3662552.

[15] P. Billoir, "Progressive track recognition with a Kalman like fitting procedure", *Comput. Phys. Commun.* **57** (1989) 390–394, doi:10.1016/0010-4655(89)90249-X.

[16] K. Rose, "Deterministic annealing for clustering, compression, classification, regression, and related optimization problems", *Proceedings of the IEEE* **86** (1998), no. 11, 2210–2239, doi:10.1109/5.726788.

[17] R. Frühwirth, W. Waltenberger, and P. Vanlaer, "Adaptive Vertex Fitting", technical report, CERN, Geneva, Mar, 2007.

[18] CMS Collaboration, "Performance of the CMS muon detector and muon reconstruction with proton-proton collisions at $\sqrt{s} = 13$ TeV", *JINST* **13** (2018), no. 06, P06015, doi:10.1088/1748-0221/13/06/P06015, arXiv:1804.04528.

[19] CMS Collaboration, "Particle-flow reconstruction and global event description with the CMS detector", *JINST* **12** (Oct, 2017) P10003–P10003, doi:10.1088/1748-0221/12/10/p10003.

[20] CMS Collaboration, "Electron and photon reconstruction and identification with the CMS experiment at the CERN LHC", *JINST* **16** (2021), no. 05, P05014, doi:10.1088/1748-0221/16/05/P05014, arXiv:2012.06888.

[21] CMS Collaboration, "Electron and photon reconstruction and identification with the CMS experiment at the CERN LHC", *JINST* **16** (May, 2021) P05014, doi:10.1088/1748-0221/16/05/p05014.

[22] J. H. Kotecha and P. M. Djuric, "Gaussian sum particle filtering", *IEEE Transactions on signal processing* **51** (2003), no. 10, 2602–2612.

[23] K. Olive, "Review of Particle Physics", *Chinese Physics C* **38** (aug, 2014) 090001, doi:10.1088/1674-1137/38/9/090001.

[24] CMS Collaboration, "Performance of τ lepton reconstruction and identification in CMS", *JINST* **7** (Jan, 2012) P01001–P01001, doi:10.1088/1748-0221/7/01/p01001.

[25] CMS Collaboration, "Performance of reconstruction and identification of τ leptons decaying to hadrons and ν_τ in pp collisions at $\sqrt{s} = 13$ TeV", *JINST* **13** (2018), no. 10, P10005, doi:10.1088/1748-0221/13/10/P10005, arXiv:1809.02816.

[26] M. Cacciari, G. P. Salam, and G. Soyez, "The anti-kt jet clustering algorithm", *Journal of High Energy Physics* **2008** (Apr, 2008) 063–063, doi:10.1088/1126-6708/2008/04/063.

[27] CMS Collaboration, "Performance of reconstruction and identification of τ leptons decaying to hadrons and τ in pp collisions at $\sqrt{s}$=13 TeV", *JINST* **13** (oct, 2018) P10005–P10005, doi:10.1088/1748-0221/13/10/p10005.

[28] CMS Collaboration, "Performance of the DeepTau algorithm for the discrimination of taus against jets, electron, and muons", *CERN Document Server* (Oct, 2019).

[29] CMS Collaboration, "Identification of hadronic tau lepton decays using a deep neural network", 2022. arXiv:2201.08458. Submitted to *JINST*.

[30] H. Kirschenmann, "Jets at cms and the determination of their energy scale", 2012.

[31] CMS Collaboration, "Determination of jet energy calibration and transverse momentum resolution in CMS", *JINST* **6** (Nov, 2011) P11002–P11002, doi:10.1088/1748-0221/6/11/p11002.

[32] M. Cacciari, G. P. Salam, and G. Soyez, "FastJet user manual", *The European Physical Journal C* **72** (Mar, 2012) doi:10.1140/epjc/s10052-012-1896-2.

[33] M. Cacciari, G. P. Salam, and G. Soyez, "The catchment area of jets", *Journal of High Energy Physics* **2008** (Apr, 2008) 005–005, doi:10.1088/1126-6708/2008/04/005.

[34] M. Cacciari and G. P. Salam, "Pileup subtraction using jet areas", *Physics Letters B* **659** (Jan, 2008) 119–126, doi:10.1016/j.physletb.2007.09.077.

[35] CMS Collaboration, "Identification of heavy-flavour jets with the CMS detector in pp collisions at 13 TeV", *JINST* **13** (may, 2018) P05011–P05011, doi:10.1088/1748-0221/13/05/p05011.

[36] D. Guest et al., "Jet flavor classification in high-energy physics with deep neural networks", *Phys. Rev. D* **94** (Dec, 2016) 112002, doi:10.1103/PhysRevD.94.112002.

[37] CMS Collaboration, "Performance of missing transverse momentum reconstruction in proton-proton collisions at $\sqrt{s} = 13$ TeV using the CMS detector", *JINST* **14** (Jul, 2019) P07004–P07004, doi:10.1088/1748-0221/14/07/p07004.

[38] CMS Collaboration, "Technical Proposal for the Phase-II Upgrade of the CMS Detector", *CMS Technical Design Report* (6, 2015).

[39] W. Adam et al., "PAT: The CMS physics analysis toolkit", *J. Phys. Conf. Ser.* **219** (2010) 032017, doi:10.1088/1742-6596/219/3/032017.

[40] G. Petrucciani, A. Rizzi, and C. Vuosalo, "Mini-AOD: A New Analysis Data Format for CMS", *Journal of Physics: Conference Series* **664** (dec, 2015) 072052, doi:10.1088/1742-6596/664/7/072052.

[41] CMS Collaboration, "NANOAOD: a new compact event data format in CMS", *EPJ Web Conf.* **245** (2020) 06002, doi:10.1051/epjconf/202024506002.

Chapter 4

Study of Radiation Damage in the CMS Hadron Calorimeter using Isolated Muons from LHC Collision Data

The CMS Hadron Calorimeter (HCAL) [1] is a sampling calorimeter designed to measure the energy of the hadrons produced in the *pp* collision at CMS. As discussed in Chapter 2, it consists of plastic scintillators as an active material interleaved in brass/steel absorber layers. Due to continuous exposure to hadrons from the *pp* collision, the scintillators experience degradation in their light output. Due to this, the energy of the incident particles measured by the HCAL may not be correct. Hence, the effect of continuous irradiation must be measured for calibrating the HCAL energy response through out the data taking period. Different methods are used by the CMS experiment to study the effect of radiation on plastic scintillators, such as the laser light calibration, radioactive source monitoring, measurements using hadrons and muons coming from the *pp* collision. This Chapter presents the measurement of radiation damage in plastic scintillators using isolated muons from the LHC collision data.

4.1 CMS Hadron Calorimeter

HCAL is a cylindrical symmetric sampling calorimeter, composed of two-half barrels and two endcap sections situated inside the solenoid magnet as shown in Figure 4.1. It is designed to capture the hadronic shower produced by the particles interacting via strong interaction such as baryons and mesons. These particles formed at the interaction point, quickly travel through the detector, depositing very little energy in the tracker and the electromagnetic calorimeter (ECAL), before reaching the HCAL. The HCAL has layers of dense matter (brass/steel) as an absorber and scintillators (such as plastic) as an active material. The role of the dense matter is to initiate and absorb the hadronic shower while the scintillator produces the light signal when the shower particles strikes the surface.

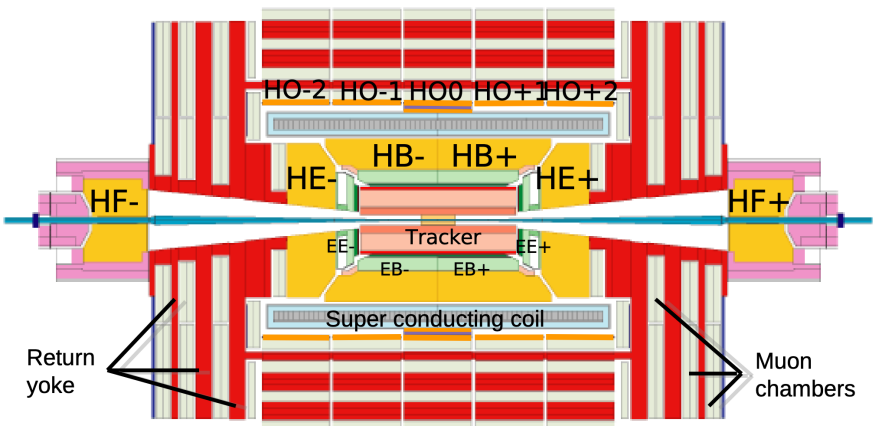

Figure 4.1: Layout of CMS Hadron Calorimeter labeled as HB and HE [2].

4.1.1 Barrel Hadron Calorimeter

The barrel hadron calorimeter (HB), as discussed in Chapter 2, lies in $|\eta| < 1.4$ region of the CMS detector. It consists of two identical half-barrels (HB+ and HB-) with 18 wedges of 20° in ϕ in each half-barrel as shown in Figure 4.2. Each half-barrel has 17 layers (0-16) of active scintillator tiles interleaved in brass (and stainless steel) absorber plates. The scintillator tile size is 0.087 wide in η and 5° in ϕ. Tiles in successive layers are aligned in a "tower". The towers are labeled using

integer indices based on their position in η and ϕ. For HB, the $i\eta$ index ranges from 1 to 16 and the $i\phi$ index ranges from 1 to 72. The $i\eta$ layout of the HB is shown in Figure 4.3. Table 4.1 describes the size of HB towers and their corresponding depth segmentation. The light output from the scintillator tiles falls in the blue-violet range and is first fed in the wavelength shifting fibers (WLS). These fibers (< 1 mm diameter) shift the blue-violet light in the green range and transports the light signal to hybrid photodiodes (HPDs) which detect and amplify the light signal. The signal from the scintillator tiles is optically added from each of the 17 active layers. The optically added layers in a tower are considered as a single depth [3] [4]. The exceptions are towers 15 and 16 located at the edge of the HB half-barrel where multiple optical readouts are present. As a result, tower 15 has two depths and tower 16 has three depths with the last depth in the endcap section as shown in Figure 4.3. More details on the HCAL geometry can be found in [5].

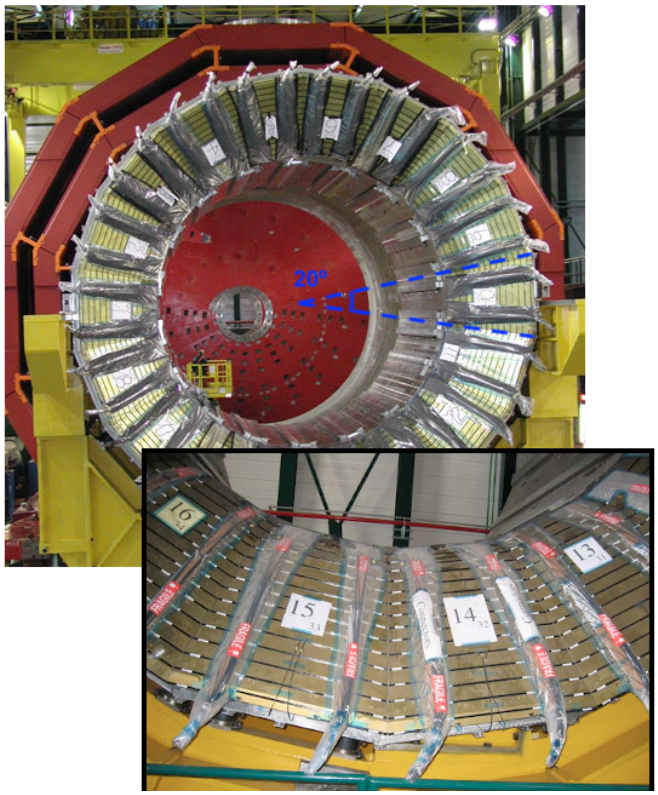

Figure 4.2: A section of HB with a closer look at the HCAL sections, showing the layers of brass and scintillator [6].

Tower index ($i\eta$)	η range		Detector	Size		Depth segments
	Low	High		η	ϕ	
1	0.000	0.087	HB	0.087	5°	HB=1
2	0.087	0.174	HB	0.087	5°	HB=1
3	0.174	0.261	HB	0.087	5°	HB=1
4	0.261	0.348	HB	0.087	5°	HB=1
5	0.348	0.435	HB	0.087	5°	HB=1
6	0.435	0.522	HB	0.087	5°	HB=1
7	0.522	0.609	HB	0.087	5°	HB=1
8	0.609	0.696	HB	0.087	5°	HB=1
9	0.696	0.783	HB	0.087	5°	HB=1
10	0.783	0.870	HB	0.087	5°	HB=1
11	0.870	0.957	HB	0.087	5°	HB=1
12	0.957	1.044	HB	0.087	5°	HB=1
13	1.044	1.131	HB	0.087	5°	HB=1
14	1.131	1.218	HB	0.087	5°	HB=1
15	1.218	1.305	HB	0.087	5°	HB=2
16	1.305	1.392	HB, HE	0.087	5°	HB=2, HE=1
17	1.392	1.479	HE	0.087	5°	HE=2
18	1.479	1.566	HE	0.087	5°	HE=5
19	1.566	1.653	HE	0.087	5°	HE=6
20	1.653	1.740	HE	0.087	5°	HE=6
21	1.740	1.830	HE	0.090	10°	HE=6
22	1.830	1.930	HE	0.100	10°	HE=6
23	1.930	2.043	HE	0.113	10°	HE=6
24	2.043	2.172	HE	0.129	10°	HE=6
25	2.172	2.322	HE	0.150	10°	HE=6
26	2.322	2.500	HE	0.178	10°	HE=7

Table 4.1: Size of HCAL towers in η and ϕ as well as their depth segmentation [1] [4].

4.1.2 Endcap Hadron Calorimeter

The endcap hadron calorimeter (HE) lies in $1.3 < |\eta| < 3.0$ and has similar structure as HB except it has 18 active scintillator layers. It has a nose-like structure, with an additional layer of absorber and scintillator for $i\eta = 18$, to increase the total interaction length for that tower as shown in Figure 4.3. Up to $i\eta = 20$, the scintillator tile size is similar to HB i.e. 0.087 in η and 5° in ϕ. In the high η region, beyond $i\eta = 20$, the ϕ-granularity of the tiles is reduced to 10° to accommodate

the bending radius of the WLS fiber readout. Hence, beyond $i\eta = 20$, the scintillator tile size is 0.090 in η and 10° in ϕ as described in Table 4.1. For HE, the $i\eta$ index ranges from 16 to 28. Up to $i\eta = 20$, the $i\phi$ index ranges from 1 to 72 while beyond it, the $i\phi$ index has only odd values i.e. 1, 3, 5, ...71 due to reduced ϕ-granularity. From Run 1 up to year 2017 data-taking, HE scintillator tiles were read by HPDs similar to HB. In the year 2018, the entire HE readout was replaced by the silicon photo-multipliers (SiPMs) leading to increased depth segmentation, better calibration and energy response. The 2018 layout and depth segmentation of HE is shown in Figure 4.3. HE is tapered to interlock with HB and to overlap with $i\eta = 16$. Hence, $i\eta = 16$ depth 4 lies in the HE whereas depth 3 does not exist due to presence of optical readout in the region. $i\eta = 17$ has two depths and $i\eta = 18$ has four depths as shown in Figure 4.3. Beyond this to $i\eta = 25$, each tower has six depth segments. To increase the total interaction length, $i\eta > 25$ has seven depth segments [7].

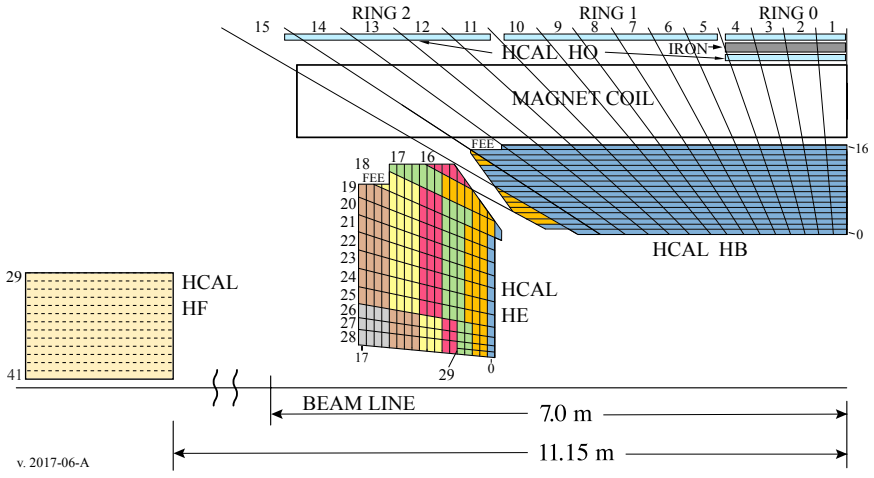

Figure 4.3: A schematic view of the tower mapping in $r - z$ plane of the HCAL barrel and endcap regions [8].

4.1.3 Radiation dose at HCAL

At the LHC, two oppositely moving proton beams collide at the center of the CMS detector. During the *pp* collision, the mean number of interactions that occur per

bunch crossing are about 37 [9]. The electrons and photons produced in the interaction get absorbed in the ECAL while the remaining particles such as hadrons and muons reach the HCAL and deposit their energy. The scintillator tiles in the HCAL are subjected to the radiation dose which depends on its position in HCAL. The dose varies in HB and HE, following the particle energy density of the *pp* collisions. It also varies with the depths in the calorimeter, following the energy deposition profile of the electromagnetic and hadron showers. The dose received by the scintillator tiles is estimated using the Monte Carlo code FLUKA 2011.2c [10] [11]. Per 68 fb^{-1} luminosity data, the doses in layer 1 range between 0.02 kGy and 2 kGy for barrel and endcap respectively, as shown in Figure 4.4. For layer 7, the doses range between 0.002 kGy and 0.4 kGy for barrel and endcap respectively. This clearly shows that layers close to the interaction point are subjected to higher doses than layers that are far. Also, the HCAL towers in the forward region of the detector (higher $i\eta$) are subjected to the highest radiation doses. These radiations influence the performance of plastic scintillators as discussed in the next Section.

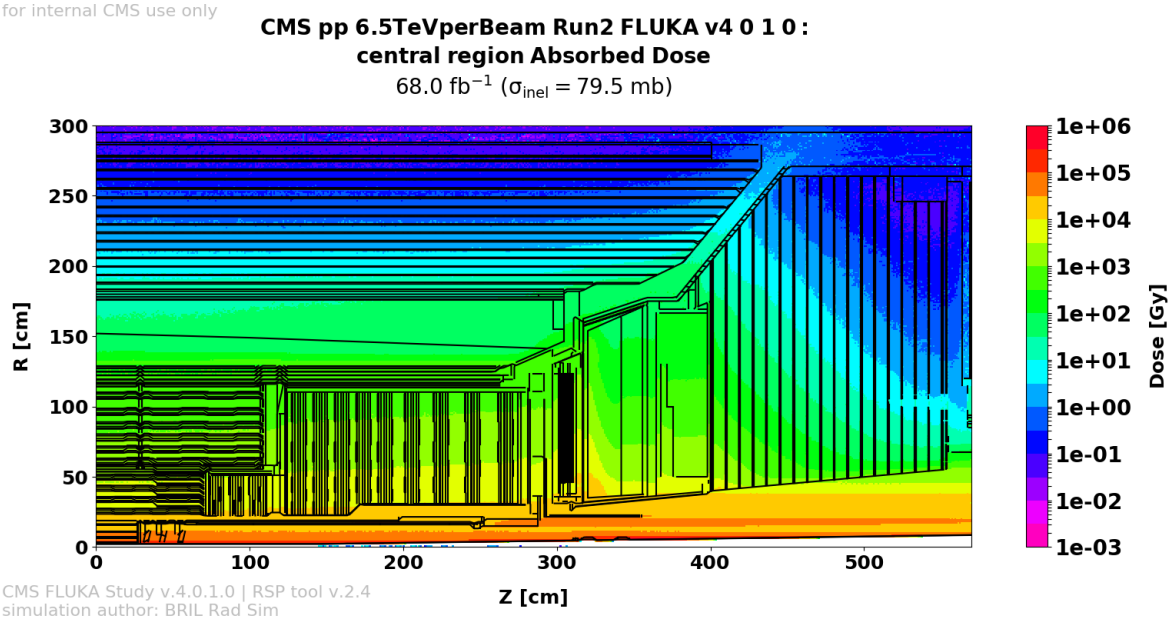

Figure 4.4: Monte Carlo estimation of the absorbed dose at CMS using FLUKA with an energy of 6.5 TeV per beam [12].

4.2 Radiation damage in plastic scintillators

The plastic scintillators are composed of a plastic substrate, either polystyrene (PS) or polyvinyltoluene (PVT) and fluorescent agents (called as primary or secondary fluors) dissolved in them. When a charged particle traverses through the scintillators, it excites the substrate molecules. These excitations are then transferred to the primary fluors via the Förster mechanism [13]. The primary fluors transfer the excitation radiatively to the secondary fluors as shown in Figure 4.5. Similarly, the

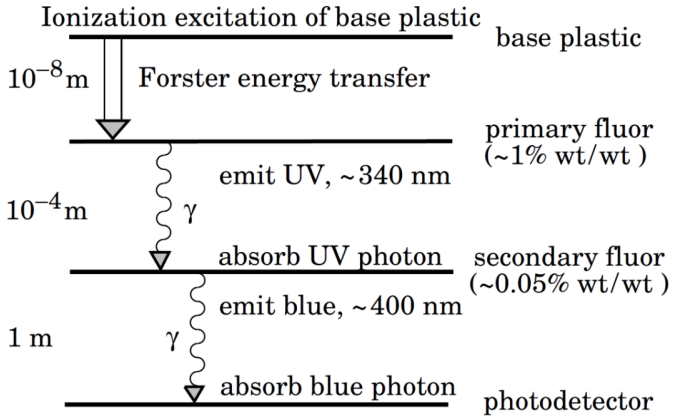

Figure 4.5: Scintillation mechanism in plastic scintillators [14].

active scintillator layers of HCAL tower are made of SCSN-81, PS-based scintillator by Kurray, Japan. In this scintillator, the absorption wavelength of primary fluors is approximately 280 nm and the emission wavelength is approximately 320-350 nm. The absorption maxima of secondary fluors is at the emission wavelength of primary fluors and the emission wavelength is 440 nm which falls in the blue spectrum of the visible range. This emitted light then traverses through the scintillators to reach the WLS fibers. If there are any defects in the scintillators due to continuous irradiation, this transmitting light signal gets reduced by the imperfections.

It has been observed that damage to the fluors due to irradiation is generally small [15] [16]. The reduction in the light output occurs mainly due to the damage in the substrate which results from creation of radicals, conjugated double bonds, carbonyl species due to reaction with oxygen and trapped electrons, and other struc-

tures that can be color centers. Color centers reduce the light output by absorbing the light produced by the secondary fluors in the scintillator. Radicals are produced when chemical bonds in the polymer are broken. The bonds can reform on a time scale, depending on the density of the radicals and the temperature. Such damage is called temporary damage, and the reforming of bonds is known as annealing. Formation of conjugated double bonds and carbonyl species due to reaction with oxygen results in permanent damage to the scintillator [17]. Figure 4.6 shows the chemical structure of PS before irradiation. Figure 4.7 illustrates the formation of complex structures resulting in permanent color centers in PS.

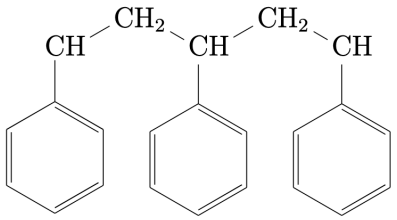

Figure 4.6: Polystyrene before irradiation [18].

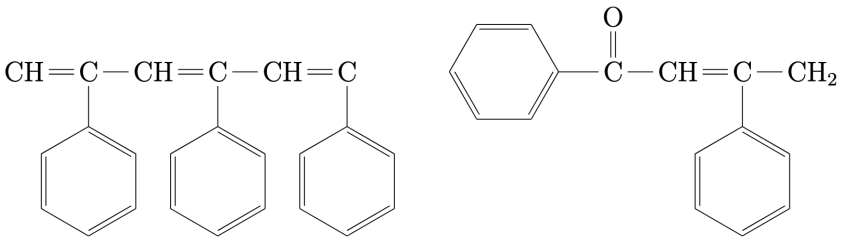

Figure 4.7: Changes in chemical structure of Polystyrene after irradiation. The change on the right occurs in the presence of oxygen [17].

The scintillator light output decreases exponentially with the dose received [19] and is given by

$$L(d) = L_0 \exp(-d/D) \tag{4.1}$$

where $L(d)$ is the light output after radiation dose d, L_0 is the light output before irradiation and D is the dose constant.The dose constant, D depends on the constituents of the scintillator and on its environmental history [20].

4.3 Methods to study the radiation effect

The methods followed by the CMS experiment to study the effect of radiation on the scintillator material are discussed as below.

4.3.1 Laser calibration system

A laser calibration system [19], composed of a triggerable nitrogen laser, is used to monitor the performance of scintillator tiles and the response of photodetectors. The laser light is fed to a filter wheel to change its intensity to control the dynamical range of photodetectors and ADC as shown in Figure 4.8. Next the light is sent to a commutator that can send the light to HB, HE and HF through outgoing quartz fibers. This light distribution system delivers ultraviolet (UV) light to the scintillator tiles of layer 1, first layer towards the interaction point and layer 7, which lies in the middle of a tower. One set of laser pulses excites the scintillator tiles directly, to monitor the scintillator and waveshifter ageing. For this, the excitation wavelength is kept at 337 nm and is derived from the primary (nitrogen) laser. This excites the primary fluors in the scintillator and the resulting light pulses are measured by a PIN diode. The second set of laser pulses have a wavelength of 430-450 nm, which measure the response of photodetectors and provide a measurement independent of the characteristics of the tiles. This method is performed between proton fills of the accelerator, when there are no collisions.

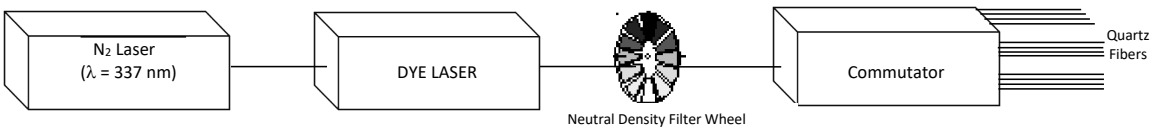

Figure 4.8: HCAL Laser Calibration System [19].

4.3.2 Radioactive source system

The Radioactive source calibration is performed for each scintillator tile in every layer of the calorimeter. Each scintillator tile in HCAL is equipped with a thin 1 mm in diameter stainless steel tube that moves the ^{60}Co radioactive source attached at the tip of a wire. The source is inserted all the way across every row of tiles. Since each tile is in a different tower, it can be read independently. The ^{60}Co source provides photons with energies of 1.17 and 1.33 MeV. The source attached to the tip of a wire moves at approximately 6 cm/s, and the signal is integrated for 0.1 s for each measurement. The resulting DC induced current by the source is used to monitor the stability of every tile in the HCAL at a varying period [19]. The change in the measured current measures the effect of radiation damage. A few layers of the HB and the HE are monitored during data taking period to verify that nothing unexpected has occurred. The primary recalibration of each tile, however, takes place during long shutdown periods when access to the source tubes is relatively easy.

4.3.3 Isolated particles produced in collision events

An additional method of measuring the effects of irradiation on the scintillator tiles is used, based on isolated particles produced in the *pp* collisions. These isolated particles include hadrons and muons resulting from the *pp* collisions. In case of the hadrons, radiation damage study is performed with a sample of isolated hadrons (pions) with momenta of 50 GeV which do not interact hadronically in the ECAL. The energy deposited by these hadrons in HB and HE towers is measured for periodic samples of luminosity distributed uniformly over the entire data-taking period. For each data-taking period, the ratio of average energy relative to that of first period (as a reference) serves as a measure of the radiation damage up to that period of data taking [18]. The measure of the level of radiation damage is then given by

$$F_{measured}(n) = \frac{E_{ave}(n)}{E_{ave}(1)} \tag{4.2}$$

where E_{ave} is the average signal measured in all readout channels with the same values of $i\eta$ and depth [18].

Alternatively, isolated muons from the collision data are also used to estimate the amount of radiation damage in the HCAL towers. The trajectories of the isolated muons are propagated to the ECAL and HCAL surfaces to determine the position of the transversing tower. The energy deposited in that HCAL tower is measured during different data-taking periods. This technique is useful as it extends the measurement to higher η regions within acceptance of the tracker and of the muon system. In addition to this, the minimum ionizing nature of muon is useful in tracking the trajectory of muon from the first layer to the last layer and estimating the amount of radiation damage in the high multiplicity environment. In this Thesis, HCAL radiation damage studies are performed using isolated muons as explained in the following Sections.

4.4 Measurement of radiation damage using muons produced in *pp* collisions

Isolated muons from the collision data are used to study the radiation damage of different channels of the barrel and endcap hadron calorimeter of the CMS experiment. Muons, being the minimum ionizing particles (MIPs) do not interact much with the calorimeter materials. Due to their less interactive or showering nature in the HCAL, it is easy to compare their responses in the HCAL layers.

4.4.1 Collision Conditions and Data

The present analysis uses the *pp* collision data at center-of-mass energy of 13 TeV collected by the CMS detector in 2018. The integrated luminosity delivered by the LHC as a function of time in 2018 is shown in Figure 4.9. The total luminosity delivered by the LHC is around 68 fb^{-1} in 2018. For this study, six luminosity periods

after delivered luminosity of 5.74, 15.40, 27.39, 36.75, 49.26, and 62.45 fb^{-1} are selected to measure the effect of radiation as a function of delivered luminosity and are represented by dotted lines in the Figure 4.9. Each of these luminosity periods consists of data spanning over approximately 4.0 fb^{-1} of integrated luminosity.

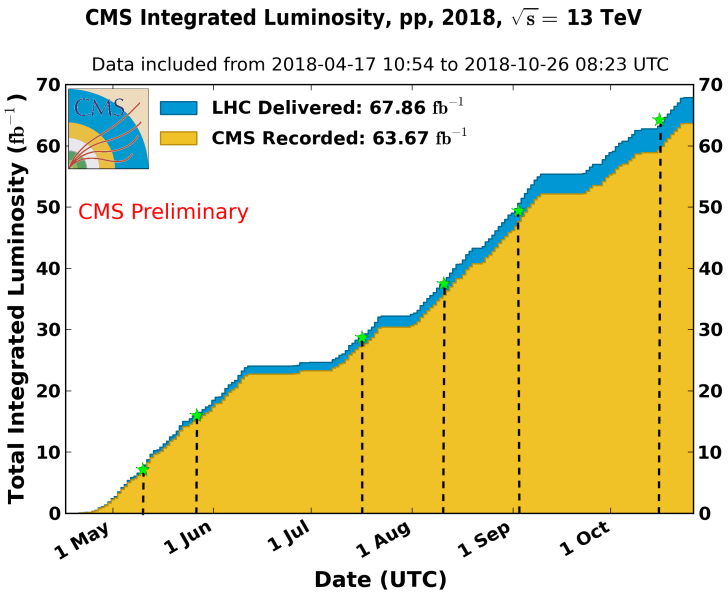

Figure 4.9: Integrated luminosity delivered to CMS by the LHC in the 2018 *pp* data-taking period, as a function of time. The intervals of constant luminosity indicate periods with no beam, e.g. technical stops. The dotted lines show the luminosity points considered for the analysis [21].

Multiple interactions occur during the same beam-beam crossing and are referred to as pileup as discussed in Chapter 2. These additional interactions lead to more than one good primary vertex per bunch crossing. The distribution for number of good primary vertices in 2018 is shown in Figure 4.10. As can be seen from the figure, the distribution peaks around 25. To ensure similar pileup condition in different luminosity periods, the number of primary vertices are restricted between 25 and 30 for this analysis which is about the mean of the number of primary vertices distribution. However, the large particle density in the forward region of the HCAL affects the charge distributions for channels at higher $i\eta$ and small depths. The extraction of the peak position due to minimum ionizing particle becomes exceedingly difficult for these channels as discussed in Section 4.4.6. The effect of high pileup is

reduced by requiring events with smaller number of primary vertices. For the towers with $i\eta = 23$, depth = 1, $i\eta = 24$ and 25, depth = 1 and 2, and all depths with $i\eta = 26$, events with number of primary vertices between 1 and 15 are used.

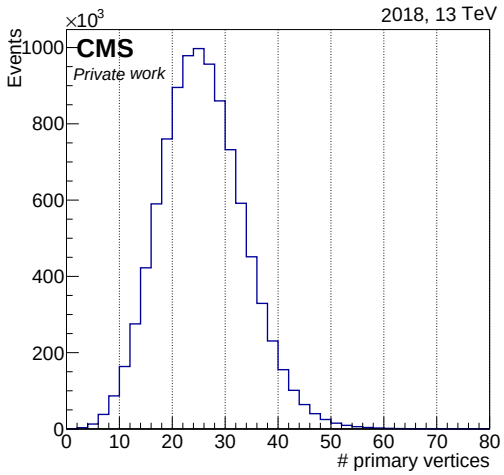

Figure 4.10: Number of primary vertices from the runs of 2018.

4.4.2 Muon selection

Muons used for the radiation damage studies are required to be isolated from other charged and neutral particles such that the energy measured in the HCAL tower is expected to be entirely due to the muons. The muon track in the HCAL is reconstructed using the hit information from each sub-detector with Particle-Flow (PF) algorithm [22] as discussed in Chapter 3. To reject the cosmic muons, the muons are required to be the global muon candidates [23] with hits both in the tracker as well as in the muon detectors. Hadronic punch-through and muons from decays in flight are rejected by requiring the χ^2/dof of the global-muon track fit to be less than 10. To further suppress muons from decays in flight, the muon candidates are required to have at least one hit in the pixel detector. In addition to this, there must be muon segments in at least two muon stations. The contamination from cosmic muons and muons from decays in flight is further suppressed by requiring the threshold on the impact parameter (d_{xy}) to be less than 2 mm with respect to the primary vertex. Besides this, the longitudinal distance (d_z) of the tracker

track with respect to the primary vertex is required to be less than 5 mm. The transverse momentum (p_T) of the muons is required to be above 20 GeV. Besides this, muons are required to be well isolated and are required to have minimal energy from the neutral and charged hadron candidates in a cone of $\Delta R = 0.4$ around the muon trajectory [24]. The muon track has to cross a given HCAL tower (not shared between towers having different $i\eta$ and $i\phi$). After selecting the desired muons, the energy of the muon candidate is measured in a given HCAL tower. The energy of the muon hit must be the highest within a 3×3 matrix surrounding that tower. The cell (or tile) with the maximum energy is considered as a signal and used to get the raw charge measurement.

4.4.3 Methodology

Muons which are produced at the interaction point traverse through the tracker, the ECAL and the HCAL before reaching the muon stations in the CMS detector. The energy deposited by the traversing muons is measured around the impact point of the muons in the HCAL tower. At the time of reconstruction, the charge output from the photodetectors is converted into energy using different calibration constants. Hence, for this study, these calibration constants are removed from the measured energy to get the raw charge measurement. The charge distribution for each cell in HB and HE is studied. The measured charge distribution is fitted to a Gaussian convolved Landau function. For a given value of $i\eta$ and depth, all the charge distributions corresponding to the 72/36 different $i\phi$ values are fitted separately for the six luminosity periods to obtain the most probable value (MPV) of the measured charge. The MPV from these individual $i\phi$ values are compared to check if they are azimuthally symmetric. In order to obtain a MPV value for a given $i\eta$ and depth in a given luminosity period, the distribution of MPVs from the individual $i\phi$ values are fitted to a Gaussian function. The mean and the width of the Gaussian fit determines the overall MPV value for a given $i\eta$ and depth and the corresponding uncertainty in it. The evolution of these MPV values with delivered

luminosity is studied to evaluate the effect of radiation damage. The change in MPV value for a given luminosity period ($MPV_{charge}(L)$) with respect to the MPV value obtained for the first luminosity period ($MPV_{charge}(0)$) is fitted with an exponential function in accordance to Eq. 4.1 to get the exponential slope (m). The loss in light output with increase in delivered luminosity is then given as:

$$MPV_{charge}(L) = MPV_{charge}(0)\exp(-m.L) \tag{4.3}$$

where L is the total delivered luminosity. The sign and the value of the exponential slope measures the level of radiation damage. The larger positive slopes depicts the larger radiation damage in a given HCAL tower.

4.4.4 Results

As discussed in the previous Section, the charged deposited by the muons in a given HCAL tower is studied in all six luminosity periods. Most of the towers in the HB has a single depth with the exception of towers $i\eta = \pm 15$ and ± 16. For a comparison of all the $i\eta$ towers, the charges in these two depths for these four towers are combined. Figure 4.11 (left) shows the measured charge distributions for $i\eta = 8$ for a given $i\phi$ value which lies in the HCAL barrel region. Figure 4.11 (right) shows the measured charge distributions for $i\eta = 24$ depth 1 which lies in the endcap region and is the first layer towards the interaction point in that tower. The smooth blue line through the black data points shows the fit with acceptable χ^2 per degree of freedom using Gaussian convolved Landau function.

The mean of the fit to the charge distribution corresponding to each $i\phi$ for a given $i\eta$ and depth gives the MPV of charge. The obtained MPV value for each $i\phi$ for a given $i\eta$ and depth are plotted as a function of $i\phi$ as shown in the Figure 4.12. The MPV values are within the $\pm 1\sigma$ bounds of the mean as represented by the solid red lines in the Figure. There are some outliers which are outside the $\pm 1\sigma$ bounds of the MPV values and are ignored in the final calculation of the MPV value as they do not contribute to the final MPV of charge . In order to obtain the MPV value

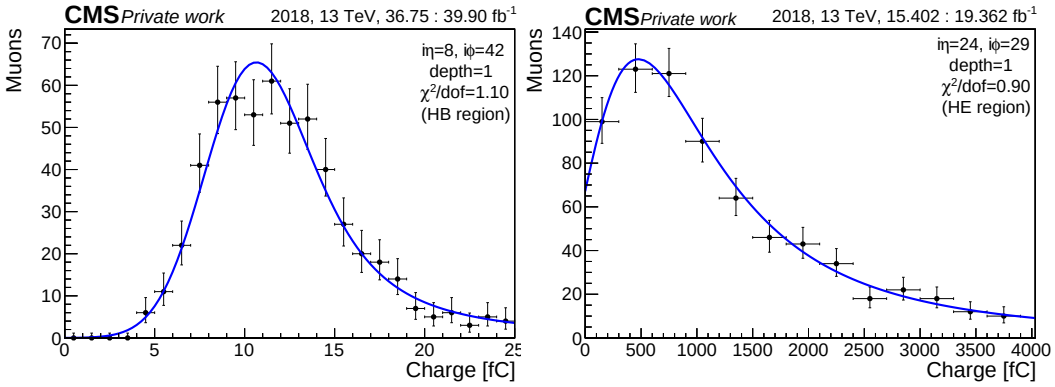

Figure 4.11: Charge distributions corresponding to $i\eta = 8$ (left) and $i\eta = 24$ depth 1 (right).

for a given $i\eta$ and luminosity period, the distributions of these 72/36 MPV values are fitted to Gaussian functions as shown in Figure 4.13. Finally, the mean of the Gaussian fit provides the MPV value of charge for a given HCAL tower and the spread in the MPV values (width of the fit) determines the uncertainty in the MPV value. The ratio of the MPV value for a given luminosity period ($MPV_{charge}(L)$) to the first luminosity period ($MPV_{charge}(0)$) are plotted as a function of delivered luminosity to get the level of radiation damage.

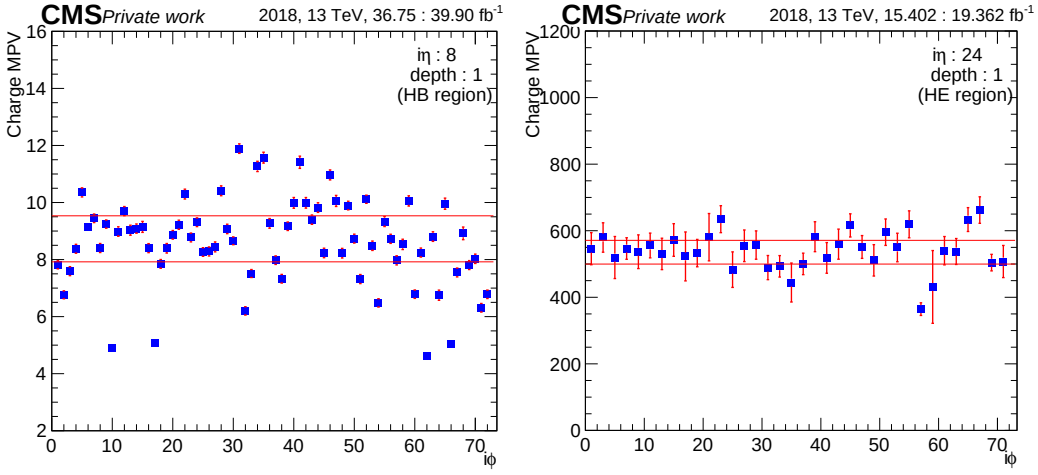

Figure 4.12: MPV values obtained from the fits to Gaussian convolved Landau functions to the charge distribution as a function of $i\phi$ corresponding to $i\eta = 8$ (left) and $i\eta = 24$ (right). The lines in the plots correspond to MPV values equal to the mean value $\pm 1\sigma$

.

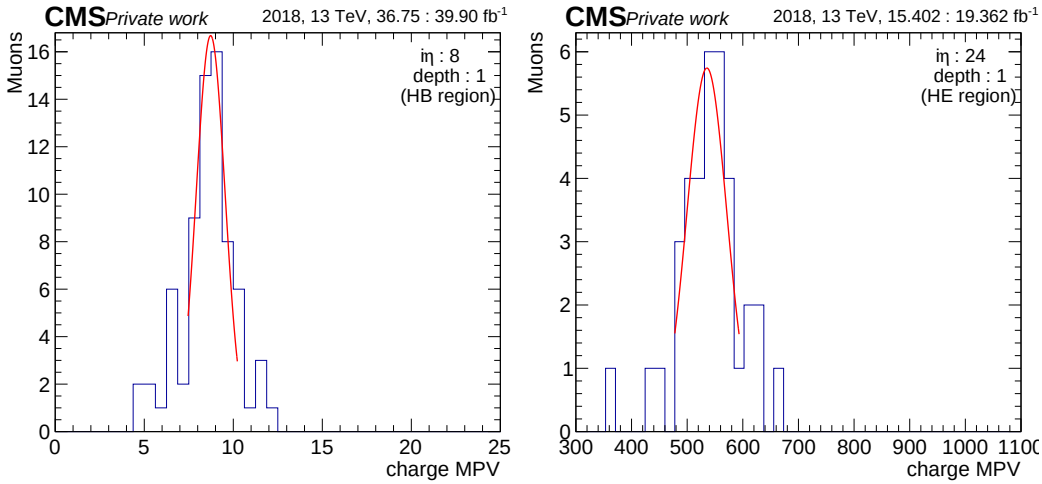

Figure 4.13: Distribution of MPV values obtained from the fits to Gaussian convolved Landau functions to the charge distributions from the different $i\phi$ values corresponding to $i\eta = 8$ (left) and $i\eta = 24$ (right). The smooth lines are results from fits to Gaussian distributions.

Figure 4.14 shows the distributions of the change in MPV values as a function of delivered luminosity for $i\eta = 8$ depth 1 (in barrel) and $i\eta = 24$ depth 1 (in endcap). These distributions are consistent with exponential functions according to Eq. 4.3 and the results of the fits are shown as smooth lines in the Figure. The exponential slope estimated from this fit measures the level of radiation damage. For $i\eta = 8$ (in barrel), the observed slope from the exponential fit is 0.0006 ± 0.0001 which shows the $\sim$4% decrease in the light output with 68 fb^{-1} using Eq. 4.3. Similarly, for $i\eta = 24$ depth 1 (in endcap), the observed slope is 0.0015 ± 0.0001 which shows the $\sim$10% decrease in the light output for this HE tower.

The slopes for each HB and HE towers are measured and are shown in Figure 4.15. Here, the slopes for all HB and HE towers towers corresponding to depth 1 are shown. As can be seen from the Figure 4.15, the towers in the central HB region (-10 $< i\eta <$ 10) show very small degradation. The level of radiation damage increases at larger $\pm i\eta$ values ($\sim$ 10% for $i\eta = 16$) [25]. The HB towers are read out using HPD devices during 2018 and consequently the degradation would be combined effect of the radiation damage of plastic scintillator and the deterioration in performance of HPD's with time. The value of the observed slope increases for HE

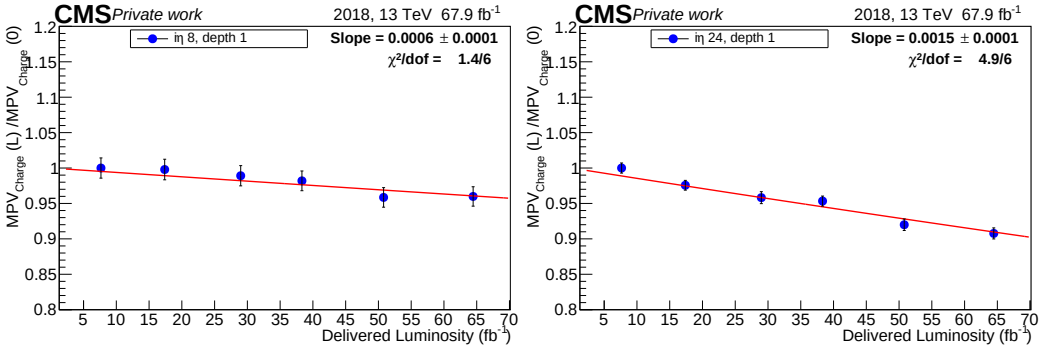

Figure 4.14: Ratio of MPV values of the charge distribution at a luminosity period to the MPV value corresponding to first luminosity period as a function of delivered luminosity for $i\eta = 8$ (left) and $i\eta = 24$ depth 1 (right).

towers ($i\eta > 16$) indicating the higher loss in light output in HE. The loss becomes as large as ∼15% at the highest $i\eta$ [26]. However, for $i\eta = 25$ and 26, the slopes become negative with large uncertainty in them. This is inconsistent as light output is not expected to increase in scintillators after irradiation. It is observed that with increase pileup activity in the forward $i\eta$ regions, the charge distribution becomes very broad. Hence, it becomes difficult to measure the MPV of charge with reasonable accuracy for these HCAL towers. Due to this, results for $i\eta = 26$, depth 1 and depth 2 are not included in this study. More studies for this are provided in the Section 4.4.6.

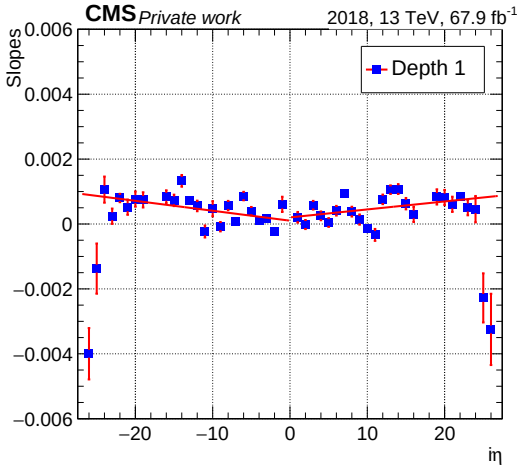

Figure 4.15: Slopes from the fits to the exponential function of the most probable charge distribution as a function of delivered luminosity as a function of $i\eta$.

Figure 4.16 shows the observed slopes as a function of $i\eta$ for HE -z side (left) and HE +z side (right) for depths 2 to 6. It is observed that the observed slope, hence the loss in light output is higher for front (lower values) of depths. As $i\eta$ increases, the observed slope increases, indicating the higher light loss in the forward region of the endcap. Some of the slopes with the assigned uncertainties have the wrong sign (being negative) [26]. This is inconsistent with the fact light will not increase under radiation. This effect is observed due to low statistics in the later depths and indicates that the assigned errors lack systematic and statistical uncertainty which will be studied in more detail in Run 3.

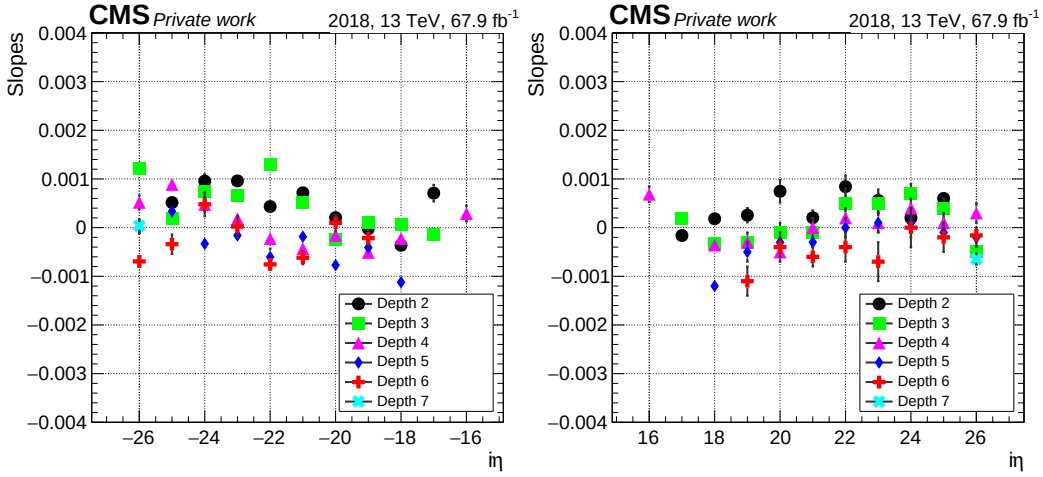

Figure 4.16: Slopes from the fits to the exponential function of the most probable charge distribution as a function of delivered luminosity as a function of $i\eta$ for HE- (left) and HE+ (right).

4.4.5 Additional methods

To estimate the slopes for a given $i\eta$ and depth in HE, the MPV value of charge is estimated using two additional methods as described below.

- **Method of truncated means**

  In this method, the high ends in the Landau tail of the accumulated charge distribution are truncated and the mean of the remaining distribution is computed. Due to large Landau tails in the accumulated charge distributions, the

truncated part contributes to 40% of the distribution in most of the cases which is around 1000-2000 fC of the measured charge. In few cases, as for the front depths of the highest $i\eta$ values, a slightly larger fraction of entries is truncated. Mean and RMS values are computed from the contents in the truncated region which determine the truncated mean and its uncertainty. Truncated mean values and the results from the fits to Gaussian convolved Landau distributions agree within two standard deviation. The truncated mean is plotted as a function of delivered luminosity to get the exponential slope for a given $i\eta$ tower and depth. It is observed that there are still some values which indicate wrong signature of radiation damage as observed in the main method.

- **Fit to distributions of combined $i\phi$ channels**

  The method of truncated means measures a very small uncertainty in the estimation of the most probable values. An alternate way of estimating the most probable values with a more realistic uncertainty is to study the accumulated charge distributions for combined channels in $i\phi$ for a given value of $i\eta$ and depth. The measured charge distributions in each luminosity period are fitted with Gaussian convolved Landau function to get the MPV value of charge for a given value of $i\eta$ and depth. The observed MPV values are plotted as a function of delivered luminosity to get the exponential slope for a given $i\eta$ and depth from this method.

The results from these methods are compared with the nominal method, referred to as "individual $i\phi$ method", used in the analysis. The results are also compared with the measurements performed by the CMS experiment using energy deposited by the hadrons from the collision data [18]. All the measurements give the large positive values of the slope for forward tiles (higher values of $i\eta$) as shown in Figure 4.17. This is also true for earlier depths where the amount of radiation is expected to be more. The slopes measured from the four methods have a reasonable agreement for all depths except depth 1. Measurements from fits to Gaussian convolved Landau function to charged distribution in the combined $i\phi$ method show the largest

discrepancy for tiles at depth 1. The discrepancy in the depth 1 is studied and is discussed in the following Section.

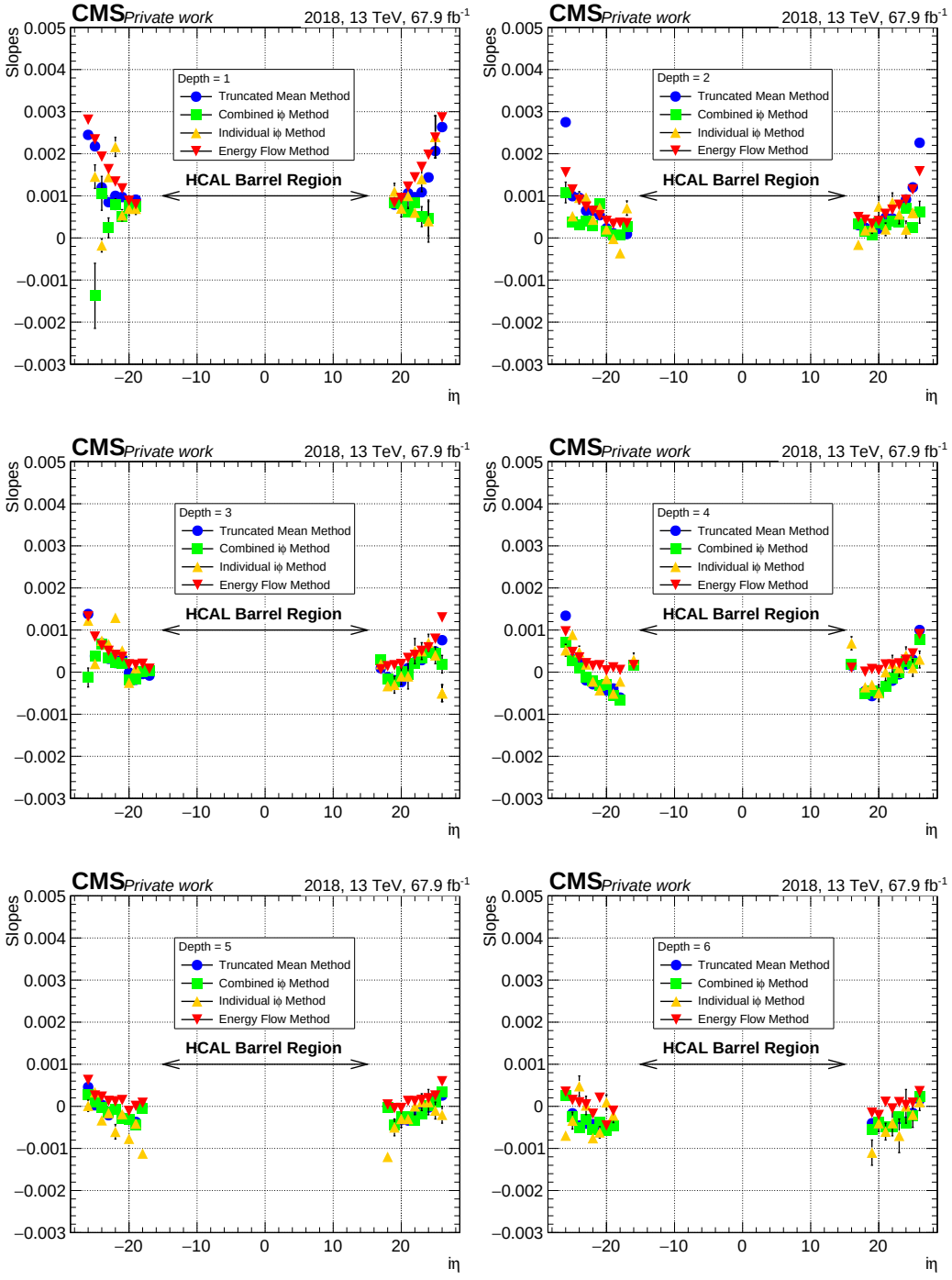

Figure 4.17: Slopes as a function of $i\eta$ for different depths: depth 1 (top left); depth 2 (top right); depth 3 (middle left); depth 4 (middle right); depth 5 (bottom left); depth 6 (bottom right).

4.4.6 Effect of pileup on measurements

As discussed in the Section 4.1.3, the forward region of the HE is subjected to high radiation doses. The front depths of these higher $i\eta$ towers, which are near to the interaction point, experience large pileup activity. Due to this, the charge distributions corresponding to these $i\eta$ towers become very broad as shown in Figure 4.18 (left) for $i\eta = 26$ depth 1. As a result, it becomes difficult to measure the MPV of charge with reasonable accuracy. To study the effect of pileup on the MPV of charge, pp collision data collected during low luminosity runs in 2018 are studied. Charge distributions from these low luminosity runs are compared with the normal luminosity runs to see any systematic difference between the MPV values. Figure 4.18 shows some of the charge distributions from the normal and low

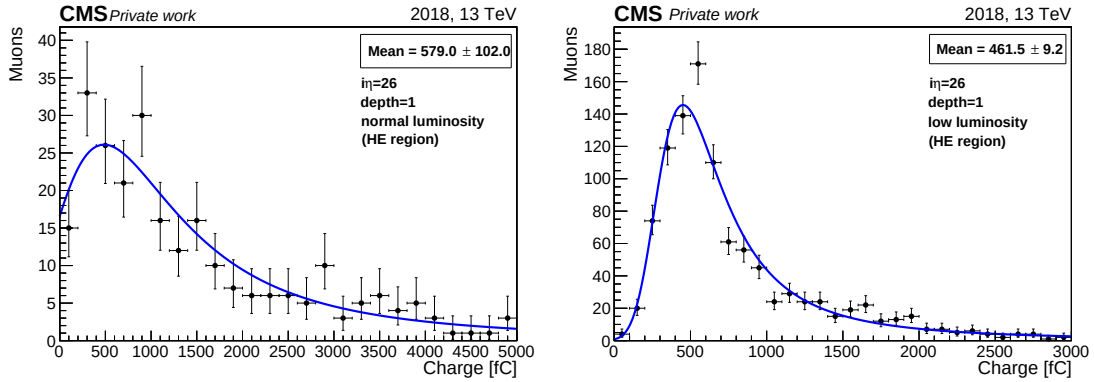

Figure 4.18: Charge distributions obtained from the normal luminosity (left) and low luminosity (right) runs in 2018. The smooth lines are results of fits to Gaussian convolved Landau functions.

luminosity runs for $i\eta = 26$ depth 1. The distributions are fitted with Gaussian convolved Landau functions to get the MPV of charge. As can be seen from these measurements, the low luminosity runs yield narrower distributions with sufficient accuracy than those from normal luminosity runs.

The MPV values, from normal luminosity and low luminosity run data, are compared for the most affected towers i.e. $i\eta$ tower 23 to 26, depth 1. As can be seen from the Figure 4.19 (left), the MPV values for $i\eta = 23$ and $i\eta = 24$ are in agreement for the two data whereas for $i\eta = 25$ and $i\eta = 26$, the low luminosity runs yield

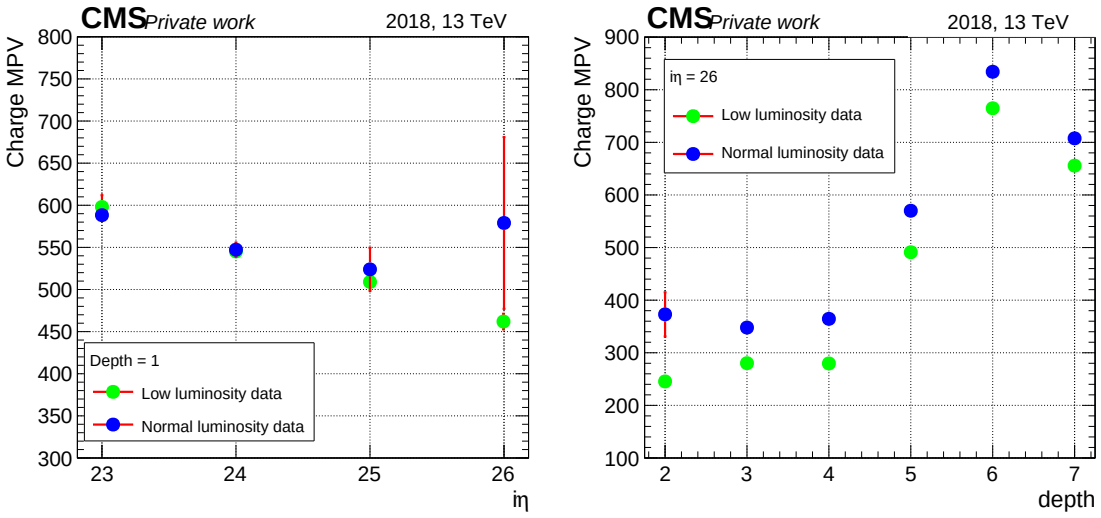

Figure 4.19: Comparison of MPV values for $i\eta = 23$ to 26, depth 1 (left) and $i\eta = 26$, depth 2 to 7 (right) from normal luminosity run data and low luminosity run data.

systematically lower values of MPV values with better precision. Similarly, the MPV values for all depths of $i\eta = 26$ are compared for the two sets of data as shown in Figure 4.19 (right). For a more careful examination of radiation damage, measurements need to be made with smaller systematic bias and hence runs with low luminosity are preferable for the estimation of level of radiation damage in the higher $i\eta$ region [27] during Run 3 which is starting in June, 2022.

Bibliography

[1] CMS Collaboration, "CMS Technical Design Report for the Phase 1 Upgrade of the Hadron Calorimeter", *CMS Technical Design Report* (9, 2012) doi:10.2172/1151651.

[2] CMS Collaboration, "HCAL performance from first collisions data", *CERN Document Server* (Jul, 2010).

[3] J. Freeman, "The CMS central hadron calorimeter", *AIP Conference Proceedings* **450** (1998) 462–473, doi:10.1063/1.56952, arXiv:https://aip.scitation.org/doi/pdf/10.1063/1.56952.

[4] CMS Collaboration, "CMS Physics: Technical Design Report Volume 1: Detector Performance and Software", *CERN Document Server* (2006).

[5] S. Banerjee, "Simulation Geometry for the CMS HCAL", technical report, CERN, Geneva, Sep, 2005.

[6] C. A. Fangmeier, "Measurement of the production cross section of four top quarks in proton-proton collisions at 13 TeV". PhD thesis, 2019. Presented 2019.

[7] CMS Collaboration, "Technical Proposal for the Phase-II Upgrade of the CMS Detector", *CMS Technical Design Report* (6, 2015).

[8] CMS Collaboration. https://cms-docdb.cern.ch/cgi-bin/DocDB/ShowDocument?docid=13342.

[9] CMS Collaboration, A. M. Sirunyan et al. https://twiki.cern.ch/twiki/bin/view/CMSPublic/LumiPublicResults.

[10] A. Ferrari, P. R. Sala, A. Fassò, and J. Ranft, "FLUKA: A multi-particle transport code (program version 2005)". CERN Yellow Reports: Monographs. CERN, Geneva, 2005. doi:10.5170/CERN-2005-010.

[11] T. Böhlen et al., "The FLUKA Code: Developments and Challenges for High Energy and Medical Applications", *Nuclear Data Sheets* **120** (2014) 211–214, doi:https://doi.org/10.1016/j.nds.2014.07.049.

[12] CMS Collaboration, "FLUKA particle flux maps for CMS Detector", *CERN Document Server* (Oct, 2013).

[13] T. Förster, "Zwischenmolekulare Energiewanderung und Fluoreszenz", *Annalen der Physik* **437** (1948) 55–75, doi:https://doi.org/10.1002/andp.19484370105.

[14] A. Belloni, "Radiation effects on plastic scintillators for current and future HEP experiments", 2018. https://indico.fnal.gov/event/18739/.

[15] K. Wick et al., "Recovery and dose rate dependence of radiation damage in scintillators, wavelength shifters and light guides", *Nuclear Instruments and Methods in Physics Research Section B: Beam Interactions with Materials and Atoms* **61** (1991) 472–486, doi:https://doi.org/10.1016/0168-583X(91)95325-8.

[16] A. Bross and A. Pla-Dalmau, "Radiation damage of plastic scintillators", *IEEE Transactions on Nuclear Science* **39** (1992) 1199–1204, doi:10.1109/23.173178.

[17] R. Clough et al., "Discoloration and subsequent recovery of optical polymers exposed to ionizing radiation", *Polymer Degradation and Stability* **49** (1995) 305–313, doi:https://doi.org/10.1016/0141-3910(95)87013-X.

[18] CMS Collaboration, "Measurements with silicon photomultipliers of dose-rate effects in the radiation damage of plastic scintillator tiles in the CMS hadron endcap calorimeter", *JINST* **15** (2020), no. 06, P06009, doi:10.1088/1748-0221/15/06/P06009, arXiv:2001.06553.

[19] CMS Collaboration, "The CMS hadron calorimeter project: Technical Design Report". Technical design report. CMS. CERN, Geneva, 1997.

[20] CMS Collaboration, "Dose rate effects in the radiation damage of the plastic scintillators of the CMS hadron endcap calorimeter", *Journal of Instrumentation* **11** (oct, 2016) T10004–T10004, doi:10.1088/1748-0221/11/10/t10004.

[21] CMS Collaboration, "CMS luminosity measurement for the 2018 data-taking period at $\sqrt{s} = 13$ TeV", technical report, CERN, Geneva, 2019.

[22] CMS Collaboration, "Particle-Flow Event Reconstruction in CMS and Performance for Jets, Taus, and MET", *CERN Document Server* (4, 2009).

[23] A. Sirunyan et al., "Particle-flow reconstruction and global event description with the CMS detector", *Journal of Instrumentation* **12** (Oct, 2017) P10003–P10003, doi:10.1088/1748-0221/12/10/p10003.

[24] CMS Collaboration, "Muon reconstruction and identification improvements for run-2 and first results with 2015 run data", CMS Detector Performance Summary CMS-DP-15-015, 2015.

[25] A. K. Virdi, S. Banerjee et al., "Study of Radiation Damage in the CMS Hadron Barrel Calorimeter using Isolated Muons from Collision Data", technical report, September, 2020. CMS DN-2020/042.

[26] A. K. Virdi, S. Banerjee et al., "Study of Radiation Damage in the CMS Hadron Endcap Calorimeter using Isolated Muons from Collision Data", technical report, August, 2021. CMS DN-2021/016.

[27] A. K. Virdi, S. Banerjee et al., "Issues in Studying Radiation Damage of the CMS Hadron Calorimeter using Isolated Muons in the 2018 Collision Data", technical report, September, 2020. CMS DN-2020/039.

Chapter 5

Search for a heavy neutral gauge boson using Vector Boson Fusion processes at $\sqrt{s} = 13\,\text{TeV}$

Many theories beyond the standard model (SM) of particle physics introduce new gauge fields and interactions in order to address the incompleteness of the SM. As discussed in Chapter 1, a common manifestation of these new gauge fields and interactions is heavy gauge bosons with TeV scale masses. One such heavy new gauge boson is the Z', which arises from extensions of the electroweak symmetry of the SM [1] [2]. Z' is a spin-1 heavy neutral gauge boson yet to be discovered. At the LHC, the ATLAS and CMS experiments have an extensive physics program to search for the Z'. A widely used model in these searches is the sequential standard model (SSM) [3], which predicts a spin-1 neutral gauge boson (Z'_{SSM}) with SM-like couplings. In these searches, Z' production via Drell-Yan (DY) processes [4] [5] is targeted i.e. $q\bar{q} \rightarrow Z' + 0j/1j$. These searches look for an excess in data over smoothly falling standard model backgrounds in the dilepton mass distributions. As discussed in Chapter 1, these searches have excluded the Z'_{SSM} below 5.15 TeV [6] by the CMS experiment and below 5.1 TeV [7] by the ATLAS experiment. In this Thesis, a new search for the Z' boson produced through vector boson fusion (VBF)

processes is presented. The distinct nature of the VBF production mechanism allows to distinguish between desired signal and SM background processes. Due to pure electroweak production of the Z' in the VBF processes, the QCD multijet background gets reduced significantly which has the high jet $\rightarrow \tau_h$ misidentification rates in the $Z' \rightarrow \tau\tau$ searches [8] [9].

In this search for the Z' produced through VBF processes, a "simplified phenomenological approach" is considered which is a modification to the traditionally used SSM Z' model. In this approach, the coupling of Z' to the SM weak bosons (Z or $W^{\pm}$) is allowed. This search also considers the model with enhanced Z' couplings to third-generation fermions motivated by the B-meson anomalies observed at LHCb, BaBar, and Belle experiments [10–13]. Extensions to the SM proposes an explanation for the high mass of the top quark and predicts Z' bosons that typically couple to third-generation fermions [14]. Therefore, the $Z' \rightarrow \tau\tau$ decay mode is considered. Additionally, since we assume the Z' couples to the SM vector bosons, then the $Z' \rightarrow WW$ decay width can be large, and thus motivates to re-interpret results for the $Z' \rightarrow WW$ decay.

In this Chapter, the studies for the search for $Z' \rightarrow \tau\tau$ (and $Z' \rightarrow WW$) with $\tau_\mu\tau_h$ and $\tau_e\tau_h$ final states are presented using the proton-proton collisions data at center-of-mass energy of 13 TeV, collected using the CMS detector during years 2016-2018, corresponding to an integrated luminosity of 27.4 fb^{-1}.

5.1 The Z' production via VBF mechanism

The signal process involves the production of Z' through fusion of two vector bosons radiated by the incoming partons of the colliding protons at the LHC. The Z' is produced in association with the two forward jets as shown in Figure 5.1. The two forward jets lie in the opposite hemisphere of the CMS detector and carry large dijet invariant mass. The dijet pair boosts the momentum of the Z' via conservation of momentum, helping to improve sensitivity in the search for heavy Z' [15].

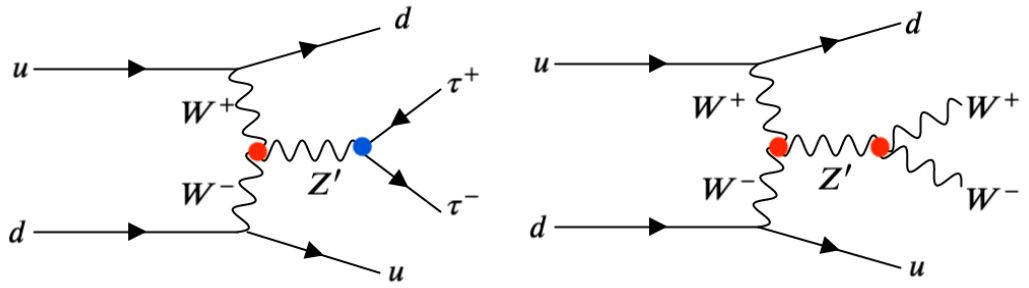

Figure 5.1: Feynman diagrams for the VBF production of Z' which further decays to $\tau^+\ \tau^-$ (left) and W^+W^- (right). The red dot shows the vertex for Z' coupling to bosons and the blue dot shows the vertex for Z' coupling to fermions.

The Z' further decays to $\tau^+\ \tau^-$ pairs or W^+W^- pairs. In case of $\tau^+\ \tau^-$ decay, one of the τ decays leptonically (either in a muon or an electron with corresponding neutrinos) and other τ decays hadronically (τ_h). In case of W^+W^- decay, one of the W decays to light leptons (e or μ) and the other W decays to τ which further decays hadronically or both Ws decay to $\tau^+\ \tau^-$ pairs which further decay to a light lepton and a hadronic tau with corresponding neutrinos. The whole decay chain is shown in Figure 5.2. The leptonic τ decays are indistinguishable from prompt production of electrons and muons. As a result, this search for Z' involves two final states for a pair of tau-leptons and W-bosons: (1) $\tau_\mu\tau_h$, (2) $\tau_e\tau_h$. The branching ratios for these final states are listed in Table 5.1.

Final State	Branching ratio (%)
$\tau\tau \to h\mu\nu_\tau\bar{\nu}_\tau\nu_\mu$	22.5
$\tau\tau \to he\nu_\tau\bar{\nu}_\tau\nu_e$	23.1
$WW \to (\tau\tau \to)h\mu\nu_\tau\bar{\nu}_\tau\nu_\mu$	2.1
$WW \to (\tau\tau \to)he\nu_\tau\bar{\nu}_\tau\nu_e$	2.2

Table 5.1: Branching ratios of $\tau\tau$ and WW decay modes.

At last, the final state consists of opposite sign μ and hadronic tau (τ_h) or e and hadronic tau (τ_h) , two forward jets and missing transverse energy (p_T^{miss}) due to neutrinos (ν_τ).

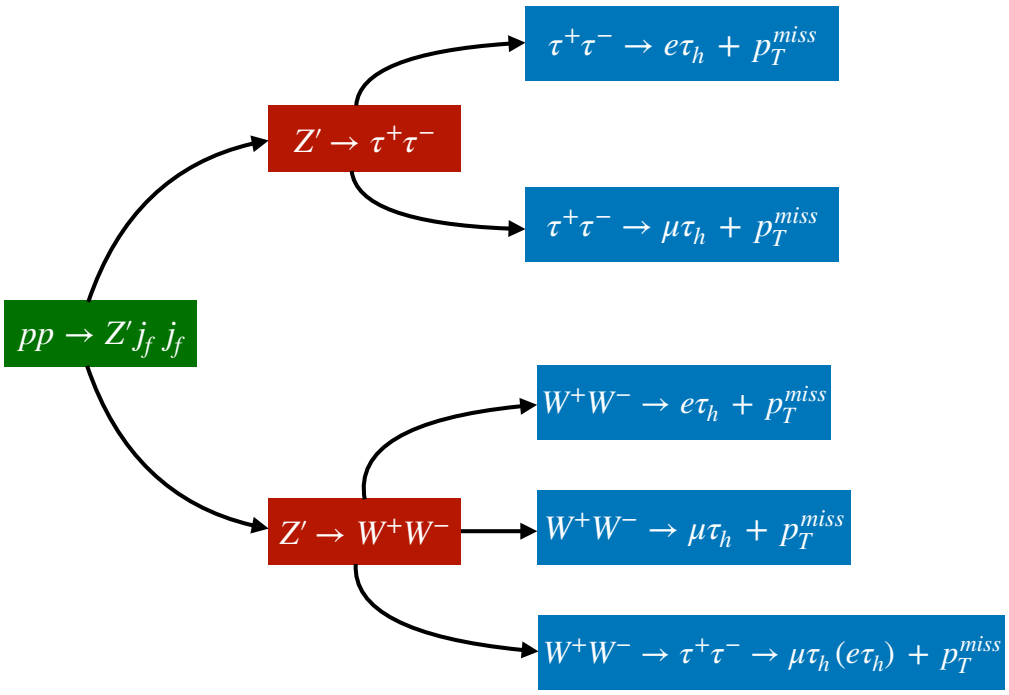

Figure 5.2: Signal process for Z' decaying to τ^+ τ^- pair and W^+W^- pair resulting to $\mu\tau_h$+p_T^{miss} and $e\tau_h$+p_T^{miss} final state.

5.2 Background Processes

The signal process consists of $\mu\tau_h$ and $e\tau_h$ as final visible objects. There are several SM processes which give the same signature as the Z' signal in the detector and act as a *background*. The details of such background processes contributing in this search are discussed below.

- **W+jets background:** W boson produced in association with the jets can mimic the VBF signal process. A true light lepton (a muon or an electron) from the decay of W boson can easily mimic the light lepton in the signal. The associated jets can be easily misidentified as hadronic taus and VBF jets. There is also a possibility, although very small, of a jet to be misidentified as a light lepton. In this case, the tau lepton from the W boson decays hadronically giving the same signature as the signal. One of the production mechanism of W boson in association with 3 jets is shown in Figure 5.3 (left).

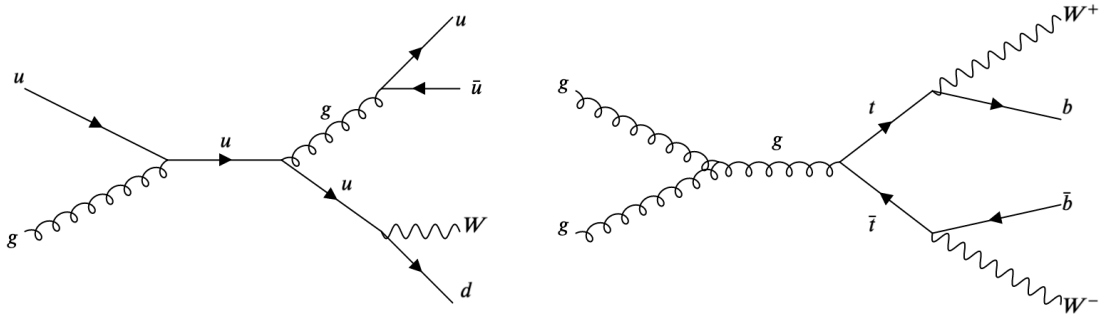

Figure 5.3: Production mechanism for W + 3 jet process (left) and $t\bar{t}$ process (right).

- ***$t\bar{t}$* background:** The top quark (antiquark) decays primarily into a bottom quark (antiquark) and a W boson as shown in Figure 5.3 (right). The electron or muon from one of the W bosons gives the same signature as the signal electron or muon. The hadronic tau from the other W boson gives the same signature as the signal hadronic taus. The jets from the hadronic decay of W boson can also be misidentified as hadronic taus.

- **QCD multijet background:** Due to large cross-section of QCD multijet process at hadron colliders, it is hard to control the contribution of QCD multijet processes faking the signal process. The scenario gets worse if the final states consist of hadronically decaying tau leptons. The quark and gluon jets are easily misidentified as the τ_h jet. Figure 5.4 (left) represents QCD 4 + jet process where one jet can be misidentified as the hadronic tau and the other is misidentified as the light lepton. There are two additional forward jets which can be misidentified as the VBF jets.

- **Z+jets (DY+jets) background:** The $\tau\tau$ decay of Z boson can give the same signature as the $\tau\tau$ decay of Z'. There is also a possibility that Z boson decays to $\mu\mu$ or ee where it mimics one of the signal light leptons and one of the jets can be misidentified as the hadronic tau. Additionally, the jets associated with the Z boson can be tagged as the VBF jets. Figure 5.4 (right) shows one of the production mechanism of Z + 2 jet process with 2 jets mimicking the VBF jets in the signal process while the taus from Z decay can mimic the

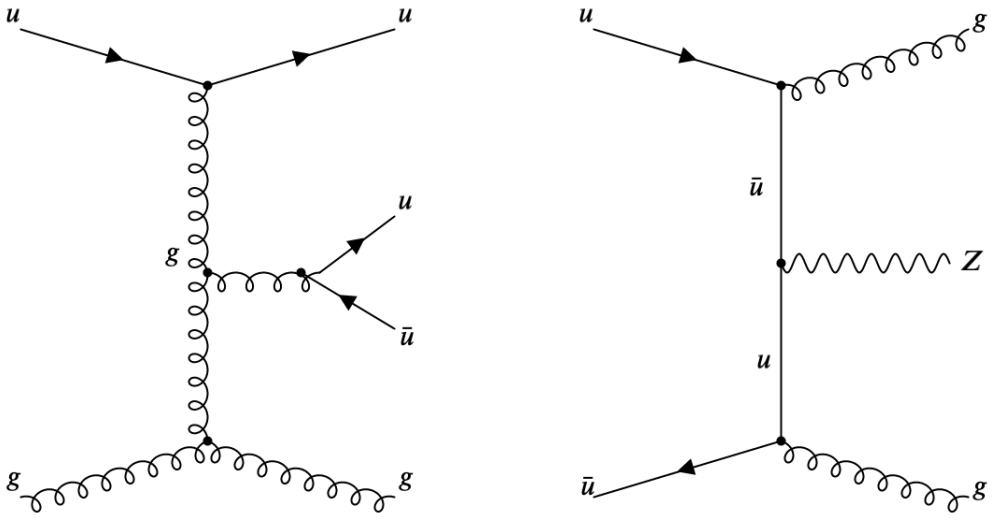

Figure 5.4: Production mechanism for QCD + 4 jet process (left) and Z + 2 jet process (right).

signal.

- **Diboson background:** The taus from the decay of the weak bosons (ZZ, WZ, WW) gives the same signature as the signal by further decaying to light leptons and a hadronic tau. The associated jets or the hadronic decay of the weak boson can give the signatures of VBF jets. Figure 5.5 shows one of the production mechanism of the WZ (left) and ZZ in association with 2 jets (right).

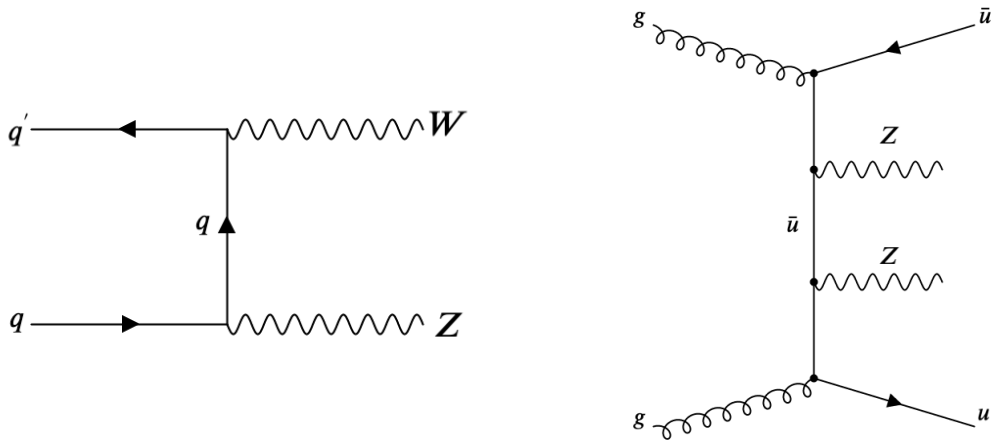

Figure 5.5: Production mechanism for diboson process.

- **Single top background:** In the single top production via t-channel, the W boson from the top quark decay can decay to light leptons and the b jet can be misidentified as the hadronic tau in the signal. In the tW associated production with the initial gluon splitting, the W bosons can decay to light leptons and a hadronic tau. The associated jets can give the signature of the VBF jets. Figure 5.6 shows the Feynman diagram for the production of single top in t-channel (left) and tW-channel (right).

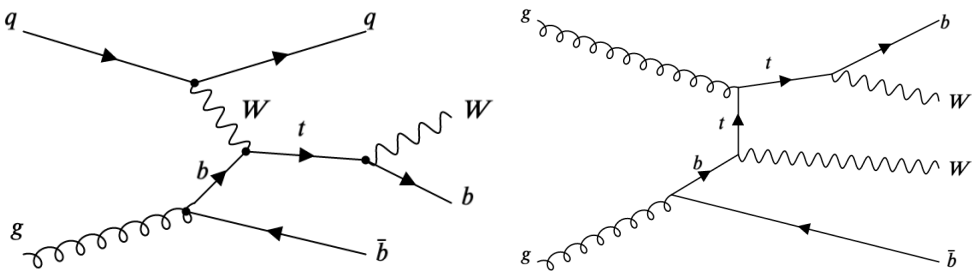

Figure 5.6: Production mechanism for Single top process.

- **VBF Higgs background:** The processes in which the Higgs boson is produced in association with two forward jets generally mimic the signal processes as shown in Figure 5.7. However, the forward jets are less energetic as compared to the signal process since mass of the SM Higgs boson is significantly lower than the masses of Z' under consideration. However, the $\tau\ \tau$ decay of Higgs boson can give the same signature as the $\tau\tau$ decay of Z'.

- **Electroweak WWjj and Zjj background:** The pure electroweak production of WW and Z with forward jets can easily mimic the signal process as shown in Figure 5.8. The leptons coming from the decay of W or Z boson give the same signature as the signal leptons along with VBF jets.

The contribution of these background processes is evaluated using simulated samples and the data driven methods.

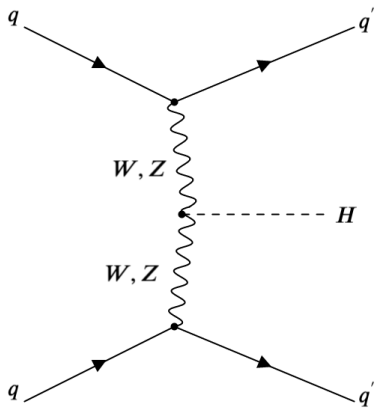

Figure 5.7: Production mechanism for VBF Higgs process.

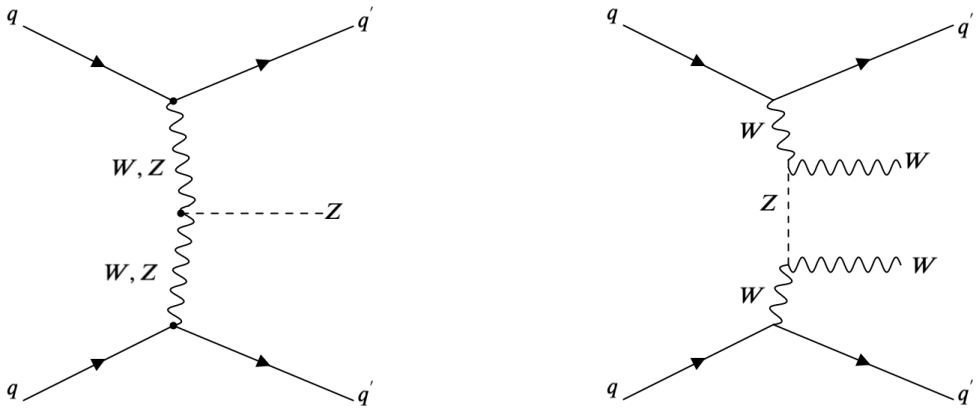

Figure 5.8: Production mechanism for SM electroweak processes with forward jets, Zjj (left) and WWjj (right).

5.3 Data and Monte Carlo samples

The present analysis uses the *pp* collisions data at the center-of-mass energy of 13 TeV, collected by the CMS detector during the years 2016-2018. The final results are measured with the 20% of the total data, which corresponds to an integrated luminosity of 27.4 fb^{-1}, as per the partial unblinding policy followed at the time of the Thesis writing.

The MC simulation samples for the signal and different contributing backgrounds are generated using different event generators for optimizing and validating the event selection criteria, estimating the part of backgrounds and calculating the

systematic uncertainties.

The VBF Z' signal samples are generated with MadGraph5_aMC@NLO version 2.4.2 [16] (denoted as MG5_aMC) along with pythia8 [17] for parton showering and hadronization. The signal events are required to consist of partons with $p_T >$ 20 GeV having a pseudorapidity gap of $|\Delta\eta| > 3.0$ between them. The samples are required to have no contribution from QCD vertex. For the search of Z' for a wide range of phase space, the samples for Z' masses 250 GeV to 2500 GeV are generated i.e. for $m_{Z'} = 250, 500, ...2500$ GeV. To study the coupling of Z' with vector bosons ($V = W\,or\,Z$), the samples are generated with five coupling points i.e. $\kappa_V = 0.1$, 0.25, 0.50, 0.75 and 1.0. To consider the models motivated by the B meson anomalies and for possible explanation for the high mass of the top quark, there is strong motivation to consider non-universal gauge couplings. To parameterize this possibility, couplings to light fermions (g_ℓ) and heavy fermions (g_h) are introduced. Two set of samples with scenarios of universal coupling to fermions ($g_\ell = g_h = 1$) and non-universal coupling to fermions ($g_\ell = 0$, $g_h = 1$) are generated. The theoretically predicted values for the production cross-section of Z' for different mass values at center-of-mass energy of 13 TeV is given in Table 5.2.

$m_{Z'}$ [GeV]	Production cross-section [pb]
250	119.2
500	5.365
750	0.8273
1000	0.1994
1250	0.06114
1500	0.02174
1750	0.008568
2000	0.003596
2250	0.001609
2500	0.0007504

Table 5.2: Production cross-section of Z' for various mass points.

The background samples for Z+jets, W+jets and QCD multijet process are generated with MadGraph5_aMC@NLO version 2.4.2 interfaced with pythia8 utilizing the FxFx merging scheme. For better reconstruction of background in the

Process	Generator	cross-section [pb]
Z→ $\ell\ell$ + 4 jets	MG5_aMC	6025.2
Z→ $\ell\ell$ + 4 jets (HT=100 to 200)	MG5_aMC	213.4
Z→ $\ell\ell$ + 4 jets (HT=200 to 400)	MG5_aMC	65.42
Z→ $\ell\ell$ + 4 jets (HT=400 to 600)	MG5_aMC	7.31
Z→ $\ell\ell$ + 4 jets (HT=600 to 800)	MG5_aMC	1.49
Z→ $\ell\ell$ + 4 jets (HT=800 to 1200)	MG5_aMC	0.661
Z→ $\ell\ell$ + 4 jets (HT=1200 to 2500)	MG5_aMC	0.119
Z→ $\ell\ell$ + 4 jets (HT=2500 to Inf)	MG5_aMC	0.0028
W→ $\ell\nu$ + 4 jets	MG5_aMC	61334.0
W→ $\ell\nu$ + 4 jets (HT=100 to 200)	MG5_aMC	1695.0
W→ $\ell\nu$ + 4 jets (HT=200 to 400)	MG5_aMC	532.40
W→ $\ell\nu$ + 4 jets (HT=400 to 600)	MG5_aMC	61.600
W→ $\ell\nu$ + 4 jets (HT=600 to 800)	MG5_aMC	12.400
W→ $\ell\nu$ + 4 jets (HT=800 to 1200)	MG5_aMC	5.7700
W→ $\ell\nu$ + 4 jets (HT=1200 to 2500)	MG5_aMC	1.0230
W→ $\ell\nu$ + 4 jets (HT=2500 to Inf)	MG5_aMC	0.0248
QCD_HT50to100	MG5_aMC	246300000.0
QCD_HT100to200	MG5_aMC	27990000.00
QCD_HT200to300	MG5_aMC	1559000.00
QCD_HT300to500	MG5_aMC	351900.00
QCD_HT500to700	MG5_aMC	29070.00
QCD_HT700to1000	MG5_aMC	5962.00
QCD_HT1500to2000	MG5_aMC	1005.00
QCD_HT2000toInf	MG5_aMC	101.80
QCD_HT50to100	MG5_aMC	20.54
TTtoHadronic	POWHEG	377.96
TTtoSemileptonic	POWHEG	365.34
TTto2L2Nu	POWHEG	88.29
ST_t-channel_top_4f	POWHEG	136.02
ST_t-channel_antitop_4f	POWHEG	80.95
ST_tW-channel_top_5f	POWHEG	38.06
ST_tW-channel_antitop_5f	POWHEG	38.06
ST_s-channel_top_4f	POWHEG	3.68
WW→ $2\ell 2\nu$+jets	POWHEG	10.480
WZ ($to2q2\nu$)	MG5_aMC	5.6060
WZ ($to3\ell\nu$)	MG5_aMC	3.0540
ZZ ($to2q2\nu$)	MG5_aMC	4.0330
ZZ ($to2\ell2\nu$)	POWHEG	0.5644
ZZ ($to2\ell2q$)	MG5_aMC	3.2220
ZZ ($\to 4\ell$)	MG5_aMC	1.2560
VBF_HToZZTo4L	POWHEG	0.0010102
VBFHToBB	POWHEG	2.183
GluGluHToZZTo4L	POWHEG	0.0129763
ZH_HToBB_ZToLL	POWHEG	0.311
ttH_HToZZ_4L	POWHEG	0.0002361

Table 5.3: List of MC simulated samples for different backgrounds.

high mass region, these samples are generated for entire H_T range (i.e. scalar sum of transverse momentum of all final state objects), concatenating samples in different H_T bins as listed in Table 5.3.

Top quark-antiquark pair ($t\bar{t}$) production is generated by POWHEG interfaced with PYTHIA8, simulating the parton shower and the hadronization processes. The diboson (WW, WZ, ZZ) background processes are simulated using MADGRAPH5_AMC@NLO and PYTHIA8 while POWHEG is used for the simulation of the single top quark processes. Table 5.3 lists the various background samples and their corresponding production cross-sections used in the analysis.

The simulated samples are processed with a detailed simulation of the CMS detector using the GEANT4 framework [18] and trigger emulation.As there are more than one interaction take place from colliding proton bunches, these additional interactions are known as *pileup* as discussed in Chapter 2. The pileup information in MC is simulated using minimum bias events by concatenating them with the generated signal event. However, the MC simulated samples consist of the pileup distribution which does not match with data as shown in Figure 5.9. Hence, MC events need to be properly weighted to match with the pileup distribution in data. The reweighing of MC events is performed by determining the probabilities to obtain "n" true interactions in data ($P_{data}(n)$) and MC ($P_{MC}(n)$). The event weights are calculated to reweigh MC events based on the true number of interactions according to the following equation.

$$w_{PU}(n) = \frac{P_{data}(n)}{P_{MC}(n)} \tag{5.1}$$

The pileup weights are calculated for individual years due to different run conditions per year. As shown in Figure 5.9, after reweighing the pileup information in MC samples matches well with data.

The event yield for MC simulated samples are normalized to their respective production cross-section (σ) and total luminosity (L) of the collision data using a

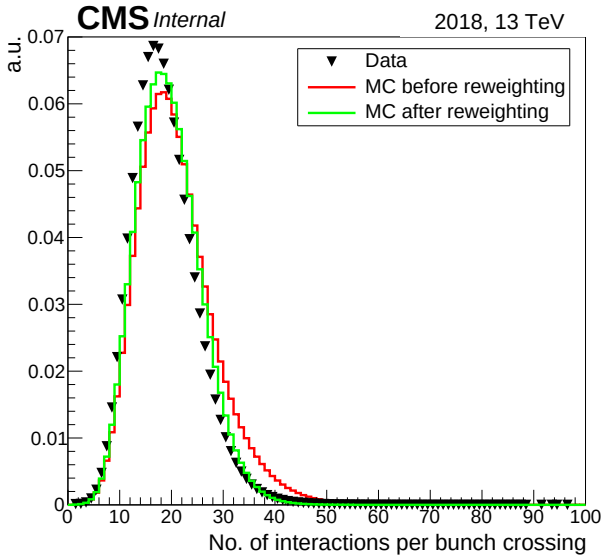

Figure 5.9: Distribution of number of pile-up interactions in a Summer16 MC sample ($Z \rightarrow \mu\mu$) before and after reweighing. The pile-up distribution in collision data is also overlayed. The pile-up distribution in MC matches with the distribution in the collision data after pile-up reweighting is applied.

weight factor (w) which is calculated as:

$$w = \frac{\sigma.L}{N} \tag{5.2}$$

Here, N represents the total number of MC simulated events for the corresponding process. The simulated samples are generated for three years (2016, 2017 and 2018) and are studied for individual years. A set of selection criteria is followed each year for better selection of signal events and suppression of background events which is discussed in the following Section.

5.4 Event Selection

The VBF Z' signal process in the detector consist of centrally produced one light lepton (μ or e) and one hadronic τ jet (τ_h) having opposite sign (OS) with two forward jets and missing transverse energy due to neutrinos. The two forward jets lie in the opposite hemispheres of the detector with large pseudorapidity gap between

them and carry large dijet invariant mass. As mentioned in Section 5.2, various SM processes give the similar final state as the VBF Z' signal process. Therefore, an appropriate event selection criteria is required to select most of the signal events with efficient rejection of background events. The event selection criteria for selecting signal events is divided into three parts: trigger selection, central event selections, and VBF event selection. These selections criteria are discussed below.

5.4.1 Trigger Selection

The trigger selection aims to select interesting events with software level selections using all information from the subdetectors. The events which passes the single muon trigger in the $\mu\tau_h$ final state and the single electron trigger in the $e\tau_h$ final state are selected. The HLT trigger paths used in the analysis are listed in Table 5.4. Each of the single muon triggers requires the events to contain at least one muon candidate with p_T greater than 24 GeV or 27 GeV in the respective years. Similarly, in case of the single electron trigger, the events are required to have one electron candidate with p_T greater than 27 GeV or 32 GeV or 35 GeV in the respective years [19].

Year	Channel	HLT Path	p_T threshold
2016	$\mu\tau_h$	HLT_IsoMu24_v*	$>$ 24 GeV
	$e\tau_h$	HLT_Ele27_WPTight_Gsf_v*	$>$ 27 GeV
2017	$\mu\tau_h$	HLT_IsoMu27_v*	$>$ 27 GeV
	$e\tau_h$	HLT_Ele35_WPTight_Gsf_v*	$>$ 35 GeV
2018	$\mu\tau_h$	HLT_IsoMu24(27)_v*	$>$ 24 (or 27) GeV
	$e\tau_h$	HLT_Ele32(35)_WPTight Gsf_v*	$>$ 32 (or 35) GeV

Table 5.4: HLT trigger paths and their p_T thresholds used in the analysis.

The efficiency of the single muon trigger and single electron trigger in data is studied using tag and probe method with $Z \to \mu\mu$ events and $Z \to ee$ events respectively [20]. Figure 5.10 (left) shows the efficiency of HLT_IsoMu24 trigger in 2018. As can be seen from the figure, the trigger efficiency is greater than 90% above muon p_T (p_T^μ) of 30 GeV. The offline p_T^μ threshold for the analysis is chosen to be 35 GeV which sits well on the plateau of the trigger efficiency curve. Similarly,

Figure 5.10 (right) shows the efficiency for HLT_Ele35_WPTight_Gsf trigger in 2018. The efficiency is observed to be greater than 80% for electron p_T (p_T^e) above 55 GeV and is chosen to be the offline p_T^e threshold in the analysis. Small drop in the efficiency can be seen for barrel-endcap transition region in ECAL around $1.44 < |\eta| < 1.56$. The events falling in this region are excluded from the analysis. Since the efficiency of these triggers is observed to be consistent for 2016, 2017 and 2018, therefore, similar offline p_T threshold are chosen for the light leptons for the three years.

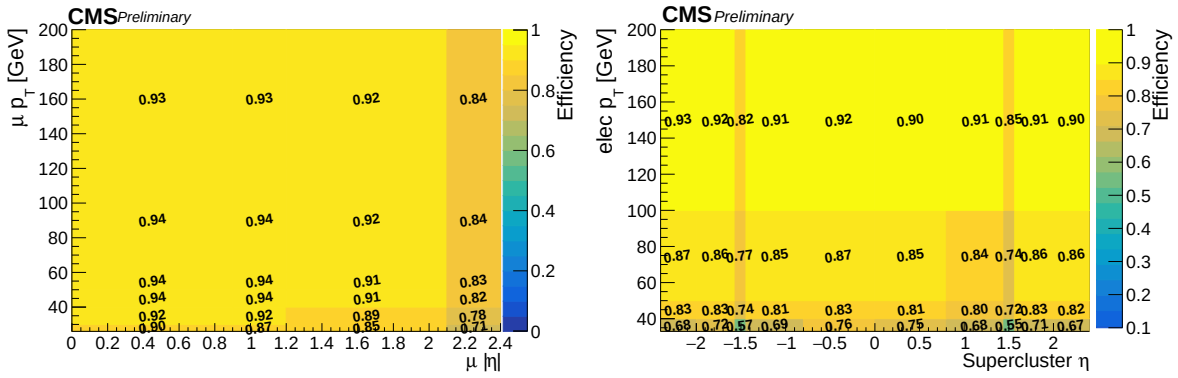

Figure 5.10: Trigger efficiency in data for single muon trigger as a function of p_T^μ and η^μ (left) and single electron trigger as function of p_T^e and η^e (right).

5.4.2 Central Event Selections

The central event selections aim to select events with OS $\mu\tau_h$ or $e\tau_h$ pairs along with the requirement of missing transverse energy. The central event selections are composed of following requirements:

- **Muon Selection:** Muons considered in the analysis are required to be well isolated and are required to have minimal energy from PF neutral and charged candidates in a cone of $\Delta R = 0.4$ around the muon trajectory. To isolate muons from the jets and the semileptonic decays of heavy quarks are suppressed by applying an isolation condition on the muon candidates. The rela-

tive isolation variable, I_{rel} for muons is defined as :

$$I_{rel} = \frac{[\sum p_T^{charged} + max(0., \sum E_T^{neutral} + \sum E_T^{\gamma} - 0.5 \sum p_T^{PU})]}{p_T^{\mu}} \quad (5.3)$$

Here, $\sum E_T^{neutral}$ and $\sum E_T^{\gamma}$ represent the scalar sum of the transverse energies of neutral hadrons and photons, respectively, within a cone of radius, $\Delta R = 0.4$ around the muon track. The quantity $\sum p_T^{charged}$ represents the p_T sum of the charged hadrons in the same cone around the muon associated with the selected vertex. Finally, $\sum p_T^{PU}$ is the p_T sum of the charged hadrons in the same cone around the muon not associated with the selected vertex. A muon is considered isolated if $I_{rel} < 0.15$. A "Tight" muon identification is used [21] which requires muon to be a global muon with hits in at least two muon stations. Besides this, the identification requires valid muon hits in the pixel tracker and hits in greater than five inner tracker layers. To suppress hadronic punch-through and muons from decays in flights, an additional requirement on the χ^2/dof for the global muon track fit to be less than 10 is added. Contamination due to Cosmic muons is suppressed by requiring the threshold on the impact parameter (d_{xy}) to be less than 2 mm w.r.t primary vertex. Furthermore, longitudinal distance (d_z) of the tracker track wrt. the primary vertex is required to be less than 5 mm.

Events are required to have exactly one muon candidate with $p_T > 35$ GeV in $|\eta| < 2.1$ in the $\mu\tau_h$ final state. The selected muon candidates are required to be well-separated from other objects in the event within cone of $\Delta R = 0.4$.

- **Electron Selection:** The selection of the electron candidates requires good geometrical matching and good agreement between the momentum of the track and the energy of the ECAL supercluster. Two quantities used to estimate the geometrical matching are $\Delta\eta_{in} = \eta_{sc} - \eta_{vertex}^{Track}$ and $\Delta\phi_{in} = \phi_{sc} - \phi_{vertex}^{Track}$. The η_{sc} and ϕ_{sc} coordinates correspond to the supercluster position and are measured using an energy weighted algorithm. The η_{vertex}^{Track} and ϕ_{vertex}^{Track} coordinates are the position of the track at the interaction vertex extrapolated, as a

perfect helix, to the ECAL detector. The good energy-momentum matching is measured by taking the ratio between the corrected energy E_{corr} in the ECAL supercluster and the momentum of the track P_{in} measured in the inner layers of the tracker. Electrons need to be within the acceptance of the tracker and the electromagnetic calorimeter, $|\eta_{sc}| < 1.44$ and $1.56 < |\eta_{sc}| < 2.1$, where the upper threshold on $|\eta_{sc}|$ is chosen based on trigger threshold and best signal significance. Signal electrons or electrons from photon conversion are separated further from misidentified jets through cuts on calorimetric variables such as the shower shape variable $\sigma_{i\eta i\eta}$, which describes the lateral extension of the shower along η. In contrast to hadronic showers, electromagnetic showers are narrower, thus making shower shape variables an effective discriminant. The ratio of energy deposited in the hadronic and the electromagnetic calorimeter is a measure for the energy leakage into the hadronic calorimeter and is typically small for electromagnetic showers. It is required to be smaller than 0.12 (0.10) in the barrel (endcaps).

Furthermore, electrons originating from converted photons are rejected by a number of cuts. The impact parameter D^{vertex} in the transverse distance xy and longitudinal distance z of closest approach of the track trajectory to the selected primary vertex need to be less than 0.2 mm and 2 mm respectively. Additionally, for prompt electrons the number of missing hits in the innermost layers of the tracker should not exceed one. A separation from other objects in the event is assured by requesting electrons to have a loose particle flow isolation. The energy deposition from other particle flow objects in a cone of $\Delta R = 0.3$ around the selected electron should be less than 15% of the electrons transverse momentum p_T [22].

Events are required to have exactly one electron candidate with $p_T > 55$ GeV in $|\eta| < 2.1$ in the $e\tau_h$ final state. The selected electron candidates are required to be well-separated from other objects in the event within cone of $\Delta R = 0.4$.

- **Tau Selection:** The taus are required to be well identified and isolated to

reduce the probability of gluon and quark jets or leptons (e or μ) to be misidentified as the hadronic tau (τ_h) candidates. Hence, for the proper identification of genuine τ_h candidates, the τ_h candidates are required to pass through a set of discriminators as discussed in Chapter 3. The selection criteria for these discriminators used in the analysis are discussed below.

- **Tau Decay Mode Reconstruction:** The τ_h candidates are selected using deep neural network (DNN) based algorithm [23]. This algorithm reconstructs one-prong, two-prong and three-prong τ_h candidates. There are no actual two-prong τ_h candidates due to conservation of tau lepton charge. The algorithm tends to reconstruct two-prong τ_h candidates due to very high p_T of the tau lepton. In this case, their visible decay products have sufficient boost, producing very collimated tracks and thus overlapping tracker hits (merged tracks), which makes it difficult to efficiently reconstruct the three-prong τ_h candidates . Therefore, the τ_h candidates with two-prongs attempt to recover some of the inefficiency for identifying three-prong high-p_T tau leptons. However, the two-prong τ_h candidates are not utilized in this analysis due to the large jet background as jets can primarily be reconstructed as two-prong τ_h candidates. Hence, τ_h candidates having one or three-prongs are considered in this analysis.
- **Rejection against muons:** To reject the muons faking the τ_h candidates, a DNN based anti-muon discriminator is used in the analysis. This discriminator searches for the muon hits in the muon subsystems, which are associated to the track of the τ_h candidates [24] [23]. Due to the presence of the signal muons in the $\mu\tau_h$, a tight selection on this discriminator is applied which has τ_h selection efficiency of 99.5%. For high signal acceptance in the $e\tau_h$ final state, a slightly looser selection on this discriminator, with τ_h identification efficiency of 99.95%, is applied to avoid the rejection of genuine τ_h candidates as there are no signal muons in this final state which can be misidentified as the τ_h candidate.

- **Rejection against electrons:** In order to discriminate genuine τ_h candidates against electrons, τ_h candidates are required to pass a DNN based anti-electron discriminator which uses the amount of HCAL energy associated to the tau track with respect to the measured momentum of the track [23]. The discriminator considers the amount of electromagnetic energy in a narrow strip around the leading tau track with respect to the total electromagnetic energy of the tau. For better background rejection of misidentified τ_h candidates in the $e\tau_h$ final state, a tight selection on the discriminator is used which has the τ_h identification efficiency of 60%. In case of $\mu\tau_h$ final state, a looser selection is applied with τ_h identification efficiency of 99% to avoid rejection of the genuine τ_h candidates.
- **Rejection against jets:** To reject gluon and quark jets to be misidentified as the τ_h candidates, the τ_h are selected with a tight selection on the DNN based anti-jet discriminator [23]. The discriminator uses the lifetime and jet multiplicity information to distinguish between quark or gluon jets from the genuine τ_h candidates. The τ_h identification efficiency of this discriminator is 50% for τ_h $p_T < 100\,\text{GeV}$ and increases to 60% for $p_T > 100\,\text{GeV}$ [23].

After selecting τ_h candidates with selections mentioned above, the τ_h candidates used in the analysis are required to have $p_T > 20\,\text{GeV}$ with $|\eta| < 2.1$. The τ_h candidates are well-separated from other objects in the event by making a selection on the ΔR to be greater than 0.4.

- **b jet tagging and rejection:** As there are no jets from the b quark in the VBF Z' production, the selected events are required to have no b-tagged jet. The b tagging is performed using the combined secondary vertex b tagging algorithm in 2016 and DNN based combined secondary vertex b tagging algorithm in 2017 and 2018 [25] [26]. The jets, with $p_T > 30\,\text{GeV}$ within $|\eta| < 2.4$ and well-separated from light leptons and τ_h candidates with $\Delta R = 0.3$, are searched for the b-tagged jets. The event with a b-tagged jet is removed from

further analysis. This requirement suppresses the contribution of events from top quark decays from processes such as $t\bar{t}$ and single top which contains a genuine b quark jet.

- $\boldsymbol{E_T^{miss}}$ **requirement:** As discussed in Section 5.1, the signal contains neutrinos which go undetected in the detector and contributes to missing transverse energy (E_T^{miss}). Hence, a requirement is set on the E_T^{miss} to be greater than 30 GeV. This requirement significantly reduces the contribution of QCD multijet and Z+jets background events.

5.4.3 VBF Event Selections

The VBF event selections are meant to select the events having at least two jets satisfying the VBF requirements from the events passing the trigger and central selections. The VBF event selections are applied to select the signal events which are discussed as below:

- The jets are clustered using the anti-k_{T} algorithm [27], with a distance parameter of $R = 0.4$. For the identification of jets in an event, a PF - based jet identification is applied. Table 5.5 shows the jet selection criteria used in 2016 and 2017/2018. The jet identification efficiency is observed to be >99% for the entire η and p_T range. The events are then required to have at least two jets with $p_T > 30$ GeV in $|\eta| < 5.0$.

Selection	Cut (2016)	Cut (2017 and 2018)
Neutral Hadron Fraction	< 0.99	< 0.90
Neutral EM Fraction	< 0.99	< 0.90
Number of Constituents	> 1	> 1
And for $\|\eta\| < 2.4$ in addition apply		
Charged Hadron Fraction	> 0	> 0
Charged Multiplicity	> 0	> 0
Charged EM Fraction	< 0.99	< 0.99

Table 5.5: Jet identification criteria in 2016 and 2017/2018.

- The jets are chosen to be well-separated from the other objects within a cone of $\Delta R = 0.4$.

- The selected jets are required to be in the opposite hemisphere of the CMS detector i.e. $\eta_{j1} \times \eta_{j2} < 0$. The jets should have large pseudorapidity gap ($\Delta\eta > 4.2$) between them [19].

The jets in the VBF Z' signal process are highly energetic as the VBF system is required to have enough energy to produce high mass Z'. Figure 5.11 shows the dijet invariant mass distribution (left) and pseudorapidity distribution of the jets (right) for major contribution backgrounds such as W+jets and $t\bar{t}$ and the signal process involving production of Z' with mass 1000 GeV. As expected, the jets in the background are mostly central and have small dijet invariant mass, while signal events are characterized by non-central jets with large dijet invariant mass.

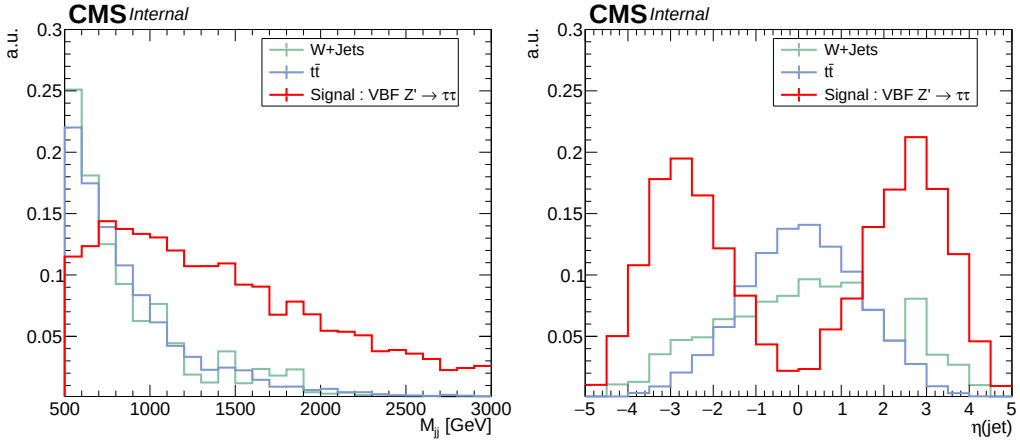

Figure 5.11: Comparison of dijet invariant mass $M(j_1, j_2)$ (left) and pseudorapidity of jets (η_{jets}) (right) distributions for signal and background processes.

As the signal has large dijet invariant mass, the events having $m(j_1, j_2) > 500$ GeV are selected to reject the background events. Table 5.6 shows the central and VBF event selection criteria used in the signal region.

After above selections, the mass of the lepton pairs ($\mu\tau_h$ or $e\tau_h$) is scanned to look for any excess above the SM backgrounds. The mass of the lepton pairs is

Trigger selection	
Isolated single μ (e)	year-dependent p_T threshold (Table [5.4])
Central event selections	
$N(\ell)$, $N(\tau_h)$	$= 1$
$\lvert\eta(\ell)\rvert$, $\lvert\eta(\tau_h)\rvert$	< 2.1
$Q(\ell) * Q(\tau_h)$	< 0
$p_{\mathrm{T}}(\mu(or\, e))$	$\geq 35(or\, 55)\,\mathrm{GeV}$
$p_{\mathrm{T}}(\tau_h)$	$\geq 20\,\mathrm{GeV}$
$E_{\mathrm{T}}^{\mathrm{miss}}$	$\geq 30\,\mathrm{GeV}$
$N(\mathrm{b-jet})$	$= 0$
VBF event selections	
$N(j)$	≥ 2
$p_{\mathrm{T}}(j)$	$\geq 30\,\mathrm{GeV}$
$\lvert\eta(j)\rvert$	< 5.0
$N(\mathrm{dijet})$	≥ 1
$\eta_{j1} \times \eta_{j2}$	< 0
$\Delta\eta(jj)$	> 4.2
$m(jj)$	$> 500\,\mathrm{GeV}$

Table 5.6: Event selection criteria for the $\ell\tau_h$ final state.

given as follows:

$$m(\ell_1, \ell_2, E_T^{miss}) = \sqrt{(E_{\ell_1} + E_{\ell_2} + E_T^{miss})^2 - (\vec{p}_{\ell_1} + \vec{p}_{\ell_2} + \vec{p}_T^{miss})^2} \tag{5.4}$$

where ℓ_1 is either a muon or an electron and ℓ_2 is hadronic tau. E_{ℓ_1} and E_{ℓ_2} is the energy of ℓ_1 and ℓ_2 respectively. p_{ℓ_1} and p_{ℓ_2} is the momentum of ℓ_1 and ℓ_2 respectively.

Different backgrounds after the signal selections : Although the signal event selections are optimized to suppress the SM background processes, still various SM processes pass these selections. Figure 5.12 shows the various SM processes (taken from their MC simulations), acting as backgrounds in the $\mu\tau_h$ final state (left) and the $e\tau_h$ final state (right). The dominant background contributing in both the final states is the jet $\rightarrow$ fake τ_h background, originating mainly from W+jets and $t\bar{t}$ processes. The VBF selections significantly suppress the contribution of QCD mul-

tijet background, which otherwise have large contribution in the searches involving τ_h candidates. The second major contribution comes from $t\bar{t}$ fully leptonic decays. Very small contribution comes from the processes involving genuine (or prompt) τ_h candidate. Since the jet $\rightarrow$ fake τ_h background is not well-modeled in the MC simulations, therefore, a dedicated data-driven method is used to estimate its contribution. A detailed description on the estimation of this major background and other backgrounds is given in the next Section.

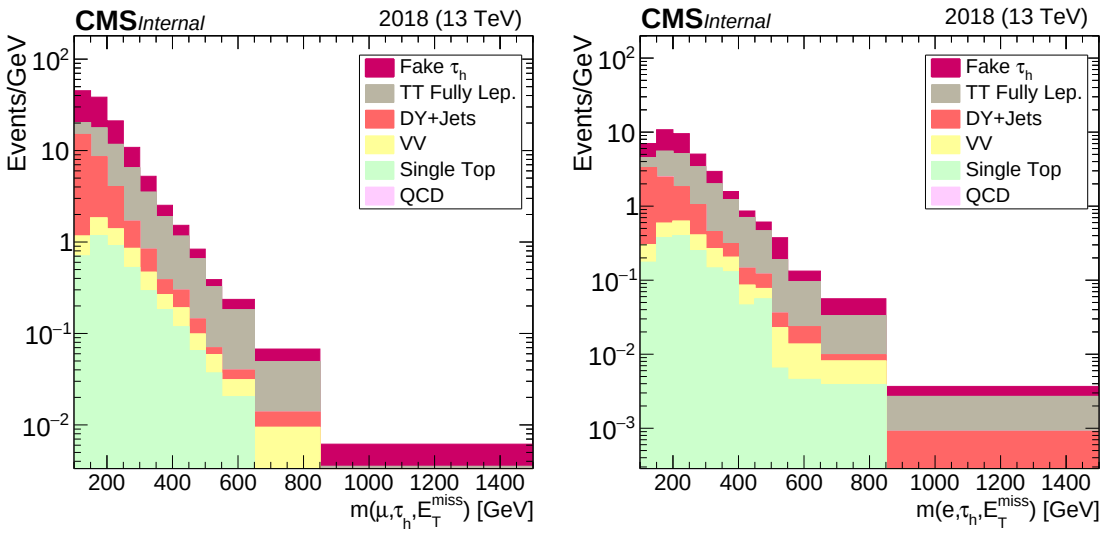

Figure 5.12: Various SM processes acting as a background in the $\mu\tau_h$ final state (left) and the $e\tau_h$ final state (right). These background events are taken from their respective MC simulations.

5.5 Background Estimation

As can be seen from Figure 5.12, the largest background contribution ($\sim$ 70%) comes from the events where a jet is misidentified as τ_h candidate, denoted as fake τ_h background. This includes $\sim$ 90% events from W+jets, $t\bar{t}$ semi-leptonic and hadronic decays and Z+jets processes. Very small contribution ($\sim$ 10%) comes from the QCD multijet, diboson events with semi-leptonic decays and single top (s-channel and t-channel) processes. The second contributing background in the $\ell\tau_h$ final state is the $t\bar{t}$ fully leptonic ($\sim$20%) in which both the leptons (ℓ : e or μ and

τ_h) comes from the decay of W bosons. In addition to this, very small contribution ($\sim 5\%$) comes from events in which both leptons are prompt such as Z(τ^+ τ^-)+jets and diboson and single top (tW-channel) processes.

Due to high probability ($\sim 10^{-2}$ for $p_T^\tau < 100\,\text{GeV}$) quark and gluon jets to be misidentified as τ_h jet [23], the largest contributing background is the one where τ_h jet is actually a misidentified quark or gluon jet. The fragmentation of quarks and gluons is a difficult process to model in simulated samples due to the inability to probe quarks and gluons as free particles. Furthermore, additional effects such as the modeling of pile-up and material budget are all important contributors to tau identification. Since the modeling of these events in the MC simulated samples is not reliable, this analysis makes use of data-driven methods to extract the jet $\rightarrow$ fake τ_h background contribution in the signal region.

The contribution of $t\bar{t}$ fully leptonic events is estimated from MC simulation after correcting them by a Data-to-MC scale factors obtained from dedicated control regions enriched in $t\bar{t} \rightarrow \mu\tau_h$ and $t\bar{t} \rightarrow e\tau_h$ events. Data-to-MC scale factors are used to correct for any mismodeling in MC after signal region selection due to object identification and isolation, misidentification rates, efficiency of the topological cuts. The contribution of other small backgrounds is estimated from their respective MC samples in the signal region, only if they have prompt leptons.

5.5.1 Jet $\rightarrow$ fake τ_h background estimation

To estimate the jet $\rightarrow$ fake τ_h background, a data-driven approach is followed in this analysis. The estimation of this background is performed mainly in two steps :

1. Estimation of jet $\rightarrow$ fake τ_h background events before any VBF selections, keeping the central selections same as the signal region and,

2. Estimation of VBF efficiency (ϵ_{VBF}).

These steps ensure the estimation of the background in a jet enriched control region and lower additional systematic bias due to VBF jet selections. The number of jets

to fake τ_h background events in the signal region are given as:

$$\mathrm{N}_{\mathrm{fake}}^{\mathrm{SR}} = \mathrm{N}_{\mathrm{fake}\tau_{\mathrm{h}}}^{\mathrm{beforeVBF}} \times \epsilon_{\mathrm{VBF}} \times \mathrm{SF}_{\mathrm{VBF}} \tag{5.5}$$

where,

$$\mathrm{N}_{\mathrm{fake}\tau_{\mathrm{h}}}^{\mathrm{beforeVBF}} = \mathrm{N}_{\mathrm{anti-iso}\tau_{\mathrm{h}}}^{\mathrm{data}} \times \mathrm{w}_{\mathrm{fake}} \tag{5.6}$$

and SF_{VBF} is the Data-to-MC simulation scale factors, used to correct for any bias in the ϵ_{VBF} estimation. w_{fake} is the jet $\rightarrow \tau_h$ fake factor, estimated from the jet $\rightarrow \tau_h$ fake ratio.

For the estimation in the before VBF control region ($N_{fake\tau_h}^{beforeVBF}$), an anti-isolated τ_h control region is used which consists of good statistics of fake τ_h events. The events in this control region contain τ_h candidates which pass the loose working point of the DeepTau anti-jet discriminator and fail the tight working point of the DeepTau anti-jet discriminator keeping all other selections same as the central selections. These events are then reweighed with a fake factor. The fake factor (w_{fake}) is estimated from jet $\rightarrow \tau_h$ fake ratio (f) which is the probability of a fake τ_h candidate (usually a jet) passing the loose τ_h anti-jet selection to also pass the tight τ_h anti-jet selection. The estimation of jet $\rightarrow \tau_h$ fake ratio (f) is discussed in the next Subsection. Other prompt backgrounds are taken from their respective MC simulations, only if they have a generator level (ℓ,τ_h) candidate matched to the reconstruction level candidate and are subtracted for the estimation of jet $\rightarrow$ fake τ_h events.

Jet $\rightarrow \tau_h$ fake ratio (f) : The jet $\rightarrow \tau_h$ fake ratio is measured in a jet enriched control region i.e. using Z($\mu\mu$) + τ_h events in which a jet is misidentified as a τ_h candidate. To ensure pure selection of Z($\mu\mu$) events in this control region, events with exactly two opposite sign muons having mass within the Z mass i.e. 60 GeV $< M(\mu\mu) <$ 120 GeV are selected. These events are further divided into two sets,

1. Events having exactly one τ_h candidate passing the tight isolation working point of the DNN based τ_h discriminator against jets and,

2. Events having exactly one τ_h candidate passing the loose isolation working point of the DNN based τ_h discriminator against jets.

These τ_h candidates are coming from the jets associated with Z boson production, hence the misidentified τ_h candidates. The contribution of other SM processes in this control region is subtracted from data using their respective MC samples, to further improve the purity of $(\mu\mu)$ + τ_h events in the data. The purity of the Z$(\mu\mu)$ + τ_h events in data is observed to be greater than 90% as shown in Figure 5.13. The purity of the Z$(\mu\mu)$ + τ_h events in data as a function of τ_h p_T with the tight τ_h isolation control region (left) and loose τ_h isolation control region (right) is shown for all three years and is observed to be consistent across years.

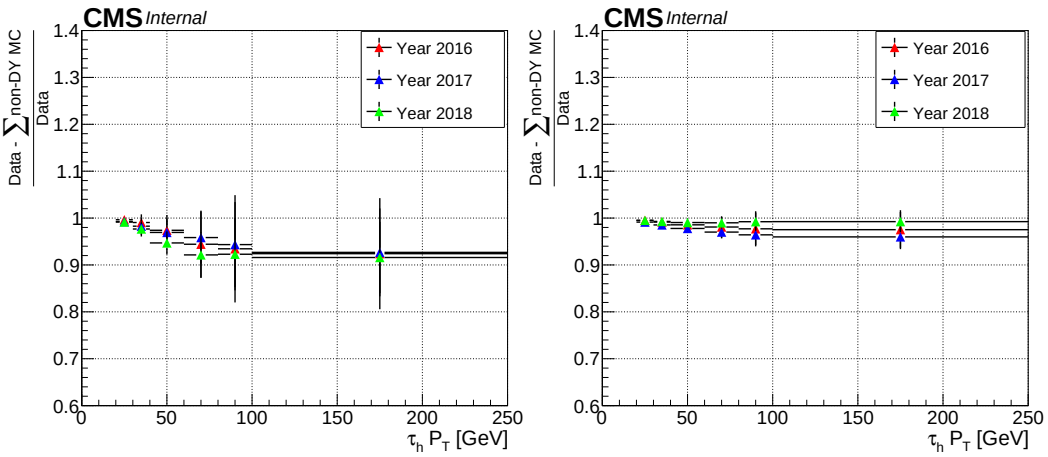

Figure 5.13: Observed purity for the Z$(\mu\mu)$ + τ_h events in data corresponding to 2016, 2017 and 2018 data-taking, with the tight τ_h isolation (left) and with the loose τ_h isolation (right). The purity is observed to be greater than 90% for the three years.

After selecting the jet enriched region, the fake ratio (f) is calculated as:

$$f = \frac{N^{tight}_{Z(\mu\mu)+\tau_h}}{N^{loose}_{Z(\mu\mu)+\tau_h}} \tag{5.7}$$

Figure 5.14- 5.16 shows the jet $\rightarrow$ τ_h fake ratio as a function of τ_h p_T and τ_h η

for 2016, 2017 and 2018 respectively. Due to high purity of Z($\mu\mu$) + τ_h events in the data, the fake ratio from data with and without subtracting the non-Z+jets background events is consistent with each other. The fake ratio is about 0.05 except for τ_h $p_T < 50\,\text{GeV}$ during 2016 data where higher fake ratio is estimated. Also, the fake ratio as a function of τ_h η is observed to be flat in both barrel and endcap with 2017 and 2018 data, whereas in the case of 2016, the fake ratio varies as a function of τ_h η. This is observed due to the effect of decrease in hit efficiency in the silicon strip tracker (substantial in Tracker Outer Barrel L1-L2) in the early 2016 data-taking [28] [29]. This behaviour was traced to saturation effects in the pre-amplifier of the APV25 readout chip [30] which was recovered in the later part of the 2016 data-taking period. Besides this, the Phase 2 upgrade of the silicon pixel tracker in 2017 (discussed in Chapter 2) led to better reconstruction and improved lifetime information of the τ_h candidates and hence, decrease in the fake ratio in 2017 and 2018. As a result, fake ratio as a function of both τ_h p_T and τ_h η is considered for 2016 as shown in Figure 5.17 and taken as a function of τ_h p_T only for 2017 and 2018. Since MC simulated events for 2016 does not describe the APV saturation effect, the fake ratio estimated using Z+jets MC simulated events is lower than that observed in data. To avoid any such kind of bias in MC prediction of jet $\rightarrow$ fake τ_h background, the MC simulated events are reweighed with fake ratio estimated from Z+jets MC events for the three years. For the estimation from the data, the fake ratio estimated from data after subtracting non-Z+jets background events is applied.

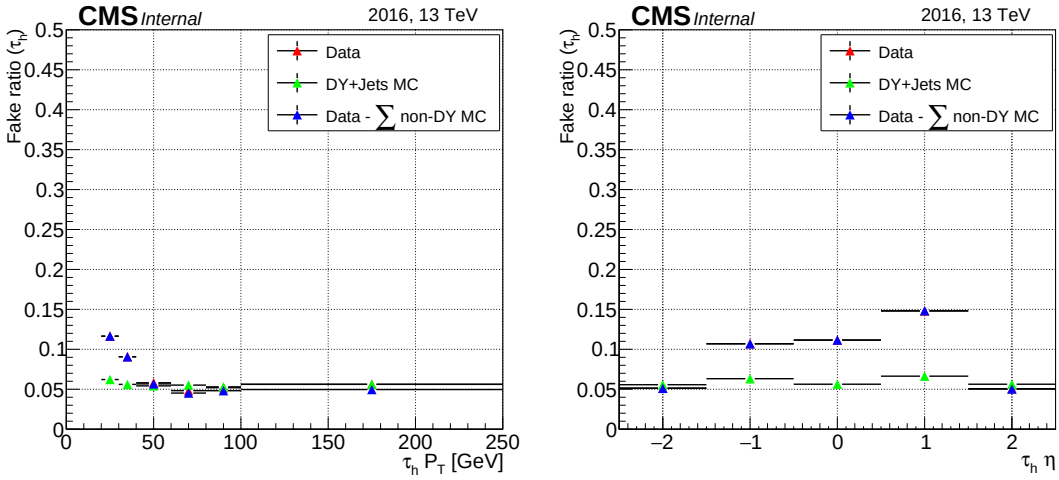

Figure 5.14: Jet $\rightarrow \tau_h$ fake ratio as a function of τ_h p_T (left) and τ_h η (right) from data, Z+jets MC simulation and from data with subtracting non-Z+jets MC simulation events for 2016.

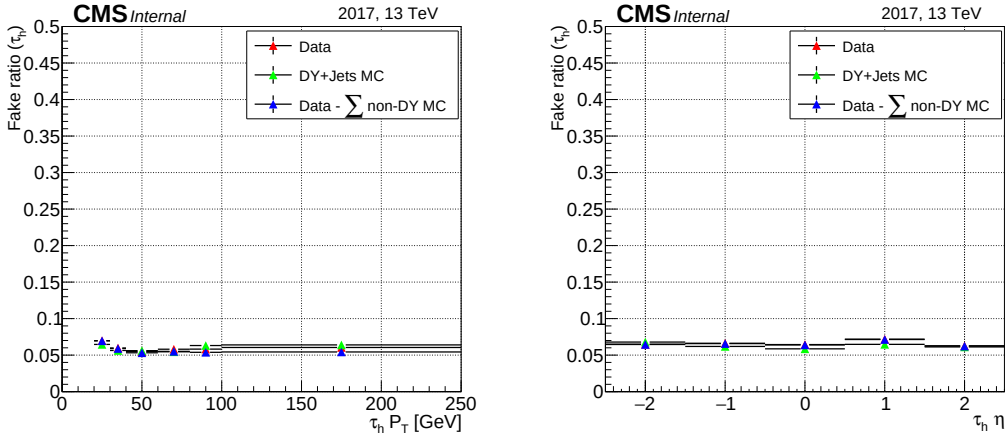

Figure 5.15: Jet $\rightarrow \tau_h$ fake ratio as a function of τ_h p_T (left) and τ_h η (right) from data, Z+jets MC simulation and from data with subtracting non-Z+jets MC simulation events for 2017.

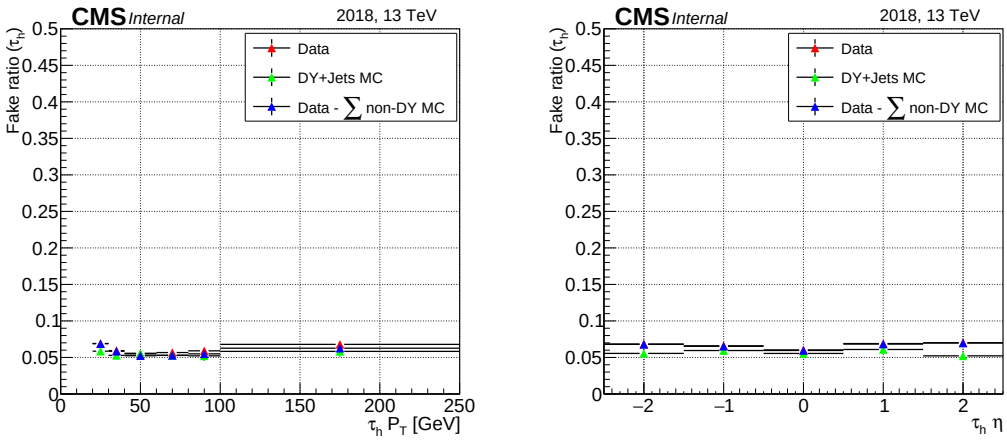

Figure 5.16: Jet $\rightarrow \tau_h$ fake ratio as a function of τ_h p_T (left) and τ_h η (right) from data, Z+jets MC simulation and from data with subtracting non-Z+jets MC simulation events for 2018.

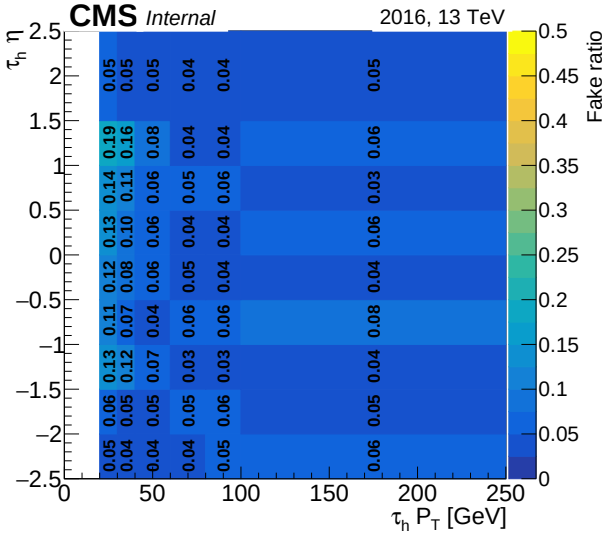

Figure 5.17: Jet $\rightarrow \tau_h$ fake ratio as a function of both τ_h p_T and τ_h η in 2016.

Determination of shape correction for $e\tau_h$ and $\mu\tau_h$ final states : After reweighing events in the anti-isolated τ_h control region with the fake factor ($w_{fake} = \frac{f}{1-f}$), jet $\rightarrow$ fake τ_h background is estimated using MC simulated events. These predicted background events are compared with the observed background events from MC simulations in the isolated τ_h control region. By construction the normalizations should agree for the predicted and observed events, yet some residual shape effects are observed due to mismodeling of E_T^{miss} due to activity of ISR jets and pileup jets. The variables that exhibit the largest differences are $\Delta\phi(\tau_h, E_{\mathrm{T}}^{\mathrm{miss}})$ and $\Delta\phi(\ell, E_{\mathrm{T}}^{\mathrm{miss}})$ ($\ell : \mu, e$). Therefore, corrections for residual shape effects are derived from simulation for the three years and are applied to each event in the anti-isolated τ_h control region to make the reweighted distributions agree with the same distributions in isolated events. Figure 5.18 shows the corrections for the $\mu\tau_h$ final state for the three years. Similarly, Figure 5.19 shows the corrections for the $e\tau_h$ final state for the three years. It is observed that, after the shape corrections, the E_T^{miss} and reconstructed mass distributions, i.e. $m(\mu, \tau_h, E_T^{miss})$ and $m(e, \tau_h, E_T^{miss})$, in the isolated region are well described by the reweighted anti-isolated events as shown in the next Section.

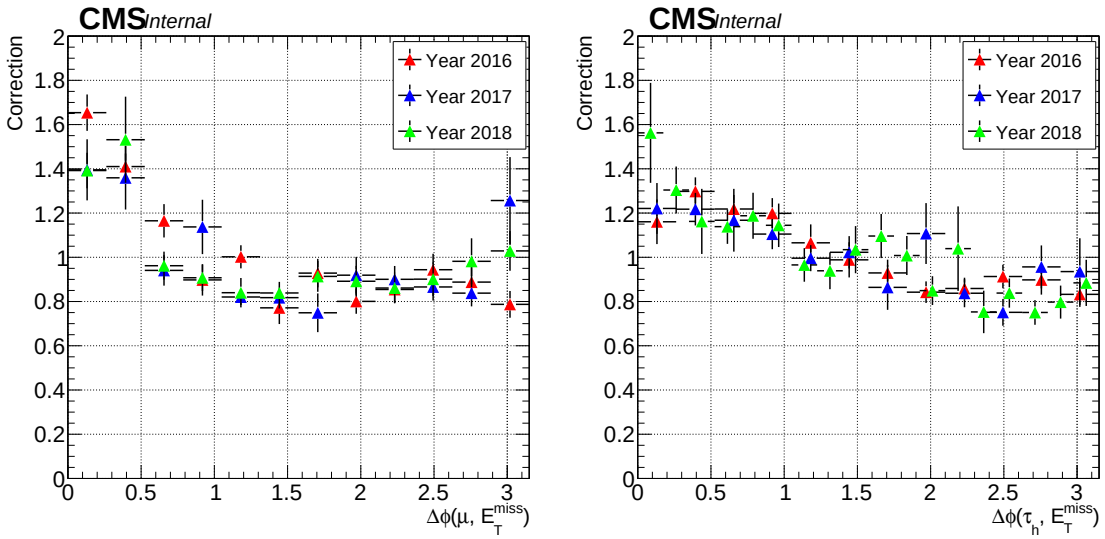

Figure 5.18: Corrections determined in the $\mu\tau_h$ control region events, after applying the fake factor to the anti-isolated τ_h control region events. The left plot corresponds to the corrections as a function of $\Delta\phi(\mu, E_{\mathrm{T}}^{\mathrm{miss}})$ for the three years. The right plot corresponds to the corrections as a function of $\Delta\phi(\tau_h, E_{\mathrm{T}}^{\mathrm{miss}})$ for the three years.

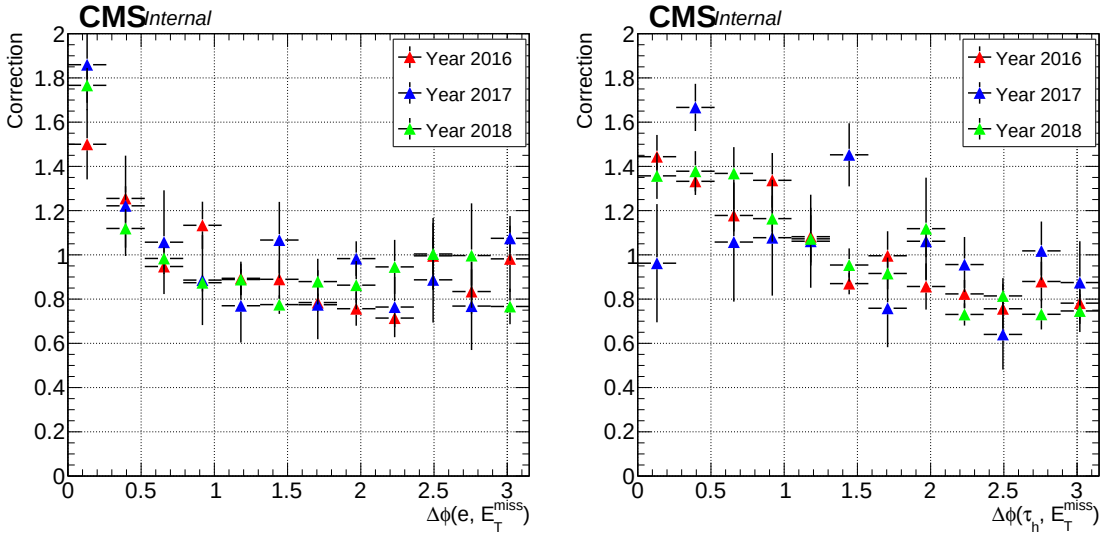

Figure 5.19: Corrections determined in the $e\tau_h$ control region events, after applying the fake factor to the anti-isolated τ_h control region events. The left plot corresponds to the corrections as a function of $\Delta\phi(e, E_{\mathrm{T}}^{\mathrm{miss}})$ for the three years. The right plot corresponds to the corrections as a function of $\Delta\phi(\tau_h, E_{\mathrm{T}}^{\mathrm{miss}})$ for the three years.

Closure test for jet → fake τ_h background A closure test is performed to validate predicted background events in the isolated τ_h control region before any VBF event selection. For this, the reconstructed dilepton mass distributions in $\mu\tau_h$ and $e\tau_h$ final states for the predicted background events using anti-isolated τ_h events are compared with the observed background events in the isolated τ_h control region. To subtract contribution of the prompt τ_h background events in the isolated τ_h control region, such as from $t\bar{t}$ fully leptonic process, diboson, single top (tW-channel) and Z($\tau\tau$)+jets, the events from their respective MC simulations are used. The resulting distributions are shown in Figure 5.20 for the three years in $\mu\tau_h$ and $e\tau_h$ final state. The distributions for observed and predicted jet → fake τ_h background agree with each other. Any residual differences are considered as an additional systematic uncertainty on this background prediction.

Estimated background events before the VBF event selections Figure 5.21 shows the estimated background events before any VBF selections in the $\mu\tau_h$ and $e\tau_h$ final states for the years 2016-2018. Here, the jet → fake τ_h background is estimated using the anti-isolated τ_h control region as discussed in the previous Section. The $t\bar{t}$ background events are taken from its respective MC simulated events passing only the signal region central selections. The other prompt background events are also from their respective MC simulated samples, only if the reconstruction level τ_h candidate matches with the generator level τ_h candidate. The data events refer to the events passing the signal region central selections only. It is observed that the estimated background events agree well with the data before any VBF selections in both $\mu\tau_h$ and $e\tau_h$ final states.

Estimation of VBF efficiency To estimate jet → fake τ_h background events in the signal region, VBF efficiency (ϵ_{VBF}) is evaluated. The ϵ_{VBF} is estimated using $\mu\tau_h$ events from W+jets MC simulation with central selections and is defined as:

$$\epsilon_{VBF} = \frac{N^{\mu\tau_h}_{after\,VBF}}{N^{\mu\tau_h}_{before\,VBF}} \tag{5.8}$$

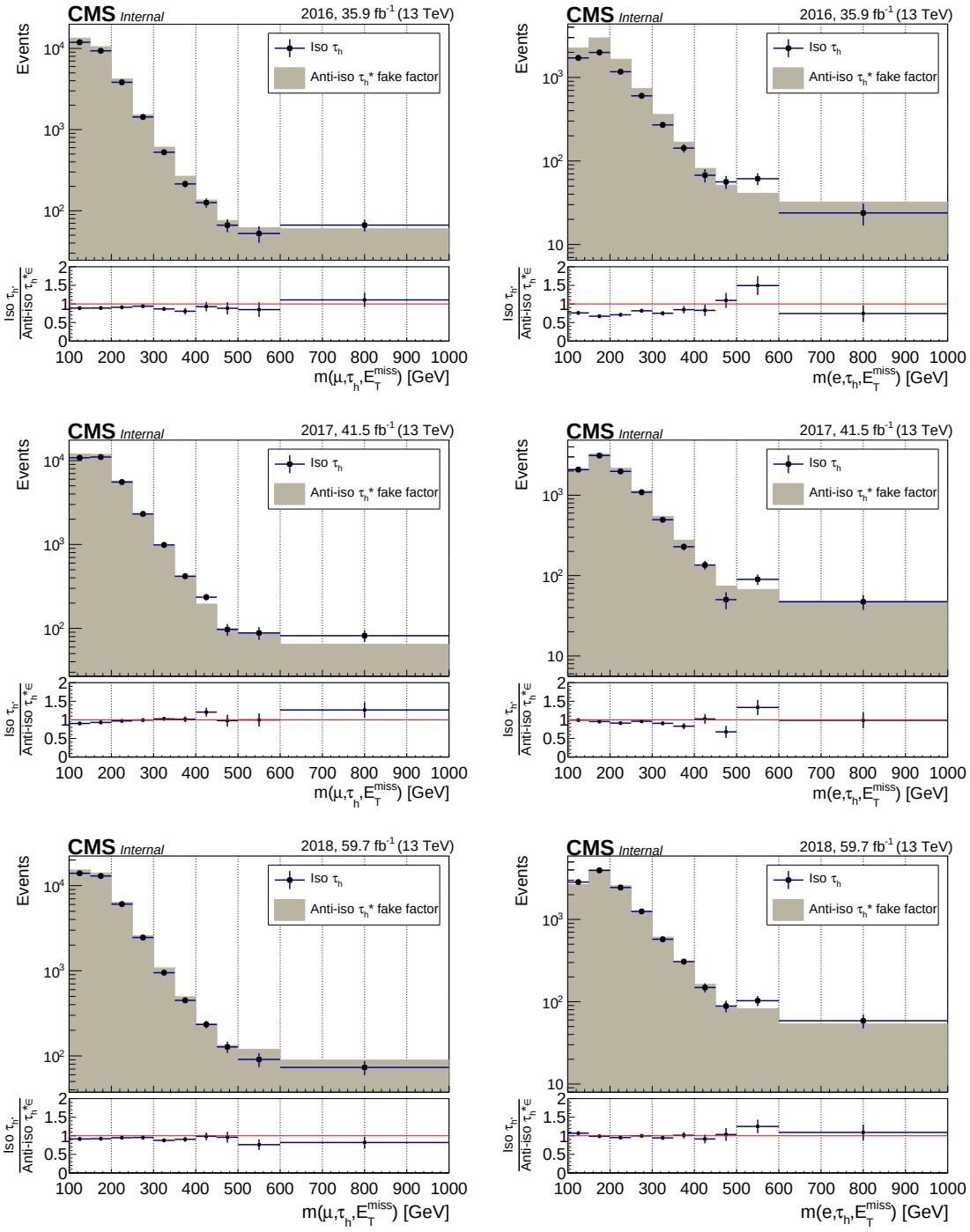

Figure 5.20: Comparison between the isolated τ_h events and anti-isolated τ_h events reweighed with fake factor and corrected with the $\Delta\phi(\ell, E_{\mathrm{T}}^{\mathrm{miss}})$ shape factors in the $\mu\tau_h$ final state (left) and in $e\tau_h$ final state (right) in 2016 (top), 2017 (center) and 2018 (bottom).

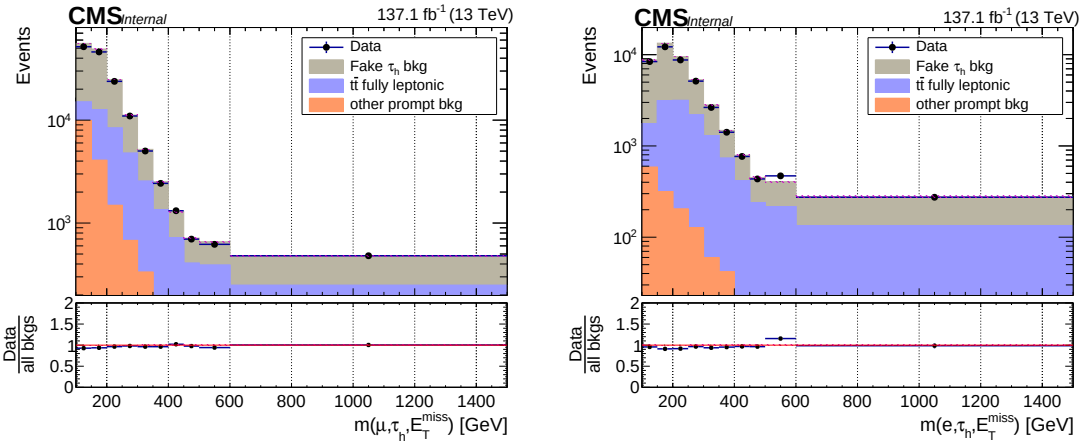

Figure 5.21: Estimated background events validation before VBF selections in the $\mu\tau_h$ (left) and $e\tau_h$ (right) final state.

The observed ϵ_{VBF} in the three years is listed in Table 5.8 and is observed to be consistent across years. The uncertainty on the observed value is based on MC statistics. Due to similar topology of the VBF jets in $\mu\tau_h$ and $e\tau_h$ final state, same values of ϵ_{VBF} are used in the $e\tau_h$ final state. A data-to-MC simulation scale factor (SF_{VBF}) is derived to correct for any bias in the W+jets MC events due to the VBF selections. The SF_{VBF} is estimated using W($\mu\nu$)+jets events. The event selections for the W($\mu\nu$)+jets control region are listed in Table 5.7.

Selection	Cut
Trigger	HLT_IsoMu24(27)
$N(\mu)$	$= 1$
$\lvert\eta(\mu)\rvert$	< 2.4
$p_{\mathrm{T}}(\mu)$	$\geq 35\,\mathrm{GeV}$
$E_{\mathrm{T}}^{\mathrm{miss}}$	$\geq 30\,\mathrm{GeV}$
$M_T(\mu, MET)$	$[50\,\mathrm{GeV}, 110\,\mathrm{GeV}]$
$N(\mathrm{bjet})$	$= 0$
$p_{\mathrm{T}}(j)$	$\geq 30\,\mathrm{GeV}$
$\lvert\eta(j)\rvert$	< 5.0
$N(j)$	≥ 2
$\Delta\eta(jj)$	> 4.2
$m(jj)$	$> 500\,\mathrm{GeV}$

Table 5.7: Event selection criteria for the W($\mu\nu$)+jets control region used to measure SF_{VBF}.

The purity of ∼70% is observed for this control region. The scale factor, SF_{VBF}, for the VBF selections can be defined as:

$$SF_{VBF} = \frac{N^{data}(W + jets)}{N^{MC}(W + jets} \tag{5.9}$$

The observed SF_{VBF} is listed in Table 5.8 for the three years. The VBF efficiency scale factors are lower for 2016 and 2017 in comparison to 2018. This is expected due to the improved JER scale factors for low-p_T forward jets in 2018. In 2016 and 2017, forward jet JER factors are not p_T-dependent, whereas the 2018 JER factors for high-η jets were measured as a function of p_T.

Year	ϵ_{VBF}	SF_{VBF}
2016	0.11 ± 0.01	0.73 ± 0.02
2017	0.13 ± 0.01	0.71 ± 0.03
2018	0.13 ± 0.01	0.84 ± 0.03

Table 5.8: Observed ϵ_{VBF} and SF_{VBF} for three years for the estimation of jet → fake τ_h background in the signal region. The listed uncertainties are statistical in nature.

To validate the observed SF_{VBF} for the VBF selections, a closure test is performed in E_T^{miss} inverted control region (i.e. $E_T^{miss} < 30\,\text{GeV}$) using $\mu\tau_h$ events. Similar methodology is utilized to estimate the jet → fake τ_h background from data in this $E_T^{miss} < 30\,\text{GeV}$ control region as for the signal region. Figure 5.22 shows the comparison of the observed and predicted background events in $m(\mu, \tau_h, E_T^{miss})$ distribution. The observed agreement is well within statistical and systematic uncertainties. Any residual differences are considered as an additional systematic uncertainty.

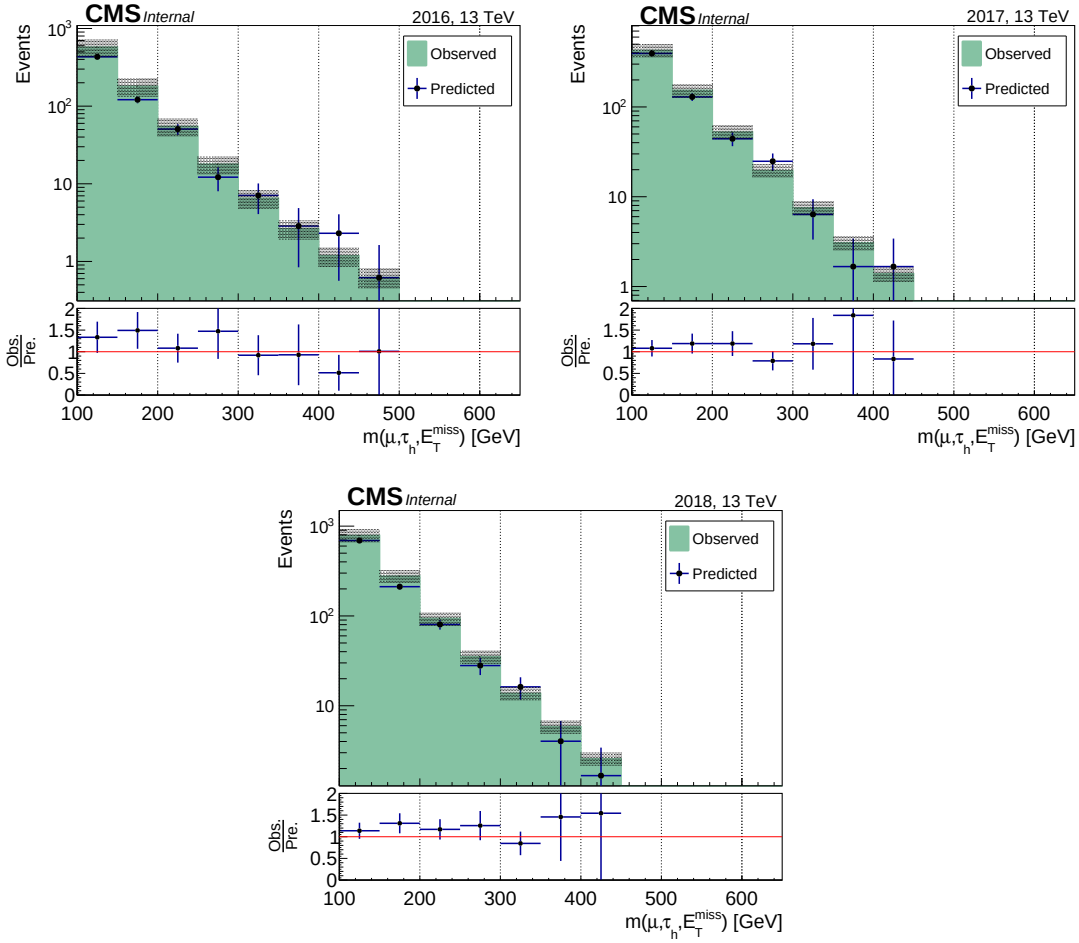

Figure 5.22: Closure test for the VBF efficiency Scale Factor (SF_{VBF}) with 2016 (top left), 2017 (top right) and 2018 (bottom) data.

5.5.2 Estimation of $t\bar{t}$ fully leptonic background

The second major contribution in the signal region is coming from the $t\bar{t}$ fully leptonic process. This background is estimated using two control regions, denoted as C and D, as shown in the Figure 5.23.

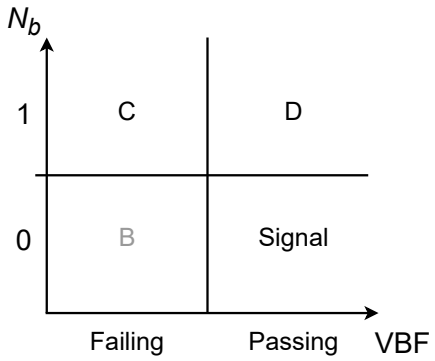

Figure 5.23: Visualization of the control regions used for the $t\bar{t}$ background estimation. Region C and D are used to derive the scale factors, that are applied to the $t\bar{t}$ MC simulation events in the signal region.

These control regions are defined by $t\bar{t}$ enriched events with 1 b jet that fail and pass the VBF selections and are used to estimate the data-to-MC simulation scale factors for the central selections and the VBF selections. All the selections are kept similar as the central selections, but with selecting events having one b jet. The data-to-MC scale factor for the central selections ($SF_{non-VBF}$) is estimated using events having one b jet and failing VBF selections, denoted as control region C. The $t\bar{t}$ fully leptonic events in the data are estimated by subtracting contribution from other processes using their respective MC samples. The $t\bar{t}$ fully leptonic events in the data are then compared with $t\bar{t}$ fully leptonic MC simulated events to get the scale factor for the central selections ($SF_{non-VBF}$) as described by Eq. 5.10. Similarly, the scale factor for VBF selections (SF_{VBF}) is estimated using events having one b jet and passing VBF selections, denoted as control region D. The scale factor from control region C ($SF_{non-VBF}$) is used to correct $t\bar{t}$ yield in the control region D before deriving SF_{VBF}. These scale factors are required to correct for any bias in MC simulated events due to object identification and mismodeling of VBF topology in the simulation. Both scale factors are estimated independently for the

$\mu\tau_h$ and $e\tau_h$ final states. The purity of $t\bar{t}$ fully leptonic events in control region C and control region D is observed to be > 75 % for the three years. The estimation of scale factors and $t\bar{t}$ fully leptonic background events in the signal region is then given as:

$$SF_{non-VBF} = \frac{N_{t\bar{t}}^{Data}}{N_{t\bar{t}}^{MC}}(CR\ C),\ SF_{VBF} = \frac{N_{t\bar{t}}^{Data}}{N_{t\bar{t}}^{MC}}(CR\ D) \tag{5.10}$$

$$N_{SR}^{t\bar{t}} = \left(N_{SR}^{t\bar{t}\ \mathrm{MC}}\right) * (SF_{VBF})\,. \tag{5.11}$$

Figure 5.24 shows the $m(\mu, \tau_h, E_T^{miss})$ distribution (left) and $m(e, \tau_h, E_T^{miss})$ distribution (right) for control region C using the 2018 data. The distributions are observed to be consistent across years. Similarly, Figure 5.25 shows the $m(\mu, \tau_h, E_T^{miss})$ distribution (left) and $m(e, \tau_h, E_T^{miss})$ distribution (right) for control region D using the 2018 data.

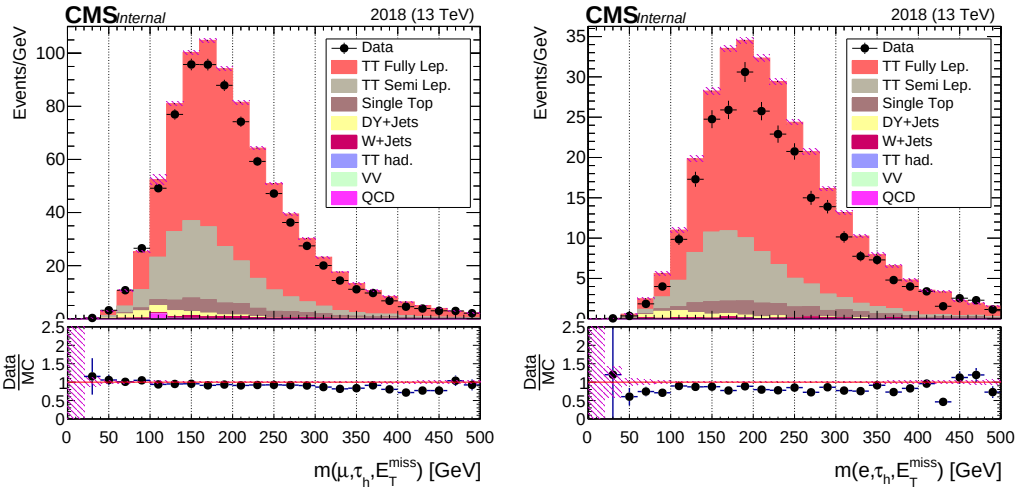

Figure 5.24: Distribution of $m(\mu, \tau_h, E_T^{miss})$ (left) and $m(e, \tau_h, E_T^{miss})$ (right) for control region C for the year 2018.

The observed scale factors in the $\mu\tau_h$ and $e\tau_h$ final states for the three years are listed in Table 5.9 and Table 5.10 respectively. The associated uncertainties are fully statistical in nature. The event yield from the MC simulation is corrected with

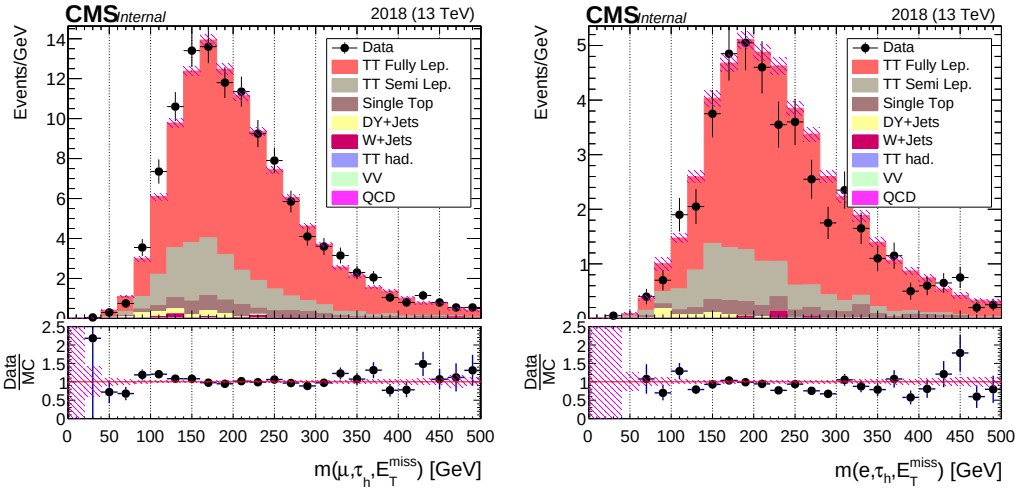

Figure 5.25: Distribution of $m(\mu, \tau_h, E_T^{miss})$ (left) and $m(e, \tau_h, E_T^{miss})$ (right) for control region D for the year 2018.

$SF_{non-VBF}$ in control region D before deriving the SF_{VBF}, to correct for any bias in simulation due to central selections. The observed SF_{VBF} is consistent in $\mu\tau_h$ and $e\tau_h$ final states. The $t\bar{t}$ fully leptonic events from its respective MC simulation in the signal region are corrected with SF_{VBF} for the estimation of the $t\bar{t}$ fully leptonic background events.

Year	$SF_{non-VBF}$	SF_{VBF}
2016	1.00 ± 0.02	0.82 ± 0.03
2017	0.96 ± 0.01	0.98 ± 0.03
2018	0.89 ± 0.01	1.04 ± 0.03

Table 5.9: The observed scale factor $SF_{non-VBF}$ and SF_{VBF} from $t\bar{t}$ control region C and D for the three years for $\mu\tau_h$ final state.

Year	$SF_{non-VBF}$	SF_{VBF}
2016	0.83 ± 0.02	0.82 ± 0.06
2017	0.80 ± 0.02	1.02 ± 0.06
2018	0.75 ± 0.02	1.25 ± 0.05

Table 5.10: The observed scale factor $SF_{non-VBF}$ and SF_{VBF} from $t\bar{t}$ control region C and D for the three years for $e\tau_h$ final state.

5.6 Event yield in the Signal Region

The criteria to select the signal events is mentioned in the Section 5.4 which involves the selection of a opposite sign $\mu\tau_h$ pair and $e\tau_h$ pair, missing transverse energy and at least two jets passing the VBF event selections. The final estimation of the dominant background i.e. jet $\rightarrow$ fake τ_h background in the signal region is given by the Eq. 5.5. The estimations of the second contributing background i.e. $t\bar{t}$ fully leptonic events in the signal region is given by the Eq. 5.11. The methodology to estimate their contribution in the signal region has been described in the previous Section. The other backgrounds with relatively smaller contribution are estimated directly from their respective MC simulations. The contribution of these small backgrounds i.e. prompt Z+jets, prompt diboson decays and single top (tW-channel) events are estimated from the events having reconstruction level leptons matched with the generator level leptons.

Table 5.11 lists the number of observed background events in the signal region for $\mu\tau_h$ final state and $e\tau_h$ final state respectively for the 27.4 fb^{-1} of data. The mentioned uncertainties in the event yields are statistical in nature. The observed data does not show an excess of events with respect to the background-only hypothesis, and 95% CL upper limits on the production cross-section of Z' are calculated, as discussed in the next Section.

Process	Event yield ($\mu\tau_h$)	Event yield ($e\tau_h$)
Data	3093.0	913.0
Jet $\rightarrow$ fake τ_h bkg.	2008.7 $\pm$ 56.9	598.9 $\pm$ 14.9
$t\bar{t}$ bkg.	649.6 $\pm$ 6.3	248.3 $\pm$ 3.9
Other prompt bkg.	167.1 $\pm$ 3.8	28.0 $\pm$ 1.2
Total bkg.	2825.4 $\pm$ 57.4	875.2 $\pm$ 15.4

Table 5.11: Event yield in the signal region for the OS $\mu\tau_h$ and OS $e\tau_h$ final states. The associated uncertainties are fully statistical in nature.

5.7 Systematic Uncertainties

The measurements can be affected by different sources of uncertainties which are discussed below:

- **Theoretical Uncertainties**

  Uncertainties on the signal cross-section: Starting from the theory uncertainties for the signal samples, the ones affecting the cross-section of the generated sample are divided in two groups: the uncertainties on the parameters used to compute the production cross-section, like Parton Distribution Functions (PDF) and α_S , and the theory uncertainties related to the renormalization (μ_R) and factorization scales (μ_F). The uncertainty in the theoretical cross-section due to the choice of PDF is observed to be 2.1%. The variation of α_S in the PDF includes additional uncertainty of the order of 0.5%. The scale uncertainty by changing the μ_R and μ_F by 2 (up and down) adds additional uncertainty of 0.4%.

  Uncertainties on the background MC simulation: The NNPDF3.0 LO and NLO [31] parton distribution functions (PDFs) are used in the background MC event generation for 2016. NNPDF3.1 is utilized for 2017 and 2018 MC event generation. The systematic effect due to the imprecise knowledge of the parton distribution functions is determined by comparing these with the default PDF and variations within the family of parametrization [32]. The maximal deviation from the central value ($\sim$6%) is used the overall systematic due to PDFs.

- **Experimental Uncertainties**

  The list of uncertainties associated to experimental measurements are assigned to both signal MC events and background events taken from MC simulations and are described below.

Uncertainties on the background prediction: The jet $\rightarrow$ fake τ_h background is estimated from data. The majority of the systematic uncertainties are derived directly from the control regions and measurements in data. As discussed in Section 5.5.1, the jet $\rightarrow \tau_h$ fake ratio is estimated using Z($\rightarrow \mu\mu$)+jets events. To estimate the systematic bias on the measurement, W($\rightarrow \mu\nu$)+jets events are chosen to perform the second set of estimations. The effect of the additional set of fake ratios is estimated on both the shape and normalization of the jet $\rightarrow$ fake τ_h background for $e\tau_h$ and $\mu\tau_h$ final states in 2016, 2017 and 2018. Any deviation from unity in the comparison of two measurements is considered as the systematic uncertainty. This systematic uncertainty is considered uncorrelated across years and channels due to different activity of jets depending on the run conditions. The difference between the jet$\rightarrow \tau_h$ fake ratios from the W+jets and the Z+jets events depends on the p_T (and thus reconstructed dilepton mass) and can be as large as about 20% in some mass bins. These bin-by-bin uncertainties are also treated as shape systematics in the final limit/significance calculations. In addition to this, the statistical uncertainty in the VBF efficiency is considered as an additional systematic uncertainty which is of the order of 10%. Similarly, the statistical uncertainty in the SF_{VBF} is considered as an additional source of systematic uncertainty for jet $\rightarrow$ fake τ_h background.

In case of $t\bar{t}$ fully leptonic background, the statistical uncertainties in the $SF_{non-VBF}$ and SF_{VBF} are considered as systematic uncertainties in both $e\tau_h$ and $\mu\tau_h$ final states for 2016, 2017 and 2018.

Luminosity: The year dependent systematic uncertainty on the measured luminosity is considered which is of the order of 1.2% for 2016, 2.3% and 2.5% for 2017 and 2018 respectively [33] [34] [35].

Pileup: The uncertainty due to pileup is obtained by shifting the minimum bias cross-section up and down by 4.6% [36]. The overall effect of 1.6% is

observed in the background MC events. The effect of 0.2% is observed with signal MC events and is considered as a systematic uncertainty.

Trigger, Reconstruction, and Selection: A 3.0% uncertainty due to the trigger efficiency is considered, which is the result of a fit to the trigger efficiency turn-on curve after the VBF event selections. The 3% is the uncertainty on the fit at the plateau, which is driven by the statistics in the data as shown in Figure 5.26. The uncertainty for reconstruction of muons and electrons is up to $\approx 2\%$ each depending on η or p_T.

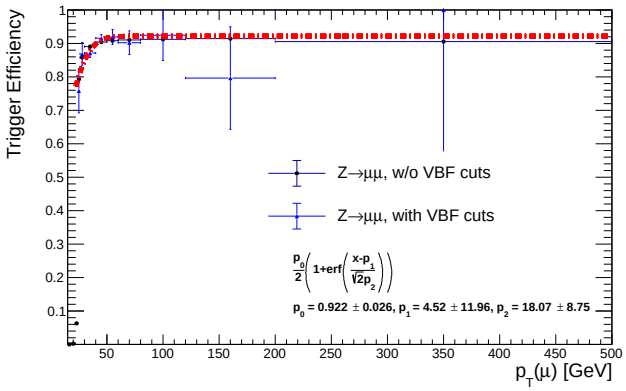

Figure 5.26: Fit to the trigger efficiency turn-on curve with $Z \to \mu\mu$ + VBF cuts in data. The fit shows ∼3% uncertainty on the fit at the plateau.

***b* jet Tagging Efficiency:** The uncertainty on the mis-tag rate [37] ($\approx 10\%$) is considered. For the case of the signal region, the systematic uncertainty on the requirement of 0 jets mistagged as b jets is determined by propagating the 10% uncertainty on the mistag rate through the following equation (which represents the signal efficiency for requiring 0 jets mistagged as b jets):

$$\epsilon^{\text{NBtag}<1} = 1 - \sum_{n=1} P(n) \cdot \sum_{m=1}^{n} C(n,m) \cdot f^m \cdot (1-f)^{n-m} \tag{5.12}$$

where $P(n)$ is the probability to obtain n additional jets (non-tau and non-lepton) in the event, $C(n,m)$ the combinatorial of n *choose* m, and f the

mistag rate. The probability to obtain at least one additional jet in the event is $\sim 10\%$. Therefore, based on the above equation, the mistag rate and the uncertainty, and the probability to obtain at least one additional jet, a systematic effect of $\sim 1\%$ on the signal is considered due to the mistag rate. The b tagging/mistagging systematics are considered 100% correlated across different MC simulations based backgrounds with similar composition (e.g. W + jets and Z + jets where there are typically no real b-jets), but completely uncorrelated to backgrounds that have different composition (e.g. $t\bar{t}$ vs. Z + jets). The b tagging uncertainties are evaluated on a per-event basis.

To determine the effect of the b jet scale factor on the background/signal yields and distributions, the scale factors are shifted up by 1σ and down by 1σ, where σ is the actual uncertainty on the scale factor, to examine the possible systematic effect on the mass distribution in the one b jet, passing VBF region for $t\bar{t}$ fully leptonic background. This is the plot in Figure 5.27 (left), where red is the mass distribution obtained with the central value of the weights, blue is the variation of the SFs down by 1σ, and green is for the variation of the SFs up by 1σ. From this plot in Figure 5.27 (left), a 2% uncertainty is applied conservatively to $t\bar{t}$ fully leptonic background to account for the uncertainty associated with utilization of the b jet scale factors.

Electron Energy Scale: The effect on the signal acceptance efficiency with 1% (2.5%) shift in the electron energy scale in the barrel (endcap) region is considered. The systematic effect is $< 1\%$ on the signal acceptance efficiency [38].

Muon Momentum Scale: The effect on the signal acceptance efficiency with 5% shift in the momentum scale is considered. The systematic effect is $< 1\%$ [39].

Jet Energy Scale: The effect of 2-5% due to the jet energy scale uncertainty on the signal acceptance is considered, depending on the η and p_T of the

considered jet. For example, for a 5% scale uncertainty, the jet 4-momentum is scaled by a factor of $k = 1.05$ or 0.95 ($p_{smeared} = k \cdot p_{default}$) and variables are recalculated using $p_{smeared}$. In Figure 5.27 (right), the green ratio is for the up-shifted distribution to the central. The blue ratio is for the down-shifted distribution to the central. Systematics for variation of JES amount to ∼10 - 15% on average. The shape based uncertainties in the fit for $m(\ell_1, \ell_2, E_{\mathrm{T}}^{\mathrm{miss}})$ are implemented based on JES.

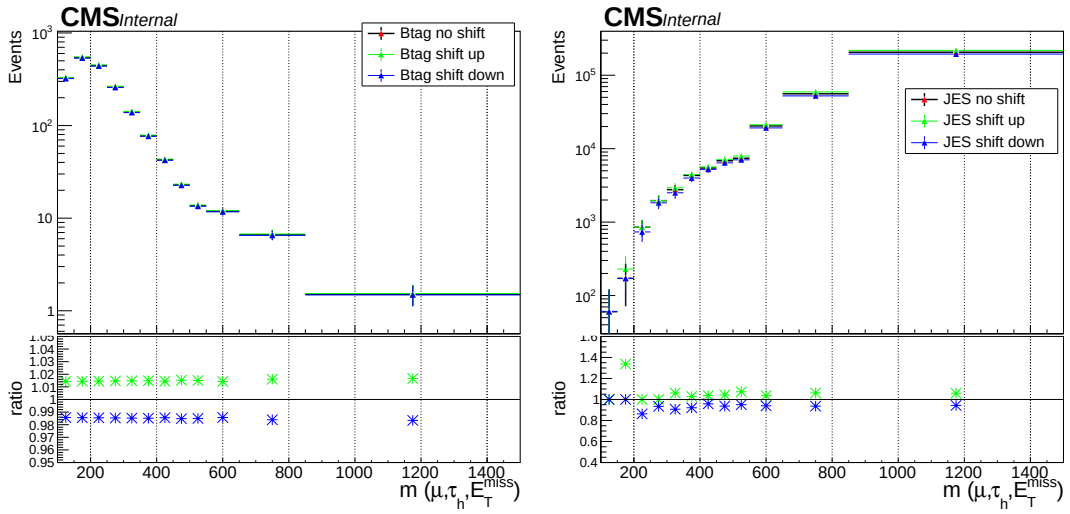

Figure 5.27: Systematic uncertainty on the $t\bar{t}$ fully leptonic MC events due to ±1 std. deviation variation in the b jet SF (left). Systematic uncertainty on the Z' signal sample of mass 1500 GeV due to jet energy scale uncertainty (right).

Statistical uncertainty: At last, bin-by-bin statistical fluctuation in the signal yield and background processes is considered as an additional uncertainty in the final calculations.

To summarize, the dominant systematic uncertainty comes from the uncertainty in the jet → τ_h fake ratio. Besides this, major systematic uncertainties in our predictions stem from uncertainties mainly due to limited simulation sample size and limited statistics of our data in the control region.

5.8 Results and Interpretation

Selected events are used for the presence of Z' signal events. Reconstructed mass of lepton pairs with associated E_T^{miss} defined in Eq. 5.4 is used as a final discriminating variable to look for an excess in data over smoothly falling SM backgrounds. The number of observed background events are summarized in Table 5.11 for the $\mu\tau_h$ and $e\tau_h$ final states. Figure 5.28 shows the reconstructed dilepton mass distribution ($m_{\ell,\ell}$) in the $\mu\tau_h$ and $e\tau_h$ final states. The oblique region represents the systematic uncertainty in the background prediction. As can be seen from the figure, the selected data events appear to be consistent with the estimated background events. To make a robust quantitative statement on the presence of the signal events, a statistical study is being performed where upper limits on the production cross-section of the Z' are calculated using the asymptotic CLs criterion [40] [41].

The branching fractions are model dependent parameters, which depend on every single coupling between Z' and all the SM particles. On one extreme, the $Z' \to \tau\tau$ branching fraction can be close to 100% if the Z' coupling to the SM weak bosons (κ_V) is relatively small with respect to the tau lepton coupling, and the $Z' \to \tau\tau$ coupling is the most relevant fermion coupling. On the other hand, if the Z' is allowed to couple strongly to many other SM particles, such as the top quark, b quark, etc., then the branching fractions can vary significantly. All of these scenarios are good possibilities from the standpoint of the B meson anomalies and constraints on the models beyond SM (Yukawa hierarchy, explanation of the top mass, Higgs hierarchy problem, matter-antimatter asymmetry, etc.). From experimental perspective, these assumptions of the model only affect the $\sigma \times B$ theory curve. The expected and observed limits are calculated for branching fractions ranging from 1% to 90% for VBF $Z' \to \tau\tau$ and VBF $Z' \to WW$. The 100 % decay of $Z' \to \tau\tau$ and WW is not possible due to unitarity violation, hence the upper value of 90% branching fraction is chosen. Besides this, the upper limits on the production cross-section of the Z' are determined for a range of couplings of Z' to vector bosons (κ_V : 0.1, 0.25, 0.50, 0.75, 1.0) with varying coupling to light fermions

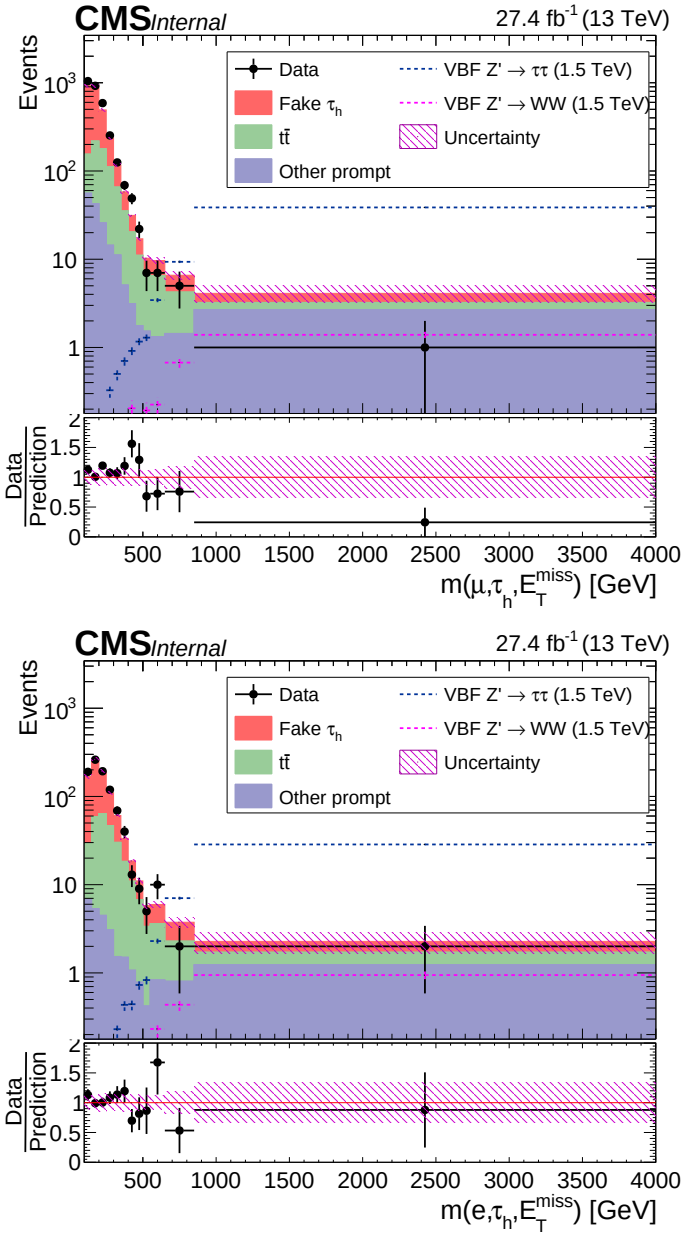

Figure 5.28: The reconstructed dilepton mass distribution $m_{\ell\ell}$ for OS $\mu\tau_h$ final state (top) and OS $e\tau_h$ final state (bottom) in the signal region. The signal scenario with $m_{Z'}$ = 1500 GeV is shown in the plots. The signal events are scaled up by a factor of 75 for visibility. The lower panel in these plots represents the ratio of the number of events in data (observation) to the total background prediction. The shaded band in the ratio plot includes both the statistical and systematic uncertainties in the background prediction.

($g_\ell = 0,\ 1$) but keeping coupling to heavy fermions ($g_h = 1$) fixed in order to allow for a broad and generic discussion about the importance of VBF Z' under various model assumptions [19].

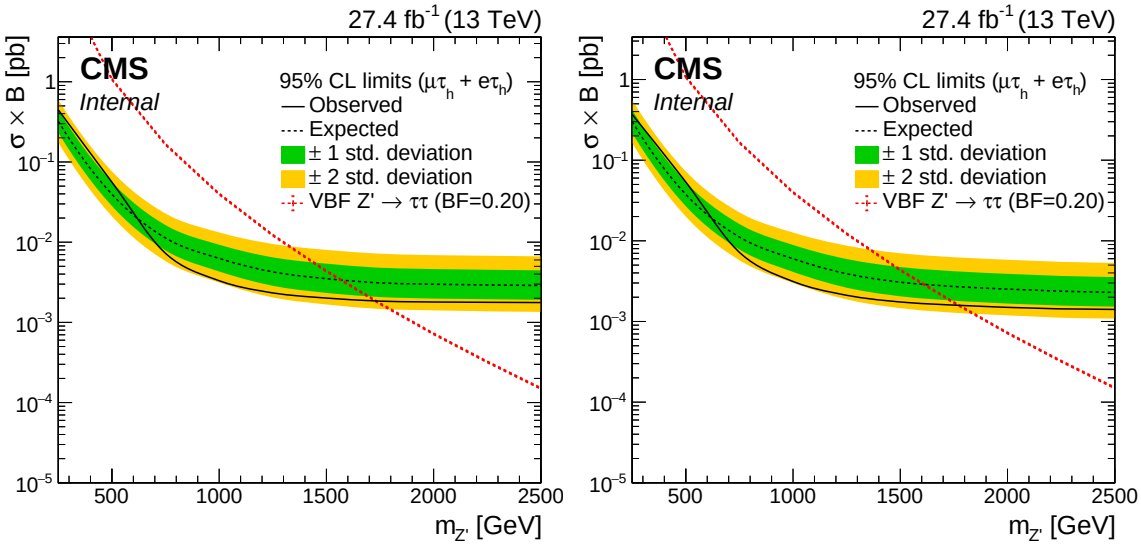

Figure 5.29: The 95% CL upper limits on the cross-section times Branching ratio for Z' decaying to $\tau\tau$ with universal coupling to light and heavy fermions (left) and enhanced coupling to heavy fermions (right) for $\kappa_V = 1$.

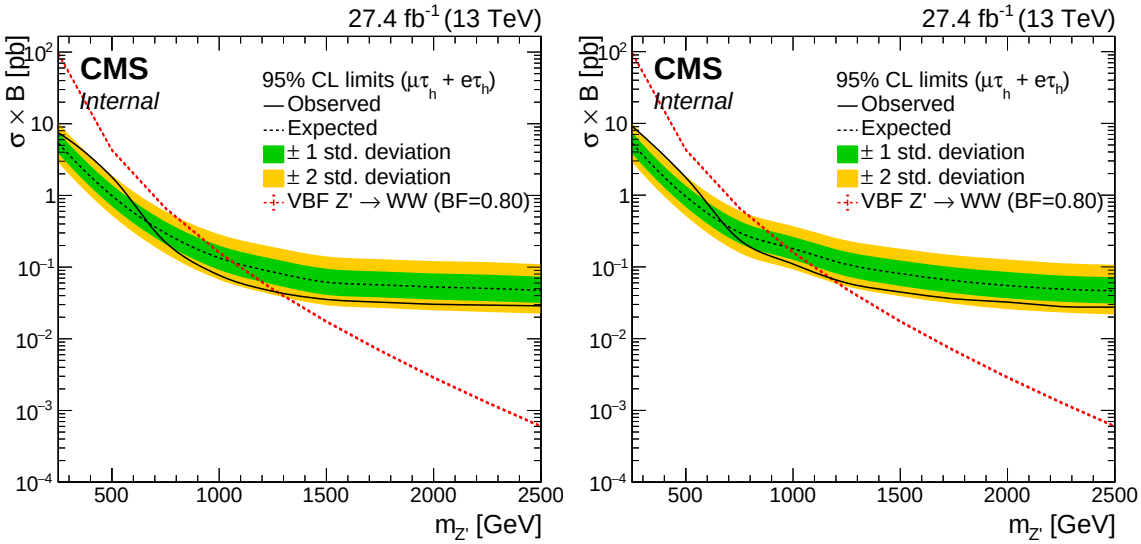

Figure 5.30: The 95% CL upper limits on the cross-section times Branching ratio for Z' decaying to WW with universal coupling to light and heavy fermions (left) and enhanced coupling to heavy fermions (right) for $\kappa_V = 1$.

Figure 5.29 shows the expected and the observed limits as functions of $m_{Z'}$

for $\tau\tau$ channel for $B = 20\%$. Here, the models with maximum coupling of Z' to the vector bosons ($\kappa_V = 1.0$) with universal coupling to light and heavy fermions i.e. $g_\ell = g_h = 1$ (left) and enhanced coupling to heavy fermions i.e. $g_\ell = 0$, $g_h = 1$ (right) are shown. As can be seen from the plots, with universal coupling to light and heavy fermions, Z' is observed to be excluded below $m_{Z'}$ to be 1.72 TeV with 20% branching fraction, whereas Z' is observed to be excluded below 1.77 TeV in the case of enhanced coupling to heavy fermions. Figure 5.30 shows the expected and the observed limits as functions of $m_{Z'}$ for WW channel for $B = 80\%$. Here also, the models with maximum coupling of Z' to the vector bosons ($\kappa_V = 1.0$) with universal coupling to light and heavy fermions i.e. $g_\ell = g_h = 1$ (left) and enhanced coupling to heavy fermions i.e. $g_\ell = 0$, $g_h = 1$ (right) are shown. As can be seen from the plots, with universal coupling to light and heavy fermions, Z' is observed to be excluded below $m_{Z'}$ to be 1.28 TeV with 80% branching fraction, whereas Z' is observed to be excluded below 1.20 TeV in the case of enhanced coupling to heavy fermions.

Figure 5.31 shows the observed and expected exclusion bounds at 95% CL as a function of coupling to vector bosons (κ_V) and $m_{Z'}$ for $Z' \to \tau\tau$ channel with universal coupling to light and heavy fermions ($g_\ell = 1$, $g_h = 1$) and enhanced coupling to heavy fermions ($g_\ell = 0$, $g_h = 1$). In the case of enhanced coupling to third generation fermions, the $Z' \to \tau\tau$ is the most relative fermion coupling. As can be seen from the figure, the enhanced coupling to third generation fermions have provided the most stringent limits in the case of $Z' \to \tau\tau$ channel.

Figure 5.32 shows the observed and expected exclusion bounds at 95% CL as a function of coupling to vector bosons and $m_{Z'}$ for $Z' \to WW$ channel with universal coupling to light and heavy fermions ($g_\ell = 1$, $g_h = 1$) and enhanced coupling to heavy fermions ($g_\ell = 0$, $g_h = 1$). Here, it is observed that for the universal coupling to light and heavy fermions scenario, as κ_V increases, better exclusion bounds are provided by this model as compared to the scenarios where the Z' coupling to third generation fermions is enhanced.

Figure 5.33 shows the observed and expected exclusion bounds at 95% CL as a function of branching fraction and $m_{Z'}$ for $Z' \to \tau\tau$ channel with universal coupling to light and heavy fermions ($g_\ell = 1$, $g_h = 1$) and enhanced coupling to heavy fermions ($g_\ell = 0$, $g_h = 1$). Here also, it is observed that the enhanced coupling to heavy fermions is a more sensitive scenario than the universal coupling to light and heavy fermions in case of $Z' \to \tau\tau$ channel.

Figure 5.34 shows the observed and expected exclusion bounds at 95% CL as a function of branching fraction and $m_{Z'}$ for $Z' \to WW$ channel with universal coupling to light and heavy fermions ($g_\ell = 1$, $g_h = 1$) and enhanced coupling to heavy fermions ($g_\ell = 0$, $g_h = 1$). As can be seen from the figure, the scenario with universal coupling to light and heavy fermions, provides better exclusion limits in the case of $Z' \to WW$ channel.

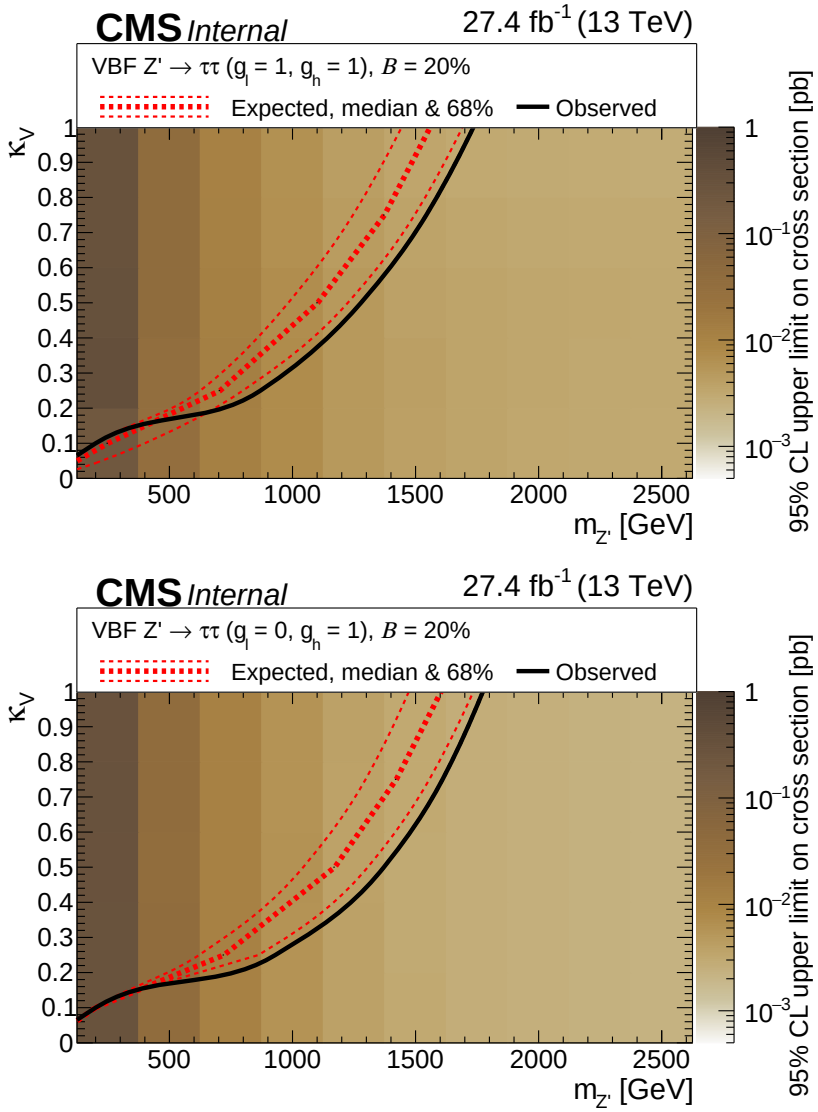

Figure 5.31: Exclusion region at 95% CL as a function of coupling to vector bosons, κ_V and $m_{Z'}$ for the $Z' \to \tau\tau$ channel with universal coupling to light and heavy fermions (top) and enhanced coupling to heavy fermions (bottom). The excluded regions are to the left of the curves. The observed exclusion bound is indicated by the black solid line. The expected exclusion region and their ± 1 standard-deviation variations is shown in dashed red curves.

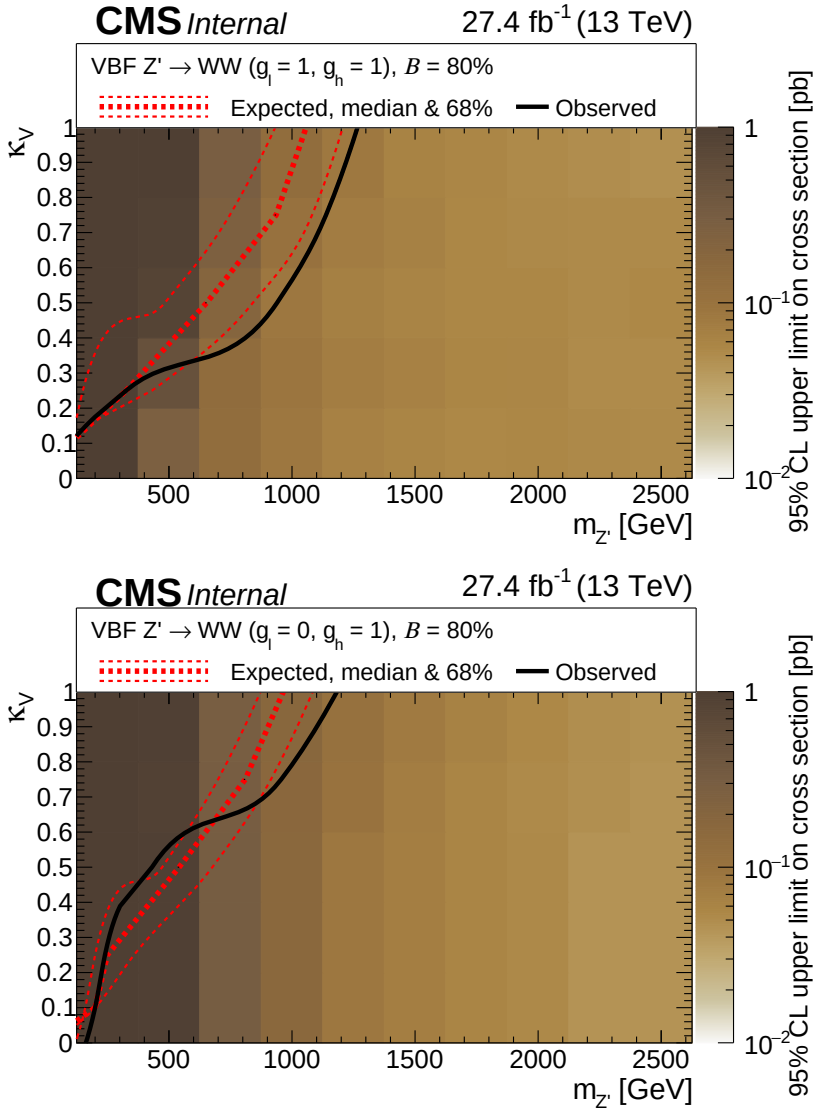

Figure 5.32: Exclusion region at 95% CL as a function of coupling to vector bosons, κ_V and $m_{Z'}$ for the $Z' \to WW$ channel with universal coupling to light and heavy fermions (top) and enhanced coupling to heavy fermions (bottom). The excluded regions are to the left of the curves. The observed exclusion bound is indicated by the black solid line. The expected exclusion region and their ± 1 standard-deviation variations is shown in dashed red curves.

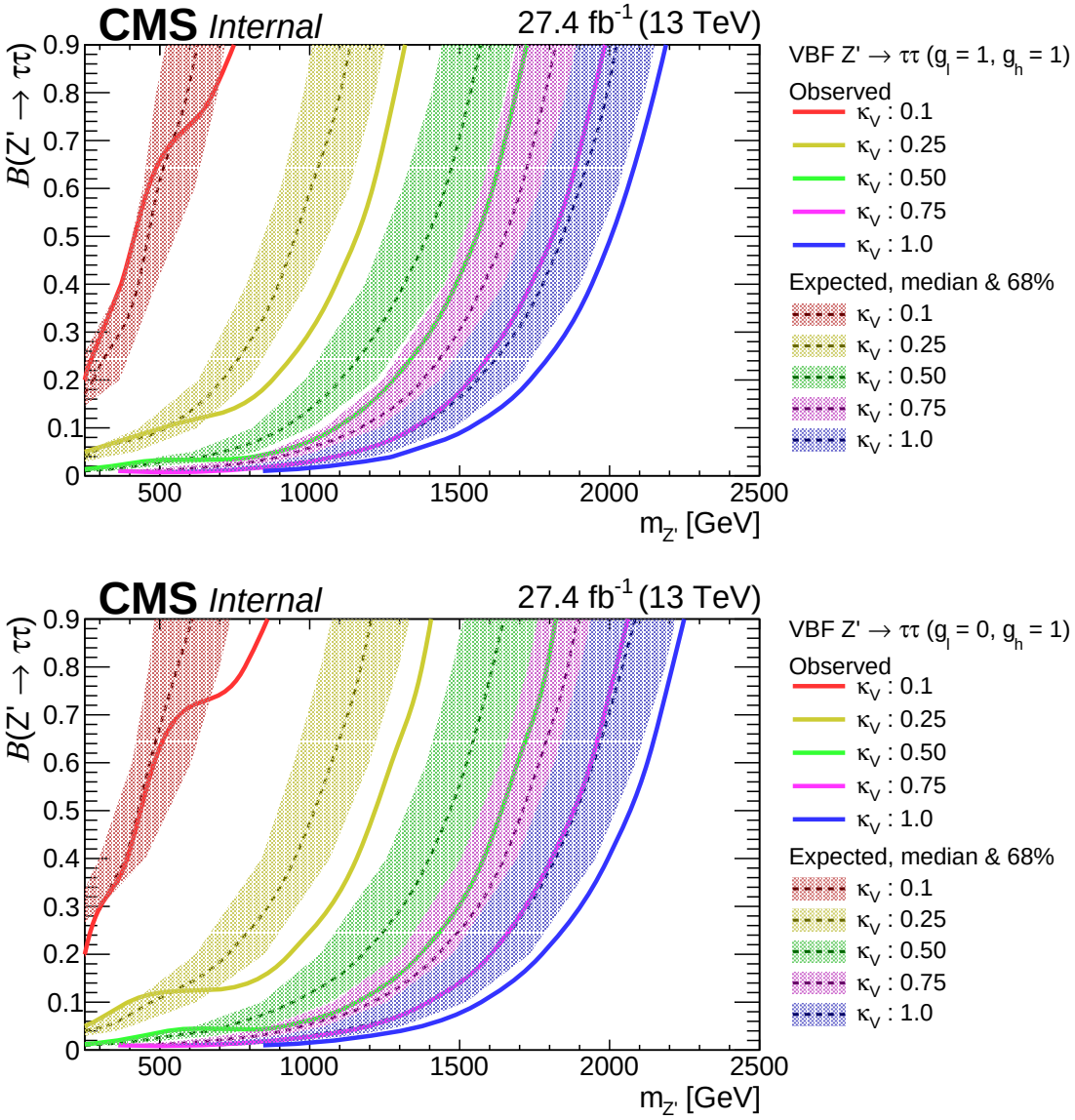

Figure 5.33: Exclusion region at 95% CL as a function of branching fraction of VBF $Z' \to \tau\tau$, $B(Z' \to \tau\tau)$ and $m_{Z'}$ with universal coupling to light and heavy fermions (top) and enhanced coupling to heavy fermions (bottom). The excluded regions are to the left of each curve. The observed exclusion bounds are indicated by the colored solid lines. The expected exclusion region and their ± 1 standard-deviation variations is shown in dashed colored curves for different κ_V scenarios.

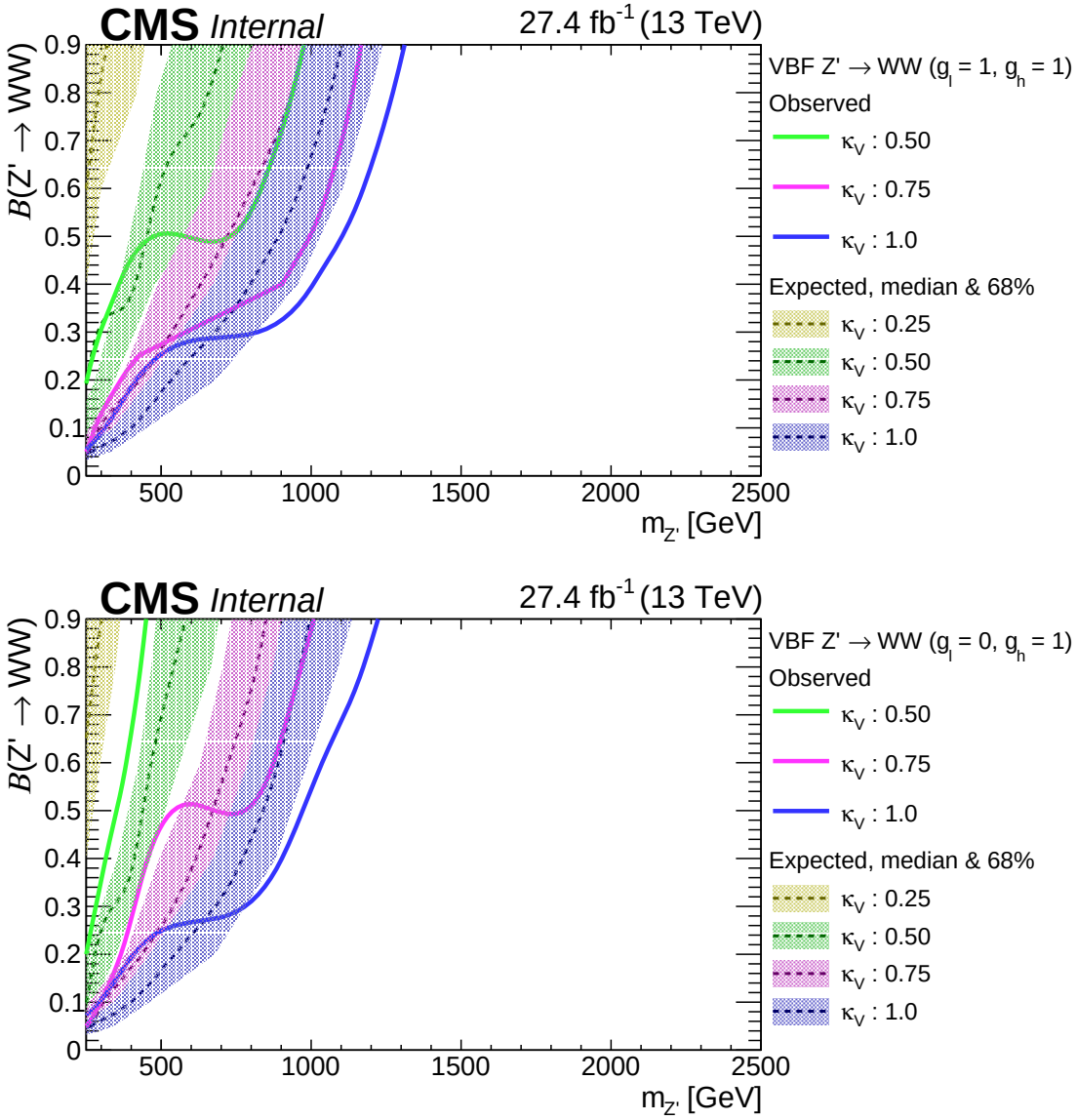

Figure 5.34: Exclusion region at 95% CL as a function of branching fraction of VBF $Z' \to WW$, $B(Z' \to WW)$ and $m_{Z'}$ with universal coupling to light and heavy fermions (top) and enhanced coupling to heavy fermions (bottom). The excluded regions are to the left of each curve. The observed exclusion bounds are indicated by the colored solid lines. The expected exclusion region and their ± 1 standard-deviation variations is shown in dashed colored curves for different κ_V scenarios.

To summarize, a first search for the heavy neutral gauge boson produced by the VBF processes is performed at the LHC with the pp collision data at center-of-mass energy of 13 TeV. No excess is observed over the estimated SM background. With this measurement, Z' below 1.77 TeV is being excluded for $B(Z' \to \tau\tau) = 20\%$ with enhanced coupling to third generation fermions. This measurement can be combined with other channels and DY Z' to further constraints the BSM parameters.

Bibliography

[1] T. G. Rizzo, "Z' phenomenology and the LHC", in *Theoretical Advanced Study Institute in Elementary Particle Physics: Exploring New Frontiers Using Colliders and Neutrinos*, pp. 537–575. 10, 2006. arXiv:hep-ph/0610104.

[2] J. L. Hewett and T. G. Rizzo, "Low-Energy Phenomenology of Superstring Inspired E(6) Models", *Phys. Rept.* **183** (1989) 193, doi:10.1016/0370-1573(89)90071-9.

[3] G. Altarelli, B. Mele, and M. Ruiz-Altaba, "Searching for New Heavy Vector Bosons in $p\bar{p}$ Colliders", *Z. Phys. C* **45** (1989) 109, doi:10.1007/BF01556677.

[4] S. D. Drell and T.-M. Yan, "Massive lepton-pair production in hadron-hadron collisions at high energies", *Phys. Rev. Lett.* **25** (Aug, 1970) 316–320, doi:10.1103/PhysRevLett.25.316.

[5] S. D. Drell and T.-M. Yan, "Massive lepton-pair production in hadron-hadron collisions at high energies", *Phys. Rev. Lett.* **25** (Sep, 1970) 902–902, doi:10.1103/PhysRevLett.25.902.2.

[6] CMS Collaboration, "Search for resonant and nonresonant new phenomena in high-mass dilepton final states at $\sqrt{s} = 13$ TeV", *JHEP* **07** (2021) 208, doi:10.1007/JHEP07(2021)208, arXiv:2103.02708.

[7] ATLAS Collaboration, "Search for high-mass dilepton resonances using 139 fb^{-1} of pp collision data collected at $\sqrt{s}$ =13 TeV with the ATLAS detector", *Phys. Lett. B* **796** (2019) 68–87, doi:10.1016/j.physletb.2019.07.016, arXiv:1903.06248.

[8] B. Dutta et al., "Vector Boson Fusion Processes as a Probe of Supersymmetric Electroweak Sectors at the LHC", *Phys. Rev. D* **87** (2013), no. 3, 035029, doi:10.1103/PhysRevD.87.035029, arXiv:1210.0964.

[9] A. G. Delannoy et al., "Probing Dark Matter at the LHC using Vector Boson Fusion Processes", *Phys. Rev. Lett.* **111** (2013) 061801, doi:10.1103/PhysRevLett.111.061801, arXiv:1304.7779.

[10] G. D'Amico et al., "Flavour anomalies after the $R(K*)$ measurement", *Journal of High Energy Physics* **2017** (Sep, 2017) doi:10.1007/jhep09(2017)010.

[11] B. Capdevila et al., "Patterns of New Physics in $b \to s\ell^+\ell^-$ transitions in the light of recent data", *Journal of High Energy Physics* **2018** (Jan, 2018) doi:10.1007/jhep01(2018)093.

[12] Belle Collaboration, A. Abdesselam et al., "Angular analysis of $B^0 \to K^*(892)^0\ell^+\ell^-$", in *LHC Ski 2016: A First Discussion of 13 TeV Results*. 4, 2016. arXiv:1604.04042.

[13] J. P. Lees et al., "Search forB→K(*)$\nu\overline{\nu}$ and invisible quarkonium decays", *Phys. Rev. D* **87** (Jun, 2013) doi:10.1103/physrevd.87.112005.

[14] C. T. Hill, "Topcolor assisted technicolor", *Phys. Lett. B* **345** (1995) 483–489, doi:10.1016/0370-2693(94)01660-5, arXiv:hep-ph/9411426.

[15] A. Flórez et al., "Searching for new heavy neutral gauge bosons using vector boson fusion processes at the LHC", *Phys. Lett. B* **767** (2017) 126–132, doi:https://doi.org/10.1016/j.physletb.2017.01.062.

[16] J. Alwall et al., "Comparative study of various algorithms for the merging of parton showers and matrix elements in hadronic collisions", *Eur. Phys. J. C* **53** (2008) 473–500, doi:10.1140/epjc/s10052-007-0490-5, arXiv:0706.2569.

[17] T. Sjostrand, S. Mrenna, and P. Z. Skands, "A Brief Introduction to PYTHIA 8.1", *Comput. Phys. Commun.* **178** (2008) 852–867, doi:10.1016/j.cpc.2008.01.036, arXiv:0710.3820.

[18] GEANT4 Collaboration, "GEANT4–a simulation toolkit", *Nucl. Instrum. Meth. A* **506** (2003) 250–303, doi:10.1016/S0168-9002(03)01368-8.

[19] CMS Collaboration, "Search for a heavy neutral gauge boson using vector boson fusion processes", *AN-18-200* (2022).

[20] Raphael Gomes De Souza. https://twiki.cern.ch/twiki/bin/view/Sandbox/TestTopic11111203.

[21] CMS Collaboration, "Performance of the CMS muon detector and muon reconstruction with proton-proton collisions at $\sqrt{s} = 13$ TeV", *Journal of Instrumentation* **13** (2018), no. 06, P06015, doi:10.1088/1748-0221/13/06/P06015, arXiv:1804.04528.

[22] A. Sirunyan et al., "Electron and photon reconstruction and identification with the CMS experiment at the CERN LHC", *Journal of Instrumentation* **16** (May, 2021) P05014, doi:10.1088/1748-0221/16/05/p05014.

[23] CMS Collaboration, "Identification of hadronic tau lepton decays using a deep neural network", 2022. arXiv:2201.08458. Submitted to *Journal of Instrumentation*.

[24] CMS Collaboration, "Performance of the DeepTau algorithm for the discrimination of taus against jets, electron, and muons", *CMS-DP-2019-033* (Oct, 2019).

[25] S. Chatrchyan et al., "Identification of heavy-flavour jets with the CMS detector in pp collisions at 13 TeV", *Journal of Instrumentation* **13** (may, 2018) P05011–P05011, doi:10.1088/1748-0221/13/05/p05011.

[26] D. Guest et al., "Jet flavor classification in high-energy physics with deep neural networks", *Phys. Rev. D* **94** (Dec, 2016) 112002, doi:10.1103/PhysRevD.94.112002.

[27] M. Cacciari, G. P. Salam, and G. Soyez, "The anti-ktjet clustering algorithm", *Journal of High Energy Physics* **2008** (Apr, 2008) 063–063, doi:10.1088/1126-6708/2008/04/063.

[28] CMS Collaboration. https://twiki.cern.ch/twiki/bin/view/CMSPublic/StripsOfflinePlots2016#2016H_25ns.

[29] CMS Collaboration, "Operation and Performance of the CMS outer tracker", *PoS* **Vertex 2017** (2018) 013, doi:10.22323/1.309.0013.

[30] M. French et al., "Design and results from the apv25, a deep sub-micron cmos front-end chip for the cms tracker", *Nuclear Instruments and Methods in Physics Research Section A: Accelerators, Spectrometers, Detectors and Associated Equipment* **466** (2001), no. 2, 359–365, doi:https://doi.org/10.1016/S0168-9002(01)00589-7. 4th Int. Symp. on Development and Application of Semiconductor Tracking Detectors.

[31] NNPDF Collaboration, "Parton distributions for the LHC Run II", *Journal of High Energy Physics* **04** (2015) 040, doi:10.1007/JHEP04(2015)040, arXiv:1410.8849.

[32] P. Nadolsky et al., "Implications of CTEQ global analysis for collider observables", *Phys. Rev. D 78 (2008) 013004, arXiv:0802.0007.*

[33] CMS Collaboration, "Precision luminosity measurement in proton-proton collisions at $\sqrt{s} = 13$ TeV in 2015 and 2016 at CMS", *Eur. Phys. J. C* **81** (2021) 800, doi:10.1140/epjc/s10052-021-09538-2, arXiv:2104.01927.

[34] CMS Collaboration, "CMS luminosity measurement for the 2017 data-taking period at $\sqrt{s} = 13$ TeV", CMS Physics Analysis Summary CMS-PAS-LUM-17-004, 2018.

[35] CMS Collaboration, "CMS luminosity measurement for the 2018 data-taking period at $\sqrt{s} = 13$ TeV", CMS Physics Analysis Summary CMS-PAS-LUM-18-002, 2019.

[36] CMS Collaboration, "Utilities for Accessing Pileup Information for Data". `https://twiki.cern.ch/twiki/bin/view/CMS/PileupJSONFileforData`.

[37] CMS Collaboration, "Performance of b–Jet Identification in CMS", *Journal of Instrumentation* **8** (2013) P04013, `doi:10.1088/1748-0221/8/04/P04013`.

[38] CMS Collaboration, "Electron and photon reconstruction and identification with the CMS experiment at the CERN LHC", *Journal of Instrumentation* **16** (2021) P05014, `doi:10.1088/1748-0221/16/05/P05014`.

[39] CMS Collaboration, "Performance of the CMS muon detector and muon reconstruction with proton-proton collisions at $\sqrt{s} = 13$ TeV", *Journal of Instrumentation* (2018) `doi:10.1088/1748-0221/13/06/P06015`.

[40] A. L. Read, "Presentation of search results: the CLs technique", *J. Phys. G* **28** (2002) 2693, `doi:10.1088/0954-3899/28/10/313`.

[41] T. Junk, "Confidence level computation for combining searches with small statistics", *Nucl. Instrum. Meth. A* **434** (1999) 435, `doi:10.1016/S0168-9002(99)00498-2`.

Chapter 6

Summary

The Large Hadron Collider (LHC) is the world's largest particle accelerator and is designed to explore the standard model (SM) physics as well as the new physics beyond the standard model. The LHC started its journey in the year 2009 by colliding proton-proton (pp) beams at the center-of-mass energy of 0.9 TeV and then at 2.36 TeV. The beam energy is progressively ramped up over the years with each LHC run, in order to reach its design energy of 14 TeV. During the Run 2 of the LHC, the pp collisions took place at the center-of-mass energy of 13 TeV. The high center-of-mass energy creates particles at the TeV scale, where new particles are predicted to exist. These new particles are expected to address various physics phenomena that SM fails to explain such as the existence of dark matter, the matter-antimatter asymmetry in the universe, the non-zero mass of neutrinos, etc.

The Compact Muon Solenoid (CMS) is a general purpose detector situated at the LHC ring and is one of the four LHC pp collision points. The CMS detector is designed to perform precise measurements of the SM physics and to search for the new physics signatures which can address a variety of physics questions. The work presented in this Thesis is based on the participation in detector R&D and physics measurements with the CMS experiment as discussed below.

6.1 Detector assembly and performance studies

During the LHC Run 2 operation, the CMS detector recorded *pp* collision data at the center-of-mass energy of 13 TeV with an instantaneous luminosity of $1.5 \times 10^{34}\,\mathrm{cm^{-2}s^{-1}}$. Different subdetectors in the CMS, placed at specific positions, measure the momentum, energy and position of the particles produced in the collisions. The muon system of the CMS detector measures the momentum of the particles and is comprised of cathode strip chambers (CSC), drift tubes (DT) and resistive plate chambers (RPC), which are based on different detection technologies to enhance the performance of the muon system. The detectors are placed in different combinations to improve the timing and the spatial resolution of the system. To further increase the muon trigger and reconstruction efficiency, the gaseous electron multiplier (GEM) chambers are installed in the muon endcap system within pseudorapidity range $1.6 < |\eta| < 2.2$ at a distance of 5.6 m from the interaction point. There are total 144 chambers installed in both endcaps, which are assembled and tested by six laboratories around the world. As a primary production site, Panjab University assembled and tested eight chambers. The detectors are assembled in the class 100 clean room, to avoid any dust particle entering inside the detector. After the assembly of GEM detectors, various quality control (QC) tests are performed at Panjab University site. All the detectors qualified the QC tests are later shipped to CERN for further testing and superchamber assembly. These detectors have already been installed in the endcap of the CMS muon system, are performing with the optimal efficiency, and are part of the data taking.

These GEM detectors are installed in the forward region of the CMS detector, and are subjected to large radiation dose which can deteriorate the performance of these detectors. The effect of these environmental background particles is estimated in Monte Carlo (MC) and is compared with data taken by test chambers installed in the CMS experiment (GE1/1) during Run 2. The simulation framework, used in this study, uses a combination of the FLUKA and GEANT4 packages to obtain the background hit rate. FLUKA provides the radiation environment around the GE1/1

chambers, which is comprised of the particle flux with momentum direction and energy spectra of neutrons, photons, $e^{\pm}$, and for charged hadrons. GEANT4 provides an estimate of detector response (sensitivity) based on the detector geometry, material composition and interaction of the particles with the various detector layers. In the present studies, it is observed that the neutrons are the major contributing background particles (84%), whereas, the second largest contribution (15%) comes from the photons. A very small contribution (1%) comes from the charged hadrons and $e^{\pm}$. These MC simulated hit rates are estimated as a function of the perpendicular distance from the beam line and agrees with the *pp* collision data within the assigned uncertainties.

The Hadron Calorimeter (HCAL) at the CMS detector is subjected to large flux of incident particles such as hadrons and muons, produced in the *pp* collision. Due to continuous exposure to these incident particles, the plastic scintillators in the HCAL experience degradation in their light output. In the present Thesis, the measurement of the loss in the light output of the plastic scintillators using the isolated muons from the *pp* collision data is presented. For this measurement, the *pp* collision data collected by the CMS detector during 2018 is analyzed which corresponds to 68 fb^{-1} of the total delivered luminosity by the LHC. The isolated muons deposit their energy in the layers of HCAL towers, which is measured as a function of the LHC delivered luminosity to measure the effect of radiation. The charge distribution of these muons is measured for each tower in $|\eta|$ and ϕ, indexed as $i\eta$ and $i\phi$. This measured charge distribution is then fitted with a Gaussian convolved Landau function to get the most probable value (MPV) of charge. It is observed that the towers in the central hadron barrel calorimeter region (-10 $< i\eta <$ 10) show very small degradation ($\sim$2%). The level of radiation damage increases at larger barrel $|i\eta|$ values ($\sim$ 10% for $i\eta = 16$). The loss in the light output further increases for hadron endcap calorimeter towers ($i\eta > 16$). The loss becomes as large as $\sim$15% at the highest $i\eta$. In addition this, these measurements are performed with two additional methods : MPV of charge from the combined $i\phi$ distribution and truncated mean method. The results are then compared with the measurements performed

by the CMS experiment using energy deposited by the hadrons from the collision data. The results obtained from the four methods are consistent with each other, except for depth 1. The depth 1 of the HCAL lies near to the interaction point and experiences a large particle flux resulting from the multiple interactions (pileup) occuring during the *pp* collision. Due to this, the measured charge distribution for the depth 1 becomes very broad. As a result, the precise measurement of the MPV of charge becomes difficult. To study the effect of pileup on the MPV of charge, the *pp* collision data collected during the low luminosity runs in 2018 are studied. The MPV values, measured from the normal luminosity runs and the low luminosity runs, are compared for the most affected towers i.e. $i\eta$ tower 23 to 26, depth 1. It is observed that the MPV values for $i\eta = 23$ and $i\eta = 24$ are in agreement for the two data, whereas, for the $i\eta = 25$ and $i\eta = 26$, where the pileup activity is higher, the low luminosity runs yield systematically lower values of the MPV of charge with better precision. Therefore, for the radiation damage studies in the higher $i\eta$ region, the measurements need to be made with the low luminosity runs.

6.2 Search for heavy neutral gauge boson using VBF processes

In this Thesis, the search for the heavy neutral gauge boson, Z' produced through vector boson fusion (VBF) processes is performed using the *pp* collision data collected by the CMS detector at the center-of-mass energy of 13 TeV. The hypothetical Z' boson arises from the extensions of the electroweak symmetry of the SM. The Z' is assumed to be produced from the fusion of the vector bosons radiated by the incoming quarks. The quarks hadronize to produce the forward jets with large pseudorapidity gap in them and carry large dijet invariant mass. The Z' is assumed to decay to $\tau^+\tau^-$ pair or W^+W^- pair, which further decays to $\mu\tau_h$ pair or $e\tau_h$ pair. Hence, the two final states presented in this Thesis consist of oppositely charged $\mu\tau_h$ pair and $e\tau_h$ pair, two forward jets and missing transverse energy due to corre-

sponding neutrinos. The selection criteria have been designed targeting exactly one light lepton (μ or e) and exactly one hadronic tau (τ_h) in the central region with missing transverse energy requirement and at least two jets with large pseudorapidity gap, lying in the opposite hemisphere of the detector with large dijet invariant mass. The dominating background process for these final states is the jet $\rightarrow$ fake τ_h background, in which jets from SM processes give the same signature as the τ_h candidate. These processes mainly include W+jets process and $t\bar{t}$ semi-leptonic process. Due to mismodeling of fakes in the MC simulation, the jet $\rightarrow$ fake τ_h background is estimated using data-driven approach. Other contributing backgrounds such as $t\bar{t}$ fully leptonic, diboson, DY+jets is estimated using their respective MC simulations. Due to suppressed hadron activity in the forward jets, the contribution of QCD multijet process is significantly reduced. The excess of events in the data above the SM backgrounds are looked for and no significant excess has been observed within uncertainties for the analysis presented in this Thesis.

The upper exclusion limits on the production cross-section times the branching ratio are calculated for different models considered in this Thesis. The dilepton mass ($m_{\ell\ell}$) distribution is used as the fit variable after combining $\mu\tau_h$ and $e\tau_h$ final states to look for an excess in data and to estimate the final results. A combined likelihood is constructed in the bins of $m_{\ell\ell}$ distribution to compute the upper limits on the Z' production cross-section at 95% CL using the asymptotic CLs criterion. Systematic and statistical uncertainties are taken into account as nuisance parameters. For a broad and generic discussion, the branching ratio ranging from 1% to 90% is considered for $Z' \rightarrow \tau\tau$ and $Z' \rightarrow WW$ decay. The branching fraction of 100% is avoided, due to unitarity violation.

As discussed in Section 5.8, the limits are computed for various coupling scenarios i.e. considering the minimum coupling of Z' to vector bosons (κ_V : 0.1) to maximum allowed coupling (κ_V : 1.0). Similarly, to target the model motivated by the B meson anomalies, the limits are computed for models having enhanced coupling to heavy (third generation) fermions besides the universal coupling to light (first and second generation) and heavy fermions.

The analysis presented in this Thesis provides the first set of results at the LHC for the search of Z' produced through VBF mechanism. The Z' is observed to be excluded below $m_{Z'}$ to be 1.72 TeV with 20% branching fraction in case of universal coupling to light and heavy fermions, whereas Z' is observed to be excluded below 1.77 TeV in the case of enhanced coupling to heavy fermions. Similarly, in the case of $Z' \to WW$ decay, with universal coupling to light and heavy fermions, Z' is observed to be excluded below $m_{Z'}$ to be 1.28 TeV with 80% branching fraction, whereas Z' is observed to be excluded below 1.20 TeV in the case of enhanced coupling to heavy fermions. For the different coupling scenarios considered in this Thesis, different exclusion limits are observed and are presented in this Thesis.

6.3 Outlook

The LHC aims to collect the pp collision data of about 4000 fb^{-1} of integrated luminosity until the year 2040. The LHC and its detectors undergo several upgrades during each run period to increase the discovery potential of rare processes. For the preparation of the High Luminosity LHC (HL-LHC) starting in 2027, the CMS detector is planned to undergo an intensive upgrade and maintenance program. The muon system of the CMS detector must be able to sustain five times larger luminosity and maintain sensitivity for the electroweak physics at the TeV scale. To cope up with the corresponding increase in the background rates and trigger requirements, additional sets of muon detectors based on the GEM technology, referred to as GE2/1, and ME0 will be installed. These additional GEM detectors will add redundancy to the forward region of the muon system and allow trigger threshold values of muons to be kept at lower transverse momentum values, which will allow higher efficiency to capture new and interesting physics aspects.

The modeling of the GE1/1 detector response to the background particles provides a reliable estimate of background rates expected during Run 3 operation of LHC and HL-LHC run period. The GE1/1 detector response during Run 3 operation is also planned to be measured. These studies will provide relevant information for

detector design and operation at HL-LHC.

At the time of writing this Thesis, the LHC Run 3 is in preparation. For Run 3, the HCAL detector has upgraded their readout system from hybrid photodiodes to silicon photomultipliers for the barrel HCAL towers. This has led to increased depth segmentation in barrel for better reconstruction of hadrons and their energy. To monitor the effect of radiation on the barrel and endcap scintillators, the energy deposited by the isolated muons from the pp collision will be examined during LHC Run 3. Muons, being the minimum ionizing particles, are the most suitable candidates for depth dependent calibration studies and radiation damage studies. Due to pileup contamination in the high η region, data from the low luminosity runs is planned to be examined. Besides this, to correct the pileup contamination in the data, deep neural network (DNN) based pileup correction weights are being developed which will be utilized during Run 3 measurements and for the HL-LHC runs.

In this Thesis, the VBF Z' search is performed with $\mu\tau_h$ and $e\tau_h$ final states with pp collision data corresponding to 27.4 fb^{-1} of integrated luminosity. The additional final states considered in the analysis, i.e., $e\mu$ and $\tau_h\tau_h$, are being measured by other groups in the CMS experiment. The results from all the four final states will be combined to get the final set of limits on the production cross-section of the Z'. Besides this, the studies will be performed with full Run 2 pp collision data, corresponding to an integrated luminosity of 137 fb^{-1}. The VBF Z' search holds a great discovery potential in the coming LHC runs due to its unique topology, leading to increased signal sensitivity and better rejection of background events from SM processes. To further improve the tagging of VBF events, a DNN based event tagger has been developed for the search for Z' produced through VBF mechanism with Run 3 LHC data. The results will be combined with traditional DY Z' searches thus far, for better exclusion limits.

Publications/Conferences

Publications and CMS Public Notes with Direct Contribution

1. CMS Collaboration, "Benchmarking LHC background particle simulation with the CMS triple-GEM detector," JINST **16**, P12026 (2021) doi:10.1088/1748-0221/16/12/P12026 [arXiv:2107.03621].

2. CMS Collaboration, "Measurements with silicon photomultipliers of dose-rate effects in the radiation damage of plastic scintillator tiles in the CMS hadron endcap calorimeter," JINST **15**, P06009 (2020) doi:10.1088/1748-0221/15/06/P06009 [arXiv:2001.06553].

3. Aashaq Shah, A. K. Virdi *et al.*, "Layout and Assembly Technique of the GEM Chambers for the Upgrade of the CMS First Muon Endcap Station," Nucl. Instrum. Meth. A **918**, 67-75 (2019) doi:10.1016/j.nima.2018.11.061 [arXiv:1812.00411].

4. A. K. Virdi *et al.*, "Study of Radiation Damage in the CMS Hadron Endcap Calorimeter using Isolated Muons from Collision Data," **CMS DN-2021/016** , Aug, 2021.

5. A. K. Virdi *et al.*, "Study of Radiation Damage in the CMS Hadron Barrel Calorimeter using Isolated Muons from Collision Data," **CMS DN-2020/042** , Oct, 2020.

6. A. K. Virdi *et al.*, "Issues in Studying Radiation Damage of the CMS Hadron Calorimeter using Isolated Muons in the 2018 Collision Data," **CMS DN-2020/039**, Sep, 2020.

7. A. K. Virdi *et al.*, "Calibration of the CMS Hadron Calorimeter using Isolated Muons from Collision Data," **CMS DN-2018/014**, April, 2018.

8. CMS Collaboration, "Search for a heavy neutral gauge boson using Vector Boson Fusion processes," **CMS AN-18-200** (2022).

[*] **CMS AN - CMS Analysis Note**

[*] **CMS DN - CMS Detector Note**

Conference proceedings

1. A. K. Virdi, S. Bansal, S. B. Beri, V. Bhatnagar, S. Chauhan, R. Gupta, J. Babbar, H. Kaur, S. Kumar and P. Kumari, *et al.* "Fabrication and Characterization of Gaseous Detector for the identification of High Energy Particles.," IOP Conf. Ser. Mater. Sci. Eng. **1033**, 012055 (2021) doi:10.1088/1757-899X/1033/1/012055

2. A. K. Virdi [ATLAS and CMS], "Exotic searches by ATLAS and CMS," J. Phys. Conf. Ser. **1690**, 012169 (2020) doi:10.1088/1742-6596/1690/1/012169

3. A. K. Virdi, M. Meena, P. Kumari, R. Gupta, J. S. Shahi, S. Bansal, V. Bhatnagar, J. B. Singh and Manisha, "Quality Control Testing of GEM Detector," DAE Symp. Nucl. Phys. **62**, 1056-1057 (2017)

Papers presented in Conferences, Workshops, Symposiums

1. A. K. Virdi *et al.*, "Calibration of the CMS Hadron Calorimeter using Isolated Muons from Collision Data,", **23^{rd} DAE-BRNS HIGH ENERGY PHYSICS SYMPOSIUM 2018,** Dec 10^{th} - 14^{th} 2018, IIT Madras, Chennai, India.

2. A. K. Virdi *et al.*, "Search for heavy neutral gauge boson Z' at LHC," **Chandigarh Science Congress (CHASCON-2019)**, March 13^{th} - 15^{th} 2019, Panjab University, India.

3. A. K. Virdi *et al.*, "Exotic searches by CMS and ATLAS," **5^{th} International Conference on Particle Physics and Astrophysics**, Oct 5^{th} - 9^{th} 2020, National Research Nuclear University, Moscow (Russian Federation).

4. A. K. Virdi *et al.*, "Study of Radiation Damage in the CMS Hadron Calorimeter using Isolated Muons from 2018 Collision Data," **24^{th} DAE-BRNS HIGH ENERGY PHYSICS SYMPOSIUM 2018,** Dec 14^{th} - 18^{th} 2020, NISER Bhubaneswar, India.

5. A. K. Virdi *et al.*, "Radiation damage of plastic scintillators in CMS hadron calorimeter at LHC," **Chandigarh Science Congress (CHASCON-2020)**, Dec 17^{th} - 19^{th} 2020, Panjab University, India.

6. A. K. Virdi *et al.*, "Search for New Heavy Neutral Gauge Boson using Vector Boson Fusion Processes at the LHC," **LHCP2021: 9th Edition of the Large Hadron Collider Physics Conference**, Jun 7^{th} - 12^{th} 2021, Paris.

7. A. K. Virdi *et al.*, "Exotic physics signatures at CMS," **Lomonosov 2021: 20th Lomonosov Conference on Elementary Particle Physics**, Aug 19^{th} - 25^{th} 2021, Moscow State University, Moscow (Russian Federation).

Publications as co-author with CMS Collaboration

1. CMS Collaboration, "Search for invisible decays of the Higgs boson produced via vector boson fusion in proton-proton collisions at $\sqrt{s} = 13$ TeV," Phys. Rev. D **105**, 092007 (2022) doi:10.1103/PhysRevD.105.092007 [arXiv:2201.11585 [hep-ex]].

2. CMS Collaboration, "Observation of $B^0 \to \psi(2S) K^0_S \pi^+ \pi^-$ and $B^0_S \to \psi(2S) K^0_S$ decays," Eur. Phys. J. C **82**, 499 (2022) doi:10.1140/epjc/s10052-022-10315-y [arXiv:2201.09131 [hep-ex]].

3. CMS Collaboration, "Precision measurement of the W boson decay branching fractions in proton-proton collisions at $\sqrt{s} = 13$ TeV," Phys. Rev. D **105**, no.7, 072008 (2022) doi:10.1103/PhysRevD.105.072008 [arXiv:2201.07861 [hep-ex]].

4. CMS Collaboration, "Measurement of the inclusive and differential $t\bar{t}\gamma$ cross sections in the dilepton channel and effective field theory interpretation in proton-proton collisions at $\sqrt{s}$ =13 TeV," JHEP **05**, 091 (2022) doi:10.1007/JHEP05(2022)091 [arXiv:2201.07301 [hep-ex]].

5. CMS Collaboration, "Search for higgsinos decaying to two Higgs bosons and missing transverse momentum in proton-proton collisions at $\sqrt{s} = 13$ TeV,"

JHEP **05**, 014 (2022) doi:10.1007/JHEP05(2022)014 [arXiv:2201.04206 [hep-ex]].

6. CMS Collaboration, "Search for single production of a vector-like T quark decaying to a top quark and a Z boson in the final state with jets and missing transverse momentum at $\sqrt{s} = 13$ TeV," JHEP **05**, 093 (2022) doi:10.1007/JHEP05(2022)093 [arXiv:2201.02227 [hep-ex]].

7. CMS Collaboration, "Search for long-lived particles decaying into muon pairs in proton-proton collisions at $\sqrt{s} = 13$ TeV collected with a dedicated high-rate data stream," JHEP **04**, 062 (2022) doi:10.1007/JHEP04(2022)062 [arXiv:2112.13769 [hep-ex]].

8. CMS Collaboration, "Measurement of the production cross section for Z+b jets in proton-proton collisions at $\sqrt{s} = 13$ TeV," Phys. Rev. D **105**, no.9, 092014 (2022) doi:10.1103/PhysRevD.105.092014 [arXiv:2112.09659 [hep-ex]].

9. CMS Collaboration, "Search for flavor-changing neutral current interactions of the top quark and the Higgs boson decaying to a bottom quark-antiquark pair at $\sqrt{s} = 13$ TeV," JHEP **02**, 169 (2022) doi:10.1007/JHEP02(2022)169 [arXiv:2112.09734 [hep-ex]].

10. CMS Collaboration, "Measurement of the inclusive $\mathrm{t\bar{t}}$ production cross section in proton-proton collisions at $\sqrt{s} = 5.02$ TeV," JHEP **04**, 144 (2022) doi:10.1007/JHEP04(2022)144 [arXiv:2112.09114 [hep-ex]].

11. CMS Collaboration, "Search for a right-handed W boson and a heavy neutrino in proton-proton collisions at $\sqrt{s} = 13$ TeV," JHEP **04**, 047 (2022) doi:10.1007/JHEP04(2022)047 [arXiv:2112.03949 [hep-ex]].

12. CMS Collaboration, "Search for heavy resonances decaying to a pair of Lorentz-boosted Higgs bosons in final states with leptons and a bottom quark pair at $\sqrt{s}$= 13 TeV," JHEP **05**, 005 (2022) doi:10.1007/JHEP05(2022)005 [arXiv:2112.03161 [hep-ex]].

13. CMS Collaboration, "Measurement of $W^{\pm}\gamma$ differential cross sections in proton-proton collisions at $\sqrt{s} = 13$ TeV and effective field theory constraints," Phys. Rev. D **105**, no.5, 052003 (2022) doi:10.1103/PhysRevD.105.052003 [arXiv:2111.13948 [hep-ex]].

14. CMS Collaboration, "Search for heavy resonances decaying to ZZ or ZW and axion-like particles mediating nonresonant ZZ or ZH production at $\sqrt{s} = 13$ TeV," JHEP **04**, 087 (2022) doi:10.1007/JHEP04(2022)087 [arXiv:2111.13669 [hep-ex]].

15. CMS Collaboration, "Search for a heavy resonance decaying into a top quark and a W boson in the lepton+jets final state at $\sqrt{s} = 13$ TeV," JHEP **04**, 048 (2022) doi:10.1007/JHEP04(2022)048 [arXiv:2111.10216 [hep-ex]].

16. CMS Collaboration, "Measurement and QCD analysis of double-differential inclusive jet cross sections in proton-proton collisions at $\sqrt{s} = 13$ TeV," JHEP **02**, 142 (2022) doi:10.1007/JHEP02(2022)142 [arXiv:2111.10431 [hep-ex]].

17. CMS Collaboration, "Search for supersymmetry in final states with two or three soft leptons and missing transverse momentum in proton-proton collisions at $\sqrt{s} = 13$ TeV," JHEP **04**, 091 (2022) doi:10.1007/JHEP04(2022)091 [arXiv:2111.06296 [hep-ex]].

18. CMS Collaboration, "Study of dijet events with large rapidity separation

in proton-proton collisions at $\sqrt{s} = 2.76$ TeV," JHEP **03**, 189 (2022) doi:10.1007/JHEP03(2022)189 [arXiv:2111.04605 [hep-ex]].

19. CMS Collaboration, "Inclusive and differential cross section measurements of single top quark production in association with a Z boson in proton-proton collisions at $\sqrt{s} = 13$ TeV," JHEP **02**, 107 (2022) doi:10.1007/JHEP02(2022)107 [arXiv:2111.02860 [hep-ex]].

20. CMS Collaboration, "A new calibration method for charm jet identification validated with proton-proton collision events at $\sqrt{s}$ =13 TeV," JINST **17**, no.03, P03014 (2022) doi:10.1088/1748-0221/17/03/P03014 [arXiv:2111.03027 [hep-ex]].

21. CMS Collaboration, "Search for long-lived particles produced in association with a Z boson in proton-proton collisions at $\sqrt{s} = 13$ TeV," JHEP **03**, 160 (2022) doi:10.1007/JHEP03(2022)160 [arXiv:2110.13218 [hep-ex]].

22. CMS Collaboration, "Analysis of the CP structure of the Yukawa coupling between the Higgs boson and τ leptons in proton-proton collisions at $\sqrt{s} = 13$ TeV," JHEP **06**, 012 (2022) doi:10.1007/JHEP06(2022)012 [arXiv:2110.04836 [hep-ex]].

23. CMS Collaboration, "Search for long-lived particles decaying to leptons with large impact parameter in proton-proton collisions at $\sqrt{s} = 13\,\text{TeV}$," Eur. Phys. J. C **82**, no.2, 153 (2022) doi:10.1140/epjc/s10052-022-10027-3 [arXiv:2110.04809 [hep-ex]].

24. CMS Collaboration, "Measurement of double-parton scattering in inclusive production of four jets with low transverse momentum in proton-proton colli-

sions at $\sqrt{s} = 13$ TeV," JHEP **01**, 177 (2022) doi:10.1007/JHEP01(2022)177 [arXiv:2109.13822 [hep-ex]].

25. CMS Collaboration, "Search for heavy resonances decaying to WW, WZ, or WH boson pairs in the lepton plus merged jet final state in proton-proton collisions at $\sqrt{s} = 13$ TeV," Phys. Rev. D **105**, no.3, 032008 (2022) doi:10.1103/PhysRevD.105.032008 [arXiv:2109.06055 [hep-ex]].

26. CMS Collaboration, "Study of quark and gluon jet substructure in Z+jet and dijet events from pp collisions," JHEP **01**, 188 (2022) doi:10.1007/JHEP01(2022)188 [arXiv:2109.03340 [hep-ex]].

27. CMS Collaboration, "Observation of Bs0 mesons and measurement of the Bs0/B+ yield ratio in PbPb collisions at Image 1 TeV," Phys. Lett. B **829**, 137062 (2022) doi:10.1016/j.physletb.2022.137062 [arXiv:2109.01908 [hep-ex]].

28. CMS Collaboration, "Observation of tW production in the single-lepton channel in pp collisions at $\sqrt{s} = 13$ TeV," JHEP **11**, 111 (2021) doi:10.1007/JHEP11(2021)111 [arXiv:2109.01706 [hep-ex]].

29. CMS Collaboration, "Measurement of the top quark mass using events with a single reconstructed top quark in pp collisions at $\sqrt{s} = 13$ TeV," JHEP **12**, 161 (2021) doi:10.1007/JHEP12(2021)161 [arXiv:2108.10407 [hep-ex]].

30. CMS Collaboration, "Measurement of differential $t\bar{t}$ production cross sections in the full kinematic range using lepton+jets events from proton-proton collisions at $\sqrt{s} = 13$ TeV," Phys. Rev. D **104**, no.9, 092013 (2021) doi:10.1103/PhysRevD.104.092013 [arXiv:2108.02803 [hep-ex]].

31. CMS Collaboration, "Probing effective field theory operators in the associated production of top quarks with a Z boson in multilepton final states at $\sqrt{s} = 13$ TeV," JHEP **12**, 083 (2021) doi:10.1007/JHEP12(2021)083 [arXiv:2107.13896 [hep-ex]].

32. CMS Collaboration, "Search for new particles in events with energetic jets and large missing transverse momentum in proton-proton collisions at $\sqrt{s} = 13$ TeV," JHEP **11**, 153 (2021) doi:10.1007/JHEP11(2021)153 [arXiv:2107.13021 [hep-ex]].

33. CMS Collaboration, "Search for chargino-neutralino production in events with Higgs and W bosons using 137 fb^{-1} of proton-proton collisions at $\sqrt{s} = 13$ TeV," JHEP **10**, 045 (2021) doi:10.1007/JHEP10(2021)045 [arXiv:2107.12553 [hep-ex]].

34. CMS Collaboration, "Measurement of the inclusive and differential Higgs boson production cross sections in the decay mode to a pair of τ leptons in pp collisions at $\sqrt{s} = 13$ TeV," Phys. Rev. Lett. **128**, no.8, 081805 (2022) doi:10.1103/PhysRevLett.128.081805 [arXiv:2107.11486 [hep-ex]].

35. CMS Collaboration, "Combined searches for the production of supersymmetric top quark partners in proton–proton collisions at $\sqrt{s} = 13\,\text{TeV}$," Eur. Phys. J. C **81**, no.11, 970 (2021) doi:10.1140/epjc/s10052-021-09721-5 [arXiv:2107.10892 [hep-ex]].

36. CMS Collaboration, "Search for Long-Lived Particles Decaying in the CMS End Cap Muon Detectors in Proton-Proton Collisions at $\sqrt{s}$ =13 TeV," Phys. Rev. Lett. **127**, no.26, 261804 (2021) doi:10.1103/PhysRevLett.127.261804 [arXiv:2107.04838 [hep-ex]].

37. CMS Collaboration, "Measurement of the inclusive and differential $t\bar{t}\gamma$ cross sections in the single-lepton channel and EFT interpretation at $\sqrt{s} = 13$ TeV," JHEP **12**, 180 (2021) doi:10.1007/JHEP12(2021)180 [arXiv:2107.01508 [hep-ex]].

38. CMS Collaboration, "Measurements of the electroweak diboson production cross sections in proton-proton collisions at $\sqrt{s} = 5.02$ TeV using leptonic decays," Phys. Rev. Lett. **127**, no.19, 191801 (2021) doi:10.1103/PhysRevLett.127.191801 [arXiv:2107.01137 [hep-ex]].

39. CMS Collaboration, "Search for electroweak production of charginos and neutralinos in proton-proton collisions at $\sqrt{s} = 13$ TeV," JHEP **04**, 147 (2022) doi:10.1007/JHEP04(2022)147 [arXiv:2106.14246 [hep-ex]].

40. CMS Collaboration, "Fragmentation of jets containing a prompt J/ψ meson in PbPb and pp collisions at sNN=5.02TeV," Phys. Lett. B **825**, 136842 (2022) doi:10.1016/j.physletb.2021.136842 [arXiv:2106.13235 [hep-ex]].

41. CMS Collaboration, "Measurement of the electroweak production of $Z\gamma$ and two jets in proton-proton collisions at $\sqrt{s} = 13$ TeV and constraints on anomalous quartic gauge couplings," Phys. Rev. D **104**, 072001 (2021) doi:10.1103/PhysRevD.104.072001 [arXiv:2106.11082 [hep-ex]].

42. CMS Collaboration, "Search for $W\gamma$ resonances in proton-proton collisions at s=13 TeV using hadronic decays of Lorentz-boosted W bosons," Phys. Lett. B **826**, 136888 (2022) doi:10.1016/j.physletb.2022.136888 [arXiv:2106.10509 [hep-ex]].

43. CMS Collaboration, "Search for a heavy Higgs boson decaying into two lighter

Higgs bosons in the $\tau\tau$bb final state at 13 TeV," JHEP **11**, 057 (2021) doi:10.1007/JHEP11(2021)057 [arXiv:2106.10361 [hep-ex]].

44. CMS Collaboration, "Study of Z boson plus jets events using variables sensitive to double-parton scattering in pp collisions at 13 TeV," JHEP **10**, 176 (2021) doi:10.1007/JHEP10(2021)176 [arXiv:2105.14511 [hep-ex]].

***** Complete list of 297 published papers as a co-author in CMS : https://inspirehep.net/authors/1505513**

Selected

Reprints

Published by IOP Publishing for Sissa Medialab

Received: *January 18, 2020*
Revised: *March 29, 2020*
Accepted: *April 16, 2020*
Published: *June 8, 2020*

Measurements with silicon photomultipliers of dose-rate effects in the radiation damage of plastic scintillator tiles in the CMS hadron endcap calorimeter

The CMS collaboration

E-mail: cms-publication-committee-chair@cern.ch

Abstract: Measurements are presented of the reduction of signal output due to radiation damage for two types of plastic scintillator tiles used in the hadron endcap (HE) calorimeter of the CMS detector. The tiles were exposed to particles produced in proton-proton (pp) collisions at the CERN LHC with a center-of-mass energy of 13 TeV, corresponding to a delivered luminosity of 50 fb^{-1}. The measurements are based on readout channels of the HE that were instrumented with silicon photomultipliers, and are derived using data from several sources: a laser calibration system, a movable radioactive source, as well as hadrons and muons produced in pp collisions. Results from several irradiation campaigns using ^{60}Co sources are also discussed. The damage is presented as a function of dose rate. Within the range of these measurements, for a fixed dose the damage increases with decreasing dose rate.

Keywords: Large detector systems for particle and astroparticle physics; Scintillators, scintillation and light emission processes (solid, gas and liquid scintillators)

ArXiv ePrint: 2001.06553

https://doi.org/10.1088/1748-0221/15/06/P06009

Contents

2020 JINST 15 P06009

1 Introduction

Because of their versatility and low cost, plastic scintillators are used in the construction of detectors built for experiments at particle colliders. They are, however, subject to a reduction in their signal output after irradiation (radiation damage) [1]. Two of the hadron calorimeters (HCAL) of the CMS detector [2] — the hadron barrel (HB) [3] and the hadron endcap (HE) [4] — at the CERN LHC [5] use tiles constructed from plastic scintillator with embedded wavelength shifting (WLS) fibers to produce their signals. There are also plans to use scintillators in the CMS endcap calorimeters upgraded for the high-luminosity LHC runs [6].

This paper presents results on the reduction of signal collected from irradiated scintillator tiles as a function of dose rate R. These results provide unique information about radiation damage at dose rates significantly lower than previously studied. The HE tiles, described in section 3, and their associated fibers, were irradiated by particles produced in pp collisions at the LHC during 2017 at a center-of-mass energy of 13 TeV, corresponding to a delivered luminosity of 50 fb^{-1}. The R range is extended by including studies of tiles placed in a moderate-R region of the CMS collision hall forward of the HE, as well as tiles irradiated using external high-dose-rate ^{60}Co sources. The reliability of the measurements is improved by using tiles that were instrumented before the

2017 data-taking period with silicon photomultipliers (SiPMs, also known as Geiger Mode Silicon Avalanche Photodiodes). The HE tile results are obtained using several complementary methods. We use a movable radioactive source that can access all the tiles to compare their signal output before and after the 2017 data-taking period. Inclusive energy deposits from pp collisions and energy deposits by isolated muons are also used to monitor the signal output. In addition, some of the HE tiles and the tiles in the moderate-R region of the collision hall are studied using a laser calibration system. The results indicate an R-dependent effect; scintillators receiving the same ionizing dose at different dose rates have different reductions in collected signal.

This study supersedes our previous results [7], which were based on data collected in 2016 using hybrid photodiodes (HPDs) as the photodetectors. Those photodetectors were subsequently shown to have suffered significant response degradation over the course of the running period because of damage to the photocathodes by ion feedback [8], and not to radiation damage. In the previous publication [7], the reduction of signal output was attributed solely to radiation damage to the scintillator tiles.

This paper is organized as follows. In section 2, we summarize what is known about radiation damage mechanisms in plastic scintillators. In section 3, we give a brief description of the CMS detector, and a more detailed description of the HE calorimeter. In section 4, we present measurements of radiation damage to the tiles embedded within the HE. The calculation of the dose is described, followed by the results obtained using a laser calibration system to monitor the signal loss, and using a radioactive source for this purpose. A parametrization of the R dependence is given. The signal loss observed in response to hadrons during collisions is studied for consistency with the laser results, and the signal loss in response to muons is also shown. In section 5, we present studies of dose-rate effects measured outside of the CMS detector using irradiation by sources as well as studies using tiles in the moderate-radiation zone of the CMS collision hall. In section 6, we summarize other relevant information and discuss the dose-rate effects. Finally, in section 7, we present a summary and the conclusions of the paper.

2 Radiation damage mechanisms

For the purpose of our studies, we refer to the HCAL tiles as objects consisting of plastic scintillator, a WLS fiber, a Tyvek™ wrapping, a clear fiber, and a transducer. Our estimates, presented below, indicate that the contribution from WLS fibers to the overall signal loss is small, and the contributions from clear quartz fibers, Tyvek™ wrappers and the SiPM transducers are negligible. Consequently, we believe that our results represent primarily the damage to the scintillator tiles.

Plastic scintillators consist of a plastic substrate, often polystyrene (PS) or polyvinyltoluene (PVT), into which fluorescent agents (fluors) have been dissolved, usually a primary and a secondary fluor. When a charged particle traverses the scintillator, the molecules of the substrate are excited. This excitation can be transferred to the primary fluor via the Förster mechanism [9] at primary fluor concentrations above approximately 1% [10]. The primary fluor transfers the excitation radiatively to the secondary fluor. For the HCAL tiles made of SCSN−81, a PS-based scintillator from Kuraray, the absorption maximum of the primary fluor is at the wavelength of approximately 280 nm, and

Kuraray, Ote Center Building, 1-1-3, Otemachi, Chiyoda-ku, Tokyo 100-8115, Japan.

2020 JINST 15 P06009

the emission is approximately at 320–350 nm. The absorption maximum of the secondary fluor corresponds to the emission maximum of the primary fluor, and the de-excitation of the secondary fluor has a wavelength of maximum emission of approximately 440 nm (blue light). This visible light must traverse the scintillator to reach the WLS fiber, and can be reduced by imperfections in the material (color centers) along its path.

Generally, the scintillator signal output decreases exponentially with the dose received, as expected for light attenuation due to radiation-induced color centers; this behavior was also observed in source measurements [4], which were used to design the HCAL optics:

$$L(d) = L_0 \exp(-d/D) = L_0 \exp(-d\,\mu), \tag{2.1}$$

where $L(d)$ is the signal output after receiving a dose d, L_0 is the signal output before irradiation, μ is a function that depends on the dose rate R, and $D = 1/\mu$. When the damage is small compared to measurement uncertainties, D fluctuates to large positive or negative numbers. Therefore μ is used to fit the data and evaluate the uncertainties. The fitted values of μ can be averaged over bins of dose rate to improve statistical accuracy. The $\langle\mu\rangle$ results are used to parametrize the R dependence (D is shown in some figures of this paper).

The value of μ depends on the materials used in the fabrication of the scintillator and on how it is handled (e.g., if it comes into contact with oils, etc.) prior to and during experimental operations. Several results have been presented on the dependence on dose rate [7, 11–18]. In refs. [17], the authors saw no change in the signal output or attenuation length for SCSN−81 down to dose rates of 2 Gy/h, whereas the authors of refs. [11, 12] saw effects at dose rates between 10 Gy/h and 10 kGy/h. A review of the causes of dose-rate effects, and particularly the prominent role played by the diffusion of oxygen and polymer oxidation, is given in section 6.

Damage to the fluors can occur [13], but it is generally small [16, 19]. Damage to the substrate often results in the creation of radicals, conjugated double bonds, carbonyl species formed by reaction with oxygen, and trapped electrons, and other structures that can be color centers. Color centers that interfere with the transfer of light between the primary and secondary fluors reduce the initial light yield. Color centers that absorb the light output by the secondary fluor reduce the absorption length of the light in the scintillator.

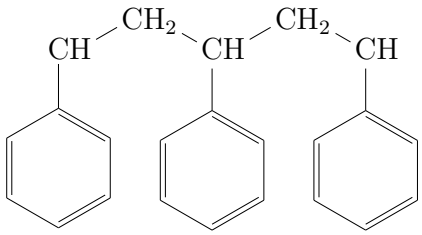

Figure 1. Polystyrene.

Radicals are produced when chemical bonds in the polymer are broken. The bonds can re-form on a time scale that depends on such factors as the density of the radicals and the temperature. Such damage is called temporary damage, and the re-forming of bonds is known as annealing. Some products cause permanent changes in the chemical structure. Figure 1 shows the chemical structure

2020 JINST 15 P06009

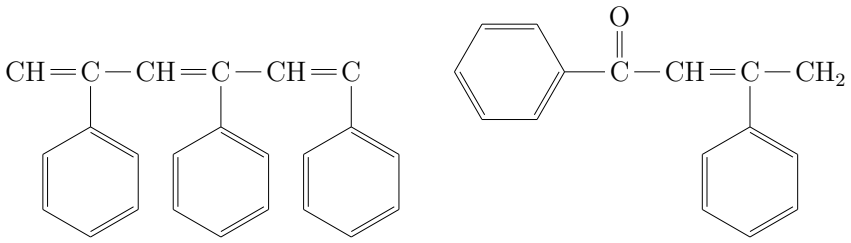

Figure 2. Examples of changes to polystyrene undergoing irradiation. The change on the right can only occur in the presence of oxygen.

of unirradiated PS. Figure 2 shows some of the permanent color centers that can be formed in PS [20].

3 CMS detector

The central feature of the CMS apparatus is a superconducting solenoid of 6 m internal diameter, providing a magnetic field of 3.8 T. Within the solenoid volume are silicon pixel and strip trackers, a lead tungstate crystal electromagnetic calorimeter (ECAL) composed of a barrel and two endcap sections, an endcap preshower, and the HB and HE.

The silicon tracker measures charged particles within the pseudorapidity range $|\eta| < 2.5$. It consists of 1440 silicon pixel and 15 148 silicon strip detector modules. Isolated particles of transverse momentum $p_T = 100$ GeV emitted at $|\eta| < 1.4$ have track resolutions of 2.8% in p_T and 10 (30) μm in the transverse (longitudinal) impact parameter [21]. Muons are measured in the range $|\eta| < 2.4$, with detection planes embedded in the steel flux-return yoke outside the solenoid that are made using three technologies: drift tubes, cathode strip chambers, and resistive plate chambers.

A more detailed description of the CMS detector, together with a definition of the coordinate system used and the relevant kinematic variables, can be found in ref. [2]. A description of the CMS trigger system can be found in ref. [22].

The scintillator tiles that exhibit damage are located in the HE, which has 18 layers of active material, denoted layers 0 through 17, over most of its η coverage. The zeroth layer of scintillator uses BC−408, a PVT-based scintillator from the Bicron division of the Saint-Gobain corporation, while the other layers use PS-based SCSN−81. Scintillators based on PVT are brighter than those based on PS.

The scintillator tiles are optically isolated. They are trapezoidal in shape, and their faces have a groove shaped like the Greek letter σ that holds a 0.94 mm-diameter Y−11 (Kuraray) WLS fiber, mirrored on one end. The tiles are wrapped in Tyvek™. Clear quartz fibers attached to the WLS fibers lead to the photodetectors. Quartz fibers are well known to be radiation hard. In CMS, we observe small radiation damage to quartz fibers embedded in the Hadron Forward calorimeter, which is located in a much higher radiation environment than the HE. The impact of radiation on the Tyvek™ wrapping is discussed in section 5 and is shown to be negligible. The tile thickness is 0.9 cm in layer 0 and 0.37 cm in the rest of the layers. When the HE was designed, a thicker and

Saint Gobain Corp, Les Miroirs, 18, avenue d'Alsace, 92400 Courbevoie, France.

2020 JINST 15 P06009

brighter scintillator in layer 0 was chosen in an attempt to mitigate the noncompensating response of the ECAL to hadrons and the large amount of dead material installed before the HE for ECAL readout.

The HE geometry is projective in η-ϕ-z space, where ϕ is the azimuth and z is the coordinate along the beam line, with the origin of the coordinate system positioned at the nominal collision point. Tiles in successive layers are aligned in a "tower". The towers are labeled using integer indices based on their η and ϕ. For the HE, the $i\eta$ index ranges from 16 to 29, covering $1.305 < |\eta| < 3$. The $i\phi$ index ranges from 1 to 72, with $i\phi = 1$ halfway up the detector and 18 and 19 at its top. A tower corresponds to the hardware associated with an $i\eta$-$i\phi$ pair. The tiles are mounted as mechanical structures called megatiles, shown in figure 3, which in the HE are installed in layers perpendicular to the beam direction, and span the range of 400–550 cm in $|z|$ and 40–260 cm in radius, depending on z.

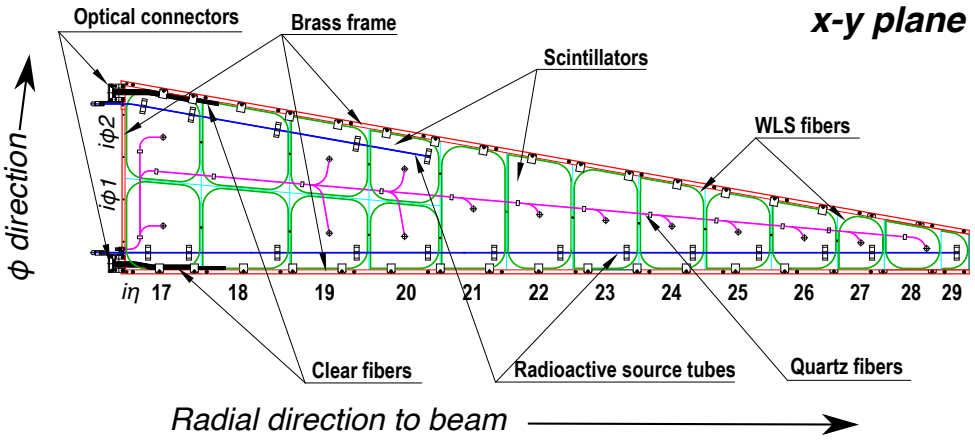

Figure 3. Details of an HE megatile showing the scintillator tiles, the WLS fibers, and the clear readout fibers. Also shown are the quartz fibers, which carry the laser light and the tubes through which the radioactive source moves. In layer 1, the inner size of the megatile is around 7.3 cm, while the outer size is 38.5 cm and the radial extent is 175 cm. The sizes (the longer base and the height) of enclosing trapezoids vary between 9.6 cm × 12.1 cm for the smallest ($i\eta = 27$), and 13.6 cm × 26.5 cm for the largest ($i\eta = 21$) tile used in this analysis.

To limit the number of readout channels, the light from several layers in a tower is fed to the same photodetector. In the schematic of the HE shown in figure 4, layers that are fed to a single SiPM have the same color ("depth").

For data taking prior to 2017, HPDs were used as the HE photodetector [23]. For the 2017 data-taking period, tiles in HE towers with $i\phi$ indices of 63–66, corresponding to a 20° sector in ϕ, were read out using SiPMs. Our analysis is based on $i\phi$s 63 and 65, because the other $i\phi$s only probed $i\eta$s below 20 where the radiation damage is too small to be measured reliably.

The HE SiPMs have 2–3 times greater quantum efficiency and better lifetime response stability than HPDs, no magnetic field sensitivity, require only medium voltage ($\approx$ 70 V) biasing, have small physical size, and allow the readout of more detector fibers supporting improved longitudinal segmentation. The SiPMs are placed at large radii in the HE, and receive a small radiation dose. Test bench measurements of SiPMs irradiated with radioactive sources showed [24] that the effect

2020 JINST 15 P06009

of 2017 radiation fluences on the HE SiPM response is negligible. Unlike the HPDs [8], their gain does not decrease because of light signals received from the tiles. The primary challenge for SiPM operation is the relatively high dark current resulting from cumulative radiation damage to the devices in situ during future running of high-luminosity LHC.

The CMS HCAL SiPM devices [25] are fabricated by the Hamamatsu Corporation. The approximate device parameters are 15 μm pixel pitch, 4500 pixels per mm^2, 8 ns pixel recovery time, and 65 V breakdown voltage. We operate the SiPMs in the Geiger mode at an overvoltage of approximately 3 V, which corresponds to an operating voltage of about 68 V. This value was chosen because it maximizes the signal-to-noise ratio. At this operating voltage, the performance parameters are approximately 40 fC per single photoelectron, 12% pixel crosstalk, and 28% photon detection efficiency. Two sizes of circular SiPMs are used: 2.8 mm diameter devices for depths with four or fewer scintillator layers and 3.3 mm devices for the other depths.

A charge-integrating ASIC (QIE) [26] is used to read out, digitize, and encode the signals from the photodetectors.

Radiation damage to scintillators is sensitive to temperature. The temperature in the CMS collision hall is about 18° C.

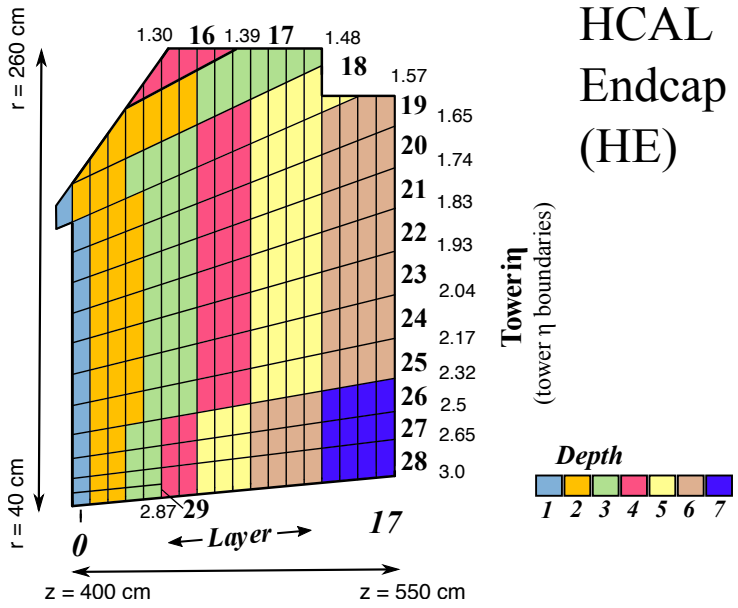

Figure 4. Schematic of the readout segmentation of the HE for channels instrumented with SiPMs. Scintillator tiles within a tower that have the same color ("depth") are connected to a single photodetector. The numbers 0–17 refer to the scintillator layers, and the numbers 16–29 on the perimeter of the figure denote the $i\eta$ indices of the towers (the η values for the boundaries of the towers are also shown).

4 Results from radiation exposure during pp collision data taking

The primary characteristics of the LHC operation relevant for this analysis are the total delivered luminosity, which determines the doses received by the tiles, and the average luminosity delivered

Hamamatsu Corporation, 325-6, Sunayama-cho, Naka-ku, Hamamatsu City, Shizuoka Pref., 430-8587, Japan.

2020 JINST 15 P06009

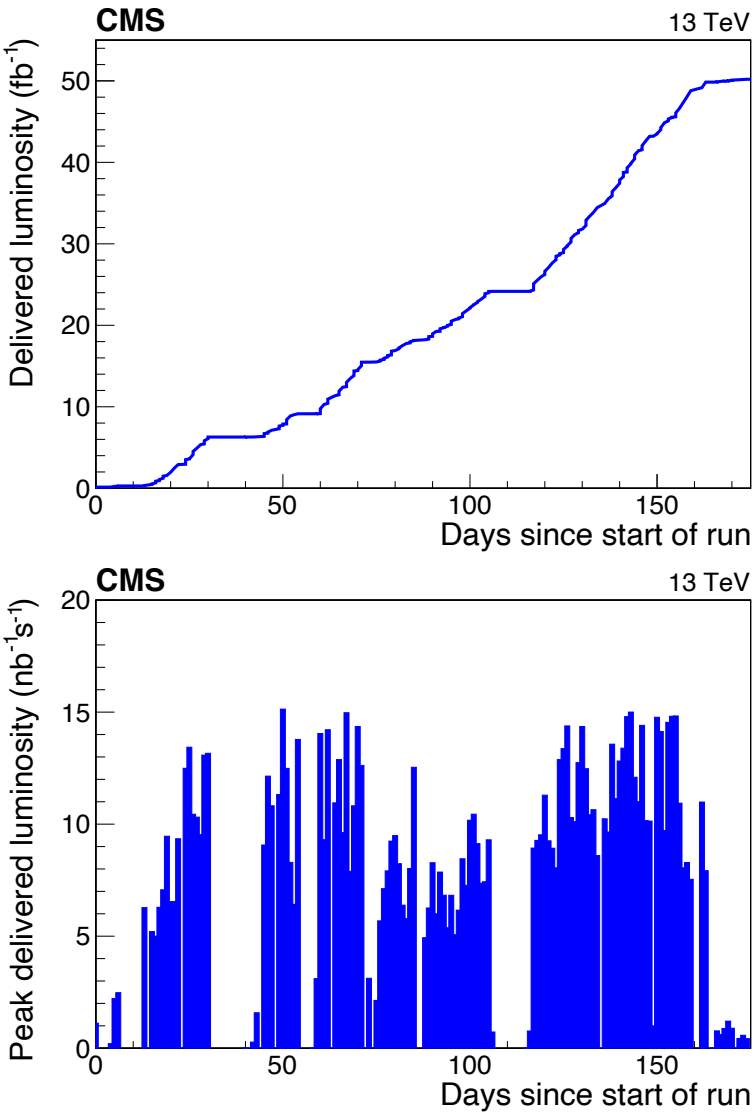

Figure 5. Integrated luminosity delivered to CMS by the LHC in the 2017 pp data-taking period, as a function of time (upper) and maximum daily (peak) luminosity delivered to CMS in 2017 (lower). Intervals of constant luminosity in the upper plot, or with no entries in the lower plot, indicate periods with no beam, e.g., technical stops.

per hour, which controls the dose rates. The integrated luminosity delivered as a function of time as well as the daily maximum instantaneous luminosity in the CMS interaction region in 2017 are displayed in figure 5. The daily peak luminosity rose rapidly and then remained at an approximately constant value throughout the year. The mean number of interactions per bunch crossing was about 37. Multiple interactions present in the recorded beam-beam crossing (event) are referred to as pileup.

2020 JINST 15 P06009

4.1 Estimation of doses and dose rates in the HE tiles

For a given luminosity, a tile is subjected to a dose and dose rate that depend on its location in the detector. The doses and dose rates vary with pseudorapidity, following the particle energy density of the pp collisions, and with depth in the calorimeter, following the energy deposition profile of the electromagnetic and hadron showers.

The dose received by each HE scintillator tile per pp interaction is calculated using simulation and scaled according to the delivered luminosity. The calculated doses are verified by in situ dosimetry. The peak luminosity versus time was fairly flat during 2017 data taking, indicating stable running conditions, as shown in figure 5 (lower). We therefore calculate the average integrated luminosity delivered per hour for the whole data-taking period as follows: for the total of 50 fb^{-1} taken over ≈1670 h of interacting beams we obtain an average integrated luminosity of 0.03 fb^{-1}/h, with an estimated systematic uncertainty of 5%. This value is converted to a dose rate (in Gy/h) for every HE tile by multiplying the average luminosity per hour by the expected dose per 1 fb^{-1}.

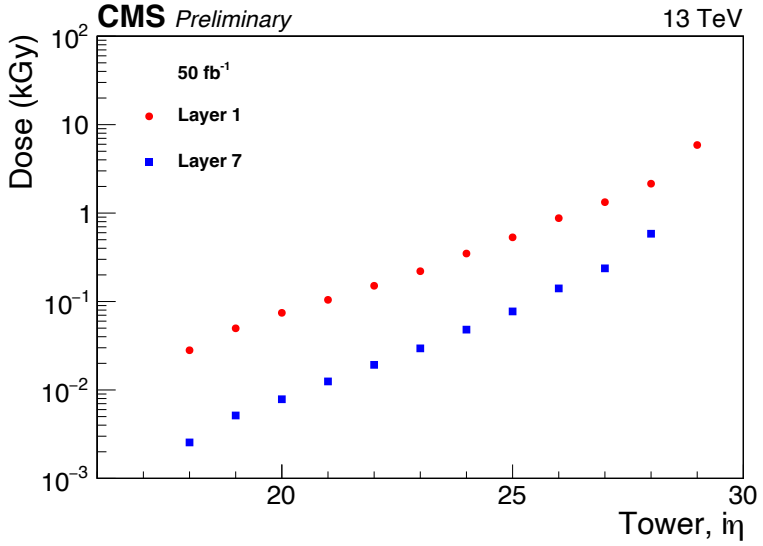

Figure 6. Doses calculated by FLUKA for the HE tiles in layers 1 and 7 as a function of $i\eta$ for 50 fb^{-1} of LHC running at 13 TeV in 2017.

Predictions of the absorbed dose in the HE scintillator layers are obtained using the Monte Carlo code FLUKA 2011.2c [27, 28]. The FLUKA predictions for collisions use a model that represents the HE in detail, with brass, Dural™ (Al, Cu, Mg, and Mn), Tyvek™, air, and scintillator layers. Since the energy loss per unit mass is more than a factor of two higher for hydrogen than for most other materials, and since plastic has a high hydrogen content, the spatial resolution in the simulation is set so that the dose estimates for tiles does not include regions that are not plastic. Per 50 fb^{-1}, doses in layer 1 range between 0.03 and 6 kGy for $i\eta$ of 18 to 29; for layer 7 they range between 0.003 to 0.7 kGy for $i\eta$ of 18 to 28. Layers 1 and 7 are located at z = 410 and 463 cm, respectively. The calculated doses for the 2017 running period for the tiles in layers 1 and 7 are presented in figure 6.

2020 JINST 15 P06009

The calculated doses are verified using measurements with 24 FWT-60 series film dosimeters, from Far West Technologies that were installed in the gaps between the absorber and the megatiles in the HE detector layers 1 and 2 during the 2015 and 2016 data-taking periods, when the detector geometry was essentially the same as in 2017. The films were measured with a FWT-92D photometer. The doses were calibrated to water equivalent, which is similar to plastic in terms of density and hydrogen content, and the uncertainty in the measurements is estimated to be 3%. A comparison between the measured and calculated doses as a function of the distance from the beam line to the film is given in figure 7. Reasonable agreement is seen for radial distances starting at about 50 cm, the location of tower $i\eta = 28$, indicating that FLUKA calculation is accurate to about 20–30% for distances 50–120 cm from the beam, where the largest radiation damage occurs for the tiles used in this analysis.

The geometry of the detector near towers 28 and 29 is irregular and the dose distribution difficult to model accurately (due to close proximity to the beam line, beam spray effects, irregular edges of the endcap preshower and electromagnetic calorimeter, mounting brackets and other construction elements, piping, etc.). For this reason, data taken for towers 28 and 29 are not included in the fits, although they are presented in some of the figures below.

4.2 Results using the laser calibration system

A laser calibration system is used to monitor the response of the HE tiles by injecting ultraviolet (UV) light that excites primary fluors in the scintillator. It consists of a triggerable excimer laser and a light distribution system that delivers UV light (351 nm) to the scintillator tiles in layers 1 and 7 via quartz fibers. During the 2017 data-taking period, pulses of laser light were injected between fills of the accelerator with protons, when there were no collisions.

Laser data were collected throughout the 2017 data-taking period. Figure 8 shows the signal output for the tiles probed by the laser calibration system at the end of the 2017 data-taking period relative to that at the start. Because the intensity of the laser light varied by up to 70% during 2017, the signals are normalized by using signals from tiles at $i\eta = 18$ in layer 7, which are expected to have less than 1% reduction in signal output. Differences between data for $i\phi$s 63 and 65 are outside the indicated statistical uncertainties. These differences contribute to the systematic uncertainties described below.

The normalized signals from individual channels exhibit an approximately exponential decrease versus integrated luminosity over most of the data-taking period. To characterize the behavior of signal loss, we fit the exponential portions of the normalized signal outputs with an exponential function of integrated luminosity, as illustrated in figure 9 for one particular tile. A deviation from the expected exponential behavior is observed during the first 7 fb^{-1} of data taking. The reason for this effect is not yet understood and this part of the data is not used in the analysis. With higher luminosity the effects are clearer so we concentrate on this part of the data. The statistical uncertainty in the measured mean signal within a single laser run is smaller than the spread observed when comparing different laser runs taken at similar integrated luminosities. In consequence, fluctuations are observed that are larger than expected based on uncertainties in the mean signal in a single laser run, indicating the presence of an additional source of scatter. We account for these fluctuations by

Far West Technologies, 330 South Kellogg Ave., Suite D, Goleta, CA 93117 U.S.A.

2020 JINST 15 P06009

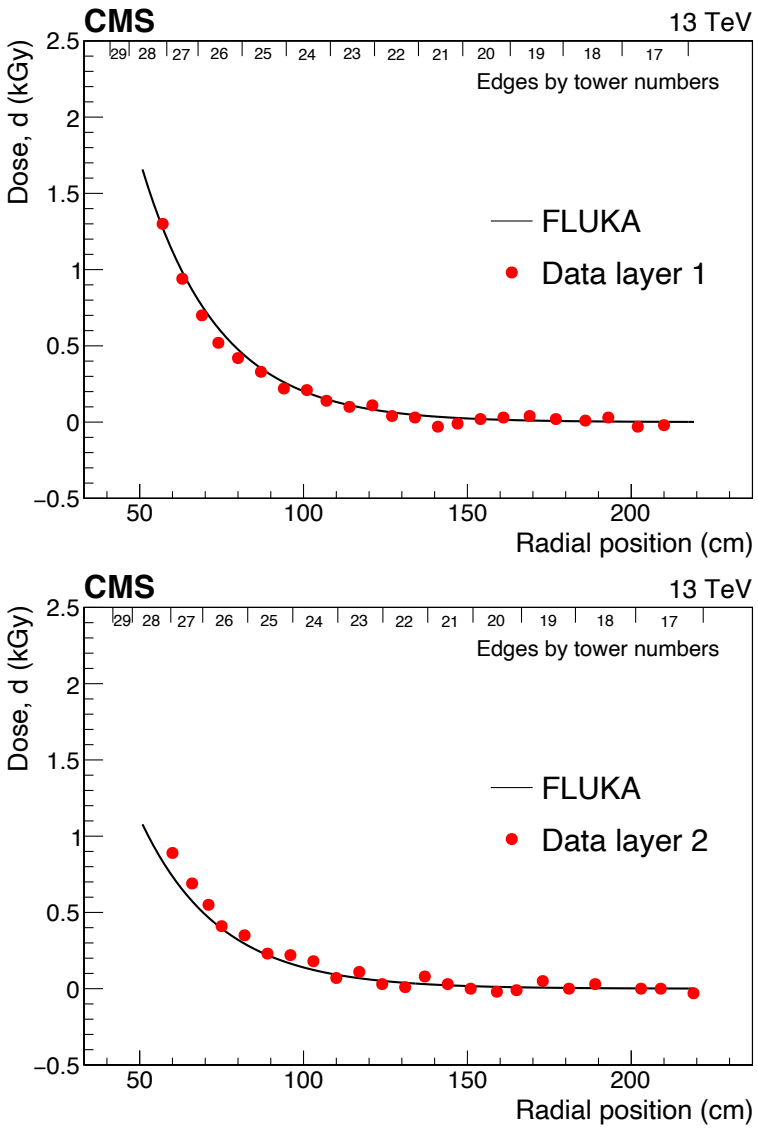

Figure 7. Comparison of doses for the 2015–2016 data-taking periods calculated using FLUKA and measured from dosimeter films in layer 1 (upper) and layer 2 (lower), as a function of radial distance from the beam. Positions of the tile edges in the radial direction are indicated along the tops of the figures.

scaling the uncertainties in individual laser points to yield a χ^2 per degree of freedom (dof) of one for the exponential fits. This conservative procedure results in larger estimates of uncertainties in the fit parameters.

Figure 10 presents relative signals versus dose for tiles with $i\eta$ = 21–27 in layer 1. The signals show an exponential decrease (as in eq. (2.1)) during periods of stable luminosity, with slopes that depend on corresponding dose rates. These results imply that at a fixed dose the damage to the scintillators increases with decreasing dose rate, within the range of our measurement.

The values of slopes μ, obtained from the exponential fits, are averaged in bins of R, and converted to $D(R) = 1/\langle\mu\rangle$ for comparisons with other measurements of D. Averaging of μ in bins

2020 JINST 15 P06009

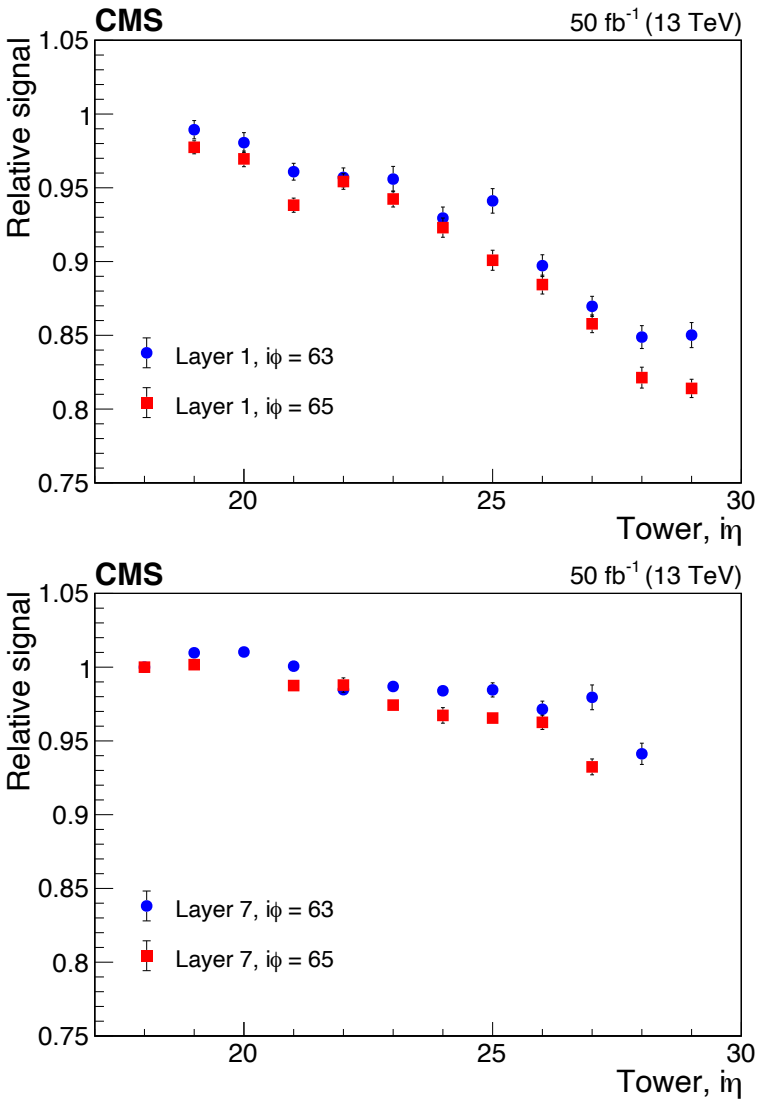

Figure 8. Signal at the end of the 2017 data-taking period from the HE SiPMs, relative to that at the start, as measured using the laser calibration system versus $i\eta$ for SCSN−81 tiles in layer 1 (upper) and layer 7 (lower). Only unscaled statistical uncertainties are shown. The differences between results for the two $i\phi$s indicates unknown systematic uncertainty.

of dose rate helps to reduce the statistical uncertainties and extends the range of the measurements to lower values of R, especially in the case of source measurements discussed in section 4.3. The results for $\langle\mu\rangle$ are discussed in section 4.4 and indicate a dose-rate dependence. A similar dose-rate dependence is also observed without averaging of μ in bins of dose rate, but with larger uncertainties in individual points.

We present results for values of R above 0.01 Gy/h. The fractional uncertainties in μ (or D) are large for tiles with little damage. The region $R > 0.1$ Gy/h is well measured with observed signal losses >3%.

2020 JINST 15 P06009

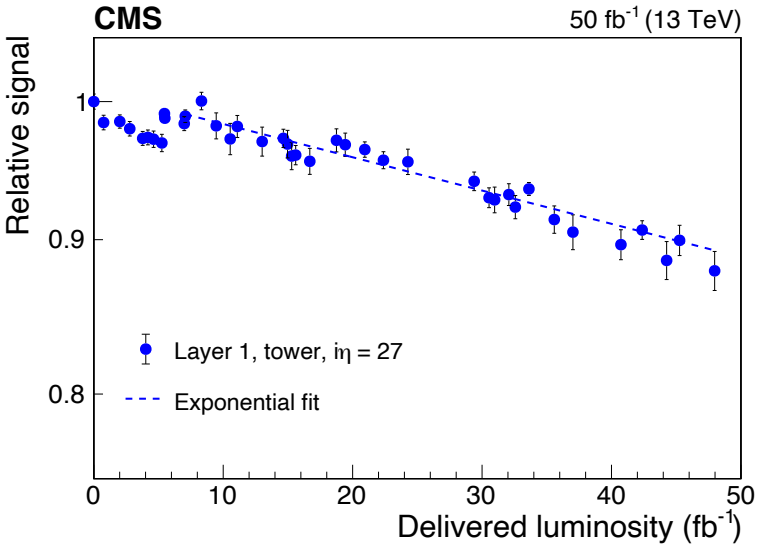

Figure 9. Relative signal measured using the laser calibration system versus delivered luminosity for the SCSN−81 tile in layer 1 with $i\eta = 27$ and $i\phi = 63$. Scaled statistical uncertainties are shown (see text). For this tile, the estimated dose at the end of data taking was $d = 1.5$ kGy, and the average dose rate was $R = 0.89$ Gy/h. The dashed line represents a fit to the data to obtain the value of the exponential slope. Note that the vertical scale is logarithmic (base 10).

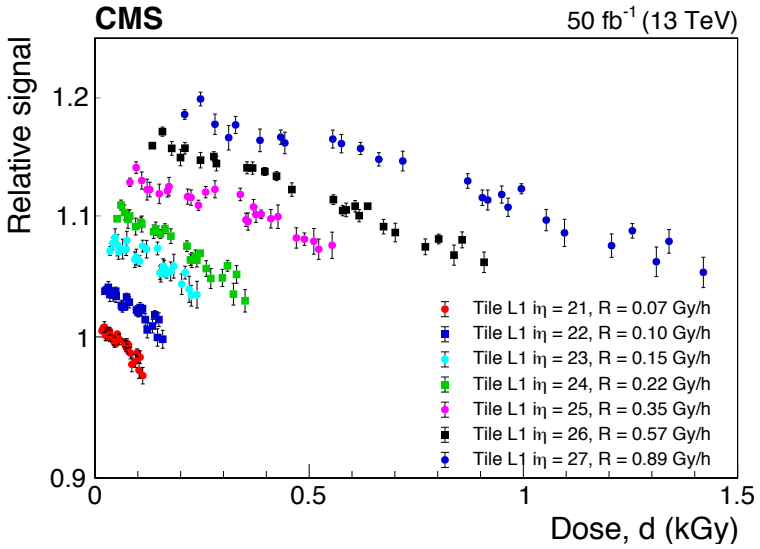

Figure 10. Relative signal for laser light versus accumulated dose for the SCSN−81 tiles in layer 1 with $i\eta = 21$–27. The average dose rates are shown for each set of points. The vertical scale is logarithmic and subsequent sets are shifted up by a factor of 1.03 relative to the previous set for better visibility. Each set starts at the dose corresponding to integrated luminosity of 7 fb^{-1}. Scaled statistical uncertainties are shown (see text).

2020 JINST 15 P06009

Various systematic effects have been evaluated. In addition to the differences between signals from different $i\phi$s, we evaluated sensitivities to the variation of the $i\eta$ choice for normalization, the data range used for fitting slopes, and the QIE gain setting. Combining these contributions, the overall systematic uncertainty in μ is estimated to be about 25%. The measurements are not corrected for the varying sizes of the tiles (see the discussion in section 5).

4.3 Results using the radioactive source

Each individual tile in the HCAL is designed to be serviced by a movable ^{60}Co radioactive source using small tubes, which are integrated into the calorimeter. The ^{60}Co source provides photons with energies of 1.17 and 1.33 MeV. The source is attached to a wire that guides it through the tubes. All tiles except those in layers 0 and 5, whose tubes have obstructions, can be accessed. The source moves at approximately 6 cm/s, and the signal is integrated for 0.1 s for each measurement. The resulting signal is used to monitor the stability of every tile in the HCAL, not just those in layers 1 and 7. The source data analyzed in this paper were collected during the periods when the LHC did not operate, both before the 2017 and 2018 data-taking periods.

The signal strength when the source was far away from a tile is used to estimate the background. The measurements of signal output before the 2018 data-taking period are corrected (divided by 0.886) for the decay of the source since the previous measurements were made before taking data in 2017. The ratio of the signal obtained before the 2018 data-taking period to that obtained before the 2017 data-taking period measures the attenuation of the signal output due to radiation damage during collisions in 2017, including any post-irradiation annealing effects. No additional normalization of signal ratios versus $i\eta$ is required. Values of the ratio averaged over $i\phi$ as a function of scintillating tile layer number and tower index $i\eta$ are shown in figure 11. The signal loss is small for tiles at large radial distance from the beam and for layers that are deeper in the calorimeter.

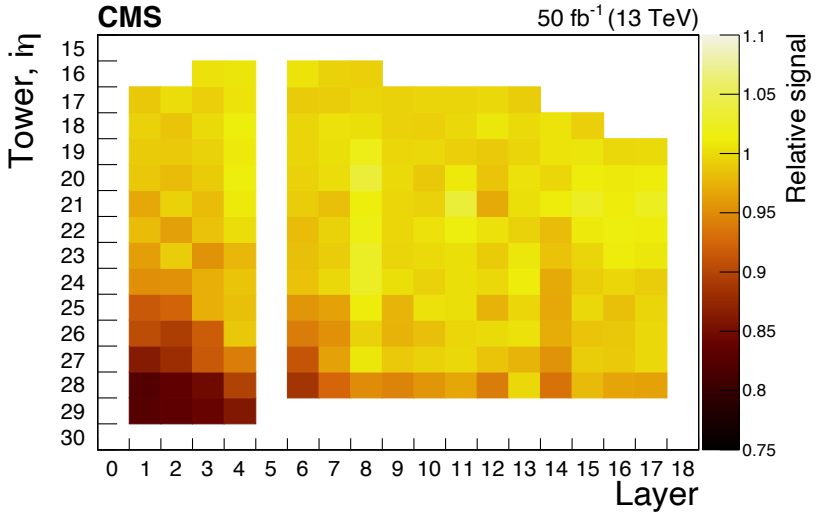

Figure 11. Ratio of ^{60}Co source signals observed before and after the 2017 data-taking period, as a function of $i\eta$ and layer number of scintillator tiles (SCSN−81) in the HE. Tubes in layers 0 and 5 have obstructions and cannot be accessed.

2020 JINST 15 P06009

At low R, measurements of signals from individual tiles scatter widely compared to the expected signal loss, due to the size of the measurement uncertainties. However, given the large number of tiles measured, a determination of signal loss can be made even at small values of R assuming that the fluctuations are uncorrelated. The calculated μ values are averaged in bins of R and are displayed in figure 12. The uncertainties in $\langle\mu\rangle$ related to the reproducibility of the measurements are included by increasing the statistical uncertainties by a factor 1.4, which results in the average scatter of points around the fit being consistent with the scaled uncertainties. The $\langle\mu\rangle$ values are somewhat lower than, but generally similar to, those from the laser calibration. The source data represent the damage integrated over the entire 2017 data-taking period and include an extended annealing time after the data taking ended. The analyzed laser data exclude the first 7 fb^{-1} and any annealing effects after the end of data taking.

4.4 Parametrization of laser and source results

Figure 12 summarizes the laser and source $\langle\mu\rangle$ results for the SCSN−81 tiles. The data are consistent with a power law dependence of $\langle\mu\rangle$ on R:

$$\langle\mu\rangle = 1/(\alpha\,\rho^{\beta}), \tag{4.1}$$

where $\rho = R/R_0$, and the constant R_0 can be chosen to minimize the correlation between parameters α and β; the fitted value of α depends on the choice of R_0. This form is equivalent to $D = \alpha\,\rho^{\beta}$. The value of $R_0 = 0.32$ Gy/h is chosen for the fits below so that the correlation between parameters α and β becomes negligible. The dashed line shown in figure 12 is the result of a power-law fit to both sets of data assuming all uncertainties are uncorrelated. The corresponding model parameters are $\alpha = 7.5 \pm 0.3$ kGy and $\beta = 0.35 \pm 0.03$ when $\langle\mu\rangle$ is in kGy^{-1} and R is in units of Gy/h. The fit χ^2/dof is 1.2. A fit to the laser data alone yields $\alpha = 7.3 \pm 0.3$ kGy and $\beta = 0.43 \pm 0.04$, with a χ^2/dof of 0.4. A fit to source data alone gives $\alpha = 7.6 \pm 0.5$ kGy and $\beta = 0.21 \pm 0.06$, with a χ^2/dof of 1.1. The fit to the laser data is inconsistent with no dose-rate effect. The fit to the source data by itself shows a smaller dose-rate effect, and is inconsistent with no dose-rate effect at the 3.5 standard deviation level. For the parameter β, which measures the dose-rate dependence, the difference between the results from the laser and source fits is 0.22 ± 0.08 (2.7 standard deviation). The tension between laser and source results may be a fluctuation. Since the $\langle\mu\rangle$ values from the source data tend to be lower than those from the laser data, additional annealing between the end of pp collisions and the source scan is a possibility. Annealing reduces damage and therefore decreases μ. A future source measurement of the HE and a measurement of annealing effects using post data-taking laser runs would help to reduce this uncertainty.

The systematic uncertainty in parameter α is assumed to be the same as the 25% systematic uncertainty in μ, discussed in section 4.2, assuming a 100% correlation between the measurements. For the parameter β, the spread of fit results between the laser and source data indicates systematic effects of the order of 0.1, when varying the range in R used in the fit.

The parametrization of our results should be used with care. It is valid for the decrease in signal output for a system consisting of scintillators, wavelength shifting fibers, and clear fibers made from the same materials we used, and constructed in the CMS tile geometry, when irradiated in the environment of the CMS collision hall. Kuraray has indicated that the current Y−11 fiber is

2020 JINST 15 P06009

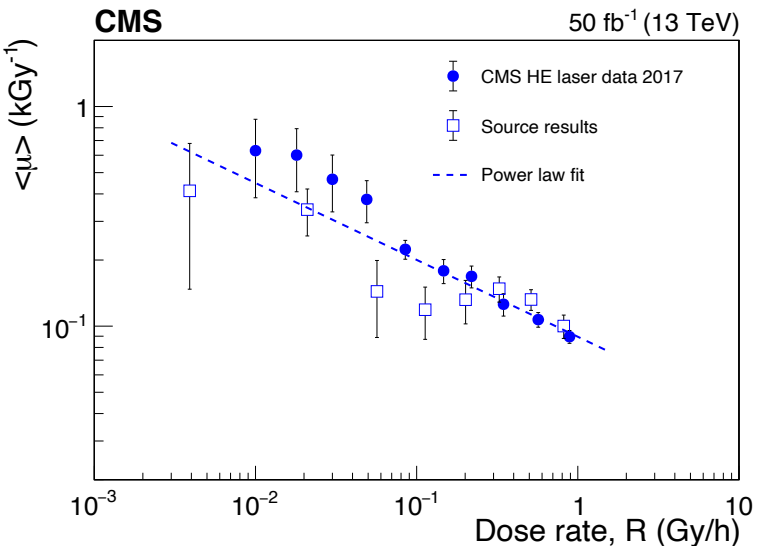

Figure 12. The value of $\langle\mu\rangle$ for SCSN−81 tiles as a function of R for laser and source data, parametrized by a power-law behavior, which is shown as a dashed line. The error bars are dominated by systematic uncertainties.

not the same as past versions. The parameter values are not generally applicable for other scintillator systems. Extrapolation of the power law above a dose rate of ≈10 Gy/h is not expected to be valid. As discussed in section 6, at R of approximately 10 Gy/h, oxygen will no longer permeate the entire tile [13, 29]. Radical creation and termination is different in regions with and without oxygen.

4.5 Cross-checks with inclusive hadrons

An additional method of measuring the effects of irradiation on the tiles is based on the 2017 collision data. Radiation damage is studied using observed energy depositions from hadrons produced in pp collisions. The energy distribution is measured for 25 subsamples distributed uniformly in delivered luminosity over the entire 2017 data-taking period. For each data-taking period n, the ratio of average energy relative to that of period 1,

$$F_{\text{meas}}(n) = \frac{E_{\text{ave}}(n)}{E_{\text{ave}}(1)}, \tag{4.2}$$

serves as a measure of the radiation damage, where E_{ave} is the average signal measured in all readout channels with the same values of $i\eta$ and depth; the average is calculated from the sum of signals above the threshold of $E_{\text{min}} = 0.5$ GeV.

The energy comparison requires a selection of events that is both independent of the HCAL and selects a well-defined set of hard interactions that is stable throughout the period under study. This is fulfilled by utilizing events satisfying a dimuon trigger. The energy ratio is studied as a function of the average number of interactions per bunch crossing, n_{PU}, to take into account the difference in the pileup structure between the periods. The number n_{PU} is estimated from the instantaneous luminosity.

2020 JINST 15 P06009

For each value of $i\eta$ and depth, the pileup dependence of F_{meas} is eliminated by fitting it versus n_{PU} with a linear function. The fits are performed in the range $20 < n_{\mathrm{PU}} < 50$ and the values of F_{meas} are extracted at $n_{\mathrm{PU}} = 35$.

The ratio $F_{\mathrm{meas}}(n)$ at $n_{\mathrm{PU}} = 35$ is observed to depend on the energy threshold E_{min}. Both the numerator and denominator of $F_{\mathrm{meas}}(n)$ are sums of energies of those individual channels that are above the threshold E_{min}. In the presence of radiation damage the ratio $F_{\mathrm{meas}}(n)$ will typically be smaller than the ratio $F(n)$ that would be obtained were the threshold not present. The higher the E_{min} threshold, the larger the discrepancy. To correct for this, a calibration is performed as follows. Using data from the first subsample, we multiply the energies contributing to the numerator by scale factors that represent hypothetical signal losses due to radiation damage, but we leave the denominator unchanged.

The values of the scale factors are varied in the range observed in the data, and for each scale factor F' a value F'_{meas} is extracted using the method described above. A linear relationship between F' and F'_{meas} is found, which is used to correct the measured values of $F_{\mathrm{meas}}(n)$ to obtain the corresponding $F(n)$. The magnitude of this correction depends on $i\eta$ and depth, and typically amounts to no more than 20% of the measured signal loss fraction $(1 - F_{\mathrm{meas}}(n))$.

The corrected signal fractions F measured for the channels in the first three depths of $i\eta = 27$ are shown in figure 13 (upper), as a function of delivered luminosity. The error bars include a systematic uncertainty of <1%, which results in fit χ^2/dof of around one. A decrease of F with delivered luminosity is clearly seen. A small shift of points near $20\,\mathrm{fb}^{-1}$ is believed to be due to residual luminosity calibration uncertainty during this period. Figure 13 (lower) presents the values of F averaged over $i\phi$ as a function of $i\eta$ and depth after $50\,\mathrm{fb}^{-1}$, showing a decrease of F with increasing $i\eta$ and decreasing depth. The behavior is consistent with that shown for individual tiles observed by the moving source for all the tiles of the HE, albeit with an increased granularity due to a readout in depths and not layers.

Depth 1 consists of a single layer (layer 0) and thus its tiles have well-defined doses and dose rates. Using the same procedure as for the laser data, these data can therefore be converted to $\langle\mu\rangle$ versus R. The results are shown in figure 14. The parameters of the power-law fit are $\alpha = 5.4 \pm 0.1\,\mathrm{kGy}$ and $\beta = 0.46 \pm 0.04$, with a χ^2/dof of 0.5, for $R_0 = 0.48\,\mathrm{Gy/h}$. The fit to the layer 0 in situ data is inconsistent with no dose-rate effect. The layer 0 tiles are constructed from PVT instead of PS, and hence their behavior can differ from that of PS-based tiles previously discussed. Nonetheless, the value of β, which parametrizes the dose-rate dependence, is similar to that from the laser measurements. At a given dose rate, the values of $\langle\mu\rangle$ are larger (and the value of the α parameter is smaller) for this PVT-based material, indicating more damage than for the PS-based tiles.

4.6 Cross-checks using isolated muons

The most probable energy deposition by a muon can also be used to estimate the amount of radiation damage. The acceptance of the tracker and of the muon system limits this measurement to portions of the HE where the damage is measured to be small.

The trajectories of forward isolated muon candidates with $p_{\mathrm{T}} > 20\,\mathrm{GeV}$ are propagated to the calorimeter surface to determine which tower they will traverse. The data-taking period is divided into subsamples. For each, a Landau distribution convolved with a Gaussian resolution function is

2020 JINST 15 P06009

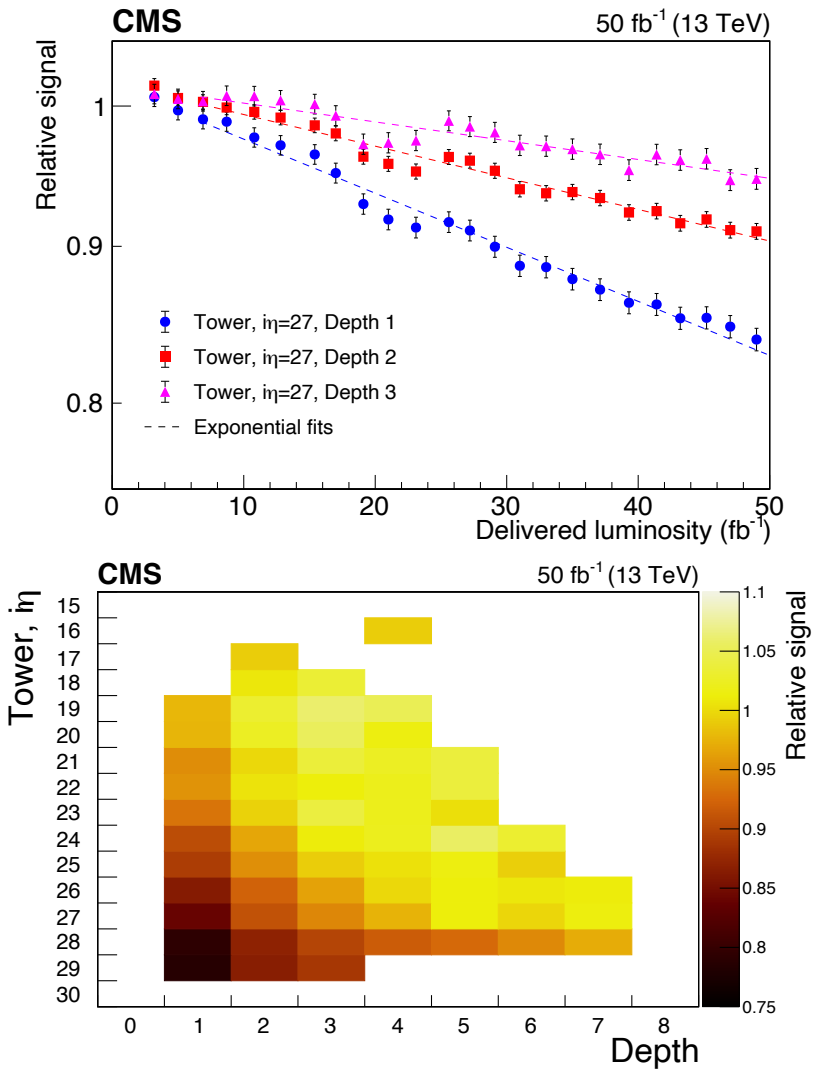

Figure 13. Upper: relative signal F for $i\eta = 27$ in depths 1, 2, and 3 versus delivered luminosity using the in situ "inclusive" method; the dashed lines show the results of fits with an exponential function, after excluding the first 7 fb^{-1} of data, as was done in the laser data analysis (section 4.2). For the tile in depth 1 (i.e., layer 0), the estimated dose at the end of data taking was $d = 1.5$ kGy and the average dose rate was $R = 0.89$ Gy/h. Lower: relative signal F for towers with $i\eta = 16$–29 at different depths measured after 50 fb^{-1} of delivered luminosity; only results with a relative uncertainty of 3% or lower on measured values of F are shown. Tiles in depth 1 are made of BC−408 and tiles in other depths are SCSN−81.

fitted to the charge distribution from the tower to obtain the most probable value (MPV) of deposited charge. A typical spectrum, including the fit, is shown in figure 15.

Because of pileup contributions to the measured signal, the isolated muon analysis uses events with a similar number of reconstructed vertices (the range 20–25 was used). The ratio of the MPV plotted as a function of delivered luminosity to that of the first subsample for $i\eta = 26$ depth 1 is shown in figure 16.

2020 JINST 15 P06009

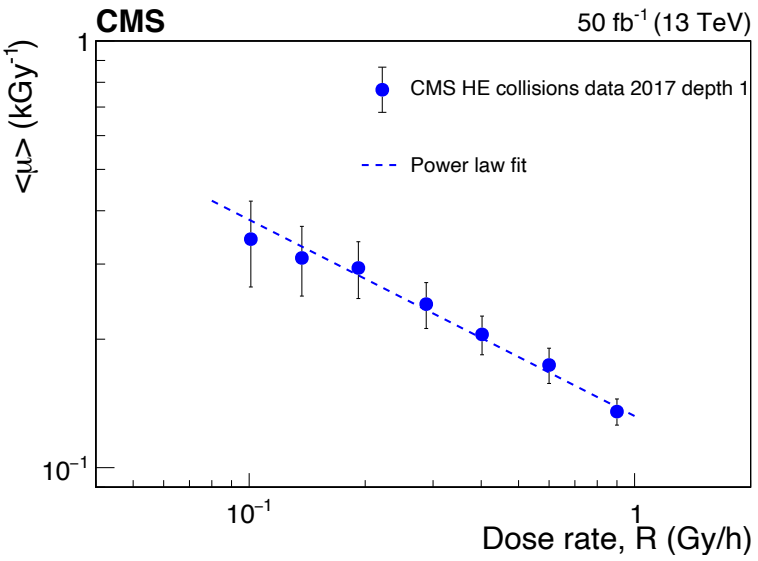

Figure 14. The value of $\langle\mu\rangle$ as a function of R for in situ collision data in depth 1 (BC−408), parametrized by a power law behavior, which is shown as a dashed line.

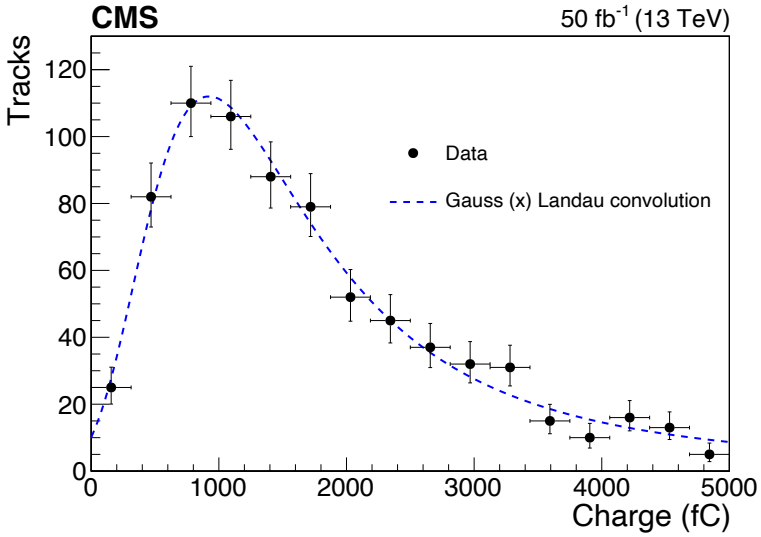

Figure 15. Fit to the charge distribution in an HE tower $i\eta = 26$ depth 1 (BC−408) due to an isolated muon from one of the event samples of 2017 data.

Only the towers at shallow depths and large $i\eta$ values are damaged sufficiently to detect the losses due to radiation damage in 2017 using this technique. Currently, this measurement is not competitive with other results for these towers. Upgrades for the CMS detector planned for future operations will have a tracking system with a larger η acceptance, extending the usefulness of this technique. Monitoring of calorimeter signals with muons has been tried for the first time using the 2017 data. It is important to develop this technique further for use in future operation.

2020 JINST 15 P06009

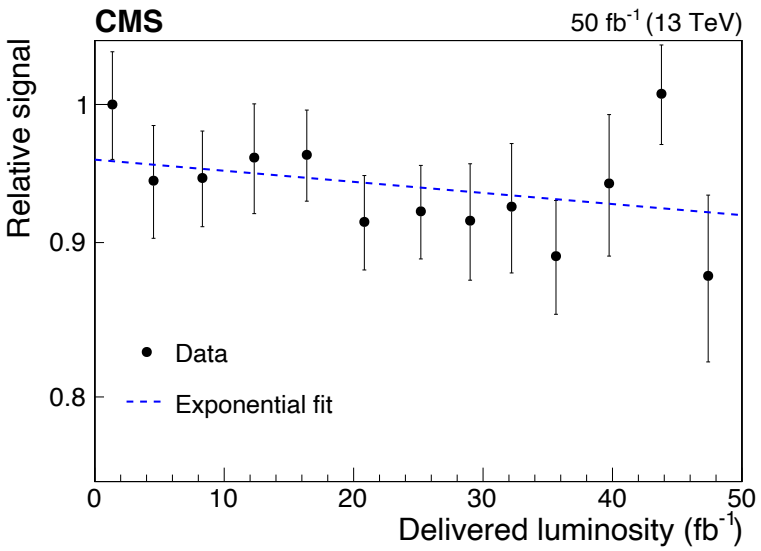

Figure 16. Relative muon signal in an HE tower with $i\eta = 26$ and depth 1 (BC−408) versus delivered luminosity. The dashed line shown on the figure is the result of a fit to an exponential distribution.

5 High-dose-rate results using sources

The CMS laser data monitor the HE tile performance for R only up to about 2 Gy/h (see figure 12). Intense radioactive sources are used to irradiate plastic scintillator tiles and obtain data at higher R, up to 1 kGy/h. To look at R-dependent effects and to avoid bias from other factors, such as tile geometry or chemical composition, only results from 10 cm × 10 cm × 0.37 cm SCSN−81 scintillator tiles read out with WLS fibers are reported here, unless noted otherwise. Although temporary damage is small for tiles irradiated in the HE, it is larger at the R values above 100 Gy/h. The values reported in this section reflect the permanent damage to the scintillator tiles remaining after annealing. This was ensured through observation of the signal output versus time.

Some of the data were taken at facilities with ^{60}Co gamma sources, located at the Kharkov Institute of Physics and Technology (KIPT), National Research Nuclear University MEPhI, Goddard Space Flight Center, Argonne National Laboratory (ANL), the Michigan Memorial Phoenix Project, the National Institute of Standards and Technology in Gaithersburg MD, and at the University of Maryland (UMD). We also include a measurement from irradiation using an electron beam at Florida State University (FSU), described in ref. [30]. For these measurements, some tiles had a fiber with a slightly smaller diameter, and a more recent formulation of Y−11 fiber from Kuraray than that used for the HE construction. The machining of the grooves in the tiles was also performed by different machinists using different toolings, and different machining rates. The temperatures of the tiles during the various irradiations are not known precisely, hence the processes affecting the annealing of radicals may differ somewhat.

For the source measurements, the signal output of the samples was measured before and after irradiation to calculate $D(R)$. The exact methods differ from study to study, but the general procedure involves the excitation of the irradiated scintillator tile by particles (e.g., cosmic rays, or

2020 JINST 15 P06009

alpha or gamma particles from a small, calibrated source placed in contact with the scintillator), and the measurement of the signal output from the WLS fiber via either a photomultiplier tube or a SiPM.

The remainder of the data were taken from samples irradiated in a region forward of CMS called the CASTOR radiation facility (CRF). These tiles were irradiated by particles originating from pp collisions during the 2016 data-taking period. They were located at radial distances from the beam line ranging from 11.8 to 25.9 cm. The doses received by the CRF tiles in 2016 were determined based on film dosimetry measurements and range from 15 to 60 kGy. An additional CRF-based measurement was performed during 2017, using tiles at the radial distance from the beam of 43.2 cm, which received a dose of about 2.3 kGy.

For the CRF measurements, a laser calibration system was used to monitor the signal output of the tiles during the data taking. As shown in figure 17, the signal loss as a function of received dose appears to be more rapid in the initial stage of irradiation. The tiles were remeasured in the laboratory after the CRF irradiation. The results of these measurements indicate that the initial drop seen in figure 17 was caused by instrumental effects and not radiation damage. The signal output follows an exponential decay for the remainder of the exposure. There is some annealing after day 44, when the exposure ended. The CRF data shown in figure 18 are corrected for the observed annealing. Measurements of the tiles after removal from the CRF and replacement of the irradiated WLS fiber with a new one indicate that about 20% of the damage occured in the fiber. The impact of radiation on reflectivity of Tyvek™ is estimated by wrapping a single tile in the various Tyvek™ wrappers from the CRF samples exposed to different doses. The light output of such sets was seen to decrease by about 0.2% per 1 kGy of the dose to the Tyvek™ wrappers. We conclude that the impact of Tyvek™ damage on the measurements of light output of the HE channels was negligible.

Figure 18 summarizes the results from the CRF and from electron beam and gamma source irradiations, along with the HE laser and source results. We are not aware of other measurements of closely comparable tile-fiber systems at the low dose rates seen by the HE scintillators. For several orders of magnitude in R, $D(R)$ shows an apparent R-dependence. The exact causes and mechanisms behind this effect remain to be understood. In the next section, we compare the observed dependence to what is known about dose-rate effects in plastic scintillators.

Tiles irradiated at gamma sources are also used to investigate the uniformity of the signal output after irradiation and to check the dependence of $D(R)$ on the tile size. A transverse scan of the signal output of a tile that received a total dose of 30 kGy at an R of 9 Gy/h is shown in figure 19. The number of photoelectrons (pe) detected in scans prior to irradiation is fairly independent of the source position. The irradiated tile retains its uniformity after absorbing this large dose, implying that it is unlikely that optical light attenuation is the major component of the observed signal loss. Reference [31] came to similar conclusions based on Raman data, albeit for a PVT-based scintillator.

In addition, tiles with a thickness of 0.37 cm and sizes of 20 cm × 20 cm, 12 cm × 9 cm, and 5 cm × 8 cm were irradiated at R of 1 kGy/h with doses of 1, 10, 20, 50, and 100 kGy. The extracted values of D are similar, to within ±20%.

We also investigated light propagation in tiles based on GEANT4 [32] ray tracing. Tile damage is simulated using the measured density of color centers. This study indicates that the effect of tile size is expected to be small (at most 20%).

2020 JINST 15 P06009

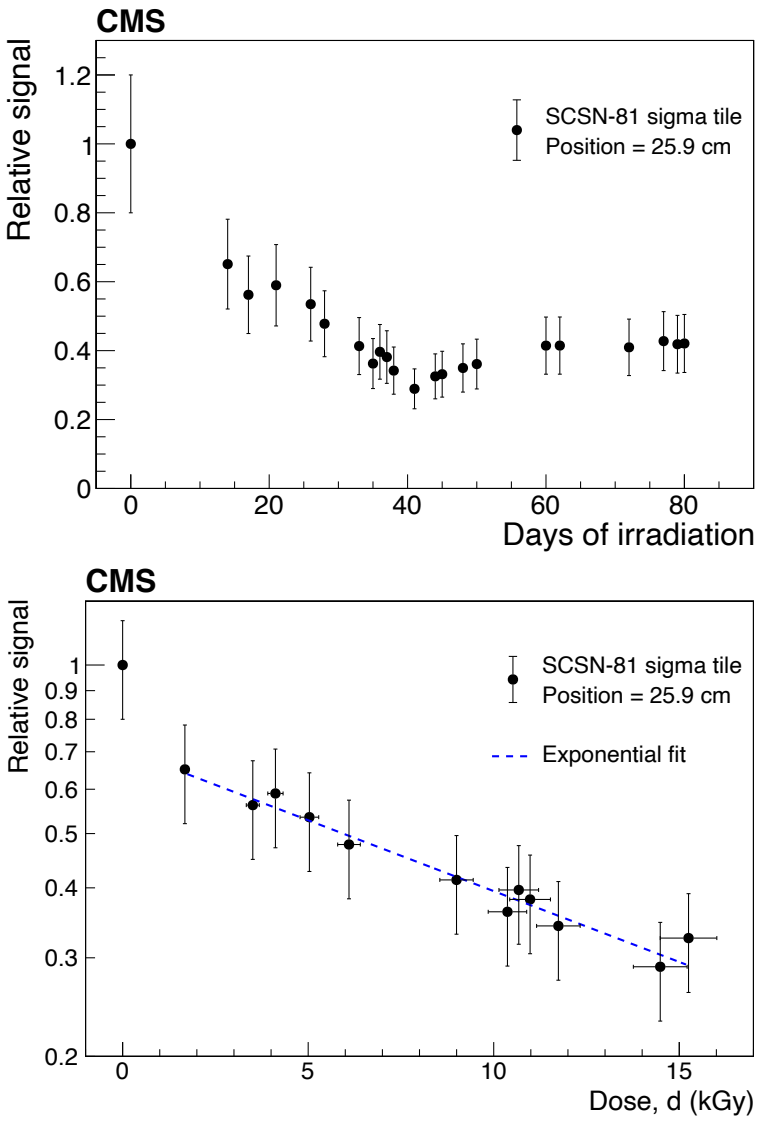

Figure 17. Relative signal for an SCSN−81 tile in the CRF radiation zone, plotted versus time (upper) and versus received dose (lower), for $R = 42$ Gy/h.

6 Discussion of dose-rate effects

Because dose-rate effects have a significant impact on the performance of scintillator-based detectors at hadron colliders, in this section we review what is known of their origins. Polymers are complex molecules, and their structure depends on the details of their preparation and the presence of additives such as antioxidants, while their behavior depends in detail on their environment. Therefore, extrapolating from measurements of a specific plastic in a specific environment to another plastic and/or environment is difficult. Measurements of new plastics and new environments will always be necessary. However, existing theory facilitates a deeper understanding of the results of our measurements.

2020 JINST 15 P06009

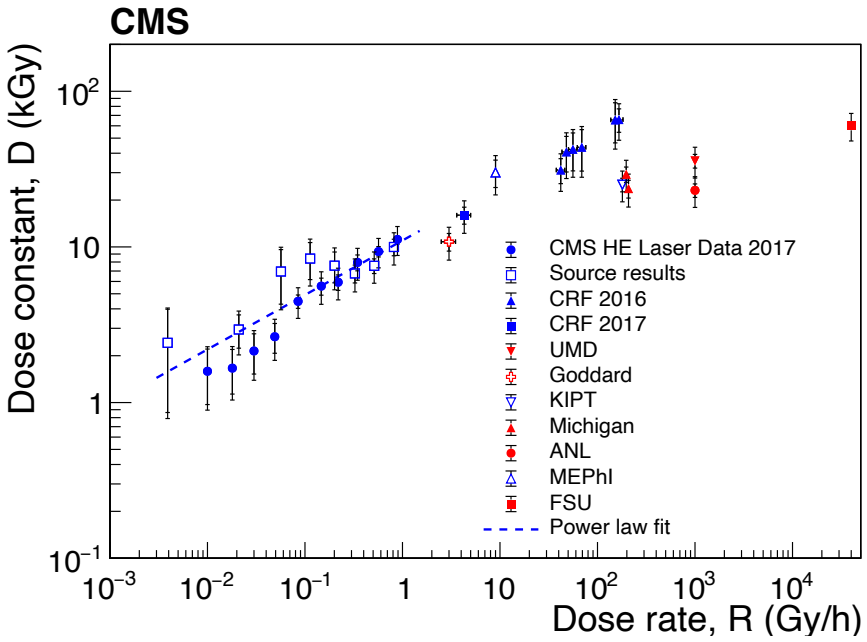

Figure 18. Values of $D(R)$ versus R for high-R data taken with gamma irradiation sources at KIPT, National Research Nuclear University MEPhI, Goddard, Michigan, ANL, and UMD, an electron beam at FSU, and in the collider environment in the CRF for SCSN−81 tiles, along with the results from the HE laser and source calibration data. The statistical uncertainties are shown as the inner bars, and the outer bars include the systematic uncertainties added in quadrature. The error bars on the irradiation data are dominated by systematic uncertainties.

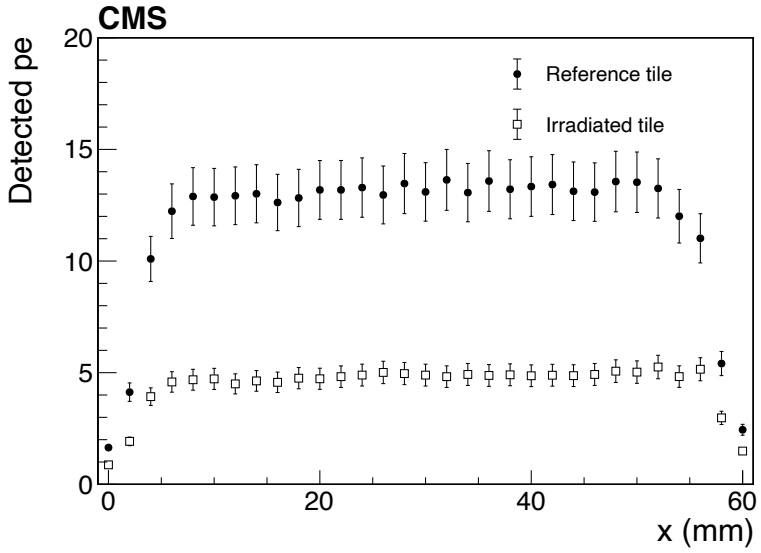

Figure 19. Number of detected photoelectrons for an SCSN−81 tile before and after an irradiation dose of 30 kGy at R of 9 Gy/h, as a function of the position of a radioactive-scan source along an axis through the center of the tile and parallel to one of its sides. The error bars are dominated by systematic uncertainty in normalization of the measurements; statistical point uncertainties are <2%.

2020 JINST 15 P06009

Two well-studied [11, 13, 33–37] sources of dose-rate effects in plastic scintillators are related to oxygen, one involving the diffusion of oxygen into the plastic during irradiation, and the other involving the rate of polymer oxidation in the areas containing oxygen. Polymer oxidation can be either beneficial or detrimental, depending on the dose rate and the details of the plastic preparation, the presence of additives such as antioxidants, and environment. While the magnitude of polymer oxidation depends on such details, theory gives us some guidance as to its dose-rate dependence.

As shown in the diagrams in figure 2, different kinds of termination, and thus permanent color centers (see section 2), are possible when oxygen is present. Oxygen is highly reactive and polymer oxidation occurs quickly after the production of the radicals [11, 13, 33–37]. In this case, there is little of the temporary damage that is indicative of radicals, and little to no annealing. Since the final products involving oxygen tend to absorb UV light, there can be considerable permanent damage that results in what is called reduction of light output [20] (see section 2). Temporary damage is larger without oxygen, as there is no oxygen to quickly bind to the radicals. However, as the radicals slowly reform bonds, the resulting stable structures sometimes have a small probability to absorb visible light, reducing the plastic's absorption length. Given the tension between these two competing effects, more experiments are needed to determine the optimum atmosphere for different materials, dose rates, temperatures, and doses. It is challenging to predict the optimal amount of oxygen for a given value of R.

For a given plastic and environment, theory allows some numerical extrapolation between different values of R. At high enough R, the density of radicals produced is high enough that oxygen cannot diffuse into the plastic fast enough to bind to and neutralize all the produced radicals, and thus cannot penetrate beyond a depth that depends on the dose rate [37, 38]. The depth z_0 for oxygen diffusion into the plastic for a rectangular slab of plastic is [37]

$$z_0^2 = \frac{2\,M\,C_0}{\Upsilon\,R} = \frac{2\,M\,S\,P}{\Upsilon\,R}, \tag{6.1}$$

where M is the diffusion coefficient for oxygen, C_0 is the oxygen concentration on its edge, Υ is the specific rate constant of active site formation, S is the oxygen solubility, and P is the external oxygen pressure. There is an abrupt transition between areas with and without oxygen. The oxygen concentration in the oxidized regions is almost uniform [29]. For PS tiles with a thickness of 4 mm, oxygen permeates the entire sample for R below (roughly, depending on the plastic preparation and environment) 10 Gy/h [13, 29]; annealing should be small below this R. For R above this value, polymer oxidation will occur only in the region permeated by oxygen, contributing to an R dependence of the damage to the scintillator.

The second source of dose-rate effects is related to the rate of polymer oxidation in regions with oxygen [33, 36]. The rate of polymer oxidation is [33, 34, 39]

$$K(C(x,t)) = -\frac{C_1\,C(x,t)}{1 + C_2\,C(x,t)}, \tag{6.2}$$

where $-K(C(x,t))$ is the rate at which oxygen is bound to the polymer, x is the position relative to the surface of the material where the rate is being measured, and $C(x,t)$ is the concentration of oxygen. The constants C_1 and C_2 depend on the kinematics of the chemical reactions. The constant C_1 is related to polymer oxidation from radicals, while C_2 is related to stable terminations of polymer

2020 JINST 15 P06009

oxidation. The constant C_1 is proportional to the square root of R for bimolecular reactions (leading to a dose-rate effect) and to R for unimolecular reactions (no dose-rate effect).

Another possible explanation for dose-rate effects involving oxygen for acrylic scintillators (PMMA) is postulated in ref. [40]. Radiation damage in PMMA is generally larger, for the same dose, than in either PS or PVT. The material produces more radicals and gas per dose than PS or PVT and does not cross link [13]. The authors suggest that oxygen ions, produced by the radiation in the atmosphere surrounding the material, may diffuse into the material and break polymer bonds, and that the damage may be accentuated in the presence of UV light. An irradiation at 0.1 Gy/h showed no damage when the samples were in a nitrogen atmosphere, while damage was clearly seen for air and oxygen atmospheres.

According to ref. [18], dose-rate effects can also be caused by a change in the relative amount of thermal- and radiation-induced damage. At low R, damage due to thermal effects becomes more important. Because thermal photons are of lower energy, they can only break the lowest energy bonds, changing what types of radicals are formed. This source of dose-rate effects is important when performing aging studies at high temperature.

Other possible sources of dose-rate effects include damage to the fluors [13], damage to the fiber, presence of ozone [41], and an unknown mechanism observed in PS at high R that is present at 22° C but not at 60° C [29].

Because dose-rate effects are seen in the HE tiles at $R < 10$ Gy/h when oxygen fully permeates the plastic, the cause cannot be its penetration depth (see eq. (6.1)), even though the power dependence close to 0.5 is suggestive. The power dependence is in between that expected for unimolecular and bimolecular terminations of radicals (see eq. (6.2)) [11, 13, 33–37]. There is a suggestion of a change of slope at a dose rate of 10 Gy/h, which, if real, could be caused by different chemical processes in the regions with and without oxygen above this dose rate.

7 Summary and conclusions

Radiation damage due to particles produced in pp collisions at $\sqrt{s} = 13$ TeV in two types of plastic scintillator tiles in the CMS hadron endcap calorimeter has been studied using data from several sources: a laser calibration system, a movable radioactive source, as well as hadrons and muons produced in pp collisions. Within the range of our measurements, the results from the various methods indicate that at a fixed dose the damage to the scintillators increases with decreasing dose rate. The dose-rate dependence is most accurately measured by the laser system, with larger uncertainties in the other measurements. The signal has an exponential decrease with dose characterized by dose constant D, which as a function of dose rate R is compatible with a power law with an exponent of about 0.4 for both PS and PVT-based tiles, in between the values predicted by bimolecular and unimolecular terminations of radicals [11, 13, 33–37]. The PVT-based tiles indicate more damage than the PS-based tiles for the same exposure. For $R \approx 100$ Gy/h, approximately 20% of the damage occurs in the fiber. The results are compared to damage produced by irradiations with ^{60}Co sources and by an electron beam. At dose rates less than 10 Gy/h, relevant for future experiments at particle colliders, where oxygen has saturated the plastic, the amount of damage does not depend on the particle type.

2020 JINST 15 P06009

The parameters of the power-law fit are functions of the detector geometry, materials, ambient conditions, etc. More studies are required to derive a general parametrization. Nonetheless, fits such as these above have been used to predict the future behavior of the CMS hadron barrel and endcap calorimeters [6, 42].

Several aspects of the data-taking conditions in the CMS detector give rise to systematic uncertainties that are difficult to estimate. A set of identical tile + WLS fiber assemblies subjected to varying dose-rate exposures in a temperature-controlled laboratory, with careful monitoring throughout a year-long exposure, would allow for a large reduction in the systematic uncertainties. At high dose rates, the amount of damage has a considerable spread, possibly indicating underestimated systematic uncertainties, motivating further studies to determine the underlying cause. It would be interesting to have data over this wide range of dose rates separately for the fibers and for the plastic tiles, to see their separate power dependencies. Studies of tiles at low dose rates in an oxygen-free environment, like a nitrogen atmosphere as suggested in ref. [40], are needed to test directly if the cause is dose-rate dependent polymer oxidation. It would also be helpful to make measurements above 10 Gy/h using a set of tiles made in a uniform way and irradiated at a known temperature.

Dose-rate effects can be large at low dose rates and should be measured for new tile systems.

Acknowledgments

We congratulate our colleagues in the CERN accelerator departments for the excellent performance of the LHC and thank the technical and administrative staffs at CERN and at other CMS institutes for their contributions to the success of the CMS effort. In addition, we gratefully acknowledge the computing centres and personnel of the Worldwide LHC Computing Grid for delivering so effectively the computing infrastructure essential to our analyses. Finally, we acknowledge the enduring support for the construction and operation of the LHC and the CMS detector provided by the following funding agencies: BMBWF and FWF (Austria); FNRS and FWO (Belgium); CNPq, CAPES, FAPERJ, FAPERGS, and FAPESP (Brazil); MES (Bulgaria); CERN; CAS, MoST, and NSFC (China); COLCIENCIAS (Colombia); MSES and CSF (Croatia); RPF (Cyprus); SENESCYT (Ecuador); MoER, ERC IUT, PUT and ERDF (Estonia); Academy of Finland, MEC, and HIP (Finland); CEA and CNRS/IN2P3 (France); BMBF, DFG, and HGF (Germany); GSRT (Greece); NKFIA (Hungary); DAE and DST (India); IPM (Iran); SFI (Ireland); INFN (Italy); MSIP and NRF (Republic of Korea); MES (Latvia); LAS (Lithuania); MOE and UM (Malaysia); BUAP, CINVESTAV, CONACYT, LNS, SEP, and UASLP-FAI (Mexico); MOS (Montenegro); MBIE (New Zealand); PAEC (Pakistan); MSHE and NSC (Poland); FCT (Portugal); JINR (Dubna); MON, RosAtom, RAS, RFBR, and NRC KI (Russia); MESTD (Serbia); SEIDI, CPAN, PCTI, and FEDER (Spain); MOSTR (Sri Lanka); Swiss Funding Agencies (Switzerland); MST (Taipei); ThEPCenter, IPST, STAR, and NSTDA (Thailand); TUBITAK and TAEK (Turkey); NASU (Ukraine); STFC (United Kingdom); DOE and NSF (U.S.A.).

Individuals have received support from the Marie-Curie programme and the European Research Council and Horizon 2020 Grant, contract Nos. 675440, 752730, and 765710 (European Union); the Leventis Foundation; the A.P. Sloan Foundation; the Alexander von Humboldt Foundation; the Belgian Federal Science Policy Office; the Fonds pour la Formation à la Recherche dans l'Industrie et dans l'Agriculture (FRIA-Belgium); the Agentschap voor Innovatie door Weten-

2020 JINST 15 P06009

schap en Technologie (IWT-Belgium); the F.R.S.-FNRS and FWO (Belgium) under the "Excellence of Science — EOS" — be.h project n. 30820817; the Beijing Municipal Science & Technology Commission, No. Z191100007219010; the Ministry of Education, Youth and Sports (MEYS) of the Czech Republic; the Deutsche Forschungsgemeinschaft (DFG) under Germany's Excellence Strategy — EXC 2121 "Quantum Universe" — 390833306; the Lendület ("Momentum") Programme and the János Bolyai Research Scholarship of the Hungarian Academy of Sciences, the New National Excellence Program ÚNKP, the NKFIA research grants 123842, 123959, 124845, 124850, 125105, 128713, 128786, and 129058 (Hungary); the Council of Science and Industrial Research, India; the HOMING PLUS programme of the Foundation for Polish Science, cofinanced from European Union, Regional Development Fund, the Mobility Plus programme of the Ministry of Science and Higher Education, the National Science Center (Poland), contracts Harmonia 2014/14/M/ST2/00428, Opus 2014/13/B/ST2/02543, 2014/15/B/ST2/03998, and 2015/19/B/ST2/02861, Sonata-bis 2012/07/E/ST2/01406; the National Priorities Research Program by Qatar National Research Fund; the Ministry of Science and Education, grant no. 14.W03.31.0026 (Russia); the Programa Estatal de Fomento de la Investigación Científica y Técnica de Excelencia María de Maeztu, grant MDM-2015-0509 and the Programa Severo Ochoa del Principado de Asturias; the Thalis and Aristeia programmes cofinanced by EU-ESF and the Greek NSRF; the Rachadapisek Sompot Fund for Postdoctoral Fellowship, Chulalongkorn University and the Chulalongkorn Academic into Its 2nd Century Project Advancement Project (Thailand); the Kavli Foundation; the Nvidia Corporation; the SuperMicro Corporation; the Welch Foundation, contract C-1845; and the Weston Havens Foundation (U.S.A.).

References

[1] C. Zorn, *Plastic and liquid organic scintillators*, in *Instrumentation in High Energy Physics*, Advanced Series on Directions in High Energy Physics, volume 9, World Scientific (1992), pp. 218–279.

[2] CMS collaboration, *The CMS Experiment at the CERN LHC*, 2008 *JINST* **3** S08004.

[3] CMS HCAL collaboration, *Design, performance and calibration of CMS hadron-barrel calorimeter wedges*, *Eur. Phys. J.* **C 55** (2008) 159.

[4] CMS collaboaration, *The CMS hadron calorimeter project*, CERN-LHCC-97-031 (1997).

[5] L. Evans and P. Bryant, *LHC Machine*, 2008 *JINST* **3** S08001.

[6] CMS collaboration, *The Phase-2 upgrade of the CMS endcap calorimeter*, CERN-LHCC-2017-023 (2017).

[7] CMS HCAL collaboration, *Dose rate effects in the radiation damage of the plastic scintillators of the CMS Hadron Endcap Calorimeter*, 2016 *JINST* **11** T10004 [*Erratum* 2019 *JINST* **14** E08001] [arXiv:1608.07267].

[8] R.A. Shukla et al., *Microscopic characterisation of photodetectors used in the hadron calorimeter of the Compact Muon Solenoid experiment*, *Rev. Sci. Instrum.* **90** (2019) 023303.

[9] T. Förster, *Zwischenmolekulare Energiewanderung und Fluoreszenz*, *Ann. Phys.* **437** (1947) 55.

[10] J.B. Birks, *The theory and practice of scintillation counting*, International Series of Monographs on Electronics and Instrumentation, volume 27, Pergamon Press (1964).

2020 JINST 15 P06009

[11] E. Biagtan, E. Goldberg, R. Stephens, E. Valeroso and J. Harmon, *Gamma dose and dose-rate effects on scintillator light output*, *Nucl. Instrum. Meth.* **B 108** (1996) 125.

[12] U. Holm and K. Wick, *Radiation Stability of Plastic Scintillators and Wave Length Shifters*, *IEEE Trans. Nucl. Sci.* **36** (1989) 579.

[13] K. Wick, D. Paul, P. Schröder, V. Stieber and B. Bicken, *Recovery and dose-rate dependence of radiation damage in scintillators, wavelength shifters and light guides*, *Nucl. Instrum. Meth.* **B 61** (1991) 472.

[14] B. Bicken, U. Holm, T. Marckmann, K. Wick and M. Rohde, *Recovery and permanent radiation damage of plastic scintillators at different dose rates*, *IEEE Trans. Nucl. Sci.* **38** (1991) 188.

[15] B. Bicken, A. Dannemann, U. Holm, T. Neumann and K. Wick, *Influence of temperature treatment on radiation stability of plastic scintillator and wavelength shifter*, *IEEE Trans. Nucl. Sci.* **39** (1992) 1212.

[16] A.D. Bross and A. Pla-Dalmau, *Radiation damage of plastic scintillators*, *IEEE Trans. Nucl. Sci.* **39** (1992) 1199.

[17] N.D. Giokaris, M. Contreras, A. Pla-Dalmau, J. Zimmerman and K.F. Johnson, *Study of dose-rate effects on the radiation damage of polymer-based SCSN23, SCSN81, SCSN81+Y7, SCSN81+Y8 and 3HF scintillators*, *Radiat. Phys. Chem.* **41** (1993) 315.

[18] K.T. Gillen and M. Celina, *Predicting polymer degradation and mechanical property changes for combined radiation-thermal aging environments*, *Rubber Chem. Technol.* **91** (2018) 27.

[19] I.B. Berlman, *The effect of massive* ^{60}Co *doses on the light output of a scintillator solution*, in *Radiological Physics Division Semiannual Report for July through December 1957*, Argonne National Laboratory, Lemont U.S.A. (1958) [ANL-5829].

[20] R.L. Clough, G.M. Malone, K.T. Gillen, J.S. Wallace and M.B. Sinclair, *Discoloration and subsequent recovery of optical polymers exposed to ionizing radiation*, *Polym. Degrad. Stab.* **49** (1995) 305.

[21] CMS collaboration, *Description and performance of track and primary-vertex reconstruction with the CMS tracker*, 2014 *JINST* **9** P10009 [arXiv:1405.6569].

[22] CMS collaboration, *The CMS trigger system*, 2017 *JINST* **12** P01020 [arXiv:1609.02366].

[23] P. Cushman, A. Heering and A. Ronzhin, *Custom HPD readout for the CMS HCAL*, *Nucl. Instrum. Meth.* **A 442** (2000) 289.

[24] Y. Musienko, A. Heering, R. Ruchti, M. Wayne, A. Karneyeu and V. Postoev, *Radiation damage studies of silicon photomultipliers for the CMS HCAL phase I upgrade*, *Nucl. Instrum. Meth.* **A 787** (2015) 319.

[25] A. Heering, Y. Musienko, R. Ruchti, M. Wayne, A. Karneyeu and V. Postoev, *Parameters of the preproduction series SiPMs for the CMS HCAL phase I upgrade*, *Nucl. Instrum. Meth.* **A 824** (2016) 115.

[26] T.M. Shaw et al., *Front-end readout electronics for the CMS Hadron Calorimeter*, in in proceedings of the *Nuclear Science Symposium Conference Record*, Norfolk, VA, U.S.A., 10–16 November 2002, pp. 194–197.

[27] A. Ferrari, P.R. Sala, A. Fasso and J. Ranft, *FLUKA: A multi-particle transport code (Program version 2005)*, CERN-2005-010 (2005) [https://doi.org/10.2172/877507].

[28] T.T. Böhlen et al., *The FLUKA Code: Developments and Challenges for High Energy and Medical Applications*, *Nucl. Data Sheets* **120** (2014) 211.

2020 JINST 15 P06009

[29] K.T. Gillen, J.S. Wallace and R.L. Clough, *Dose-rate dependence of the radiation-induced discoloration of polystyrene*, *Radiat. Phys. Chem.* **41** (1993) 101.

[30] V. Hagopian et al., *Single tile-fiber unit of SDC calorimeter*, *Radiat. Phys. Chem.* **41** (1993) 401.

[31] H. Jivan et al., *Radiation hardness of plastic scintillators for the Tile Calorimeter of the ATLAS detector*, *J. Phys. Conf. Ser.* **645** (2015) 012019.

[32] GEANT4 collaboration, *GEANT4: A Simulation toolkit*, *Nucl. Instrum. Meth.* **A 506** (2003) 250.

[33] R.L. Clough and S.W. Shalaby, *Radiation effects on polymers*, *ACS Symp. Ser.* **475** (1991) 457.

[34] J.L. Bolland, *Kinetic studies in the chemistry of rubber and related materials. I. The thermal oxidation of ethyl linoleate*, *Proc. Roy. Soc.* **A 186** (1946) 218.

[35] J.L. Bolland, *Kinetic studies in the chemistry of rubber and related materials. VII. — influence of chemical structure on the α-methylenic reactivity of olefins*, *Trans. Faraday Soc.* **46** (1950) 358.

[36] L.Q. Bateman, *Olefin oxidation*, *Q. Rev. Chem. Soc.* **8** (1954) 147.

[37] A.V. Cunliffe and A. Davis, *Photo-oxidation of thick polymer samples — Part II: The influence of oxygen diffusion on the natural and artificial weathering of polyolefins*, *Polym. Degrad. Stab.* **4** (1982) 17.

[38] T. Seguchi, S. Hashimoto, K. Arakawa, N. Hayakawa, W. Kawakami and I. Kuriyama, *Radiation induced oxidative degradation of polymers — I: Oxidation region in polymer films irradiated in oxygen under pressure*, *Radiat. Phys. Chem.* **17** (1981) 195.

[39] K.T. Gillen and R.L. Clough, *Rigorous experimental confirmation of a theoretical model for diffusion-limited oxidation*, *Polymer* **38** (1992) 1929.

[40] Y. Sirois and R. Wigmans, *Effects of Long Term Low Level Exposure to Radiation as Observed in Acrylic Scintillator: Cause and Prevention of Radiation Disease in Uranium Calorimeters*, *Nucl. Instrum. Meth.* **A 240** (1985) 262.

[41] R.L. Clough and K.T. Gillen, *Polymer degradation under ionizing radiation: The role of ozone*, *J. Polym. Sci.* **A 27** (1989) 2313.

[42] CMS collaboration, *The Phase-2 Upgrade of the CMS Barrel Calorimeters*, CERN-LHCC-2017-011 (2017).

2020 JINST 15 P06009

Jinst

Published by IOP Publishing for Sissa Medialab

Received: *June 16, 2021*
Revised: *August 21, 2021*
Accepted: *November 22, 2021*
Published: *December 16, 2021*

Benchmarking LHC background particle simulation with the CMS triple-GEM detector

M. Abbas,[n] **M. Abbrescia,**[t] **H. Abdalla,**[h,j] **A. Abdelalim,**[h,k] **S. AbuZeid,**[h,i] **A. Agapitos,**[d] **A. Ahmad,**[af] **A. Ahmed,**[q] **W. Ahmed,**[af] **C. Aimè,**[y] **C. Aruta,**[t] **I. Asghar,**[af] **P. Aspell,**[ak] **C. Avila,**[f] **I. Azhgirey,**[ag] **J. Babbar,**[p] **Y. Ban,**[d] **R. Band,**[am] **S. Bansal,**[p] **L. Benussi,**[v] **V. Bhatnagar,**[p] **M. Bianco,**[ak] **S. Bianco,**[v] **K. Black,**[ap] **L. Borgonovi,**[u] **O. Bouhali,**[al] **D. Bozzato,**[ak,1] **A. Braghieri,**[y] **S. Braibant,**[u] **S. Butalla,**[aq] **S. Calzaferri,**[y] **M. Caponero,**[v] **F. Cassese,**[x] **A. Castaneda,**[ae,*] **N. Cavallo,**[x] **S.S. Chauhan,**[p,*] **A. Colaleo,**[t] **A. Conde Garcia,**[ak] **M. Dalchenko,**[al] **A. De Iorio,**[x] **G. De Lentdecker,**[a] **D. Dell Olio,**[t] **G. De Robertis,**[t] **W. Dharmaratna,**[aj] **S. Dildick,**[al,2] **B. Dorney,**[a] **R. Erbacher,**[am] **F. Fabozzi,**[x] **F. Fallavollita,**[ak] **A. Ferraro,**[y] **D. Fiorina,**[y] **E. Fontanesi,**[u] **M. Franco,**[t] **C. Galloni,**[ap] **D. Gancarcik,**[ak,3] **P. Giacomelli,**[u] **S. Gigli,**[y] **J. Gilmore,**[al] **M. Gola,**[q] **M. Gruchala,**[ak] **A. Gutierrez,**[an] **R. Hadjiiska,**[c] **T. Hakkarainen,**[l] **J. Hauser,**[ao] **K. Hoepfner,**[m] **M. Hohlmann,**[aq] **H. Hoorani,**[af] **T. Huang,**[al] **P. Iaydjiev,**[c] **A. Irshad,**[a] **A. Iorio,**[x] **F. Ivone,**[m] **W. Jang,**[ab] **J. Jaramillo,**[g] **V. Jha,**[s] **A. Juodagalvis,**[ad] **E. Juska,**[al] **B. Kailasapathy,**[ah,ai] **T. Kamon,**[al] **Y. Kang,**[ab] **P. Karchin,**[an] **A. Kaur,**[p] **H. Kaur,**[p] **H. Keller,**[m] **H. Kim,**[al] **J. Kim,**[aa] **S. Kim,**[ab] **B. Ko,**[ab] **A. Kumar,**[q] **S. Kumar,**[p] **H. Kumawat,**[s] **I. Kurochkin,**[ag] **N. Lacalamita,**[t] **J.S.H. Lee,**[ab] **A. Levin,**[d] **Q. Li,**[d] **F. Licciulli,**[t] **L. Lista,**[x] **K. Liyanage,**[aj] **F. Loddo,**[t] **M. Luhach,**[p] **M. Maggi,**[t] **Y. Maghrbi,**[ac] **N. Majumdar,**[r] **K. Malagalage,**[ah] **S. Malhotra,**[al] **S. Mallows,**[n] **S. Martiradonna,**[t] **N. Mccoll,**[ao] **C. McLean,**[am] **J. Merlin,**[t] **M. Misheva,**[c] **D. Mishra,**[s] **G. Mocellin,**[m] **L. Moureaux,**[a] **A. Muhammad,**[af] **S. Muhammad,**[af] **S. Mukhopadhyay,**[r] **M. Naimuddin,**[q] **P. Netrakanti,**[s] **S. Nuzzo,**[t] **R. Oliveira,**[ak] **L. Pant,**[s] **P. Paolucci,**[x] **I.C. Park,**[ab] **L. Passamonti,**[v] **G. Passeggio,**[x] **A. Peck,**[ao] **A. Pellecchia,**[t] **N. Perera,**[aj] **L. Petre,**[a] **H. Petrow,**[l] **D. Piccolo,**[v] **D. Pierluigi,**[v] **G. Raffone,**[v] **M. Rahmani,**[aq] **F. Ramirez,**[g] **A. Ranieri,**[t] **G. Rashevski,**[c] **B. Regnery,**[am] **M. Ressegotti,**[y,4] **A. Riabchikova,**[ag] **C. Riccardi,**[y] **M. Rodozov,**[c] **E. Romano,**[y] **C. Roskas,**[b] **B. Rossi,**[x] **P. Rout,**[r] **D. Roy,**[aq] **J.D. Ruiz,**[g] **A. Russo,**[v] **A. Safonov,**[al] **A.K. Sahota,**[p] **D. Saltzberg,**[ao] **G. Saviano,**[v] **A. Shah,**[q] **A. Sharma,**[ak] **R. Sharma,**[q] **T. Sheokand,**[p] **M. Shopova,**[c] **F.M. Simone,**[t] **J. Singh,**[p] **U. Sonnadara,**[ah] **E. Starling,**[a] **B. Stone,**[ao] **J. Sturdy,**[an] **G. Sultanov,**[c] **Z. Szillasi,**[o] **D. Teague,**[ap] **D. Teyssier,**[o] **T. Tuuva,**[l] **M. Tytgat,**[b] **I. Vai,**[w]

[1]Also at Karlsruhe Institute of Technology, Karlsruhe, Germany.
[2]Now at Rice University, Houston, Texas, U.S.A.
[3]Also at Czech Technical University (CZ), Prague, Czech Republic.
[4]Now at INFN Sezione di Genova, Genova, Italy.

https://doi.org/10.1088/1748-0221/16/12/P12026

2021 JINST 16 P12026

N. Vanegas,[g] **R. Venditti,**[t] **P. Verwilligen,**[t] **W. Vetens,**[ap] **A.K. Virdi,**[p] **P. Vitulo,**[y] **A. Wajid,**[af] **D. Wang,**[d] **K. Wang,**[d] **I.J. Watson,**[ab] **N. Wickramage,**[aj] **D.D.C. Wickramarathna,**[ah] **S. Yang,**[ab] **Y. Yang,**[a] **U. Yang,**[aa] **J. Yongho,**[z] **I. Yoon,**[aa] **Z. You,**[e] **I. Yu**[z] **and S. Zaleski**[m]

[a] *Université Libre de Bruxelles, Bruxelles, Belgium*
[b] *Ghent University, Ghent, Belgium*
[c] *Institute for Nuclear Research and Nuclear Energy, Bulgarian Academy of Sciences, Sofia, Bulgaria*
[d] *Peking University, Beijing, China*
[e] *Sun Yat-Sen University, Guangzhou, China*
[f] *University de Los Andes, Bogota, Colombia*
[g] *Universidad de Antioquia, Medellin, Colombia*
[h] *Academy of Scientific Research and Technology — ENHEP, Cairo, Egypt*
[i] *Ain Shams University, Cairo, Egypt*
[j] *Cairo University, Cairo, Egypt*
[k] *Helwan University, also at Zewail City of Science and Technology, Cairo, Egypt*
[l] *Lappeenranta University of Technology, Lappeenranta, Finland*
[m] *RWTH Aachen University, III. Physikalisches Institut A, Aachen, Germany*
[n] *Karlsruhe Institute of Technology, Karlsruhe, Germany*
[o] *Institute for Nuclear Research ATOMKI, Debrecen, Hungary*
[p] *Panjab University, Chandigarh, India*
[q] *Delhi University, Delhi, India*
[r] *Saha Institute of Nuclear Physics, Kolkata, India*
[s] *Bhabha Atomic Research Centre, Mumbai, India*
[t] *Politecnico di Bari, Università di Bari and INFN Sezione di Bari, Bari, Italy*
[u] *Università di Bologna and INFN Sezione di Bologna, Bologna, Italy*
[v] *Laboratori Nazionali di Frascati INFN, Frascati, Italy*
[x] *Università di Napoli and INFN Sezione di Napoli, Napoli, Italy*
[y] *Università di Pavia and INFN Sezione di Pavia, Pavia, Italy*
[w] *Università di Bergamo and INFN Sezione di Pavia, Pavia, Italy*
[z] *Korea University, Seoul, Korea*
[aa] *Seoul National University, Seoul, Korea*
[ab] *University of Seoul, Seoul, Korea*
[ac] *College of Engineering and Technology, American University of the Middle East, Dasman, Kuwait*
[ad] *Vilnius University, Vilnius, Lithuania*
[ae] *Universidad de Sonora, Hermosillo, Mexico*
[af] *National Center for Physics, Islamabad, Pakistan*
[ag] *Institute for High Energy Physics of NRC Kurchatov Institute, Protvino, Russia*
[ah] *University of Colombo, Colombo, Sri Lanka*
[ai] *Trincomalee Campus, Eastern University, Sri Lanka, Nilaveli, Sri Lanka*
[aj] *University of Ruhuna, Matara, Sri Lanka*
[ak] *CERN, Geneva, Switzerland*
[al] *Texas A&M University, College Station, U.S.A.*
[am] *University of California, Davis, Davis, U.S.A.*

*Corresponding author.

2021 JINST 16 P12026

[an] Wayne State University, Detroit, U.S.A.
[ao] University of California, Los Angeles, U.S.A.
[ap] University of Wisconsin, Madison, U.S.A.
[aq] Florida Institute of Technology, Melbourne, U.S.A.

E-mail: castaned@cern.ch, schauhan@cern.ch

Abstract: In 2018, a system of large-size triple-GEM demonstrator chambers was installed in the CMS experiment at CERN's Large Hadron Collider (LHC). The demonstrator's design mimicks that of the final detector, installed for Run-3. A successful Monte Carlo (MC) simulation of the collision-induced background hit rate in this system in proton-proton collisions at 13 TeV is presented. The MC predictions are compared to CMS measurements recorded at an instantaneous luminosity of 1.5×10^{34} cm^{-2} s^{-1}. The simulation framework uses a combination of the FLUKA and GEANT4 packages. FLUKA simulates the radiation environment around the GE1/1 chambers. The particle flux by FLUKA covers energy spectra ranging from 10^{-11} to 10^{4} MeV for neutrons, 10^{-3} to 10^{4} MeV for γ's, 10^{-2} to 10^{4} MeV for $e^{\pm}$, and 10^{-1} to 10^{4} MeV for charged hadrons. GEANT4 provides an estimate of the detector response (sensitivity) based on an accurate description of the detector geometry, the material composition, and the interaction of particles with the detector layers. The detector hit rate, as obtained from the simulation using FLUKA and GEANT4, is estimated as a function of the perpendicular distance from the beam line and agrees with data within the assigned uncertainties in the range 13.7-14.5%. This simulation framework can be used to obtain a reliable estimate of the background rates expected at the High Luminosity LHC.

Keywords: Detector modelling and simulations I (interaction of radiation with matter, interaction of photons with matter, interaction of hadrons with matter, etc); Interaction of radiation with matter; Micropattern gaseous detectors (MSGC, GEM, THGEM, RETHGEM, MHSP, MICROPIC, MICROMEGAS, InGrid, etc); Detector modelling and simulations II (electric fields, charge transport, multiplication and induction, pulse formation, electron emission, etc)

ArXiv ePrint: 2107.03621

2021 JINST 16 P12026

Contents

2021 JINST 16 P12026

1 Introduction

Most of the modern high energy particle physics experiments use colliding particle beams or a single beam impinging on a fixed target. Due to the high collision rate and the interaction of beam particles with matter, a hostile radiation environment is created. This radiation field is mainly composed of low energy neutrons, photons (γ), electrons/positrons ($e^{\pm}$) and charged hadrons, namely kaons ($K^{\pm}$), pions ($\pi^{\pm}$), and protons (p) [1]. These particles are commonly referred to as background particles. Due to the large interaction cross sections, background particles can cause damage to detector elements and front-end electronics [2]. Additionally, they can induce spurious signals that degrade the detector performance. A strategy for mitigating radiation effects is crucial to the design and upgrade of the LHC experimental facilities [3]. The strategy described in this paper uses estimates obtained with Monte Carlo (MC) simulation and measurements. Dedicated data taking campaigns are used to collect background data to understand the detector behaviour with respect to variations in the experimental parameters such as the instantaneous luminosity and the location of the detector element with respect to the interaction point. Additionally, new detector technologies are studied using high radiation doses in dedicated facilities such as the CERN High Energy AcceleRator Mixed Field (CHARM) [4] and the Gamma Irradiation Facility (GIF++) [5] at CERN. A set of detectors based

on the triple-GEM technology [6] is being installed in Muon system of the Compact Muon Solenoid (CMS) detector [7] for Run-3 and the Phase-2 (High Luminosity LHC) muon upgrade program [8]. A similar technology has been adopted for the upgrade of the ALICE TPC [9]. Background studies are crucial to understand the impact of radiation on the detector performance. Detector simulations (GEANT4 [10] and FLUKA [11] in this study) that reproduce the measurements will allow us to evaluate the impact of radiation in muon detection performance. For instance, an overestimation of the neutron flux would lead to a larger probability of misreconstruction of muons. To study the radiation environment and its impact on the detector performance, dedicated simulation tools involving a description of complex physics processes and particle decay chains are used.

The present study for the CMS GE1/1 detector system extends our previous work [8, 12] and provides a foundation for future studies of the response to background particles by other detector systems in CMS and other experiments. This study includes a detailed simulation strategy and methodology, an accurate detector description, and the response of a triple-GEM detector as a function of the incident particle's kinematic properties. Variations of the detector configuration are considered to show the validity of the estimates and robustness of the simulation model. Furthermore, the simulation model is compared with experimental data collected in 2018 by the GE1/1 slice test at the CMS detector. Reliable modeling of the detector response will serve for future studies relevant to the preparation for the High Luminosity LHC [13] where the luminosity will increase by one order of magnitude and different detector technologies will be exposed to a harsher radiation environment. This work can be useful for simulation of the response of other muon systems to background particles [14, 15].

This article is organized as follows: section 2 gives an overview of the CMS GE1/1 GEM detector and the experimental setup of the detectors in the CMS experiment. Section 3 presents a simulation study of the response of a single triple-GEM detector to various particles and the simulation framework. The response and its variation as a function of energy and angle of incident particles are compared with previous simulation studies. In section 4, results for the response of superchambers for a given geometry and the actual readout conditions during the slice test are presented. A prediction of hit rates using the FLUKA simulation and its systematic uncertainties are given in sections 5 and 6. A comparison of these predictions with measurements taken during LHC running is presented in section 7, followed by a summary in section 8.

2 Overview of the CMS GE1/1 detector and slice test

2.1 CMS GE1/1 detector

The GE1/1 station in each muon endcap is upstream of the Muon Endcap Station-1 (ME1/1), as shown in figure 1 in the R-z plane. Here, R is the perpendicular distance from the beamline. The CMS coordinate system is a right-handed cartesian coordinate system with the origin at the collision point, the x-axis pointing towards the center of the LHC ring, the y-axis pointing upwards and the z-axis along the beam direction. The polar angle θ is measured from the positive z-axis to the x-y plane and the azimuthal angle ϕ is measured from the positive x-axis in the x-y plane. The pseudorapidity η is defined as $\eta = -\ln[\tan(\theta/2)]$ and gives the information about angle of particle relative to beam axis.

The GE1/1 detector system in each endcap consists of 36 superchambers where each superchamber is comprised of a pair of trapezoidal-shaped triple-GEM detectors, covering a ϕ slice of

2021 JINST 16 P12026

10.15°. The superchambers are arranged in a staggered configuration with an overlap of 0.075° to provide full 2π coverage in ϕ. The superchamber design maximizes the detection of muons. The superchambers alternate in ϕ between a long version covering a pseudorapidity region of $1.55 < |\eta| < 2.18$ and a short version covering $1.61 < |\eta| < 2.18$ (figure 2 right). The use of long and short superchambers provides maximal η coverage within the mechanical envelope of the existing endcap. The dimensions of the long and short chambers are summarized in table 1. The triple-GEM detector of a superchamber closer to the interaction point of the pp collision is called Layer-1 and the other detector of the pair is called Layer-2, as shown in figure 2 right. Moreover, each triple-GEM detector is segmented into eight η partitions, referred to as i_η (=1 to 8) and each partition has 384 radial readout strips.

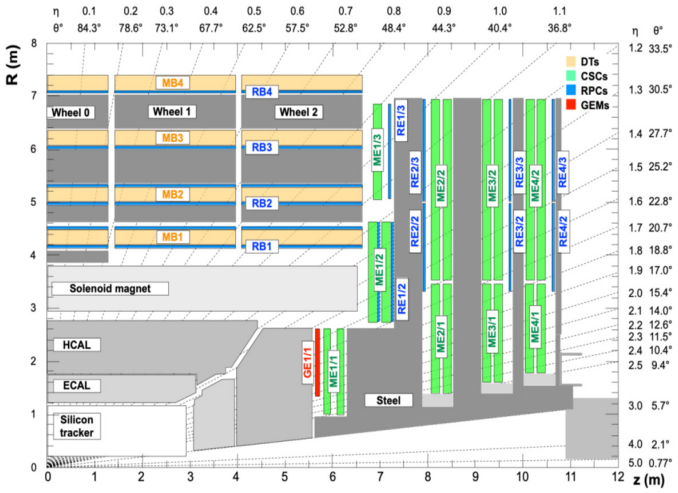

Figure 1. An R-z cross section of a quadrant of the upgraded CMS detector highlighting the location of the GE1/1 station (in red) with triple-GEM technology in the muon endcap region. Also shown are the previously existing muon stations, i.e., drift tubes (MB), cathode strip chambers (ME), and resistive plate chambers (RB, RE), and the flux-return steel yoke (dark areas).

Table 1. Dimensions of long and short trapezoidal-shaped triple-GEM detector.

Configuration	Long Chamber	Short Chamber
Height	1283.0 mm	1135.0 mm
Short Base Length	282.2 mm	282.2 mm
Long Base Length	510.0 mm	483.7 mm

2.2 GE1/1 slice test

Five triple-GEM pre-production superchambers were installed in the CMS experiment and exposed to pp collisions at 13 TeV in the period from 2017 to 2018 as shown in figure 3. This served as a demonstrator to obtain operational experience with the detector control system (DCS), the data

2021 JINST 16 P12026

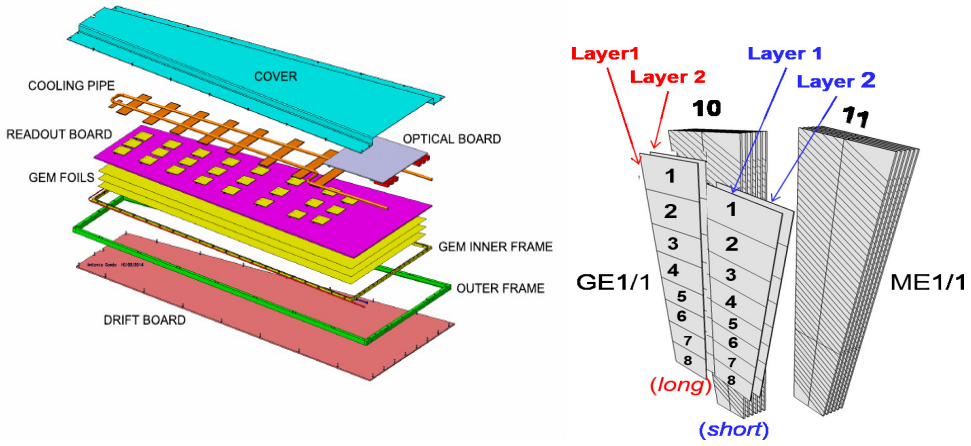

Figure 2. Single triple-GEM detector with various parts (left). Long (red) and short (blue) superchambers are mounted upstream of the ME1/1 station and cover the ranges in pseudorapidity $1.55 < |\eta| < 2.18$ and $1.61 < |\eta| < 2.18$, respectively, in a staggered configuration, with an overlap of 0.075°(right).

acquisition (DAQ) system, and the data quality monitoring (DQM) system, as well obtaining the first data to assess the performance of the detector with pp collisions. The design of these demonstrator superchambers is very similar to that of the final superchambers installed in the CMS endcap except for the use of an improved version of the front-end electronics mounted on the chamber. The improved version was realized by increasing the values of the protection resistor of each VFAT channel and the decoupling resistor for the chamber HV filter [16]. Figure 2 left shows a schematic drawing of the demonstrator chamber.

Superchambers 27, 28, 29, 30 ($\Delta\phi$ = 40°) in Slot-1 (shown in figure 3) were used to detect muons, while superchamber 1 ($\Delta\phi$ = 10°) in Slot-2 tested the upgraded electronics and a new GEM high voltage (HV) system [17] to be used in Run-3. The GE1/1 slice test chambers were operated at a gas gain amplification of ~1×10^4 with Ar/CO_2 gas mixture. Strip readout thresholds of 3 fC (i_η = 3-8), 4.0 fC (i_η = 2), and 8.8 fC (i_η = 1) were applied to the VFAT electronics based on electronic noise level. These thresholds are further discussed in detail in sections 3 and 4.

It should be noted that an irreversible channel loss was observed from April 2017 through December 2018 caused by discharges from one of the GEM foils nearest to the anode plane. As a result, only Layer-2 of superchamber 28 was operating with minimal channel loss (< 0.5%) throughout the slice test. The channel loss occurred both in the presence and the absence of particle beams in the LHC. Further details of the slice test setup and performance studies based on the data can be found in [18].

3 Response of a single triple-GEM detector to collision-induced background particles

In this section, the sensitivities (defined below) of a single triple-GEM detector of the CMS GE1/1 design, without electronics and aluminium frame, are evaluated and compared with results reported

2021 JINST 16 P12026

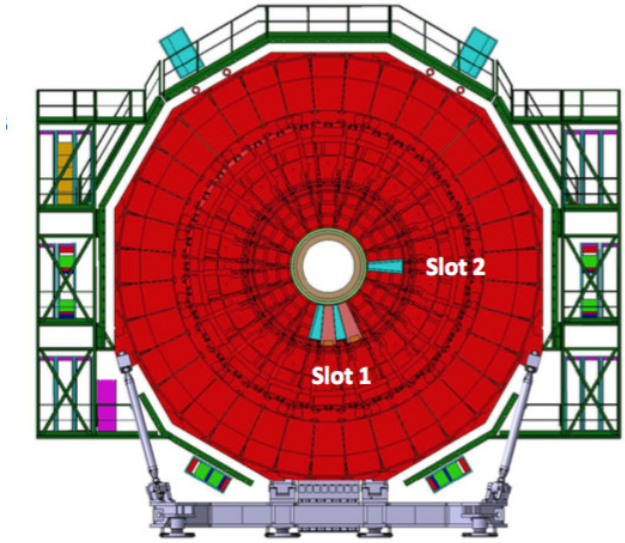

Figure 3. Schematic drawing of the negative muon endcap, showing the location of the five slice test superchambers.

in the GE1/1 Technical Design Report [8] and with studies done at the CHARM facility [12]. It should be noted that the response of the single triple-GEM detector is affected by material of other triple-GEM detectors within the superchamber.

3.1 Single triple-GEM detector geometry

The detector response is modeled using a GEANT4 [10] simulation with the geometry of a triple-GEM detector [8] and incident background particles with properties consistent with those generated in pp collisions at the LHC. A single triple-GEM detector is shown in figure 2. Chamber dimensions and material composition are presented in tables 1 and 2, respectively. Figure 4 shows a simplified schematic transverse view of a triple-GEM detector's gas gap configuration.

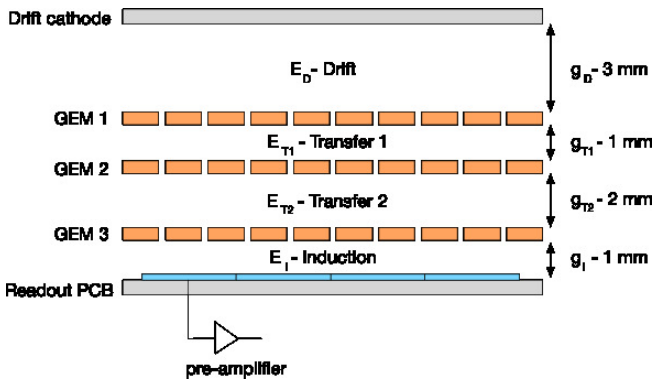

Figure 4. Representation of a transverse view of a triple-GEM detector.

2021 JINST 16 P12026

Table 2. Material and dimensions of the different layers in a single triple-GEM detector.

Layer	z-Dimensions	Material
Drift Board	35 µm / 3.2 mm / 35 µm	Copper / FR4 / Copper
Drift Gap	3 mm	Ar / CO_2
GEM1	5 µm / 50 µm / 5 µm	Copper / Kapton / Copper
Transfer-1 Gap	1 mm	Ar / CO_2
GEM2	5 µm / 50 µm / 5 µm	Copper / Kapton / Copper
Transfer-2 Gap	2 mm	Ar / CO_2
GEM3	5 µm / 50 µm / 5 µm	Copper / Kapton / Copper
Induction Gap	1 mm	Ar / CO_2
Readout Board	35 µm / 3.2 mm / 35 µm	Copper / FR4 / Copper

3.2 Simulation

The physics processes and decay chains are simulated using GEANT4 version 10.6 with the physics list recommended for standard HEP processes (FTFP_BERT_HP). The list includes all standard electromagnetic processes, the Bertini-style cascade for hadrons (<5 GeV), and the FTF (Fritiof) model for high energies (>4 GeV). It also includes a dedicated model for neutrons below 20 MeV [19].

The simulation setup has "source planes" that generate primary particles. The source planes are the same size as the drift board of the GEM detector and are located at a distance of 3 mm from the detector, on both sides. This configuration captures all possible incident angles and path lengths of the primary particles hitting the surface of the detector and traversing its sensitive volume. The response of the detector to the primary incident particles is estimated separately on each side for each source plane. The average is used to estimate the final response of the detector. Although the simulation considers the interaction of particles and the creation of secondaries in the different gaps of the triple-GEM detector, the detector response is extracted from the first two gas gaps, namely the drift and transfer-1 gaps (figure 4).

The signal induction is due to the production of a charged particle inside the detector originating from the interaction of neutral or charged background particles (e.g., neutrons, γ's, electrons, and charged hadrons). Other meaningful processes in signal evolution (such as electron drift, multiplication, charge transfer, and electronic response) are not covered in this study. Studies of the optimization of signal detection [20] using other simulation packages were used for the detailed design of the CMS GEM detectors.

The detector response is characterized using the *sensitivity* variable. *Sensitivity* is defined as the probability for a charged particle to deposit energy in the sensitive volume (e.g., Ar/CO_2 gas mixture), and to produce primary ionized electrons [8, 12]. Primary electrons go through a multiplication process, so that the charge is large enough to be detected by a readout system with charge thresholds. The charge threshold is related to the energy deposit required to separate signal

2021 JINST 16 P12026

from noise. Hence the sensitivity can be expressed as:

$$Sensitivity = \frac{N_{\text{hits}}}{N_{\text{total}}} \tag{3.1}$$

Here, N_{total} is the total number of incident particles entering the active surface of a GEM detector from any direction and N_{hits} is the number of total "hits" recorded above a certain energy threshold. The "hits" are counted for a given incident particle at a given incident energy and angle through the triple-GEM detector.

The simulated energy depositions in the first two gaps of a triple-GEM detector are converted to charge depositions using corresponding amplification factor, and required to be above the minimum threshold value of the VFAT chip. Although the readout electronics have a threshold of 3 fC, a value of 1.69 fC is used, corresponding to one electron in the drift gap, in order to study the effects of low levels of noise. Later in section 4.2, the energy thresholds are set to match the operational configuration of the GE1/1 chambers in CMS.

The minimum energy deposits required are estimated as follows:

- The gas gain amplification (G) was set to 1×10^4, corresponding to 24, 22, and 20 multiplications, respectively, in the transfer-1, transfer-2, and induction gaps.
- The readout thresholds for the strips were set to 1.69 fC for i_η = 1 to 8. Hence, to achieve this threshold a total of ~ 10547 (= 1.69 fC /1.6021$\times$ 10^{-19} C) electrons are required.
- The minimum average number of electrons required to be produced in the drift gap and the transfer-1 gap are 1 (= 10547/G) and 24 (= 10547/$G^{2/3}$), respectively.
- The effective average energy required to remove an electron due to ionization for an Ar/CO_2 gas mixture (in the ratio of 70/30) is $\langle W_i \rangle$ = 28.1 eV [21, 22]. Thus, energy losses of 28.1 eV and 674.4 eV (= 24$\times$ 28.1 eV) are needed to count as "hits" in drift and transfer-1 gaps, respectively. Those electrons produced in the drift and transfer-1 gaps are amplified by 10^4 and 440, respectively, at the readout strips. If the energy loss of a particle, simulated by GEANT4, is above the threshold, a "hit" is counted for (N_{hits}) in equation (3.1).

Due to the fact that GEANT4 does not report charged particles with a track length less than 0.7 mm [23], instead of counting secondary charged particles, we impose requirements on the amount of energy deposited in the gaps. This procedure is consistent with previously published results in ref. [12].

The detector response depends on the particle type, its kinematic properties, and the composition of the material in which the particle interacts. The dominant energy loss processes for neutrons are inelastic scattering at high energy (> 10 MeV), elastic scattering at intermediate energy (10^{-5} to 10 MeV), and neutron capture at low energy (< 10^{-5} MeV). The dominant processes for γ's are pair production at high energy (> 10 MeV), Compton scattering at intermediate energy (10^{-1} - 10 MeV), and the photoelectric effect at low energy (< 10^{-1} MeV). The dominant processes for $e^{\pm}$ are bremsstrahlung at high energy (> 1 MeV) and ionisation at low energy (< 1 MeV). Neutral particles (neutrons and γ's) interact before they produce a charged particle. The estimated sensitivity, as a function of kinetic energy and angle, is presented as a 2D map for neutrons (figure 5

2021 JINST 16 P12026

left) and γ's (figure 5 right). The one-dimensional projection of sensitivity as a function of incident energy for different particles at normal incidence to the detector is presented in figure 6 left. The sensitivity as a function of the incident angle for different particle types, at two energy values (1 and 100 MeV), is presented in figure 6 right.

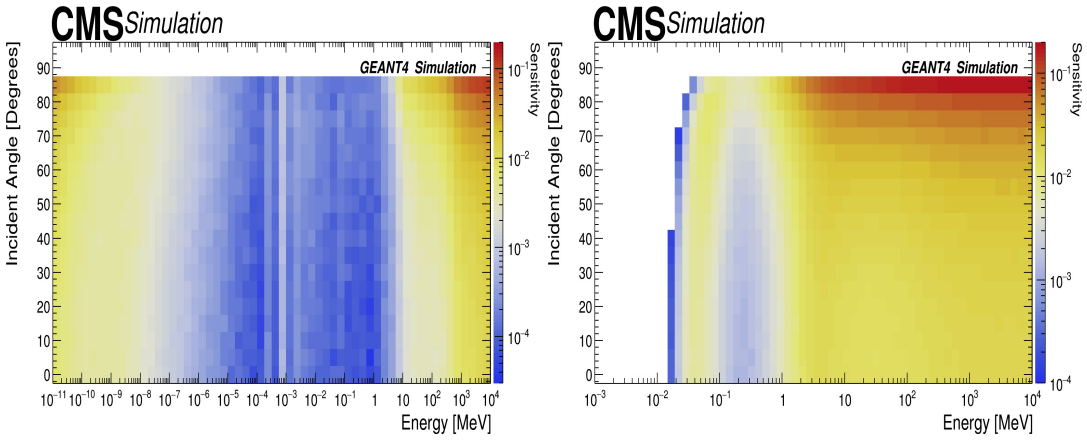

Figure 5. Sensitivity map for neutrons (left) and photons (right). The x-axis is kinetic energy and the y-axis is incident angle.

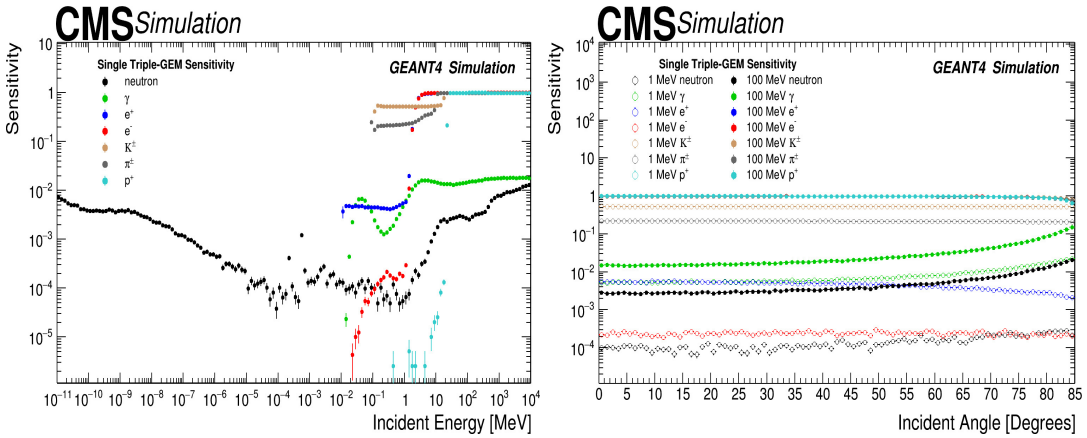

Figure 6. Sensitivity as a function of kinetic energy, for neutrons, photons and electrons, at normal incidence to the detector (left). Sensitivity as a function of incident angle for different types of particles for energy values of 1 MeV and 100 MeV (right).

The sensitivity is strongly dependent on the energy and incidence angle. The probability for an interaction is correlated to the detector width and the incidence angle. If the incidence angle increases the particle will traverse a larger distance inside the detector, so more material will be available as target for the interaction. The probability to interact is also process and energy dependent. To estimate the sensitivity, we take into account the energy spectrum of the incident particles, the energy dependent interaction probability, and the path length.

2021 JINST 16 P12026

Sensitivities are obtained using large simulated samples with $O(10^7)$ events. The statistical uncertainty depends on the type of particle under study and the region in the sensitivity map. Statistical uncertainties lie in the ranges 0-16% for neutrons, 0-2.1% for γ's, and 0-10.0% for $e^{\pm}$.

It is important to note that the sensitivities were obtained without constraints from a particular radiation environment. The only information considered was the energy ranges for the different types of particles. Thus, the results can be used for any facility in which similar triple-GEM detectors are installed [12].

The sensitivities for a single triple-GEM detector, shown in figure 6 left, are independent of the shape of the surface of the detector. These results are qualitatively similar and quantitatively compatible with those presented in ref. [12]. The main difference, for neutron sensitivity at low energies, is attributable to several reasons. The GEANT4 version used in this simulation has updated modeling for thermal neutrons. Energy thresholds for drift and transfer-1 gaps were applied in this study but not in the previous one. Lastly, the previous study simulated a detector with an additional layer of Kapton (50 µm) and FR4 (1.2 mm).

The sensitivity for photons found here is consistent with that found in the previous study. Note that a GEM detector that is part of a superchamber installed in the CMS experiment will have a response different from that of the single chamber considered here. In the following sections, the background modeling is adapted to the characteristic radiation environment of the CMS experiment and the specific detector geometry of the GE1/1 muon upgrade project.

4 Collision-induced background particles on the GE1/1 chambers

The prediction of background rate in the GE1/1 detectors requires two components: the simulation of the radiation environment and the detector response. The radiation environment is simulated with FLUKA for collision of the LHC proton beams with a center of mass energy of 13 TeV in the configuration of the CMS experiment. The simulation models particle interactions and transport through the different layers of the CMS detector. The estimation of detector response follows an approach that is similar to that described in section 3, but using the geometry of a superchamber. Both components are described in the following sections.

4.1 Radiation environment for GE1/1

The information for incoming particles reaching the GE1/1 system is extracted from a FLUKA simulation for the conditions during data-taking in Run-2, with instantaneous luminosity of 1.5×10^{34} cm^{-2} s^{-1}. The cross section of the CMS detector geometry used in the FLUKA simulation is shown in figure 7 top-left. A key property estimated with the FLUKA simulation is the flux of particles: the number of particles per unit area and per unit time weighted for their tracklength in a volume defined by the detector of interest. This distribution is presented in figure 7 top-right. Other important distributions that characterize the incoming particles are those for energy, shown in figure 7 bottom-left, and incident angle, shown in figure 7 bottom-right. These distributions are needed for the subsequent GEANT4 simulation.

The results in figure 7 are consistent with an earlier study using the FLUKA simulation [24]. The major contribution in the region where the GE1/1 detectors are located comes from low energy neutrons (10^{-11} to 10^4 MeV), γ's (10^{-3} to 10^4 MeV), $e^{\pm}$ (10^{-2} to 10^4 MeV) and charged hadrons

2021 JINST 16 P12026

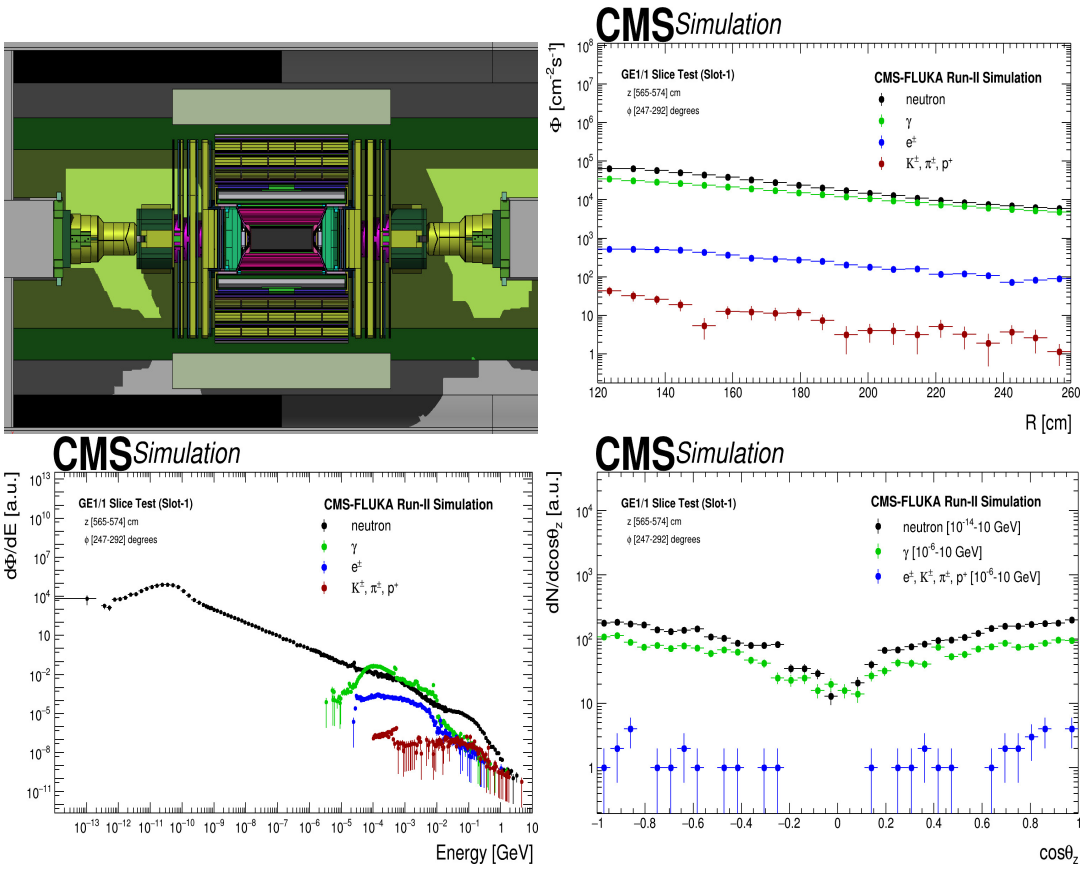

Figure 7. CMS geometry used in FLUKA simulation run v3.31.4.2 (top-left). Flux of particles, normalized to the instantaneous luminosity, arriving at the GE1/1 volume (top-right). Energy spectra of incoming particles (bottom-left) and distribution of direction cosine with respect to the normal to the detector surface for different particles (bottom-right).

(10^{-1} to 10^{4} MeV). Minor contributions to the radiation field, such as muons from gauge boson decays, are neglected as their production cross sections are an order of magnitude lower than those shown in figure 7.

4.2 Detector response for a superchamber

The detector response to background radiation depends on all the materials of the triple-GEM detector, including the electronics, cooling system, and mechanical support. The triple-GEM detectors used in the CMS experiment have additional components compared to the simple triple-GEM configuration described in section 3. Table 3 lists some of these important additional components and their details. For this study, a long chamber configuration is used, as shown in tables 1 and 2. The superchamber has a total thickness of 73.1 mm, including a space of 3.7 mm between the two detectors.

Each triple-GEM detector unit has a GEM Electronics Board (GEB) with the readout electronics and a cooling system that consists of cooling pads and cooling pipes. The cooling pipes contain

2021 JINST 16 P12026

circulating chilled water. Copper is used for the cooling pipes and pads because of its good thermal conductivity. A main component of the readout electronics for a superchamber are the VFAT-3 ASICs, based on the earlier Very Forward ATLAS and TOTEM (VFAT) ASICs [25, 26] and an Opto-Hybrid board. The VFAT-3s are used for reading, digitizing and processing the signals from the 384 strips of each η-sector of a superchamber layer. The Opto-Hybrid board is plugged into the GEB and contains Giga-Bit Transceiver (GBT) chip sets, optical receivers and transmitters, and a Field Programmable Gate Array (FPGA). Further details of the front-end electronics can be found in [8]. Figure 8 shows a GEANT4 based image of a superchamber, as used in this study.

Table 3. Additional material, layers and their dimensions used in the triple-GEM detector configuration in the CMS experiment.

Layer	z-Dimensions	Material
GEB	0.1 mm / 0.9 mm	Copper / FR4
VFAT and Opto-Hybrid	1.0 mm / 1.6 mm	FR4 / FR4
Cooling Pads	1.0 mm	Copper
Cooling Pipes	8.0 mm external, 6.0 mm internal	Copper (Filled with H_2O)
Spacers	3.0 mm / 1.0 mm / 2.0 mm / 1.0 mm	FR4
External Frame	7.2 mm	FR4
Aluminium Frame	11.5 mm	Aluminium
Cover	1.0 mm	Aluminium

The sensitivity is calculated by simulating the detailed detector configuration as described above, that is the same configuration used in the GE1/1 slice test [18]. Thresholds used in simulation are summarized in table 4 and estimated as discussed in section 3.2 but with an energy deposit threshold corresponding to 3 fC, as used in the slice test [18].

Table 4. The energy thresholds and related parameters used in the simulation of the drift and the transfer-1 gaps of the triple-GEM detector configuration. The effective gain is set to 1×10^4 and the charge threshold for readout is 3 fC.

Parameters	Drift Gap	Transfer-1 Gap
Minimum no. of electrons in the gap	2	43
Energy thresholds	56.2 eV	1.21 keV

5 Collision-induced background hit rates in GE1/1 superchambers

The hit rate is defined as the number of particles detected per unit of time in single chamber. In the slice test, the hit rate was measured for the GE1/1 superchambers as a function of instantaneous luminosity and detector area [18]. The hit rate is one of the most important quantities to measure for detector calibration and monitoring. It depends on the convolution of particle flux and sensitivities

2021 JINST 16 P12026

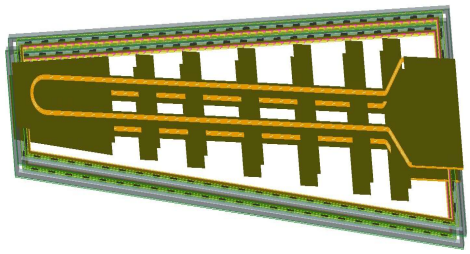

Figure 8. GEANT4 visualization of a superchamber containing two triple-GEM detectors.

for each particle type (neutrons, γ's, $e^{\pm}$, charged hadrons) as functions of energy and incident angle, as described in equation (5.1).

$$\text{Hit Rate} = \sum_{type} \text{Sensitivity}(type, E, \theta) \otimes \text{Flux}(type, E, \theta, R) \tag{5.1}$$

Here *type* is the kind of particle (*i.e.* neutrons, γ's, $e^{\pm}$ and charged hadrons), E is the energy of the incident particle and θ is the angle with respect to the normal to the detector surface. The perpendicular distance from the beamline is denoted by R. The particle flux is estimated using FLUKA as presented in figure 7 top-right and multiplied by an average sensitivity. The average sensitivity is obtained from the convolution of the sensitivity at a given energy and incident angle with the normalized abundance of particles at that energy and incident angle. The convolution over a given energy range gives the average sensitivity. The FLUKA simulation provides the information needed for all possible particle types arriving from different directions at a given position and time. The average sensitivity is used to convert the particle flux into total hits at that position.

The simulation technique used here for the sensitivity estimation is similar to that described in section 3. The main difference is that here we have a superchamber and additional material due to the presence of an extra triple-GEM detector. This affects the sensitivity of the other detector layers since sensitivity is measured for incident particles arriving at the superchamber surface from different directions. The sensitivities for Layer-2 of the superchamber, as a function of the energy of the primary incident particles arriving at the chamber surface, is shown in 9 for neutrons, photons, electrons/positrons and charged hadrons. It is convoluted over all possible incident angles and contribution from incident primary particles reaching the chamber surface from both sides are used.

The average sensitivity, estimated using the energy spectrum of the incident background particles, and the sensitivity for different energies are presented in table 5 for both Layer-1 and Layer-2. The method of using the average sensitivity is preferred over obtaining the sensitivity for different η-sectors because the detectors have a uniform response for each η-sector, as verified with X-rays during quality control tests [27].

The effect of detector material and configuration on the sensitivity can be seen by comparison of figure 6 left for the simplified geometry and figure 9 for the superchambers in the CMS experiment.

6 Systematic uncertainties

The accuracy of the sensitivity estimates relies on the correct description of the physics processes and on realistic detector modeling. The physics processes considered in this simulation are well

2021 JINST 16 P12026

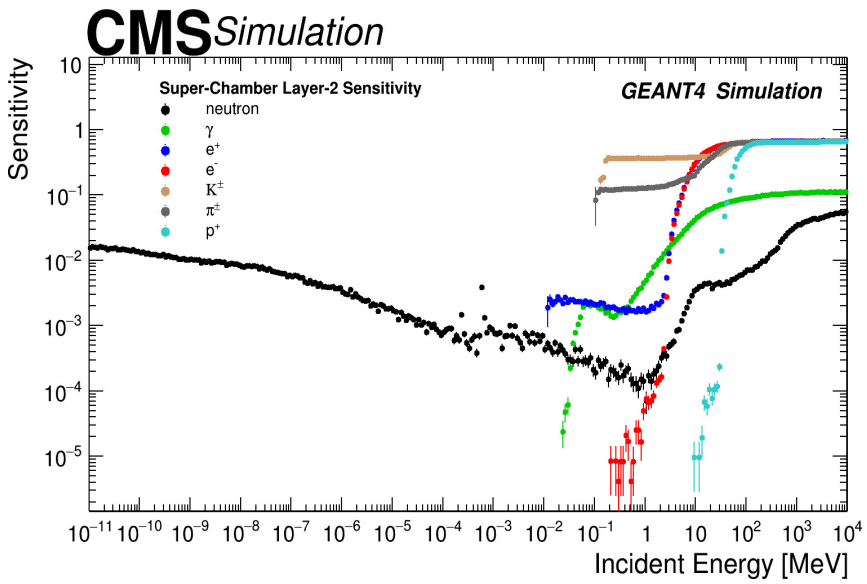

Figure 9. Sensitivity of Layer-2 as a function of incident energy for different particles. The sensitivity is convoluted over all possible incident angles.

Table 5. Average Sensitivity for each type of particle for Layer-1 and Layer-2 of the superchamber configuration used for data taking in 2018.

Particle	Average Sensitivity of Layer-1 (%)	Average Sensitivity of Layer-2 (%)
Neutron	0.64 ± 0.01 (stat.)	0.76 ± 0.01 (stat.)
γ	0.28 ± 0.01 (stat.)	0.22 ± 0.01 (stat.)
$e^{\pm}$	1.24 ± 0.04 (stat.)	0.31 ± 0.01 (stat.)
Charged Hadrons ($K^{\pm}$, $\pi^{\pm}$, p)	26.29 ± 1.24 (stat.)	24.29 ± 1.14 (stat.)

known and have been validated in the GEANT4 framework in several studies reporting comparisons with experimental data [28, 29]. To quantify the impact of the detector modeling on the sensitivity estimates the following parameters are varied.

- Drift Gap Width (DGW) variations could arise from mechanical deformations during detector assembly. Variations [8] of ±10% are used in the simulation for both layers of the superchamber. The impact on the average sensitivity of Layer-2 is shown in table 6.

- Gas Mixture Proportion (GMP) for the Ar/CO_2 (in the ratio 70/30) gas was monitored during detector operation and quality control testing and found to be negligible. However, conservative variations of (60/40) and (80/20) were considered in the simulation. The impact on the estimated average sensitivity of Layer-2 is shown in table 6.

2021 JINST 16 P12026

The impact of the parameter variations depends on the type of incident particle, kinetic energy and incident angle. We found that a single detector is less sensitive compared to the experimental configuration. The impact of parameter variations on the sensitivity for different energy ranges is also estimated. The energy ranges for neutrons are low energy (LE) from 10^{-11} to 10^{-2} MeV, intermediate energy (IE) from 10^{-2} to 1 MeV, and high energy (HE) from 1 to 10^{4} MeV. The energy ranges for γ's, $e^{\pm}$, and charged hadrons are LE from 10^{-2} to 1 MeV and HE from 1 to 10^{4} MeV. For neutrons, the maximum variation in sensitivity due to GMP variations is 1.0% for LE, 5.6% for IE, and 4.6% for HE. For γ's, $e^{\pm}$, and charged hadrons the variation in LE (HE) is estimated to be 0.8% (0.5%), 2.1% (0.3%), and 1.2% (0.1%), respectively. For DGW uncertainties, variations are similar to those for GMP, except for the neutron case in the IE region for which the statistics are low.

The systematic uncertainty is also evaluated arising from changes in the setup of the primary source near the surface of the detector. The distance of the source surface from the detector is varied by ±2 mm from the nominal value of 3 mm and the average sensitivity is re-calculated to measure the impact on the hit rate. A total variation of 0.5-0.8%, 0.0-1.0%, 0.2-0.4%, and 3.9-8.8% on the average sensitivity is estimated for neutrons, γs, $e^{\pm}$, and charged hadrons, respectively. These uncertainties are also summarized in table 6.

Table 6. Variations of simulation parameters and their impact on estimated average sensitivity. The change in sensitivity is relative to that obtained using the average sensitivity of Layer-2 shown in table 5.

Parameters	Values for Variations	Impact on average sensitivity of Layer-2 (in %)			
		Neutron	γ	$e^{\pm}$	Charged Hadrons
DGW	Drift Gap: 2.7 mm	0.6	1.4	1.0	0.5
	Drift Gap: 3.3 mm	0.3	0.4	0.0	0.6
GMP	Ar/CO_2 (60/40)	1.0	0.4	0.3	0.5
	Ar/CO_2 (80/20)	0.1	0.9	0.9	0.2
source z-position	1 mm	0.6	0.4	0.9	4.0
from superchamber	5 mm	1.0	1.4	0.9	9.9

Another systematic uncertainty comes from variation of the x-y dimensions of the source planes. The maximum variation for a 10% larger size of the source planes is about 1.3% or less for any type of incident particle. A 10% smaller size gives a maximum variation of 6.7% or less.

The uncertainties described in table 6 for different types of incident particles result in uncertainties on the hit rate. The overall uncertainty on the hit rate is dominated by neutron and photon contributions.

The systematic uncertainty associated with the particle flux is estimated by comparing the Run-2 scenario in FLUKA with an alternative scenario. In this alternative scenario, the material composition of the shielding in front of the Hadron Forward (HF) calorimeter is changed, replacing borated polyethylene by non-borated polyethylene; this change impacts the number of particles reaching the muon stations. The uncertainty is evaluated by comparing the particle flux between the two scenarios and a variation of 10 to 20% is found, depending on R, with a mean value of 15%. The latter value is considered as the associated uncertainty.

2021 JINST 16 P12026

The uncertainties in the hit rate from the FLUKA simulation and the GEANT4 detector simulation are added in quadrature. The total systematic uncertainty is about 14.5%.

7 Comparison of background modeling and experimental data

A comparison between simulation and measurement is used to validate the model presented in this study. Figure 10 compares the measured hit rate of Layer-2 of superchamber 28 with the prediction from simulation. The hit rate from simulation is obtained from the convolution of the average sensitivity shown in table 5 and the particle flux shown in figure 7 top-right. The data points in figure 10 correspond to different perpendicular distances R from the beamline to the centers of the η-sectors. As expected, the hit rate is higher at lower R (higher η) because the flux from the collision is higher in this region. The bottom panel of figure 10 shows the ratio of data to simulation and the estimated systematic uncertainty. The contributions from different types of particles to the total hit rate are shown in figure 11 for Layer-2. The largest contribution comes from neutrons while photons contribute about ∼15%. Charged hadrons and $e^{\pm}$ contribute about 1% only.

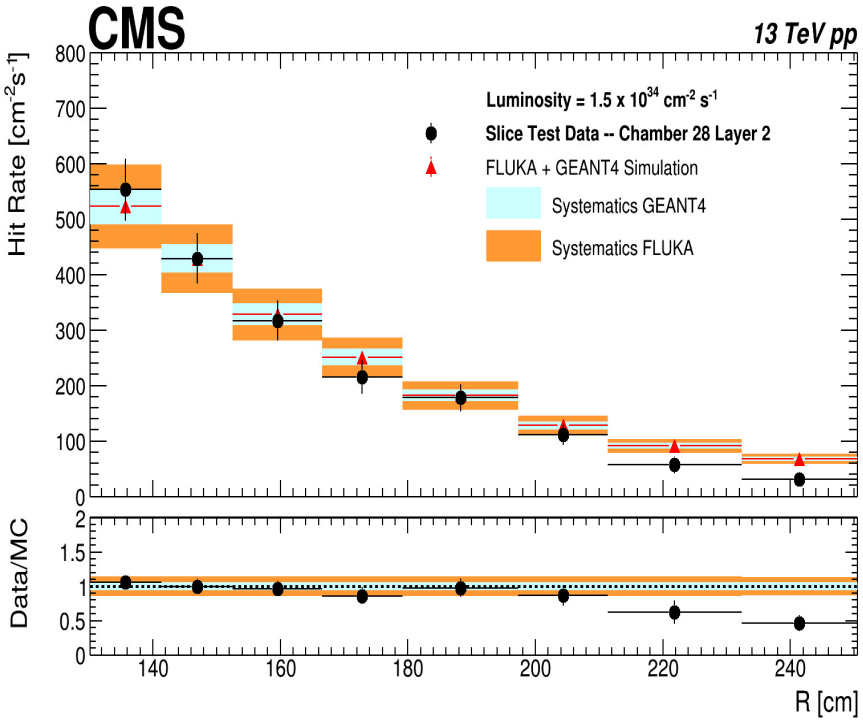

Figure 10. Comparison of the measured hit rates on Layer-2 of superchamber 28 in the slice test with the particle flux from the FLUKA simulation weighted by the sensitivity. The systematic uncertainties from the detector modelling (by the GEANT4 simulation) are shown as shaded blue bands around the prediction. The systematic uncertainties from the flux modelling for the CMS experimental configuration (by the FLUKA simulation) are shown as orange bands after adding them in quadrature with the systematic uncertainties shown in the blue band. The bottom panel shows the ratio of hit rates from data to those predicted from the simulation.

2021 JINST 16 P12026

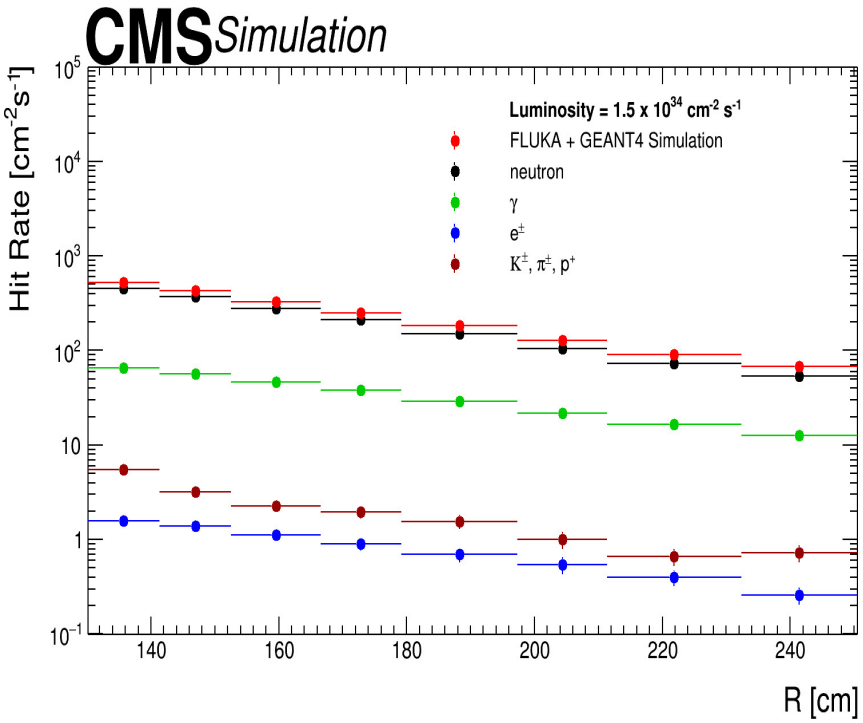

Figure 11. Prediction from simulation for hit rate contribution from different background particles at Layer-2 of superchamber 28.

The measured hit rates for the triple-GEM detector agree with those predicted from the simulation within the uncertainty except for η-sectors 1 and 2 for which data were taken with higher than nominal readout thresholds. The total uncertainty includes both the statistical uncertainty and the systematic uncertainties, described in the previous section, added in quadrature. The uncertainty of the hit rate in data includes the statistical uncertainty and uncertainties on the instantaneous luminosity measurement.

The hit rate data for $i_\eta = 1$ and 2 (sectors with $R > 210$ cm) in figure 10 are lower than the prediction. This can be explained by the higher than nominal thresholds for the VFAT-3 readout electronics during the data taking. The thresholds for $i_\eta = 1$ and 2 were 8.8 and 4.0 fC, respectively, corresponding to 6 and 3 electrons per strip in the drift gap. For $i_\eta = 1$, an energy loss of 168.6 eV ($= 6 \times 28.1$ eV) is needed to count as a "hit", resulting in a low sensitivity. In this way, the applied thresholds caused a distortion of the strip multiplicity distributions for $i_\eta = 1$ and 2. The detection efficiency for muons at $i_\eta = 1$ was most affected by the higher threshold at the strip level. While a threshold of 3 fC is low enough for our simulation model to reasonably reproduce the data, a threshold of 8.8 fC is not low enough, especially since the interaction of particles with Ar/CO_2 gas (energy loss rate) [30] and electron multiplication (gas gain) are non-linear phenomena. While it is difficult to reproduce the non-linear effects in the current simulation framework a future study could be improved with a detailed description of the electron multiplication (avalanche) e.g. using the GARFIELD [31] software package, as well as a simulation of the electronics.

2021 JINST 16 P12026

8 Summary

Collision-induced background hit rates in the CMS triple-GEM detector in pp collisions at the LHC were evaluated by modeling the radiation environment and detector response using a framework of the FLUKA and GEANT4 simulation packages. The FLUKA simulation provides kinetic energy and angular distributions of incident particles in the radiation environment. The GEANT4 simulation models particle interactions based on an accurate material description of each GEM detector. The simulated hit rates were obtained by combining the sensitivity and particle flux, and compared with measurements at a luminosity of 1.5×10^{34} cm^{-2} s^{-1} at 13 TeV. The predicted hit rates and experimental data are found to agree within their uncertainties for detector sectors with nominal operating parameters.

The framework presented in this article is generic, so it can be used for evaluation of hit rates on other detectors at High-Luminosity LHC, providing a better understanding of trigger rates and longevity of detectors.

Acknowledgments

We gratefully acknowledge support from FRS-FNRS (Belgium), FWO-Flanders (Belgium), MES and BNSF (Bulgaria), MOST and NSFC (China), BMBF (Germany), CSIR (India), DAE (India), DST (India), UGC (India), INFN (Italy), NRF (Korea), CONACYT (Mexico), MoSTR (Sri Lanka), DOE (U.S.A.), and NSF (U.S.A.).

References

[1] M. Huhtinen, *The radiation environment at the CMS experiment at the LHC*, master thesis, HU-SEFT-R-1996-14, Helsinki U. Tech., Helsinki, Finland (1996).

[2] Y. Musienko, A. Heering, R. Ruchti, M. Wayne, A. Karneyeu and V. Postoev, *Radiation damage studies of silicon photomultipliers for the CMS HCAL phase I upgrade*, *Nucl. Instrum. Meth. A* **787** (2015) 319.

[3] CMS collaboration, *The CMS muon project: technical design report*, Tech. Rep. CERN-LHCC-97-032, CERN, Geneva, Switzerland (1997) [CMS-TDR-3].

[4] R. Froeschl, M. Brugger and S. Roesler, *The CERN High Energy Accelerator Mixed Field (CHARM) facility in the CERN PS east experimental area*, in *Proceedings,* 12$^{\text{th}}$ *meeting of task-force on shielding aspects of accelerators, targets and irradiation facilities*, (SATIF-12), Batavia, IL, U.S.A., 28–30 April (2014).

[5] D. Pfeiffer et al., *The radiation field in the Gamma Irradiation Facility GIF++ at CERN*, *Nucl. Instrum. Meth. A* **866** (2017) 91 [arXiv:1611.00299].

[6] F. Sauli, *The Gas Electron Multiplier (GEM): operating principles and applications*, *Nucl. Instrum. Meth. A* **805** (2016) 2.

[7] CMS collaboration, *The CMS experiment at the CERN LHC*, 2008 *JINST* **3** S08004.

[8] A. Colaleo, A. Safonov, A. Sharma and M. Tytgat, *CMS technical design report for the muon endcap GEM upgrade*, Tech. Rep. CERN-LHCC-2015-012, CERN, Geneva, Switzerland (2015) [CMS-TDR-013].

[9] ALICE TPC collaboration, *Development of GEM-based read-out chambers for the upgrade of the ALICE TPC*, 2014 *JINST* **9** C04035.

2021 JINST 16 P12026

[10] GEANT4 collaboration, *GEANT4 — a simulation toolkit*, *Nucl. Instrum. Meth. A* **506** (2003) 250.

[11] A. Ferrari, P.R. Sala, A. Fassò and J. Ranft, *FLUKA: a multi-particle transport code (program version 2005)*, CERN yellow reports monographs CERN-2005-010, CERN, Geneva, Switzerland (2005),

[12] CMS Muon Group collaboration, *Triple-GEM discharge probability studies at CHARM: simulations and experimental results*, 2020 *JINST* **15** P10013.

[13] D. Contardo, M. Klute, J. Mans, L. Silvestris and J. Butler, *Technical proposal for the phase-II upgrade of the CMS detector*, Tech. Rep. CERN-LHCC-2015-010, CERN, Geneva, Switzerland (2015) [LHCC-P-008] [CMS-TDR-15-02].

[14] CMS collaboration, *Background rate study for the CMS improved-RPC at HL-LHC using GEANT4*, *Nucl. Instrum. Meth. A* **936** (2019) 430.

[15] C.U. Estrada et al., *RPC radiation background simulations for the high luminosity phase in the CMS experiment*, 2019 *JINST* **14** C09045.

[16] F. Ivone, *Discharge mitigation strategies for the CMS GE1/1 triple-GEM detectors*, 2020 *JINST* **15** C05009.

[17] M. Abbas et al., *Detector control system for the GE1/1 slice test*, 2020 *JINST* **15** P05023.

[18] M. Abbas et al., *Performance of a triple-GEM demonstrator in pp collisions at the CMS detector*, 2021 *JINST* **16** P11014 [arXiv:2107.09364].

[19] GEANT4 collaboration, *Physics reference manual*, in *GEANT4 — a simulation toolkit. Manual* **1** (2019) 1.

[20] M. Abi Akl, O. Bouhali, A. Castaneda, Y. Maghrbi and T. Mohamed, *Uniformity studies in large area triple-GEM based detectors*, *Nucl. Instrum. Meth. A* **832** (2016) 1.

[21] A. Sharma, *Properties of some gas mixtures used in tracking detectors*, SLAC-J-ICFA-16-3, (1998) [SLAC-JOURNAL-ICFA-16-3].

[22] F. Sauli, *Principles of operation of multiwire proportional and drift chambers*, CERN-77-09, (1977).

[23] Geant4 collaboration, *Recent developments in GEANT4*, *Annals Nucl. Energy* **82** (2015) 19.

[24] D. Abbaneo, *Impact of the radiation background on the CMS muon high-eta upgrade for the LHC high luminosity scenario*, *PoS* **TIPP2014** (2014) 086.

[25] P. Aspell et al., *VFAT2: a front-end "system on chip" providing fast trigger information and digitized data storage for the charge sensitive readout of multi-channel silicon and gas particle detectors.*, *IEEE Nucl. Sci. Symp. Conf. Rec.* (2008) 1489.

[26] P. Aspell et al., *VFAT3: a trigger and tracking front-end ASIC for the binary readout of gaseous and silicon sensors*, *IEEE Nucl. Sci. Symp. Med. Imag. Conf. Rec.* (2018) 1.

[27] M. Abbas et al., *Performance of prototype GE1/1 chambers for the CMS muon spectrometer upgrade*, *Nucl. Instrum. Meth. A* **972** (2020) 164104.

[28] A. Howard, G. Folger, J.M. Quesada and V. Ivanchenko, *Validation of neutrons in GEANT4 using TARC data — production, interaction and transportation*, *IEEE Nucl. Sci. Symp. Conf. Rec.* (2008) 2885.

[29] J. Apostolakis et al., *Validation and verification of GEANT4 standard electromagnetic physics*, *J. Phys. Conf. Ser.* **219** (2010) 032044.

[30] Particle Data Group collaboration, *Review of particle physics*, *PTEP* **2020** (2020) 083C01.

[31] R. Veenhof, *GARFIELD, recent developments*, *Nucl. Instrum. Meth. A* **419** (1998) 726.

2021 JINST 16 P12026

Exotic searches by ATLAS and CMS

A Kaur on behalf of ATLAS and CMS collaborations
Department of Physics, Panjab University, Chandigarh (IN)
E-mail: amandeep.kaur@cern.ch

Abstract. ATLAS and CMS are two general-purpose detectors setting almost opposite to each other at the LHC ring. Both detectors resulted in the discovery of Higgs Boson in 2012. With successful data taking during Run-II, ATLAS and CMS recorded up to $139fb^{-1}$ of integrated luminosity and probes for rare and exotic decays and sets exclusion limits on various models searching beyond standard model physics.

1. Introduction

The standard model (SM) of particle physics successfully explains the structure of matter and forces acting between them but still, it fails (i) to include the fourth fundamental force i.e. gravitational force (ii) to explain matter-antimatter in the universe (iii) to explain the 95% dark energy and dark matter forming the universe and so on.

There are several models evolved with time to explain the physics beyond the standard model and are known as "Beyond Standard Model (BSM)". Some examples of these models are Sequential-SM, E_6 model, Grand Unified Theories (GUT). Different search strategies have been incorporated at the LHC to find answers to the above questions.

LHC successfully recorded data up to December, 2018 around $\sim 139fb^{-1}$ of integrated luminosity from p-p collisions at 13 TeV as shown in figure 1.

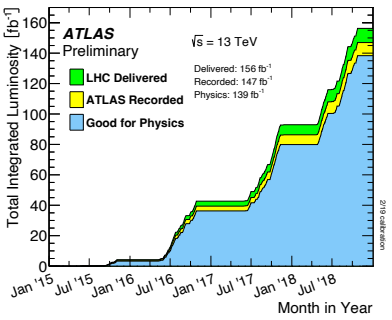

Figure 1. Luminosity recorded by the ATLAS experiment.

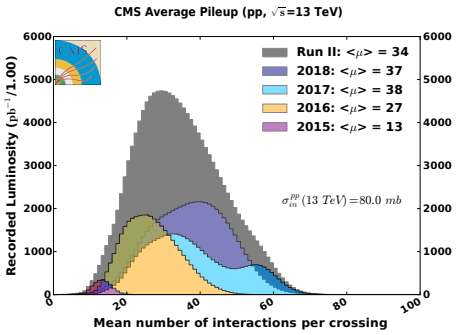

Figure 2. Mean number of interactions per bunch crossing.

This marks the end of Run-II. The luminosity obtained at the LHC helps to investigate the different extensions of the Standard Model. The biggest challenge due to this large instantaneous

luminosity is the number of simultaneous collisions (called pile-up events) which increase the background and complicates the reconstruction as shown in figure 2.

Due to space constraints, we are providing a snapshot of the latest results recorded by ATLAS and CMS detectors and are classified into four major categories: heavy resonances, new leptons and quarks, dark matter, and new leptons and quarks based on theoretical motivations.

2. Heavy resonances

The most striking signature for the existence of new physics beyond the standard model is the existence of heavy resonance such as excited quarks, new heavy gauge bosons, gravitons or dark matter which eventually decay to standard model particles giving pairs of jets, leptons, photons, or more complicated objects like W and Z bosons and top quarks as the possible final states. Dedicated reconstructions mechanisms and background estimation methods have been utilized by both ATLAS and CMS to search for such kind of signatures.

2.1. Dijet resonance search

The dijet resonance search is the best approach to search for extremely high masses due to large production cross-section of jet final states. But, with the large sensitivity towards the signal, the biggest challenge in these searches is the handling of QCD or other jet backgrounds.

In this search [1] carried out by CMS, a new data-driven method is introduced for $m_{jj} > 2.4$ TeV which predicts the background from a control region where the pseudorapidity separation of the two jets ($|\delta\eta|$) is large. This new method termed as "ratio method" leads to improvement in the sensitivity for broad resonances by a factor of two depending on the resonance width and mass. Also, to reduce analysis sensitivity to final state radiations (FSR), two close-by jets are combined forming a wide jet with a cone size of 0.8 as shown in figure 3.

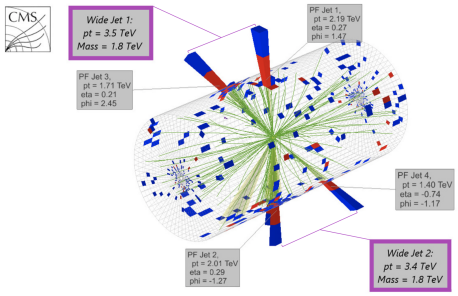

Figure 3. Event display containing four jets depositing energy in CMS calorimeters grouped together to two wide jets.

Due to better data-driven background estimate from "ratio method" than the traditional "fit method", larger signal significance has been observed with the ratio method. With this search, limits are improved by 200 GeV TO 800 GeV for narrow resonances relative to those reported in previous CMS dijet resonance searches. Figure 4 describes the exclusion limits for various models predicting new resonances.

Another benchmark was set with analyzing data collected at high-level trigger (HLT) level to get sensitivity in lower masses. With this technique called Data Scouting, events containing three jets are reconstructed, selected, and recorded in a compact form with lower thresholds using only calorimeter information by the high-level trigger. The spectrum of the dijet invariant mass, calculated from the two jets with the largest transverse momenta in the event, is used to search for resonance. No significant excess has been observed over a smoothly falling background. This search [2] presents the most stringent upper limits in the mass range between 350 and 450 GeV as shown in figure 5.

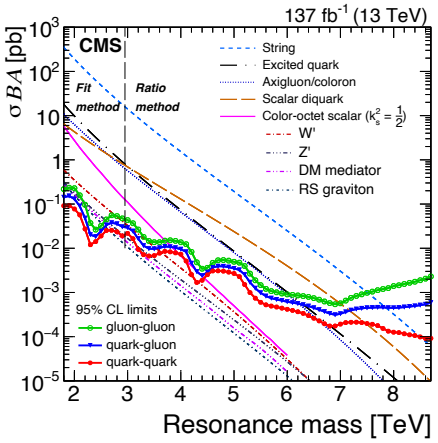

Figure 4. The observed 95% CL upper limits on the product of the cross-section, branching fraction, and acceptance for quark-quark, quark-gluon, and gluon-gluon type dijet resonances.

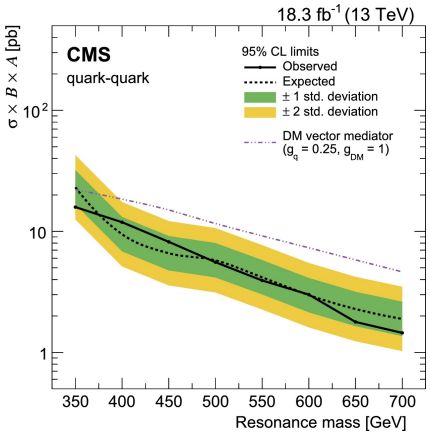

Figure 5. Upper limits at 95% CL on the product of the cross-section, branching fraction, and acceptance as a function of resonance mass for a narrow resonance decaying into a pair of quark jets using data-scouting technique.

Another search [3] for $t\bar{t}$ resonance decaying to fully hadronic final states has been carried out by ATLAS experiment exploiting an advanced top-tagger based on deep neural network (DNN) technique. In this technique, a single large-R jet captures the top-quark decay products and accordingly multiple jet-level discriminants are used as input to the DNN tagger such as jet transverse momentum and mass, information about the dispersion of the jet constituents, splitting scales and energy correlation functions. The signal region is further divided into two regions containing 1b or 2b jets tagged as variable radius (VR) track jets containing b-hadrons identified using multivariate classification technique with an artificial deep neural network to combine track information within a jet. A parametric fit has been performed over data and no significant excess has been observed. Upper limits are set on the production cross-section times branching fraction for Z' in the topcolor-assisted-technicolor model, resulting in the exclusion up to 3.9 and 4.7 TeV for decay widths of 1% and 3%, respectively as shown in the figure 6.

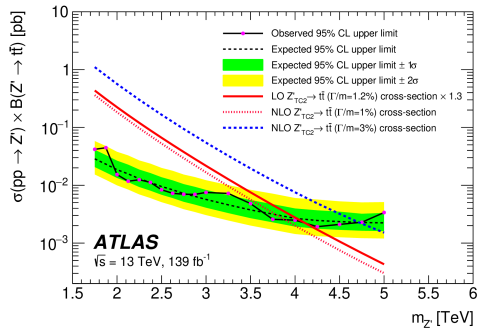

Figure 6. Observed and expected upper limits on the cross-section times branching fraction of the Z' $\rightarrow t\bar{t}$ as function of Z' mass.

However, improved analysis techniques have provided 65% improvement in the expected cross-section limit at 4 TeV with the same data set.

2.2. Diboson resonance search

For the diboson resonance searches, the search becomes more challenging. Due to the production of heavy bosons in the TeV scale, the decay products produced are generally boosted and hence it becomes critical to combine the calorimeter information with the tracker angular information. ATLAS and CMS have extensive search strategies to search for diboson resonances. With the increasing centre of mass energy, the novel techniques have been developed such as 3D likelihood fits and anomaly detection techniques for broadening the scope of these searches. Both ATLAS and CMS search for diboson resonances [4] [5] with all possible final states i.e. 0-lepton, 2-lepton final state with associated jet from H decay. ATLAS also considered the fully hadronic decay [6] of the diboson resonance. Whereas, to enhance sensitivity for the search, CMS considered the VBF production mechanism of the ZH resonance. As no significant excess has been observed, upper limits with 95% CL are set on masses for Z' for 0-lepton, 2-lepton channel and in fully hadronic final states by ATLAS and is shown in figure 7. Similarly, CMS sets exclusion limits for VBF 0-lepton and 2-lepton final state with 95% confidence level for the HVT benchmark Model C where Z' couples only to the SM bosons as shown in figure 9.

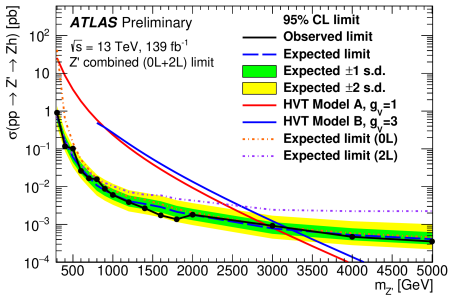

Figure 7. Upper limits at the 95% CL on the product of the cross section for pp $\rightarrow$ Z' and their respective branching fraction to ZH from the combination of the 0-lepton and 2-lepton channels.

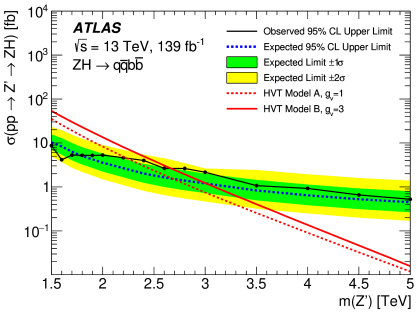

Figure 8. Upper limits at the 95% CL on the product of the cross section for pp $\rightarrow$ Z' and their respective branching fraction to ZH for fully hadronic channel.

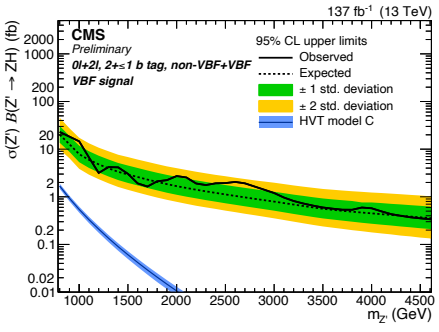

Figure 9. Upper limits at the 95% CL on the product of the cross section for pp $\rightarrow$ Z' and their respective branching fraction to ZH from the combination of the 0-lepton and 2-lepton channels with VBF signal.

3. New leptons and quarks

One of the biggest questions remains unanswered by the standard model theory is the symmetry between the quarks and lepton families. Several models such as Grand unified theories, technicolor models etc foresee new particles that carry both lepton and baryon number and are knows as 'Leptoquarks (LQ)". Recently, LQ search gained more importance because it may explain B-meson anomalies.

ATLAS probes for the LQ with two search categories: LQ decaying to τ lepton and top quark [8] and to e (or μ) and top quark [9]. In the former case, five final states, based on the multiplicity and flavour of lepton candidates, are considered and each of them is divided into several event categories to constrain several leading background in each final state. No significant excess above the Standard Model expectation is observed and 95% CL upper limits are set on the production cross section as a function of the LQ mass, under different assumptions for the branching fractions into $t\tau$ and $b\nu$ as shown in figure 10.

For the scalar LQ decaying to a top quark and either an electron or a muon, the normalization of dominant backgrounds such as Z+jets and $t\bar{t}$ is determined with profile likelihood fit to a binned BDT in the signal region and two dedicated control regions. The observed data distributions are compatible with the expected Standard Model background and lower limits on the production cross-section are set at 1.48 TeV and 1.47 TeV for the electron and muon channels, respectively as shown in figure 11.

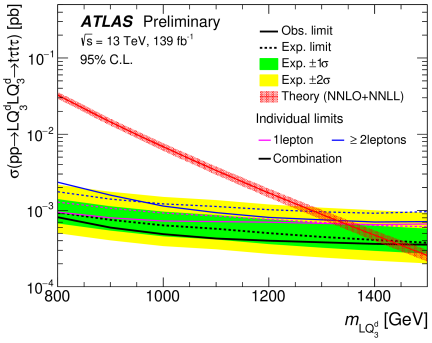

Figure 10. Observed (solid line) and expected (dashed line) 95% CL upper limits on the LQ_3^d pair production cross-section as a function of $m_{LQ_3^d}$.

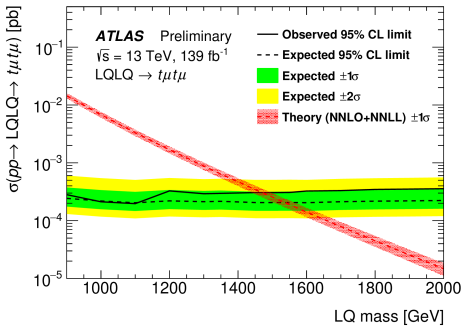

Figure 11. Observed (solid line) and expected (dashed line) 95% CL upper limits on the cross section of LQ pair production as a function of LQ mass assuming B($LQ \rightarrow t\ell^{\pm}$) = 1, for muon channels.

Recently, CMS considered the search for LQ [9] in which LQ may couple to a top quark plus a τ lepton ($t\tau$) or a bottom quark plus a neutrino ($b\nu$, scalar LQ), or else to $b\tau$ or $t\nu$(vector LQ), leadingt o the final states $t\tau\nu b$ and $t\tau\nu$. The channel in which both the top quark and the τ lepton decay hadronically is investigated, including the case of a large LQ-t mass splitting giving rise to a boosted top quark whose decay products may not be separated on the scale of the spatial resolution of the jet. Such a signature has not been previously examined in searches for physics beyond the standard model. The observations are found to be in agreement with the standard model prediction.Exclusion limits are given in the plane of the LQ-lepton-quark vertex coupling λ and the LQ mass for scalar and vector LQ. The range of lower limits on the

LQ mass, at 95% CL,is 0.98-1.73 TeV, depending on λ and the LQ spin as shown in figure 12.

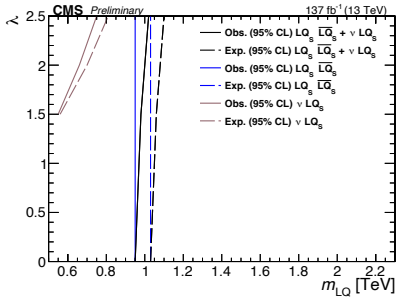

Figure 12. The observed and expected (solid and dotted lines) 95% CL LQ exclusion limits in the plane of the LQ-lepton-quark vertex coupling and the mass of the LQ for single (brown lines),pair (blue lines) production, and considering their sum (black lines).

4. Dark matter searches

Gravitational effects on astrophysical scale provide convincing evidence for the existence of non-luminous and Weakly interacting matter which constitutes up to 26% of the matter-energy content of the Universe. At hadron colliders, searches for this weakly interacting DM have to rely on one or more visible particles being produced in association with the invisible DM candidate. Large missing energy in the collision events is the only experimental signature for the DM search.

Several models populate the "theory space" of all possible realizations of physics beyond the SM with a particle that is a viable DM candidate. A common model to interpret the observations known as "simplified DM model" assumes a vector, axial-vector, scalar, or pseudoscalar mediator, which decays into a pair of fermionic DM particles and interacts with SM particles. More complete models involve a 2HDM+a model (or two-Higgs-doublet) in which the pseudoscalar mediator coupling to DM also couples to Higgs boson. ATLAS and CMS have an extensive search program to search physics beyond standard model after the discovery of Higgs boson.

ATLAS presents its first measurements [10] for processes where the pseudo-scalar mediator is produced in association with a single top quark. Several final states are considered, including either one or two charged leptons (electrons or muons) and a significant amount of missing transverse momentum. No significant excess is found with respect to Standard Model predictions. The results are expressed as 95% confidence level limits on the 2HDM+a signal models as shown in figure 13.

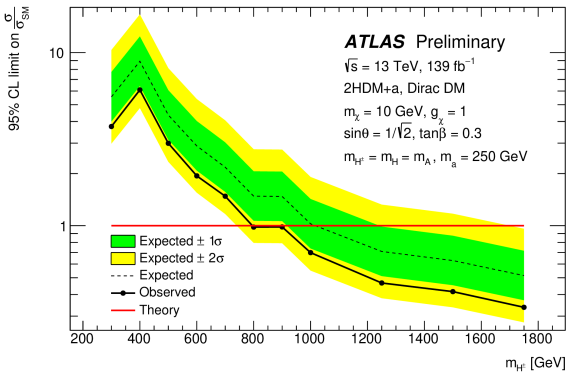

Figure 13. The expected and observed cross-section exclusion limits as a function of $m_{H^\pm}$ for signal models with $m_a = 250$ GeV.

Also, a search [11] with an energetic jet and large missing transverse momentum is reported by ATLAS. Compared to previous publications, in addition to an increase of almost a factor of

four in the data size, the analysis implements several improvements in the signal selection and the background estimation leading to enhanced sensitivity. Events are required to have at least one jet with transverse momentum above 150 GeV and no reconstructed leptons (e, μ *or* τ) or photons. Several signal regions are considered with increasing requirements on the missing transverse momentum starting at 200 GeV. An overall agreement is observed between the number of events in data and Standard Model predictions. Model-independent 95% confidence level limits on visible cross sections for new processes are obtained in the range between 861 fb and 0.3 fb as shown in figure 14.

Another pioneering search [12] is performed by ATLAS for dark matter particles produced in association with a Dark Higgs boson decaying to VV where V= $W^{\pm}, Z$. The $s \to V(q\bar{q})V(q\bar{q})$ decays are reconstructed with a novel technique using reclustered jets with a cone parameter R=0.8 based on R=0.4 calorimeter jets and tracking information. The observed data are found to agree with Standard Model predictions. The results provide exclusions in the previously uncharted parameter space of the Dark Higgs model for m_s >160 GeV as shown in figure 15.

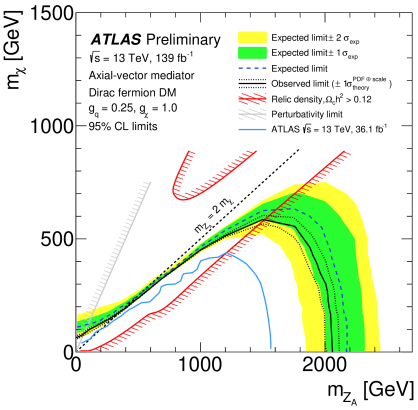

Figure 14. 95% CL exclusion contours in the m_{Z_A}–m_χ parameter plane for the axial-vector mediator model.

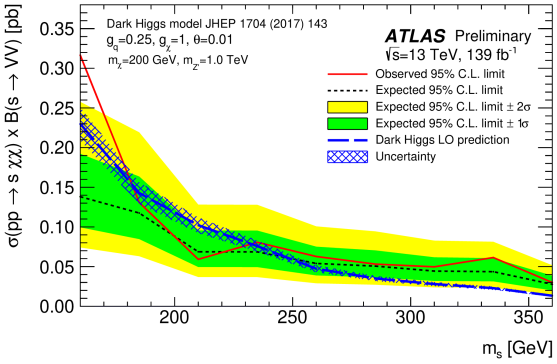

Figure 15. Observed excluded $\sigma(pp \to s\chi\chi) \times B(s \to VV)$ for the Dark Higgs model at a 95 C.L., compared to the SM-only expectation.

CMS presents a search [13] for a scalar boson H produced in the Vector Boson Fusion (VBF) production mode and decaying to an undetected particle and a photon. Such Higgs boson decays are predicted by several BSM models. In this search, the target final state is qqH($\to \gamma\gamma_D$), where the final state quarks (q) arise from the VBF process and γ_D is a massless dark photon that couples to the Higgs boson through a charged dark sector. The dark photon escapes the CMS detector undetected. No significant excess of events above the expectation from the standard model background is found. The results are used to place limits on the product of the signal cross section for VBF production and the branching fraction for such decays of the Higgs boson,in the context of a theoretical model where the undetected particle is a massless dark photon as shown in figure 16.

5. Unconventional signatures

The existence of long-lived particles and unconventional signatures are features of both standard model (SM) and beyond standard model (BSM) scenarios and are predicted by many extensions of the SM, like several SUSY scenarios (e.g. Gauge Mediated Supersymmetry Breaking or

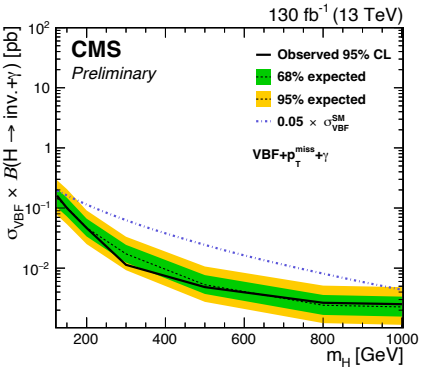

Figure 16. Expected and observed upper limits at 95% CL on the product of σ_{VBF} and $B(H \rightarrow invisible + \gamma)$ as a function of m_H.

scenarios with mass-degenerate gauginos) and in models where there is a hidden sector that couples very weakly to visible sector fields. These new long-lived particles would show up in several different topologies in detectors: delayed photons, displaced track vertexes, displaced jets and leptons, disappearing tracks, almost stable charged particles, particles stopped in the detector, and emerging jets. The LHC detectors were not originally intended to detect particles that decay further than a few centimeters from the beamline and the original focus for displaced signature was only on detecting jets containing bottom or charm quarks, which decay a few hundred micrometers from the beam axis.

CMS has presented results for long-lived particles decaying into jets. The analysis [14] examines the distinctive topology of displaced tracks and displaced vertices within a dijet system.To discriminate against SM backgrounds such as QCD, a multivariate discriminant is constructed based on variables such as: Vertex track multiplicity, Vertex L_{xy} significance, Cluster RMS and κ. For the multivariate discriminant , the Gradient Boosted Decision Trees (GBDT) is utilized and due to insufficient statistics of simulated QCD, data is used for the training and testing. The signal yields in the final signal region are used to set limits on a variety of models. The expected and observed 95% CL upper limits on the branching fraction of the SM Higgs boson to decay to two long-lived scalars, assuming the gluon-gluon fusion SM Higgs production cross section of 49 pb at 13 TeV with m_H=125 GeV, shown in figure 17 at different masses and $c\tau_0$ for the scalar S.

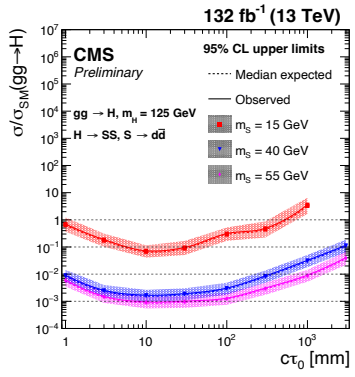

Figure 17. The expected and observed 95% CL upper limits on the branching fraction of the SM Higgs boson to decay to two long-lived scalars.

Talking of unconventional signatures comes the violation of the assumption that the number of leptons in each family is conserved in interactions known as Lepton Flavour Violation (LFV). LFV is not possible in the SM, even though no fundamental principles forbid it. The observation

of neutrino oscillations, where neutrinos (the neutral leptons) of one flavour transform into that of another, indicates that LFV processes do occur in Nature. It reveals that neutrinos have mass, and this constitutes the first experimental evidence of new phenomena beyond those originally predicted by the SM. The ATLAS experiment sets a new strong constraint on Lepton Flavour Violation effects in weak interactions, searching for Z boson decays into a τ-lepton and another lepton of a different flavour (e *or* μ) with opposite electric charge [15]. Only events with a τ-lepton that decays hadronically are considered. Neural network classifiers are used in a novel way for optimal discrimination of signal from backgrounds and improved sensitivity in the measurement of LFV effects from the data using a binned maximum-likelihood statistical fit. The LHC Run 2 result is combined with a previous LHC Run 1 result to further improve sensitivity. These results set stringent constraints on LFV Z decays involving τ-leptons, superseding the otherwise most stringent ones set by the LEP experiments. Using a combination of LHC Run 1 and Run 2 proton-proton collision data, the branching fractions for these decays are now measured by the ATLAS experiment to be less than 9.5 x 10^{-6} ($\mu\tau$) and 8.1 x 10^{-6} ($e\tau$) at 95% confidence level as shown in figure 18.

	Observed (expected) upper limit on $\mathcal{B}(Z \to \ell\tau)$ [$\times 10^{-6}$]	
Experiment, polarisation assumption	$e\tau$	$\mu\tau$
ATLAS Run 2, unpolarised τ	8.1 (8.1)	9.9 (6.3)
ATLAS Run 2, left-handed τ	8.2 (8.6)	9.5 (6.7)
ATLAS Run 2, right-handed τ	7.8 (7.6)	10 (5.8)
ATLAS Run 1, unpolarised τ [53]		17 (26)
ATLAS Run 1 and Run 2, unpolarised τ		9.5 (6.1)
LEP OPAL, unpolarised τ [10]	9.8	17
LEP DELPHI, unpolarised τ [11]	22	12

Figure 18. The expected (median) and observed upper limits on the signal branching fraction at 95% CL.

6. Conclusion

The outstanding performance of the LHC led to $\sim 140 fb^{-1}$ of data accumulated at $\sqrt{s} = 13$ TeV, exceeding the expectations. This large amount of data has allowed for a multitude of searches for beyond Standard Model scenarios involving striking new signatures, like heavy resonances, new leptons and quarks, long-lived particles, and dark matter. Unfortunately, no significant excess of events has been observed above standard model expectations and the measurements are consistent with the Standard Model. While moderate improvements for extremely high mass searches are expected in future, there are several new approaches, targeting low and intermediate-mass regions and using novel experimental techniques, which will explore new territories during next years.

References

[1] Adam W *et al.* (CMS Collaboration) 2020 J. High Energy Phys. JHEP33(2020)
[2] Sirunyan A M *et al.* 2020 (CMS Collaboration) *Phys. Lett.* B **805** 135448
[3] Aad G *et al.* (ATLAS Collaboration) 2020 *Preprint* CERN-EP-2020-055 URL http://cds.cern.ch/record/2717782
[4] Aad G *et al.* (ATLAS Collaboration) *Preprint* ATLAS-CONF-2020-043 URL http://cds.cern.ch/record/2728053
[5] Sirunyan A M *et al.* (CMS Collaboration) 2019 *Preprint* CMS-PAS-B2G-19-006 URL http://cds.cern.ch/record/2725672
[6] Aad G *et al.* (ATLAS Collaboration) 2020 *Preprint* CERN-EP-2020-073 URL http://cds.cern.ch/record/2723644
[7] Aad G *et al.* (ATLAS Collaboration) 2020 *Preprint* ATLAS-CONF-2020-029 URL http://cds.cern.ch/record/2725735
[8] Aad G *et al.* (ATLAS Collaboration) 2020 *Preprint* ATLAS-CONF-2020-033 URL http://cds.cern.ch/record/2725739
[9] Sirunyan A M *et al.* (CMS Collaboration) 2019 *Preprint* CMS-PAS-EXO-19-015 URL https://cds.cern.ch/record/2725349
[10] Aad G *et al.* (ATLAS Collaboration) 2020 *Preprint* ATLAS-CONF-2020-034 URL http://cds.cern.ch/record/2727741

[11] Aad G *et al.* (ATLAS Collaboration) 2020 *Preprint* ATLAS-CONF-2020-048 URL http://cds.cern.ch/record/2728058
[12] Aad G *et al.* (ATLAS Collaboration) 2020 *Preprint* ATLAS-CONF-2020-036 URL http://cds.cern.ch/record/2727743
[13] Sirunyan A M *et al.* (CMS Collaboration) 2020 *Preprint* CMS-PAS-EXO-20-005 URL https://cds.cern.ch/record/2724995
[14] Sirunyan A M *et al.* (CMS Collaboration) 2019 *Preprint* CMS-PAS-EXO-19-021 URL http://cds.cern.ch/record/2717071
[15] Aad G *et al.* (ATLAS Collaboration) 2020 *Preprint* ATLAS-CONF-2020-035 URL http://cds.cern.ch/record/2727742

CERTIFICATE

This is to certify that

Amandeep Kaur

Panjab University, India

Took part in the conference LHCP2021 online and presented the following poster

"*Search for New Heavy Neutral Gauge Boson using Vector Boson Fusion Processes at the LHC*"

Connie Potter
For
The Local Organising Committee

Certificate

Amandeep Kaur

has successfully participated and presented a talk titled

Study of Radiation Damage in the CMS Hadron Calorimeter using Isolated Muons from 2018 Collision Data

XXIV DAE-BRNS Symposium on High Energy Physics

held **ONLINE** by the

National Institute of Science Education and Research

Jatni 752050 Odisha India

during

December 14-18, 2020

Prof. Bedangadas Mohanty
(Chair)

Prof. Sanjay Swain
(Co-Chair)

Sponsors & Organizers